VERY HIGH FREQUENCY THERMAL-PIEZORESISTIVE RESONATORS AND SELF-SUSTAINED OSCILLATORS

by

Harris J. Hall

B.S., Rensselaer Polytechnic Institute 1999

M.S., Air Force Institute of Technology 2001

A thesis submitted to the Faculty of the Graduate School of the University of Colorado in partial fulfillment of the requirement for the degree of

Doctor of Philosophy

Department of Mechanical Engineering

2013

This thesis entitled:
Very High Frequency Thermal-Piezoresistive Resonators and Self-Sustained Oscillators
written by Harris Hall
has been approved for the Department of Mechanical Engineering

_____
Victor. M. Bright
Committee Chairman, Dept. of Mechanical Engineering

_____
J. Scott Bunch
Dept. of Mechanical Engineering

_____
Y.C. Lee
Dept. of Mechanical Engineering

_____
Siavash Pourkamali
University of Texas at Dallas, Dept. of Electrical and Computer Engineering

_____
Robert Fitch
Air Force Research Laboratory Sensors Directorate

Date_____

The final copy of this thesis has been examined by the signatories, and we
find that both the content and the form meet acceptable presentation standards
of scholarly work in the above mentioned discipline.

Hall, Harris J. (Ph.D., Department of Mechanical Engineering)

Very High Frequency Thermal-Piezoresistive Resonators and Self-Sustained Oscillators

Thesis directed by Professor Victor M. Bright

ABSTRACT

Microelectromechanical resonators utilizing active transduction schemes are emerging as a strong alternative to traditional capacitive and piezoelectric devices. Thermally actuated piezoresistive readout devices are one such class that shows unique promise. Their unique ability to self-oscillate under DC bias through internal feedback is especially promising for both on-chip sensing and clocking applications. Previous work theorized through a lumped parameter system model that further miniaturization of designs should both increase the operating frequency and improve resonator performance.

This work examined this assertion experimentally with the design, fabrication, and characterization of devices with area footprints as low as 50 μm^2 (pad interconnects removed). Devices were fabricated in multiple I-shaped geometries on 340 nm and 2 μm thick n-type single crystal silicon (SCS) using different submicron patterning methods. Device operation in the VHF regime as both resonators and self-sustained oscillators was achieved in both ambient air and low vacuum conditions (50-70 Torr). Resonators were demonstrated up to 206 MHz, over 3x higher frequency than previous work, demonstrating quality factors >20,000 in vacuum and >10,000 in ambient air. Self-sustained oscillation was demonstrated up to 160 MHz (4x higher than prior work) in ambient air with peak-peak signal amplitudes up to 40 mV. Device operation as oscillators was examined using a laser sensing testbed to verify the mechanical frequency of oscillation and explore changes in device response to illumination. Frequency tuning and on/off control of the self-sustained oscillation was demonstrated by adjusting the laser power. Modeling and simulation was performed using COMSOL multiphysics software to examine structural modes and electrothermomechanical response in support of experimental findings.

This dissertation is dedicated to my wife Jessica, and to my children Hannah, Xavier, Eva, Isaac, and Desmond.

“Nothing in the world can take the place of Persistence.
Talent will not; nothing is more common than unsuccessful men with talent.
Genius will not; unrewarded genius is almost a proverb.
Education will not; the world is full of educated derelicts.
Persistence and determination alone are omnipotent.
The slogan 'Press On' has solved and always will solve the problems of the human race.”

Calvin Coolidge (1872 - 1933)
30th President of the United States

ACKNOWLEDGEMENTS

Experimental research is almost always an interdisciplinary effort requiring a variety of skill sets and technical expertise to accomplish. This work was no exception. I consider myself extremely fortunate to have been able to leverage the expertise and resources necessary for the completion of this work through the efforts of several exemplary individuals and organizations whom I will now attempt to enumerate.

To begin, my ability to attend graduate school was largely predicated upon the financial support I received from the DOD SMART scholarship program and the Air Force Research Laboratory. I am extremely grateful to both for affording me the unique privileged opportunity to both pursue my graduate studies and be able to continue to work in service of my country. My SMART mentor, Dr. Bill Siskaninetz, has been supportive both during my summer internships and throughout my work.

I decided to apply and attend graduate school at the University of Colorado largely due to the positive feedback I received from my advisor's former students. Professor Bright was generous in his support of me from the very beginning and throughout my studies, both technically and financially. Like many graduate students, I endured significant failures prior to achieving success and I am grateful for his patient support of me throughout these years.

My research efforts at CU-Boulder spanned three different projects, the third of which became the subject of this thesis. Throughout this time, the Bright group provided thoughtful discussion, mentorship, and friendship. I am grateful to Brad Davidson for introducing me to the world of nanoscale fabrication and its challenges. In particular I would like to thank the postdocs of the group Joe Brown and Jason Gray. Both provided guidance and insight critical to the success of this work. Joe Brown additionally spent many hours collecting most of the FIB SEM images shown in this work and supported the FIB milling of devices

From the beginning of my studies I also became very reliant upon the assistance and knowledge of Prof Scott Bunch and his research group. I have had the privilege of working with all the students in his group (Steven Koenig, Xinghui Lui, Luda Wang and Lauren Cantley) on a variety of different pursuits through the years. In particular, the optical sensing testbed used for device characterization is maintained and operated by Luda Wang, without whom these results would not have been possible. Additionally, Mr. Tim May of the ITLL was instrumental in providing the equipment needed for this portion of the work.

The Pourkamali group at the University of Denver, which originally conceived and developed the in-plane thermal-piezoresistive resonators that were the focus of this work, also deserves considerable recognition. All the electrical testing of these devices was performed using the test equipment in their lab. Amir Rahafrooz spent many hours discussing the testing

methods and device operation with me. He performed the initial data analysis for our first devices and educated me on wire bonding and equipment usage, for which I am very grateful. Arash Hajjam, Emad Mehdizadeh, Xiaobo Guo, and other members of the group also provided support and fruitful discussion.

Experimental work in microsystems is predicated upon actually having functional devices to test, making device fabrication a linchpin to success. To this end I am deeply appreciative of both the efforts of the staff at the Colorado Nanofabrication Lab, namely Jan van Zeghbroeck, Tomoko Borsa and Prof Bart van Zeghbroeck's research group, and personnel at the Air Force Research Laboratory Sensor Directorate, namely Dr. Robert Fitch, Dr. Dennis Walker Jr., Mr. Steve Tetlak, Mr. Kelson Chabak, and Mr. Andrew Browning. Without the support from these individuals the devices presented in this work would not exist.

The financial support needed for device fabrication was provided in part by the National Science Foundation (Award Number 1056068) and the Defense Advanced Research Projects Agency (DARPA) Center on Nanoscale Science and Technology for Integrated Micro/Nano-Electromechanical Transducers (iMINT), N/MEMS S&T Fundamentals program under grant no. N66001-10-1-4007 issued by the Space and Naval Warfare Systems Center Pacific (SPAWAR). The Colorado Nanofabrication Laboratory a member of the NNIN sponsored by the National Science Foundation under Grant No. ECS-0335765. Additional funding was provided by the Air Force Research Laboratory for the use of cleanroom facilities.

Additionally, I would like to thank Prof Alan Mickelson, and Dr. Pavel Kabos for technical discussion during the course of this work as well as Ms. Sharon Anderson for being exceptionally diligent in ensuring I've met the graduate school's logistical challenges. I supported the USAF Scientific Advisory Board as a USAFR reservist throughout my studies and I am grateful to my supervisor Col Ed Ryan and the SAB staff for providing the flexibility I required in order to accommodate the rigorous work schedule I pursued.

Last, but certainly not least, I want to recognize my wife Jessica who provided much needed solace throughout the ups and downs of graduate school life and endured many days and nights raising our children (including our newborn twins) in my absence while I was toiling in the lab or library. While my children, Hannah, Xavier, Eva, Desmond and Isaac, may not realize it they too played an important role in keeping me grounded throughout this exciting period of our lives. I feel tremendously blessed to have them a part of my life.

TABLE OF CONTENTS

Abstract iii

Acknowledgements vi

Table of Contents viii

List of Figures xi

List of Tables xxii

1. Introduction 1

1.1. Unique Characteristics of On-Chip Thermal-Piezoresistive Resonant Devices 1

1.2. Overview, Scope and Organization of this Research 1

1.3. Primary Accomplishments 2

2. Background and Literature Review 4

2.1. Resonant Device Terminology 4

2.2. Forced Harmonic Vibration of the Mass-Spring-Damper System 6

2.3. Quality Factor of Resonant Systems 10

2.4. Advantages and Applications of Micromechanical Resonators 13

2.5. Performance Considerations for Micromechanical Resonators 15

2.6. Brief Summary of On-chip Silicon RF Resonators 16

2.7. High Frequency (HF) Thermally Actuated Resonant Devices 19

2.7.1. Summary of In-situ Thermally Actuated Resonant Devices 20

2.7.2. I-Shaped Device Geometry 22

2.7.3. Lumped Parameter System Model and Performance Scaling 24

2.7.4. Self-Q Enhancement and Self-Sustained Oscillation 27

2.8. Effects on Single Crystal Silicon (SCS) Material Properties 31

2.8.1. Young's Modulus 31

2.8.2. Electrical Resistivity and Piezoresistive Effect 32

2.8.3. Coefficient of Thermal Expansion 38

2.8.4. Specific Heat 40

2.8.5. Quality Factor Degradation Mechanisms 41

3. Device Modeling and Simulation 45
3.1. Baseline Settings and Parameters 45
3.2. Unstressed Modal Analysis 47
3.3. DC steady-state analysis 52
3.4. Prestressed Modal Analysis 54
3.5. DC Temporal Analysis 55
3.6. AC and DC Temporal Analysis 55
3.7. Forced Harmonic Analysis 57
3.8. Transfer Function Analysis 59
4. Device Fabrication 61
4.1. Previous micron scale device fabrication 61
4.2. Fabrication processing for submicron thick devices (h=340 nm) 63
4.2.1. NPGS-based Electron Beam Lithography process 63
4.2.2. Focused Ion Beam Milling process 67
4.3. Fabrication processing for high aspect ratio devices (h=1.5-2.0 μm) 70
4.3.1. Deep Silicon Etching (DSE) 70
4.3.2. Wafer/Chip Scale EBL/DRIE processing 76
4.4. Fabrication Results 78
4.4.1. Submicron thickness (h=340 nm) devices 78
4.4.2. High-aspect ratio (h=1.5-2.0 μm) devices 82
5. Performance of VHF Thermal-Piezoresistive Resonators 84
5.1. Experimental Setup and Methods 84
5.1.1. Advantages and Limitations of Test Setup 85
5.1.2. The S_{21} Parameter and Data De-embedding 87
5.2. Measured Performance 91
5.2.1. Submicron thickness (h=340 nm) devices 92
5.2.2. High-aspect ratio (h=1.5-2.0 μm) devices 97
5.3. Performance Comparison to Lumped Parameter Model 106
6. Performance of Self-Sustained Thermal-Piezoresistive VHF Oscillators 110
6.1. Electrical Characterization 110

6.2. Optical Sensing of Electrically Driven Self-Sustained Oscillations 118
6.3. Optical Tuning and Control of Electrically Driven Self-Sustained Oscillation 122
7. Conclusions and Suggestions for Future Work 129
References 131
Appendix 1 – Lumped Parameter Resonator Model Derivation 139
Appendix 2 – Alternate Data Analysis Methodology 146

LIST OF FIGURES

Figure 2.1: 2nd order damped harmonic oscillator systems w/ governing system ODE for a sinusoidal forcing functions (left) mass-spring-damper mechanical system (right) RLC electrical circuit. 5

Figure 2.2: Free MSD system response for f_o=10 Hz , b=10, and m=1, with the initial conditions of x(0)=1 and x'(0)=1. The dashed envelopes are defined by the damping coefficient (for this example $\beta=0.5$). 7

Figure 2.3: Sinusoidal steady-state frequency response for the damped harmonic oscillators (left) amplification and (right) phase. 9

Figure 2.4: Exterior (left) and interior (right) of the Epson Toyocom SG-310 series quartz-based oscillator. The package contains both the off-chip quartz crystal and the CMOS die required to drive the resonator. (images and caption from [12]) 14

Figure 2.5: Graphical depiction of internal (lower left) and external (lower right) transduction (from [12]). The appropriate electric displacement field equations are shown for each. 16

Figure 2.6: Examples of different MEMS resonator schemes (a) Silicon square plate Lame mode 4.26 MHz capacitive resonator [35] (b) Piezoelectric AlN on silicon resonator (24 MHz)with oxide pillars to decrease frequency-temperature sensitivity (from [32]), (c) Dielectrically actuated Si Bar resonator 4.5 GHz [45], and (d) Capacitive actuated piezoresistive sensed 1.1 GHz silicon resonator(from [40]) 19

Figure 2.7: Summary of previously reported thermally actuated resonant devices with separate heating elements embedded in the structure. All of these devices incorporate a piezoresistive readout scheme utilizing implanted resistors. 21

Figure 2.8: Summary of previously reported in-plane thermally actuated resonant device geometries that utilize inherent piezoresistance of n-type single-crystal silicon structure. The device geometry shown in d) is the focus of this work. 23

Figure 2.9: Graphical schematic of I-shaped or dogbone resonator geometry with dimensions. Colors are indicative of an arbitrary steady state temperature distribution for DC applied voltage with the support anchor ends acting as heat sinks at a fixed temperature. The temperature

gradient evident in the actuator arms (width = W, length = L) is amplitude modulated by the addition of an AC drive voltage. 23

Figure 2.10: Block diagram of lumped parameter thermoelectromechanical model (adapted from [61]) 24

Figure 2.11: a) Equivalent circuit for thermal subsystem, b) Equivalent circuit for mechanical subsystem, and c) Equivalent circuit for electrical subsystem (from [61]) 25

Figure 2.12: Equivalent circuit for thermal-piezoresistive resonators (from [61]) 26

Table 2.4: Reported performance of previous MEMS scale device of this geometry (from Rahafrooz and Pourkamali [61]) 27

Figure 2.13: Sequence of phenomena causing an internal positive feedback loop in the thermal-piezoresistive resonators biased with a constant current that lead to self-sustained oscillation (from [63]) 30

Figure 2.14: Closed Loop Feedback System 31

Figure 2.15: Young's modulus of Silicon, (100) plane (from [69]) 32

Figure 2.16: Plot of resistivity for n-type (red) and p-type (blue) uniformly doped silicon at room temperature. The markers show the resistivity for a doping level of 4E+18 cm^{-3} which is the approximate doping level for the devices in this work. (from van Zeghbroeck [73]). 34

Figure 2.17: Room temperature piezoresistive coefficients in the (100) plane (from [77] after Kanda [78]). These are considered accurate for low doping conditions. 36

Figure 2.18: Probable constant energy surfaces in momentum space for a longitudinally strained sample of n-type Si in the test configuration shown. The applied potential, E, and applied strain, e, are depicted in for proper crystal orientation. The electrons are located in six energy valleys (each of the three shown is also mirrored in the negative axial direction) at the centers of the constant energy ellipses, which are shown greatly enlarged. The effect of longitudinal stress in the [100] direction on the two valley energies shown is indicated by the dotted ellipsoids. The mobilities of the several groups of charge carriers in various directions are roughly indicated by the arrows. Figure is from [77] after Smith [80] who performed the first measurements of piezoresistance in silicon and germanium while at Bell Laboratories in 1954. 37

Figure 2.19: Experimental piezoresitive factor P(N) for the longitudinal piezoresistive coefficient in n-type silicon (from [81] in 2009, the "this work" reference). To obtain the longitudinal piezoresistive coefficient for a specific doping, N, multiply the P(N) value by the room temperature piezoresistive coefficient ($\mathbf{102 \times 10 - 11}$ Pa^{-1} per Kanda [78]).....37

Figure 2.20: Summary of experimental measurements of the variation of piezoresistive coefficient for n-type silicon with temperature (from [82]) For the <100> direction, $\boldsymbol{\pi 11}$ is equivalent to longitudinal piezoresistive coefficient.....38

Figure 2.21: Temperature dependence of linear coefficient of thermal expansion of silicon based upon Okada and Tokumaru [89] empirical formula {2-60} 39

Figure 2.22: Specific heat capacity of single-crystal silicon as a function of temperature (from [91]) 40

Figure 2.23: Specific heat capacity of single-crystal silicon for temperature (from [92]). T_m is the melting point of silicon.....41

Figure 2.24: Classification of loss mechanisms for a mechanical resonator (from [12]).....42

Figure 2.25: Pressure dependence of the unloaded (mechanical) Q-factor for 32 kHz and 55 MHz capacitive MEMS resonators. The 32 kHz capacitive MEMS resonator requires a cavity pressure below 0.01 mbar in order not to limit its Q-factor by air damping, while the capacitive 55 MHz MEMS resonator can tolerate up to 10 mbar before air damping starts to limit the Q-factor (from [12]) 43

Figure 2.26: Overview of reported values of the mechanical Q-factor vs. frequency (from [12]). The predicted *f-Q* limit lines for silicon (red), AlN (purple), and quartz (black) are shown.....44

Figure 3.1: (top) Top view of meshed solid model of device with bonding pads (bottom) Oblique magnified view of the meshed device structure which served as the baseline model for this chapter.....47

Figure 3.2: Different mode shapes generate using modal analysis for the I-shaped geometry subject of this work. The in-plane longitudinal mode which the devices in this work are intended to operate is at 119.8 MHz.....49

Figure 3.3: Results of unstressed modal analysis sweeps of the in-plane longitudinal mode for different aspects of device geometry. The trends displayed correspond to those expected from Eq {3-3}. The stars indicate the baseline geometry shown in Table 3.1. Fits to the results are displayed (dashed green line) when appropriate with units of frequency in Hz (unless noted otherwise) and the units of the dependent variable corresponding to that shown on the plot. 51

Figure 3.4: (left) Top view of filleted 2D layout, fillet radius = 25 nm (right) resulting meshed solid model 52

Figure 3.5: Effects of filleting as a function of fillet radius on frequency of the in-plane longitudinal mode. The dashed blue line shows the un-filleted baseline device frequency. 52

Figure 3.6: Steady-state DC response of baseline device (left) average. maximum, and minimum temperature in actuator arms for a DC current sweep (right) corresponding total displacement (in-plane) of the upper plate edge.....53

Figure 3.7: Steady-State DC response of baseline device at I_{DC}=2.0 mA (left) temperature distribution (right) current density norm.....53

Figure 3.8: Variation of resonant frequency of the in-plane longitudinal mode by the incorporation of a prestressed condition prior to modal analysis established by performing a steady-state DC analysis with both joule heating and thermal expansion. The black curve (diamonds) utilizes the temperature dependent Young's modulus described by Eq {3-4}. The red curve (squares) utilizes a fixed Young's modulus and shows an increase in frequency from structural stress added from thermal expansion.....54

Figure 3.9: Time-dependent DC analysis of the baseline device for I_{DC} = 2 mA showing maximum, minimum, and average temperatures of an actuator arm. (left) 10 μsec stepped sweep used to determine the steady-state temperature (right) 1 μsec sweep used to determine the 63% rise time, the range of which is indicated by the dashed blue lines.....55

Figure 3.10: Temporal response of temperature at the actuator arm centerpoint and the top plate edge displacement. The responses indicate that the displacement lags the temperature by ~90° which corresponds to the lumped parameter transfer function for the mechanical subsystem.....56

Figure 3.11: Temporal response of temperature at the actuator arm centerpoint and the voltage at the edge of the support beam. The responses indicates that the temperature lags the voltage by ~90° which corresponds to the lumped parameter transfer function for the thermal subsystem. .57

Figure 3.12: Top view of the temperature deviation from steady-state at t=1.2044E-7 sec, which is a time step corresponding to an AC temperature peak . The scale bar is in units of Kelvin. The majority of temperature fluctuation occurs in the actuator arms as desired, however significant fluctuation occurs in the support arms. The amount of temperature deviation outside of the actuator arms is an indicator of the degree of parasitic heating occurring in the structure. 57

Figure 3.13: Direction and location of mechanical loads needed to simulate thermal expansion of the actuator arms. 58

Figure 3.14: Forced Harmonic Response of the Baseline Device for T_{AC} = 0.15 K with Eq {3-5}. 59

Figure 3.15: Device A3 transfer functions for the thermal (left) and mechanical (right) subsystems 60

Figure 3.16: Device A3 total system transfer functions for a negative piezoresistive coefficient (left) and positive piezoresistive coeffient (right). At device resonance the negative piezoresistive coefficient offers 0° of phase shift, allowing self-sustained oscillation to be possible while the positive case has -180° phase shift which provides negative feedback. 60

Figure 4.1: SOIMEMS process flow utilizing conventional lithography for micron scale devices (from [16]) 62

Figure 4.2: Electron Beam Lithography (EBL) Based Fabrication Process for h=340 nm thick devices. 64

Figure 4.3: Images of optical masks and EBL write and alignment patterns for an individual device. (left) the overall bowtie shape of the Cr/Au metal stack is shown [in gray] with guide markers for manual positioning to the pre-write beam focus area [lower green square] (right) closeup view of the device area indicating a notional EBL write pattern [in red] over the connecting bridge [in gray], the Au optical mask [in green] which was equivalent to the available ebeam write area for the magnification setting used, the alignment markers [dark blue] in which metal is absent, and the alignment scan windows [in cyan]. 65

Figure 4.4: (a-e) Optical Imagery (x100, top view) of representative device at different stages of fabrication a) post-PMMA development (step 4), b) post Cr etch – metal bridge in exposed area has been removed, c) Post-PMMA stripping (step 5), d) Post-RIE and Cr removal, e) Post-Release (step 7), f) SEM image (top view) of fabricated device. (* steps a) and b) are actually from a different device with the same EBL write mask on a sister chip) 67

Figure 4.5: Focused Ion Beam (FIB) Milling based Fabrication Process. 67

Figure 4.6: (a) SEM Image (x12500) of Device J immediately after FIB milling (step 3 in Figure Figure 4.5); (b) FIB bitmap image used; (c) Close up SEM Image (x40000) of corner of lower proof mass showing the layers of material. Device J was significantly over etched with minor detriment to the final result. In this instance some undercutting of the silicon device layer from the RIE reached the device patterning area causing some minor roughness at the corner. 69

Figure 4.7: SEM Image x10000 of a 3μm deep device patterning attempt into a 2μm thick SOI DL. 70

Figure 4.8: Schematic viewgraph of an advanced three-pulse Bosch process (from Abdolvand [106]) 72

Figure 4.9: High aspect ratio dependent effects in high-density plasma etching of silicon (from Rangelow [107]) 73

Figure 4.10: EBL and DSE Based Fabrication Process for h=1.5-2.0 μm thick devices 77

Figure 4.11: SEM Image (x20,000, 45° tilt) of a 2 μm thick device geometry immediately after 20 cycles (~1 min) DSE was performed using the settings in Table 4.1. The majority of etching is accomplished in the first 7-8 cycles as determined by counting the number of scallops on the sidewall. The white arrow points to the thin, comparatively darker, layer of oxide visible from overetching the underlying BOX layer (image courtesy of AFRL Sensors Directorate). 77

Figure 4.12: SEM Images of different 5 μm thick device geometries (left) (x5000, 30° tilt) prior to release (right) (x5500, 30° tilt) after release and subsequent oxidation. The images were contrast adjusted to show the lingering silicon (indicated by white arrows) in the narrower trench regions. It is also evident from the visible undercutting of the BOX that the larger gap regions adjacent above and below the devices etched faster. Both of these characteristics were a result of ARDE. 78

Figure 4.13: (left) SEM Image (x12,500, 52° tilt) of EBL based fabricated Device A after release (upper right) Example measurements used to measure the sidewall angle (~14.4° for this device) (lower right) closeup view of individual actuator arm region (highlighted by yellow square) 80

Figure 4.14: SEM images (x25,000, top view) of the actuator arms for Device A (left) and Device B (right). 80

Figure 4.15: SEM Images of suspended FIB milled devices (a) Device I [x7,500, 30° tilt] , (b) Device F [x7000, 27° tilt], and (c) Device K [x10000, top view] 81

Figure 4.16: SEM images of Device A3 (left) (45° tilted, oblique) (middle) close up view of the actuator arms (right) top view with dimension labels added for reference 82

Figure 4.17: (left) Graphic depicting tilt correction for height using oblique view SEM images (right) SEM image showing direct measurements of device thickness at the plate edge of Device A3. Direct measurements yielded an average thickness of 1.57 μm, while the average corrected oblique measurement yielded 1.53 μm, verifying the technique to within 50 nm. 83

Figure 5.1: Image of printed circuit board (supplied by the DU NEMS group) used to implement the circuit shown in Figure 5.2 with test chip mounted. Please note, this board had additional components on it (not connected) to support other research efforts. 85

Figure 5.2: Electrical Test Circuit Schematic used for device testing as resonators. The bias resistors were 5.6 kΩ for the h=340 nm devices, and 5kΩ for the h ~ 2 μm thick devices. Testing was accomplished with the substrate wirebonded to ground for the h=340 nm devices, which adds pad capacitance to the model as shown. The h~2 μm devices did not have the substrate wirebonded to ground for the majority of testing as no appreciable difference was detectable in device response. 86

Figure 5.3: Representation of test circuit as two-port network of complex impedances 89

Figure 5.4: De-embedding of data using both magnitude and phase information. The example shown is for the high aspect ratio Device D4 at I_{DC}=3.5 mA at 50-70 Torr. The results of processing of this example using the alternate method are shown in Appendix 2, Figure A2.2 . 90

Figure 5.5: Measured frequency responses of Device B under DC bias current of 1.3 mA, directly taken from the network analyzer. (from [19]) 93

Figure 5.6: Measured $|S_{21}|$ data for Device H in Ambient Air (left) and Device J in Vacuum (50-70 Torr) (right) 94

Figure 5.7: Measured frequency responses for device D with different bias currents. Red and blue plots refer to air and vacuum testing conditions respectively (from [19]). 96

Figure 5.8: Plot of $FWHM^{-1}$ vs. power density of actuators for each of the EBL devices under vacuum. Second order polynomial fit curves are presented for reference. 96

Figure 5.9: Plot of $FWHM^{-1}$ vs. power density of actuators for each of the FIB cut devices under vacuum. 97

Figure 5.10: Measured $|S_{21}|$ data (vacuum) indicating position of resonant modes for Device C6. The AC mode data shown (~33.9 MHz and 44.7 MHz) was collected at +10 dBm input power with I_{DC} 1.45 mA and I_{DC} =0.747 mA respectively. The AC+DC (~67.8 MHz and ~88.9 MHz) were both collected at I_{DC} = 1.45 mA with -30 dBm input power. Inset are the two corresponding resonant structural mode shapes produced using COMSOL modal analysis (unstressed, Temp=285 K, E=130 GPa) and their resonant frequencies. The 73.1 MHz mode shown is a longitudinally symmetric flexural mode, while the 95.5MHz mode shown is the in-plane longitudinal mode. Device A3 (not shown) exhibited a similar response with $f_{o(\#1)}$=~81.6 MHz and $f_{o(\#2)}$=~105.6 MHz although the corresponding AC mode at $f_{o(\#1)}/2$ was below the noise floor. 99

Figure 5.11: Measured responses of Device D4 (top) AC only excitation responses at I_{DC} = 1mA, 50-70 Torr (bottom) conventional AC+DC responses at DC currents listed. 100

Figure 5.12: Measured $|S_{21}|$ data (ambient air) of Device C6 at $\omega_{o(\#1)}$ (Top) and $\omega_{o(\#2)}$ (Bottom) at different I_{DC} values with network analyzer power of -20 dBm. 101

Figure 5.13: Measured Device A3 frequency tuning with DC current in vacuum and ambient air for the presumed in-plane longitudinal mode at $\omega_{o(\#2)}$ ~105 MHz 105

Figure 5.14: Measured quality factor and motional conductance values for Device A3 (top) and Device E6 (bottom) at their $\omega_{o(\#2)}$ frequencies, presumed to be the in-plane longitudinal mode. The gradual trends in quality factor, such as that shown in A3, should be considered with caution as they could be artificial from the alternate de-embedding method. 106

Figure 6.1: Electrical Test circuit for self-sustained oscillators 111

Figure 6.2: Measured oscilloscope data with least square fit (a) Device A3 in ambient air I_{DC}=3.075 mA with ~99.5% content at 162.2 MHz (b) Device A3 in ambient air I_{DC}=3.117 mA with 62.3% content at 80.83 MHz and 37.7% at 161.67 MHz (c) Device C6 I_{DC}=2.5 mA in vacuum with 50.7% at 67.19 MHz and 49.3% at 134.39 MHz (d) Device E6 I_{DC}=3.51mA in vacuum with 93.2% content at 60.35 MHz and 6.8% content at 120.71 MHz. 112

Figure 6.3: Top view of actuator arms torsional deformation in longitudinally symmetric flexural mode (deformation amplified for visualization). 114

Figure 6.4: Device A3 self-sustained oscillation experiment #1 results- increasing and decreasing I_{DC} sweep conducted at 50-70 Torr. (a) AC output signal peak to peak voltage variation with I_{DC} (b) LS fitted fundamental oscillating frequency (f_o) variation with I_{DC} (c) fractional content by LS fitted amplitude at f_o ["+" ~81 MHz] and $2f_o$ ["x" ~162 MHz] variation with with I_{DC}. Device oscillated 65 min continuously during testing. 115

Figure 6.5: Device A3 self-sustained oscillation experiment #2 results - increasing I_{DC} sweep conducted at ambient air conditions. Oscillation shutoff occurred between I_{DC} = 3.175-3.18 mA. (a) AC output signal peak to peak voltage variation with I_{DC} (b) LS fitted fundamental oscillating frequency (f_o) variation with I_{DC} (c) fractional content by LS fitted amplitude at f_o ["+" ~81 MHz] and 2 f_o ["x" ~162 MHz] variation with with I_{DC}. Device oscillated 31 min continuously during testing. 115

Figure 6.6: Device A3 self-sustained oscillation experiment #3 results - increasing I_{DC} sweep conducted at 50-70 Torr - with Experiment #1 results shown in gray (a) AC output signal peak to peak voltage variation with I_{DC} (b) LS fitted fundamental oscillating frequency (f_o) variation with I_{DC} (c) fractional content by LS fitted amplitude at f_o ["+" ~81 MHz] and 2 f_o ["x" ~162 MHz] variation with with I_{DC}. Device oscillated 15 min continuously during testing. 116

Figure 6.7: SEM Images (left – 6,000x, 45° tilt, right - 12,500x 45° tilt) of Device A8 which despite significant damage to the actuator arms during processing exhibited self-Q enhancement and operated as a self-sustained oscillator at a lower order structural mode (peak performance measured at fo = 16 MHz, Vp-p = 7.45 mV, I_{DC} = 2.075 mA, P_{DC} =16.1 mW) 117

Figure 6.8: Sensing testbed (ambient air) used for sensing the spectral response of the structural mode while measuring electrical output of the device in self-sustained oscillation. Position of laser shown on inset SEM image. 119

Figure 6.9: Measured photodiode output from spectrum analyzer with 1D Lorentzian fit and corresponding electrical output recorded by the oscilloscope (top) Device C6 at I_{DC} = 2.70 mA (w/ laser), 2.75 mA (w/o laser), P_{LASER}=1.21 mW, $V_{p\text{-}p}$=3.9 mV, f_o (7%)=67.8 MHz, $2f_o$(93%)=135.6 MHz (Middle) Device A3 at I_{DC} =3.13 mA (w/laser), 3.079 mA (w/o laser) , P_{LASER}=1.26 mW, $V_{p\text{-}p}$=4.75mV f_o (14%)=81.1 MHz, $2f_o$(86%)=162.2(Bottom) Device B8 at I_{DC} =2.36 mA (w/laser), 3.34 mA (w/o laser) , P_{LASER}=0.58 mW, $V_{p\text{-}p}$=3.49 mV, f_o (34%)=66. 2 MHz, $2f_o$(66%)=132.4 MHz. The HeNe laser was positioned at the edge of the top plate for each device. 121

Figure 6.10: Effect of HeNe Laser Power on mechanical oscillation frequency and DC current (top) Device A3 – shutoff of mechanical oscillation coincided with electrical signal shutoff (bottom) Device B8 – electrical signal shutoff occurred prior to mechanical self-sustained oscillation shutoff. After shutoff, self-sustained oscillation was observed again upon lowering the laser power below the shutoff threshold. 123

Figure 6.11: Variation in maximum $V_{p\text{-}p}$ with HeNe laser power as measured by oscilloscope for Devices A3 (left) and B8 (right). Corresponding measured signals are shown for high (red circle) and low (blue circle) laser powers. 124

Figure 6.12: Equivalent circuit model for device operating as a self-oscillating photoresistor. The un-illuminated device resistance was ~2.7kΩ and 2.8 kΩ for Device A3 and B8 respectively. 125

Figure 6.13: Flowchart depicting impact of decreased device resistance due to photoconductivity in thermal-piezoresistive self-sustained oscillators. 127

Figure 6.14: Comparison of the (left) LS fitted 1D Lorentzian peak frequencies generated from measured data at each laser power and the (right) COMSOL prestressed modal analysis frequencies for the relevant flexural mode utilizing the equivalent device voltage levels and overall fractional change in resistivity calculated from the measured data as simulation inputs. 128

Figure A1.1: Generalized equivalent circuit for thermal subsystem 140

Figure A1.2: Mechanical subsystem: (left) mass-spring-damper block diagram (right) generalized equivalent circuit..... 142

Figure A1.3: Electrical subsystem circuit diagram 144

Figure A2.1: Electrical Equivalent Circuit for the measurement of G_m 147

Figure A2.2: Example of alternate de-embedding method using a resistive model with magnitude only. The data shown is for Device D4 at I_{DC}= 3.5 mA , 50-70 Torr. 148

LIST OF TABLES

Table 2.1: Mass-Spring-Damper Mechanical Frequency Response Solution in Polar and Rectangular Forms 8

Table 2.2: RF Spectrum bands as defined by the International Telecommunication Union (from [28]) 14

Table 2.3: Summary of governing equations for internal and external transduction for piezoelectric and electrostatic resonators. Dimensions follow Figure 2.5. 17

Table 3.1: Summary of Example Device Dimensions (after Figure 2.9) and Material Parameters 46

Table 4.1: Time-multiplexed Deep Silicon Etch Recipe used with Cr hard mask 76

Table 4.2: Average measured dimensions of EBL fabricated devices as defined in Figure 2.9 (thickness h = 340 nm). . Measurement statistics are listed for the actuator arms as indicators of roughness and asymmetry present. 80

Table 4.3: Measured dimensions of FIB milled devices as defined in Figure 2.9 (thickness h = 340 nm). 81

Table 4.4: Summary of Chip 2W1 Device Dimensions with average device dimensions [n=7] in μm. Device label with an asterisk (*) indicate that these devices operated as self-sustained oscillators in addition to resonators 83

Table 5.1: Measured EBL fabricated device performance. The data in bold corresponds to that depicted in Figure 5.5. Shaded cells correspond to data obtained during device operation in vacuum pressure (50-70 Torr) 92

Table 5.2: Measured Device Performance for devices fabricated with FIB milling. Shaded cells correspond to data obtained during device operation in vacuum pressure (50-70 Torr) 94

Table 5.3: Measured device resistance values of FIB milled devices before and after testing 95

Table 5.4: Measured Device Performance of High-Aspect Ratio devices (h=1.5-2.0 μm) in the in-plane longitudinal mode. Shaded cells correspond to data obtained during device operation in

vacuum pressure (50-70 Torr) Items in bold green were generated with both magnitude and phase information. The devices with a *operated as self-sustained oscillators 103

Table 5.5 : Measured Device Performance of High-Aspect Ratio devices (h=1.5-2.0 μm) at ω_o(#1) mode where self-sustained oscillation was experienced. Shaded cells correspond to data obtained during device operation in vacuum pressure (50-70 Torr). Items in bold green were generated with both magnitude and phase information. The devices with a *operated as self-sustained oscillators 104

Table 5.6: Measured HAR device resistance values before and after testing (if applicable) (* indicates the device operated as a self-sustained oscillator) 105

Table 5.7: Comparison of measured and predicted (*in italics*) motional conductance forthe submicron EBL devices 108

Table 5.8: Comparison of measured and predicted (*in italics*) motional conductance forthe submicron FIB cut devices 108

Table 5.9: Comparison of measured and predicted (*in italics*) motional conductance for the HAR devices 109

Table 6.1: Summary of Device Electrical Performance as Self-Sustained Oscillators 113

Table 6.2: Averaged Loaded Quality Factor values (with standard deviation) of devices operating as self-sustained oscillators. Note: *These values are presented to provide a general sense of the order of magnitude of the loaded Q*. The standard deviation in the measurement indicates they are not precise enough accurately portray individual device performance 122

1. Introduction

1.1. Unique Characteristics of On-Chip Thermal-Piezoresistive Resonant Devices

This work advances the state-of-the-art for the relatively new class of thermally actuated, piezoresistive readout microelectromechanical resonant devices which offer:

- Simple CMOS compatible fabrication – using silicon thorough SOIMEMS fabrication processing
- Frequency scalability with geometry
- Demonstrated utility as
    - Self-contained on-chip DC powered oscillators at radio frequencies (RF) without additional external circuitry
    - Temperature insensitive measurement devices for mass, vapor, pressure, and particle sensing, etc.

To further emphasize the last two bullets, the motivation for developing MEMS based resonators for RF applications, has been to serve as very narrow band electronic filters. One of the most pursued areas of their use being the replacement of quartz crystals as a frequency reference for oscillator circuits. Thermal-piezoresistive devices are unique in that they are active devices (i.e. require additional DC power) that can exploit internal feedback to create self-sustained electronic oscillation (i.e. no external circuitry required). The second main application is for low-cost resonant sensing. The simplicity and robustness of such devices make them attractive for this application as resonators alone, however their ability to self-oscillate potentially makes them even more appealing as it forgoes the need for an external AC source or sustaining amplifier to operate the device.

1.2. Overview, Scope and Organization of this Research

The central focus of this work was to expand the "operational envelope" of in-situ thermal-piezoresistive resonant devices in both frequency and performance (ratio of motional conductance to power) by further miniaturizing the design used to smaller scales (i.e. submicron scales). This project grew from an initial collaboration with the originators of such devices, the Pourkamali group at the University of Denver, to experimentally examine linear device performance using very thin (340 nm) silicon. Since this initial collaboration it grew into a more significant effort including the development of thicker devices and additional modeling using the COMSOL multiphysics software package.

This dissertation begins in Chapter 2 by presenting the fundamental mathematics of mechanical resonators and provides a sense for what has been accomplished in this field. Specific emphasis on thermally actuated devices and their operation is provided, including the larger scaled MEMS devices that preceded this work. Discussion is also provided on the

relevant material parameters and how they change with elevated temperature, to offer proper input into device models.

While initial analytical theory from a lumped parameter model was used to motivate and guide this research, it was of significant interest to expand upon the modeling previously accomplished through the use of commercial software. For this work the COMSOL multiphysics package was leveraged to develop a model from which a variety of relevant simulations could be run. The goal of this work was not to generate performance predictions from the onset, but to rather serve as a vehicle which could take the experimental data collected and use it to validate model settings so future predictions could potentially be made. Chapter 3 therefore uses a single baseline geometry to walkthrough the different simulations developed, building up to a forced harmonic response for the device.

Three different fabrication methods were developed and employed for this work to create test devices. The most challenging of these was developed in the pursuit of 2-5 μm thick structures with submicron spacing through the use of electron beam lithography and deep silicon etching. Chapter 4 describes these efforts in detail, with additional emphasis on the deep silicon etching employed, as the Cr mask and recipe used are somewhat unconventional for this scale of patterning.

The devices developed were experimentally examined as linear electrical resonators. Chapter 5 describes the experimental setup and methods employed toward this end and presents the results ultimately concluding with a comparison to the lumped element model. The thicker devices developed, performed strongly as resonators, although in a mode that was unexpected, the ultimate cause of which remains unexplained.

The performance of these devices was sufficient in several cases to allow for the self-sustained oscillation phenomena previously reported to occur. These devices were experimentally examined both electrically and optically through a laser sensing testbed to verify the frequency of mechanical oscillation. During the course of this testing it became apparent that the both frequency tuning and on/off control of the self-sustained oscillation were possible by adjusting the incident power of the laser. These characterization efforts are described in Chapter 6.

Chapter 7 summarizes the conclusions that can be drawn from this work and offers some suggestions into further aspects to explore with these devices in future work.

1.3. Primary Accomplishments

Thus far this research has resulted in two conference proceedings (one accepted for presentation in June 2013) and one journal article

Journal Articles:

- (In-press) Hall, H. J., Rahafrooz, A., Brown, J. J., Bright, V. M., & Pourkamali, S. (2012). "I-shaped thermally actuated VHF resonators with submicron components". *Sensors and Actuators A: Physical* doi:10.1016/j.sna.2012.12.006

Conferences Proceedings:

- (Accepted) Hall, H.J., D.E. Walker, L. Wang, R.C. Fitch, J.S. Bunch, S. Pourkamali, V.M. Bright (2013) "Mode Selection Behavior of VHF Thermal Piezoresistive Self-Sustained Oscillators" *TRANSDUCERS 2013 The 17th International Conference on Solid-State Sensors, Actuators, and Microsystems*, June 16-20, 2013, Barcelona, Spain
- Hall, H. J., Rahafrooz, A., Brown, J. J., Bright, V. M., & Pourkamali, S. (2012). "Thermally Actuated I-Shaped Electromechanical VHF Resonators," *Proceedings of IEEE 25th International Conference on Micro Electro Mechanical Systems*, pp. 737-740, Jan 2012, Paris, France.
- H.J. Hall, B.D. Davidson, S.M. George, and V.M. Bright, "ALD enabled nickel MEMS switches for digital logic," *Proc. ASME 2011 International Mechanical Engineering Congress and Exposition, paper number: IMECE2011-63763*, 9 pages, Nov. 2011, Denver, CO.

Technical Contributions

- Demonstrated thermal-piezoresistive resonator operation in the VHF regime
  - Up to 240 MHz in both ambient and vacuum
  - Strong Q and motional conductance values obtained
  - Demonstrated operation outside of in-plane longitudinal mode
- Demonstrated thermal-piezoresistive self-sustained oscillator operation in the VHF regime
  - Achieved through frequency doubling of lower frequency mode
  - Up to 160 MHz with V_{p-p} of 40 mV
- Developed electrothermomechanical simulation of device operation using commercial multi-physics software
- Demonstrated frequency tuning and on/off control of electrically driven self-sustained oscillations using incident laser power

2. Background and Literature Review

Nano and microelectromechanical resonators have been the subject of research for many years and offer a rich and interesting history. This chapter provides a primer on this research field and specifically highlights prior work on thermally actuated resonators and self-sustained oscillators. Section 2.1 begins with an introduction to the terminology used. Section 2.2 reviews the mathematics of forced harmonic vibration of the 1D mass-spring damper system which is the model commonly used to portray resonant systems. Section 2.3 expands the quality factor a fundamental parameter used to describe and compare resonant systems. Sections 2.4 and 2.5 describes in brief a summary of the applications of resonant systems and their performance considerations. Section 2.6 summarizes the different types of RF MEMS resonators. Section 2.7 summarizes past work specific to thermally actuated resonators and provides detailed background on the operation and 1D modeling of the I-shaped structures that are the subject of this work. Section 2.8 concludes this chapter by discussing effects on the relevant material parameters which drive this 1D modeling, including how the quality factor in impacted.

2.1. Resonant Device Terminology

A clear understanding of the terminology associated with resonant devices is necessary to begin any discussion of this work. From Senturia [1], "A *resonator* is a device with a vibratory natural response. A *linear resonator* is a resonator that can be described in terms of a linear transfer function. That is, [in the parlance of s-plane stability] it has a complex pole pair near the imaginary axis of the complex plane". While nearly all resonators can be driven into a non-linear operating regime, the scope of this work primarily considers mechanical structures functioning as linear resonators. Senturia continues by stating "An *oscillator* is a resonator plus an external circuit that provides the energy to sustain steady-state oscillation" [1]. This definition is somewhat limiting as the devices in this work do not necessarily require external circuitry to function as oscillators. A more general definition for an oscillator, suitable for this work, would be a resonator which has a mechanism employed, internal or external, to sustain steady state oscillation.

However, the aforementioned terminology is only relevant in the context of physical devices. In physics and mathematics, any system which experiences oscillatory motion, sustained or unsustained, is commonly termed as being an oscillator (e.g. the classic simple harmonic oscillator). In this broader context, the most rudimentary oscillators of practical significance are termed *driven (*or *forced) damped harmonic oscillators* [2]. Often these systems are of greatest interest when driven by a form of sinusoidal input, as is the case in this work. In mathematics coursework these systems are commonly presented in conjunction with the solution of 2nd order nonhomogeneous ordinary differential equations as they provide a clear physical basis with which solutions can be interpreted [3]. The two most often presented are the idealized mass-spring-damper mechanical system and the series LCR electrical tank circuit as

shown in Figure 2.1 with their governing system ODE for a sinusoidal forcing function. The mass-spring-damper (MSD) system consists of a mass M, connected to a fixed surface by a massless spring with a spring constant of k, and a massless damper element, which applies resistive force proportional to velocity of the mass by the coefficient b. The series RLC circuit consists of an inductor, capacitor, and resistor connected in series to a voltage source. In-depth presentations on the solutions of these systems using different techniques, can be found in numerous undergraduate mathematics, physics, and engineering texts as they arise in a variety of applications (e.g.[3–6]).

Mechanical resonators of nearly all geometries, including (N/MEMS) resonators, can be represented with the one dimensional MSD model through *lumped parameterization*, which approximates *effective* quantities for M, k , and b based on the specific design of the system. However, since N/MEMS resonators are commonly applied as electronic devices, namely filters and sensors, it has become common for them to portrayed in this manner as well. Specifically, representing the MSD system using the mathematically equivalent LRC series circuit has become the defacto standard in the N/MEMS community. To emphasize the fact that the equivalent LRC circuit elements (inductance, capacitance, resistance) for mechanical resonators are representative of a physical moving structure and not actual electronic elements they are commonly preceded by term "*motional"* and collectively called *motional parameters* of the system.

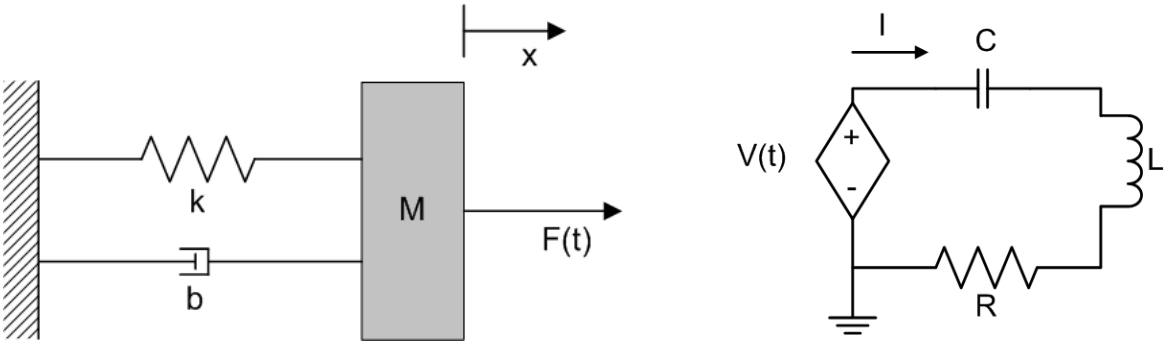

$$F_o \cos \omega t = M\ddot{x} + b\dot{x} + kx \qquad \omega V_o \cos \omega t = L\ddot{I} + R\dot{I} + \frac{1}{C} I$$

Figure 2.1: 2nd order damped harmonic oscillator systems w/ governing system ODE for a sinusoidal forcing functions (left) mass-spring-damper mechanical system (right) RLC electrical circuit.

The following section elaborates upon the solution to the MSD system. However, it is important to remember, that the derived equations and parameters can be represented in terms of motional

parameters by making the appropriate substitutions (i.e. ωV_o for F_o, L_m for M, R_m for b, and C_m for $1/k$).[1]

2.2. Forced Harmonic Vibration of the Mass-Spring-Damper System

By applying the principle of force conservation (Newton's second law) to the block diagram in Figure 2-1(left) the governing 2nd order ordinary differential equation can be derived to be

$$F(t) = M\ddot{x} + b\dot{x} + kx \qquad \{2\text{-}1\}$$

As is the case in most mechanical resonating devices, the solution for this system under sinusoidal (or *harmonic*) excitation, $F(t) = F_o \cos \omega t$, is of greatest interest and is termed the *harmonic response*. The classical solution to the resulting non-homogenous ODE is accomplished by applying the method of undetermined coefficients to solve for the particular (or steady-state) solution, $x_{ss}(t)$, in the *time domain* (see Kreyszig [3] for complete derivation). A less algebraically intense method is to both represent the forcing function $F(t)$ as a complex exponential, $F(t) = F_o e^{j\omega t}$, and recognize that the resulting displacement in the steady-state will also be of a complex exponential form, $X(t) = x_o e^{j\omega t}$. This effectively allows for a solution for $x_o(\omega)$ in the *frequency domain*. Substituting these expressions into {2-1} yields

$$F_o e^{j\omega t} = M(j\omega)^2 x_o e^{j\omega t} + b(j\omega) x_o e^{j\omega t} + k x_o e^{j\omega t} \qquad \{2\text{-}2\}$$

Solving for x_o, yields the following <u>complex</u> expression

$$x_o(\omega) = \frac{F_o}{M(j\omega)^2 + b(j\omega) + k} \qquad \{2\text{-}3\}$$

At this point it is important to recognize the definitions for *k* and *b* that originate with the *unforced* (or *free*) MSD system responses. The *unforced undamped* mass-spring system is described by Eq {2-1} under the condition $b = 0$ and $F(t) = 0$. Its solution for the displacement $x(t)$, is in the form

$$x(t) = A\cos\omega_o t + B\sin\omega_o t$$
$$\omega_o = \sqrt{\frac{k}{M}}, \qquad \{2\text{-}4\}$$

where ω_o is defined as the *natural* frequency (angular) of the system, as it is unimpeded by any damping or forcing. Similarly, in the *free* MSD system, described by Eq {2-1}under the condition $F(t) = 0$, has a solution basis in the form

---

[1] The extra ω term may not be immediately obvious. The fundamental governing equation for the LRC circuit from Kirchoff's law is $LI'(t) + RI(t) + \frac{1}{C}Q(t) = V(t)$, which in turn is equivalent to $LQ''(t) + RQ'(t) + \frac{1}{C}Q(t) = V(t)$. Differentiating this yields the expression in Figure 2.1.

$$x_1(t) = e^{\lambda_1 t}, \qquad x_2(t) = e^{\lambda_2 t}$$
$$\lambda_1 = -\beta + \gamma, \qquad \lambda_2 = -\beta - \gamma$$
$$\beta = \frac{b}{2M}, \qquad \gamma = \frac{1}{2M}\sqrt{b^2 - 4Mk} \qquad \{2\text{-}5\}$$

where the value of b, assuming a fixed k and M, determines the form of the solution. Resonant devices are *underdamped* (i.e. $b^2 < 4Mk$) systems, and in this case λ_1 and λ_2 are complex quantities resulting in a damped oscillatory solution for $x(t)$. Specifically, in this case $\gamma = i\omega_1$ where, $\omega_1 = \sqrt{\omega_o^2 - \beta^2}$ and the solution can be expressed in the real form

$$x(t) = e^{-\beta t}\left(A\sin\omega_1 t + B\cos\omega_1 t\right) = Ce^{-\beta t}\cos(\omega_1 t - \delta)$$
$$\delta = \arctan(B/A) \qquad \{2\text{-}6\}$$

where the value β, represents the *decay time constant* for the resonant response envelope[2]. Figure 2.2 shows an example free MSD system response indicating the damping envelope.

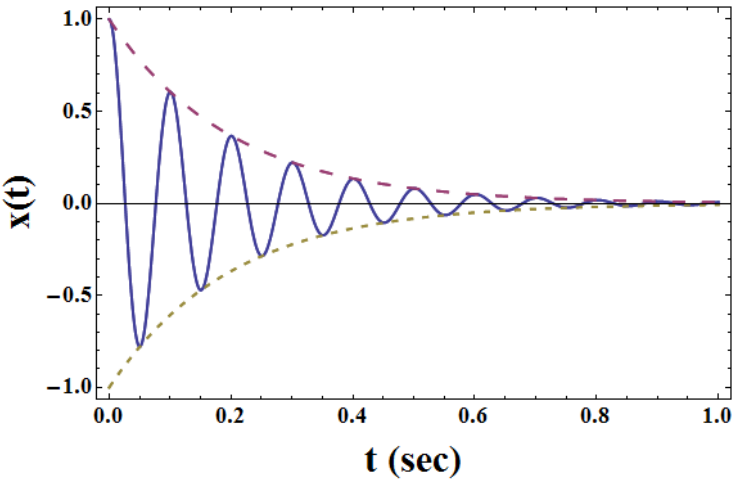

Figure 2.2: Free MSD system response for f_o=10 Hz , b=10, and m=1, with the initial conditions of x(0)=1 and x'(0)=1. The dashed envelopes are defined by the damping coefficient (for this example β=0.5).

Utilizing Eqns {2-4} and {2-5}, which effectively define both k and b as being proportional to the mass M , Eq {2-3} can be rewritten as

[2] It is worth mentioning that textbooks on this subject often non-dimensionalize the solution to the MSD system specifically by expressing the damping term defined in Eq. {2-1} in terms of a *damping coefficient* $\xi = \frac{b}{2\sqrt{mk}}$ whose value ranges from 0 to 1 and by utilizing frequency ratio, $r = \frac{\omega}{\omega_o}$. This results in dimensionless units for the resulting transfer function. A thorough treatment in this manner is described by Dukkipati [121].

$$x_o(\omega) = \frac{{}^{F_o}/_{M}}{({\omega_o}^2 - \omega^2) + (2\beta)j\omega} \quad \{2\text{-}7\}$$

Like all complex expressions, Eq {2-7} can in turn be expressed in either polar or rectangular (Euler) form as summarized in Table 2.1.

Table 2.1: Mass-Spring-Damper Mechanical Frequency Response Solution in Polar and Rectangular Forms

Polar Form (Magnitude and Phase)		Cartesian (Rectangular) Form ("In-phase" and "Out-of-phase" components)	
$x_o(\omega) = \lvert x_o(\omega)\rvert e^{j\varphi}$ $x_o(\omega) = \left(\sqrt{X^2 + Y^2}\right) e^{j(\arctan(\frac{Y}{X})}$	{2-8}	$x_o(\omega) = X + jY$ $x_o(\omega) = \lvert x_o(\omega)\rvert(\sin\varphi + j\cos\varphi)$	{2-9}
$\lvert x_o(\omega)\rvert = \frac{F_o/M}{\sqrt{({\omega_o}^2 - \omega^2)^2 + 4\omega^2\beta^2}}$	{2-10}	$X(\omega) = \frac{(F_o/M)({\omega_o}^2 - \omega^2)}{({\omega_o}^2 - \omega^2)^2 + 4\beta^2\omega^2}$	{2-11}
$\varphi(\omega) = \arctan\left(\frac{2\omega\beta}{({\omega_o}^2 - \omega^2)}\right)$	{2-12}	$Y(\omega) = \frac{(F_o/M)2\beta\omega}{({\omega_o}^2 - \omega^2)^2 + 4\beta^2\omega^2}$	{2-13}

In Eq {2-8}, $|x_o|$is the response *amplitude* and φ is the *phase angle* or *phase lag (*as it measures the lag of the output phase with respect to that of the input forcing sinusoid). The equivalent expression for {2-7} in the time domain is

$$x_{ss}(t) = |x_o|\cos(\omega t - \varphi) \quad \{2\text{-}14\}$$

It's worth noting , that the amplitude response described by {2-10} is in the form of a 1D Lorentzian line shape. When considered individually, the $X(\omega)$ and $Y(\omega)$ rectangular components of the response are "in-phase" (Eq {2-11}) and 90° "out-of-phase", also known as "quadrature", (Eq {2-13}) respectively, when compared to the forcing function *F(*t).

By examining when $\frac{d|x_o(\omega)|}{d\omega} = 0$, the maximum amplitude and the frequency at which it occurs can be found to be

$$\omega_{max} = \sqrt{\omega_o^2 - \frac{b^2}{2M^2}} = \omega_o\sqrt{1 - 2\beta^2} \quad \{2\text{-}15\}$$

$$|x_o(\omega_{max})| = \frac{2mF_o}{b\sqrt{(4M^2\omega_o^2 - b^2}} \quad \{2\text{-}16\}$$

Equation {2-15} shows that resonant behavior for the *forced* MSD system will only occur when the system is considered *underdamped* ($\beta < 1/\sqrt{2}$) and that as the damping of the system approaches zero the resonant peak will occur at ω_o. Figure 2-1 shows the amplification (the

ratio of output to input amplitude, $|x_o(\omega)|/F_o$) and phase plots of this system for different degrees of damping.

From the perspective of linear systems theory, the MSD system described by {2-1} has the following system transfer function in the frequency domain (a.k.a the frequency response function)

$$H(j\omega) = \frac{X(j\omega)}{F(j\omega)} = \frac{1}{(M(j\omega)^2 + b(j\omega) + k)} \qquad \{2\text{-}17\}$$

where the system poles are equivalent to the roots $\lambda_{1,2}$ in Eq. {2-5}. The units of {2-17} are in m/N, meaning that the transfer function represents spectral compliance, the inverse of stiffness.

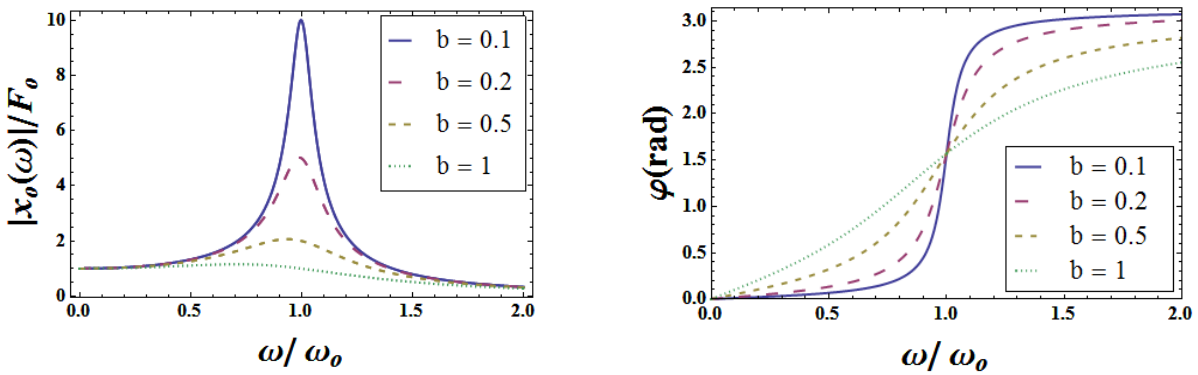

Figure 2.3: Sinusoidal steady-state frequency response for the damped harmonic oscillators (left) amplification and (right) phase.

It is important to remember the physical origins and significance of resonance. Resonance occurs in a vibratory system at the frequency where the imaginary components of the system impedances cancel each other. This implies that the excitation of the system is in phase with its natural response frequency and thus the exchange of energy between the energy storage elements of the system (springs and masses for mechanical circuits, inductors and capacitors for electrical circuits) is maximized (i.e. impedance is minimized). The impedance of a mechanical system can be examined directly as a mechanical circuit (as shown in [7]), however it is often easiest to simply translate the mechanical system variables into electrical ones for discussion (i.e. Force $\rightarrow \omega V$, Velocity $\rightarrow I$, $M \rightarrow L_m$, $b \rightarrow R_m$, and $1/k \rightarrow C_m$). As already discussed, for the MSD system this translation simply results in viewing the system as a series RLC circuit (per Figure 2.1) from which the complex input impedance can be written as

$$Z_{in} = Z_m = R_m + j\omega L_m - \frac{j}{\omega C_m} = R_m + j(\omega L_m)(1 - \frac{1}{\omega^2 C_m L_m}) \qquad \{2\text{-}18\}$$

Thus solving for $\omega^2 C_m L_m = 1$ results in

$$\omega_o = \frac{1}{\sqrt{L_m C_m}} \qquad \{2\text{-}19\}$$

Which is the equivalent to the expression for resonant frequency gained by substituting motional parameters directly into Eq {2-4}.

2.3. Quality Factor of Resonant Systems

Quality factor, abbreviated as *Q*, is a measure of the energy loss in a resonant system. As described in an interesting history by E.I. Green, [8], it is a parameter first coined in 1925 by K.S. Johnson of the Western Electric Company's engineering department[3], as a metric for the performance of inductor coils. Due to the near ubiquity in the application of the principle of resonance to describe physical phenomena throughout science and engineering, its usage has become just as widespread. Fundamentally, *Q* can be defined as

$$Q = \frac{E_S}{\left[-dE_S \big/ d\theta \right]} \qquad \{2\text{-}20\}$$

where E_S is the total stored energy in the resonant system, and the denominator is the energy loss from the system per radian [9]. Expressing the parameter in terms of angular frequency, $\omega_o = \frac{d\theta}{dt}$, yields more commonly cited forms of its definition (see [10] and [11]) shown below

$$Q = \frac{E_S}{\left[\frac{-dE_S \big/ d\theta}{d\theta \big/ dt} \right]} = \omega_o \frac{E_S}{P_D} = \left(\frac{2\pi}{T} \right) \frac{E_S}{P_D} = 2\pi \frac{E_S}{E_D} \qquad \{2\text{-}21\}$$

where $P_D = -\frac{dE_S}{dt}$ is the power dissipated in the system, *T* is the period for a given angular frequency, and E_D is the energy dissipated per cycle.

With the context of the MSD system in mind, the quality factor is a parameter inherent to the system and is completely independent on the amount of forcing applied. The expression for *Q* of the MSD system can be derived by directly examining the total system energy of the *unforced* underdamped system response, specifically

$$E_S(t) = \frac{1}{2} k (x(t))^2 + \frac{1}{2} M \left(\frac{d(x(t))}{dx} \right)^2 \qquad \{2\text{-}22\}$$

where the first term indicates the energy stored in the effective spring and the second term is the kinetic energy of the mass. Utilizing the solution for *x(t)* shown in Eq 2.6 the following expression for total stored energy can be found to be

[3] Western Electric Company's engineering department later became Bell Laboratories in 1925

$$E_S(t) = \frac{C^2 M e^{-2\beta t}}{2}[(\beta^2 + \omega_o{}^2)\cos^2(\omega_1 t - \delta) + 2\omega_1\beta\sin(\omega_1 t - \delta)\cos(\omega_1 t - \delta) + \omega_1{}^2\sin^2(\omega_1 t - \delta)] \quad \{2\text{-}23\}$$

The average energy can be found by assuming that the $e^{-2\beta t}$ term remains invariant over the first several cycles of decay and integrating Eq {2-23} over a single cycle time (the portion in brackets) which yields

$$\langle E_S(t)\rangle = \frac{C^2 M e^{-2\beta t}}{2}[\omega_o{}^2 + \beta^2 + \omega_1{}^2] = \frac{C^2 M \omega_o{}^2 e^{-2\beta t}}{2}. \quad \{2\text{-}24\}$$

Taking the derivative of Eq {2-24}yields

$$P_D = \frac{d}{dt}\langle E_S(t)\rangle = -2\beta\langle E_S(t)\rangle. \quad \{2\text{-}25\}$$

Finally, substituting the average values shown in Eq {2-24}and Eq {2-25}into Eq {2-21} yields

$$Q = \omega_o \frac{E_S}{P_D} = \frac{\omega_o}{2\beta} = \frac{M\omega_o}{b} = \frac{\sqrt{Mk}}{b} \quad \{2\text{-}26\}$$

which is the quality factor for the MSD system.

It can be further shown that the quality factor can be directly related to the *full width half maximum (FWHM)* of the *forced harmonic* response of the MSD system. The *FWHM, $\Delta\omega$,* or Γ[4], describes the spectral width of the resonant amplitude peak. As the name implies it is the frequency span between the half maximum points about the peak. The derivation is accomplished by examining the magnitude of the harmonic energy in the spring element of the system, which utilizing Eq {2-10}is

$$E(\omega) = \frac{1}{2}k\left|x(\omega)\right|^2 = \frac{1}{2}\frac{F_o^2}{M}\frac{\omega_o{}^2}{(\omega_o+\omega)^2(\omega_o-\omega)^2 + 4\omega^2\beta^2} \quad \{2\text{-}27\}$$

By assuming that at resonance $\omega \approx \omega_o$, Eq {2-27}can be approximated as

$$E(\omega) \approx \frac{1}{8}\frac{F_o^2}{M}\frac{1}{(\omega_o-\omega)^2 + \beta^2} \quad \{2\text{-}28\}$$

From Eq {2-28}, it becomes clear that the spectral energy decreases by a factor of 2 at values $\omega = \omega_o \pm \beta$, thus $\Delta\omega = 2\beta$ and the quality factor can be written as

$$Q = \frac{\omega_o}{2\beta} = \frac{\omega_o}{\Delta\omega} \quad \{2\text{-}29\}$$

The relation shown in Eq {2-29}is of significant use since it allows for determine the quality factor of a resonator from its spectral response, which can be measured by experiment. It is also worth noting that sometimes the *half-power fractional bandwidth (BW)* of a resonator is cited in

[4] In the physics community the variable Γ is often used in place of 2β in formulating the MSD system

place of Q [10]. This parameter is simply the fraction of FWHM relative to the resonant frequency or

$$BW = \frac{\Delta\omega}{\omega_o} = \frac{1}{Q} \qquad \{2\text{-}30\}$$

For completeness, the quality factor of a resonator can also be derived in terms of its motional parameters for the equivalent series LRC circuit from the definition shown in Eq {2-21}. The stored energy is for this circuit is

$$E_S = \frac{1}{2} L_m {I_{pk}}^2 = \frac{1}{2} C_m (I_{pk} R_m)^2 \qquad \{2\text{-}31\}$$

Where I_{pk} is the peak value of the AC current amplitude and V_{pk} is the peak value of the AC voltage amplitude. Eq {2-31} states that at resonance the total energy stored can be described by the maximum energy storage in the magnetic field of the inductor or in the stored charge of the capacitor. At resonance, the impedance is purely resistive and thus the energy dissipated per cycle is

$$E_D = \langle P_D \rangle T = \left(\frac{I_{pk}}{\sqrt{2}} \right)^2 R_m \left(\frac{2\pi}{\omega_o} \right) = \frac{\pi {I_{pk}}^2 R_m}{\omega_o} \qquad \{2\text{-}32\}$$

where $<P_D>$ is the average dissipated power. Thus from Eq {2-21} the quality factor is

$$Q = \frac{\omega_o L_m}{R_m} = C_m R_m \omega_o = \frac{1}{R_m} \sqrt{\frac{L_m}{C_m}} \qquad \{2\text{-}33\}$$

which are forms equivalent to what would be obtained by direct motional parameter substitution into Eq {2-29}. Note that the first two forms of Q shown in Eq {2-33} are simply the ratio of the reactance to the resistance of the circuit at resonance, which is the definition of Q commonly presented in reference to individual reactive components (inductors and capacitors) [6].

While N/MEMS resonators are mechanical structures, the actuation and sensing of their response are often accomplished electrically. The coupling of external circuitry to them can affect their effective impedance and ultimately degrade the system performance. Thus the quality factor definition shown in Eqs {2-29}and{2-33} is for the system operating in complete isolation, and is called the *unloaded Q*. The *loaded* or *effective Q* is the value for Q when coupled to the external circuitry.

Electrical loading is just one of several factors that can degrade the Q of a real mechanical resonators. Also it has been shown that Q of a resonator can have theoretical limits for the frequency it is operating at based on the material it is constructed of. Thus the *f-Q* product is also commonly reported to reflect how close performance is to these theoretical limits and provide comparison to other resonant device technologies. Further discussion on Q degradation and the f-Q product (and R-Q product) is presented in Section 2.8.5.

Finally, since the devices in this work can operate as both resonators and self sustained oscillators, it is important to know that the quality factor can be reported for both. However, the quality factor for an oscillator is not equivalent to that shown for a resonator. However, the definition expressed in Eq {2-21}can be applied with some caveats. When the oscillator is operating in steady-state, generating a sinusoidal signal, the energy lost is supplied by an external source (the DC power supply for this work). Thus the denominator in Eq {2-21} should be interpreted as the energy supplied by the source [11].

2.4. Advantages and Applications of Micromechanical Resonators

Electrical resonant circuits, those consisting of transistor based amplifiers and resistive, capacitive or inductive elements have Q factors no greater than about 10 [12]. Mechanical resonant devices can have high Q-factors up to several million. Conventional vibrating mechanical resonant devices include quartz crystals, ceramic resonators, surface acoustic wave (SAW) resonators, and film bulk acoustic resonators (FBAR). However, these technologies all require realization as off-chip components due to fabrication incompatibilities with traditional integrated circuit processing, most notably CMOS. Micro- and nanoelectromechanical resonators are emerging as an on-chip solution which can match the high-Q of the current off-chip technologies while allowing lower cost in the form of IC fabrication compatibility and compact footprint.

Generally speaking, micro and nano-scale mechanical resonators are intended for two classes of applications. The first are sensing applications. These include mass or particle sensing [13–19], vapor/gas sensing [20], [21], chemical sensing in liquid [22], [23], temperature sensing [24], flow sensing [25], etc. The basic premise of operation for these devices is in measuring the shift in resonant frequency which occurs in some proportion with changes to the sensed parameter. This is accomplished either by altering either the undamped natural frequency response of the structure itself (e.g. deposition of molecules on the resonator changing the effective mass [13–18]) or the force input which drives the structure (e.g. flow velocity changing the fluid drag force on the resonator [25]).

An example of the former case is mass or particle sensing. Mass sensitivity can be found by simply taking the derivative of Equation {2-4} as shown below (in non-angular form)

$$\frac{\delta f}{\delta m} = \frac{\delta}{\delta m}\left(\frac{1}{2\pi}\sqrt{\frac{k}{m}}\right) = \frac{-1}{2m}\left(\frac{1}{2\pi}\sqrt{\frac{k}{m}}\right) = \frac{-f_o}{2m} \qquad \{2\text{-}34\}$$

Higher frequency and lower mass thus improve the device mass sensitivity enabling a larger frequency shift for detection. However, assuming the design is restricted from changing the material system of the resonator, higher frequency and lower mass require physically smaller devices. In the case of mass sensing this reduces the device surface area available for particles to deposit on, which reduces the dynamic range and saturation limit of the detector. This is just one example of the kind of tradeoffs encountered in micro- and nano scale resonant sensor design. In

nearly all resonant sensors higher Q is beneficial as it affords a sharper frequency response, which translates directly into detector frequency resolution.

The second class of applications for micro or nano-scale resonators is radio frequency (RF) signal processing, which is primarily driven by the wireless communication industry. For clarity of terminology, Table 2.2, provides the official International Telecommunication Union band designations for the portion of RF spectrum relevant to this work. As explained by Kuhn et al., these applications require analog based solutions due to the power consumption challenges inherent in a digital filter approach for high frequencies [26]. While there is interest in devices spanning the RF spectrum, according to Nguyen [27], specific interest lies in the 800 MHz – 2.4 GHz regime, for the wireless transceivers in mobile personal electronic devices. Many present day communication transceivers utilize the previously mentioned conventional mechanical resonator technologies to perform both frequency band filtering and signal generation when applied to an oscillator circuit [27]. Micro and nanomechanical resonators offer a way around this bottleneck for further improvements towards miniaturization and packaging efficiency. The current state-of-the-art for using MEMS resonators as oscillators is detailed in a recent (2012) review paper by van Beek and Puers [12]. Figure 2.4 an example of the packaging currently required for a high performance resonant device.

Table 2.2: RF Spectrum bands as defined by the International Telecommunication Union (from [28] **)**

	Band Designations	**Frequency**	**Wavelength**
HF	High Frequency	3-30 MHz	10-100 m
VHF	Very High Frequency	30-300 MHz	1 – 10 m
UHF	Ultra High Frequency	300-3000 MHz	10 – 100 cm

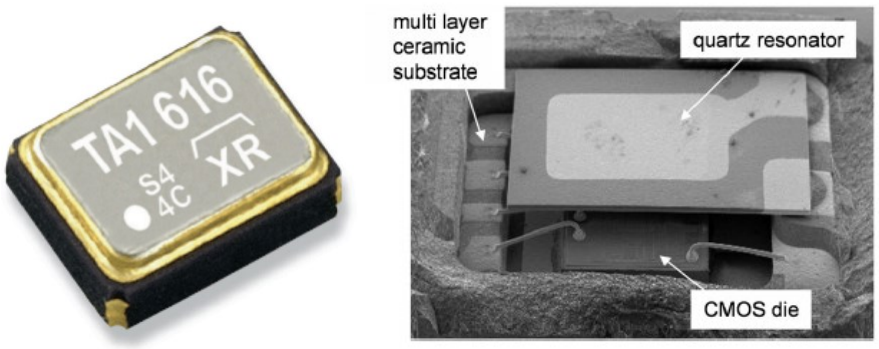

Figure 2.4: Exterior (left) and interior (right) of the Epson Toyocom SG-310 series quartz-based oscillator. The package contains both the off-chip quartz crystal and the CMOS die required to drive the resonator. (images and caption from [12] **)**

2.5. Performance Considerations for Micromechanical Resonators

The quality factor, *Q*, full width half maximum, *FWHM*, and half power fractional bandwidth, *BW*, discussed in Section 2.3, are all used as standard measures for resonator performance with regards to spectral response quality. However, there are several other performance considerations for resonant devices.

Arguably the most important of these is **power consumption**. It is important to note that the thermally actuated devices presented in this work are *active devices*, that is they require power to exhibit a resonant response. Most other resonant devices are *passive components*, which will operate in the presence of a signal without additional power, although the amplitude of the device output is attenuated. While both types can be used for sensing applications, in general passive resonators are better suited as candidates for filtering of RF signals on-chip as they have minimal power requirements. However, the devices in this work have been demonstrated to exhibit a phenomena known as *self-Q enhancement*, which as the name implies, means that power used to drive the resonator also can be tapped to improve its effective quality factor. This is significant for two main reasons, 1) it potentially allows resonators to exceed their natural performance at higher frequencies, 2) that allows for the operation of these devices as oscillators without any external feedback circuitry. This property is unique to these devices and offers a considerably simpler and less expensive alternative than existing oscillator solutions. Discussion of device operation is presented in Section 2.3.1.

Frequency-temperature sensitivity is another major performance consideration for resonant devices. In most applications it is ideal to have zero variation in frequency response with temperature. As stated by Hopcroft [24], "Silicon resonators have an inherent frequency-temperature f-T sensitivity of approximately −30 ppm/ °C, or nearly 4000 ppm over a −40 to 85 °C operating range." High performance quartz oscillators, such as temperature controlled crystal oscillators (TCXO) and oven-controlled crystal oscillators (OCXO) can have f-T sensitivities < 10 ppb over a similar temperature range [29]. Using these control systems approaches typically requires additional control circuitry, temperature sensing, and especially in the case of "ovenizing", appropriate packaging of the devices.

Non-deterministic noise is the third significant consideration for resonant devices. For resonators, the sources of noise depend upon the type of readout and the environment it is operating in. Since the devices in this work are driven by joule heating, the primary noise consideration is Johnson noise is generated within the resonant structure. Noise is largely an issue for oscillators. As explained by van Beek and Puers in [12] "Noise of the oscillator's wave front can be decomposed in amplitude noise and phase noise. Amplitude noise can typically be filtered out in the oscillator loop and is not a critical parameter for most applications. In contrast, phase noise cannot be filtered out and is an important performance indicator of any oscillator." Phase noise was not examined for the self-sustained oscillators presented in this

work, but has been reported for similar devices operating in the HF by Rahafrooz's examination of jitter in the time domain [30].

2.6. Brief Summary of On-chip Silicon RF Resonators

MEMS resonators are traditionally classified by actuation method into two groups, piezoelectric transduced and capacitive (electrostatic) transduced. Both traditionally consist of a single pair of electrodes which electrically act as a capacitor and utilize the application of voltage to achieve the deflection of the structure. The motion of the structure is expressed (sensed) in the variation of the current passing between the two terminals according to the electro-mechanical coupling factor for the device. Piezoelectric transduction incorporates the piezoelectric effect, in which a material will experience mechanical strain in the presence of a voltage (and vice versa). This form of actuation requires deposition of a piezoelectric material between the electrodes, which has almost exclusively been PVD AlN [31], [32] although ZnO has also been demonstrated [33]. Capacitive transduction is accomplished through the principle of electrostatic actuation, which is purely a result of the electrostatic force between the two electrodes. This actuation simply requires a dielectric medium present between the electrodes, often air or vacuum. In the context of the mass-spring model presented in Section 2.1, the electrodes can either be positioned across the "spring" element of the system, for *internal* transduction, or located between the resonator and fixed external electrode, *external* transduction [12]. The difference between these two schemes is shown graphically in Figure 2.5.

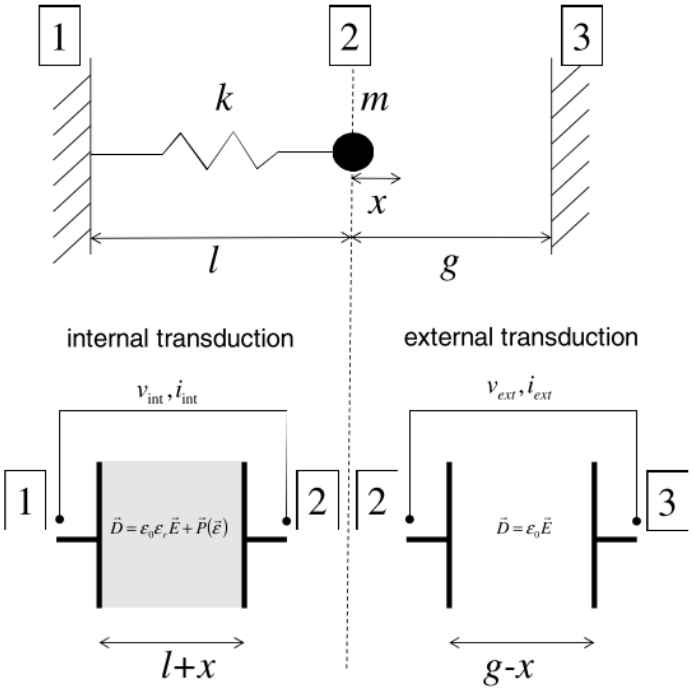

Figure 2.5: Graphical depiction of internal (lower left) and external (lower right) transduction (from [12]**). The appropriate electric displacement field equations are shown for each.**

As summarized in [12], the output current for both transduction schemes can be derived by taking the time derivative of the electric displacement field. Table 2.2 summarizes the resulting equations for output current.

Table 2.3: Summary of governing equations for internal and external transduction for piezoelectric and electrostatic resonators. Dimensions follow Figure 2.5.

Internal transduction	External transduction (parallel plate)
$i_{int} = C_{int}\frac{\partial v_{int}}{\partial t} - (\eta_{int,cap} - \eta_{int,piezo})\frac{\partial x}{\partial t}$	$i_{ext} = C_{ext}\frac{\partial v_{ext}}{\partial t} - \eta_{ext,cap}\frac{\partial x}{\partial t}$
$\eta_{int,cap} = V\frac{\varepsilon_o \varepsilon_r A_{int}}{l^2}$	$\eta_{ext,cap} = V\frac{\varepsilon_o A_{ext}}{g^2}$
$\eta_{int,piezo} = \frac{e_{xx} A_{int}}{l^2}$	$C_{int} = \frac{\varepsilon_o A_{ext}}{g}$
$C_{int} = \frac{\varepsilon_o \varepsilon_r A_{int}}{l}$	

The coupling factors listed above can be used to describe the resonators motional impedance by the following relation

$$R_m = \frac{b}{\eta^2} \qquad \{2\text{-}35\}$$

where η is the appropriate coupling factor. The internal and external capacitive coupling factors are explicitly listed in Table 2.3. Devices that incorporate internal capacitive transduction (no piezoelectric material present) are typically referred to as dielectrically actuated devices (ex. [34]). The piezoelectic coupling factor is the difference between the internal capacitive, $\eta_{int,cap}$, and internal piezoelectric, $\eta_{int,piezo}$, coupling factors.

Each of these traditional transduction approaches has clear strengths and weaknesses. Typically the piezoelectric coupling factor is heavily dominated by the $\eta_{int,piezo}$ term, which tends to be orders of magnitude larger than the capacitive term. Thus per Eq {2-35}, piezoelectric devices tend to have much lower impedances then capacitive devices. The downside to piezoelectric resonators is two-fold. First, they require a piezoelectric materials, which are not standard for CMOS processing. And, second, they often require the material to be patterned in conjunction with another for electrode formation. This creates a material interface which promotes energy loss and reduced *Q* (see Section 2.8.5). Thus piezoelectric devices tend to have reduced *Q*.

Capacitive transduced resonators tend to be fabricated from a single homogeneous material and thus can experience very high values of *Q* when sealed in vacuum [35–37]. The relatively weak coupling factor of capacitively driven resonators though generally implies high motional impedance. For the extrinsically transduced resonators the gap between the resonator and electrodes is independent of the structure. Thus the gap distance, electrode area, and

positioning of the electrodes can be adjusted to boost coupling factor. Combinations of capacitive and piezoelectrically actuated schemes have also been reported [38].

It is important to note that in all forms of capacitive and piezoelectric resonators, coupling factor is directly proportional to electrode area. Therefore miniaturization tends to decrease the coupling factor and increase motional impedances. In addition, as explained in Section 2.8.5, the quality factor also tends to degrade with miniaturization due to increased surface losses. Thus the highest performance resonators (i.e. devices which have the strongest amplitude and sharpest resonant peaks, necessary for oscillators and many sensors, tend to be larger microscale devices.

An alternative to these traditional approaches is to incorporate an active transduction scheme. Such schemes require additional DC power, but allow for the possibility of signal amplification, with output currents many time larger compared to capacitive devices [12]. Examples of these types of devices include FETs with a suspended movable terminal [39] and capacitively actuated piezoresistively sensed MEMS resonators [40], [41]. The thermal-piezoresistive devices of this work fall into this active classification and their operation is discussed in the following section.

For reference, Figure 2.6 provides images of some examples of the on-chip resonator schemes discussed all fabricated from silicon. The classification of MEMS resonators into the electrostatic, piezoelectric, and active transduction categories is by no means all inclusive. There are other examples of unique resonator schemes such as magnetically actuated resonators [42] and novel variations such as PN junction resonators [43].

In addition to actuation and readout the mode shape selected is also a factor in on-chip resonators. Waggoner et al. [44] experimentally showed that resonant devices operating in in-plane modes interact less with the surrounding fluid medium than flexural out-of-plane modes, yielding reduced viscous dampening, and higher Q. Also in some cases, exciting higher harmonic modes for a structure can reduce the motional impedance at the higher frequency [45].

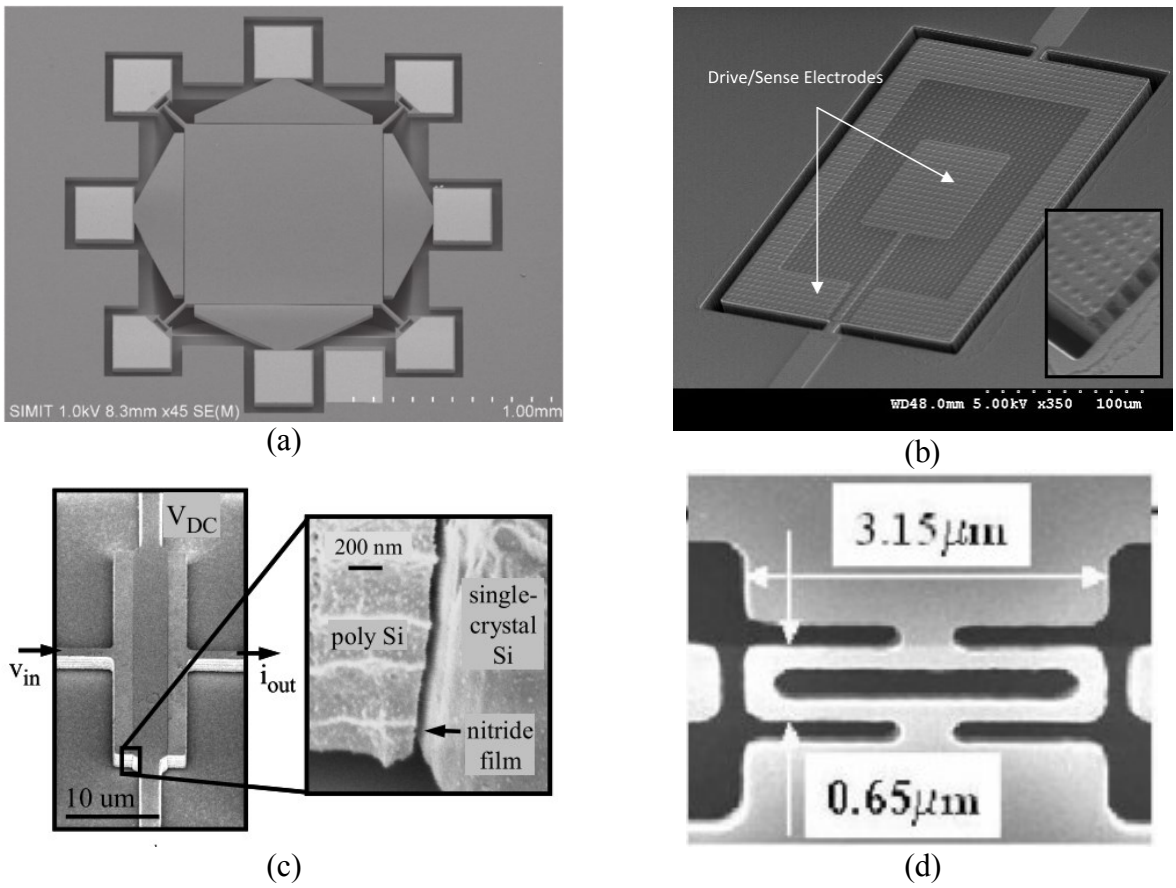

Figure 2.6: Examples of different MEMS resonator schemes (a) Silicon square plate Lame mode 4.26 MHz capacitive resonator [35] **(b) Piezoelectric AlN on silicon resonator (24 MHz)with oxide pillars to decrease frequency-temperature sensitivity (from** [32]**), (c) Dielectrically actuated Si Bar resonator 4.5 GHz** [45]**, and (d) Capacitive actuated piezoresistive sensed 1.1 GHz silicon resonator(from** [40]**)**

2.7. High Frequency (HF) Thermally Actuated Resonant Devices

Thermal actuation has been considered as a means for microscale actuation for a considerable amount of time. The following section summarizes the reported work for *in-situ* thermally actuated devices, that is devices with heating elements built-in. It is worthy of mention though that thermal actuation of resonators is also commonly achieved through external radiative means. Per Venkatesh in [46], using intensity-modulated light to photothermally drive metal coated quartz resonators at their natural modes of vibration was first reported in 1982 by Dieulesaint et al [47]. Since then optical drives have been applied to numerous resonators [48–51]. Of particular interest is the autoparametric optical drive reported by Zalalutidinov et al. [48], [49] which describes Q-enhancement and mechanical self-oscillation (limit cycle oscillation) with a CW laser. This phenomena is analogous to the self-Q enhancement reported for the device geometry of this work shown in Section 2.7.4. More recently (2009) using microwave frequencies for thermal excitation has also been reported [52].

2.7.1. Summary of In-situ Thermally Actuated Resonant Devices

The first *in-situ* thermally actuated device is probably the "Resonistor" reported in 1968 by Wilfinger et al. [53] pictured in Figure 2-6 a). While a rather large scale device (350 x 30 x 5 mil cantilever) it represents the first steps at both fabricating mechanical resonators from silicon and using thermal actuation to drive them. A diffused resistor at the base of the cantilever acts as a localized thermal heating element. When current is passed through the resistor, joule heating occurs and a vertical temperature gradient is created within the beam, as the base is attached to the rest of the substrate which acts as a heat sink. Similar to the devices in this work, a combination of an AC and DC current is required for excitation frequency to occur at the applied AC frequency (see Appendix 1 – thermal subsystem for full explanation). When the applied frequency coincides with out-of-plane natural resonant modes of the mechanical structure, resonance occurs, resulting in amplification of vibration amplitude proportional to that of the Q-factor. To readout the deflection, resistors are diffused into the surface of the cantilever at it's base (area of greatest strain). The resistance of these readout resistors is proportionally modulated by the piezoresistive effect which corresponds to a signal change based upon the readout electronics (typically a bridge circuit is used to account for changes with temperature) [53]. Section 2.4.3 explains the piezoresistive effect in detail.

This concept was not reportedly used again until 1987 with the work of Othman and Brunnschweiller [54], who improve upon it by incorporating a low temperature coefficient polysilicon drive resistor in the surface separated from the silicon beam by an additional oxide barrier layer. The significant thermal resistance of the oxide layer helps enhance the vertical thermal gradient. The low temperature coefficient polysilicon allows the drive resistor to also be used as the readout resistor. Since then the concept has been refined for different materials, smaller scaling, and in-plane modal geometries [55–60]. Figure 2.6 shows selected images of these various devices. The simplicity of the approach in both fabrication and readout and its robustness for challenging sensing environments continue to hold significant interest in the MEMS/NEMS device community today.

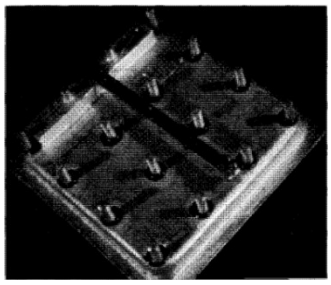

a) The "Resonistor" (1968, from [53]**)**

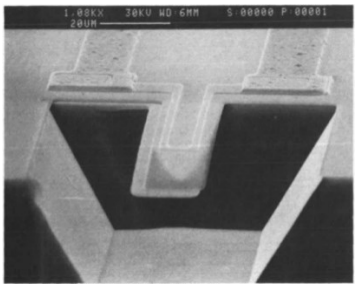

b) Si/SiO2/PolySi cantilever (1987, from [54]**)**

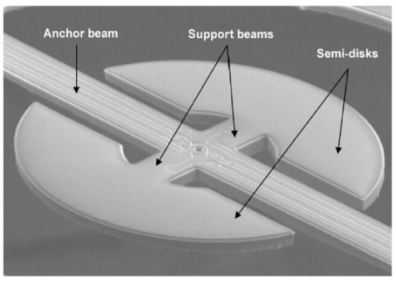

c) Split disk resonator (2008, from [55]**)**

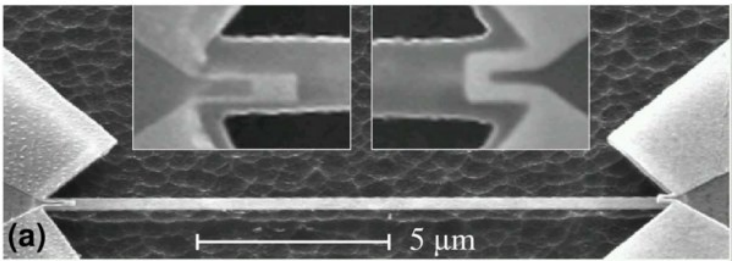

d) NEMS 3C-SiC fixed-fixed beam resonator
Separate readout (left) and drive (right) metal film loops inset
(2006, from [56]**)**

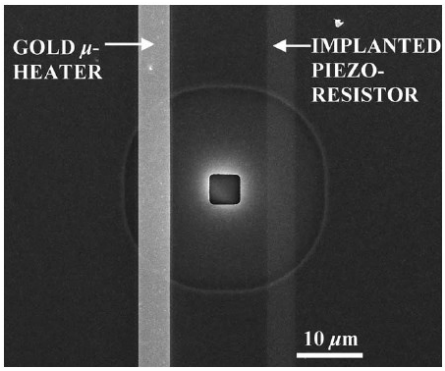

e) Polysilicon shell-type resonator
(2006, from [57]**)**

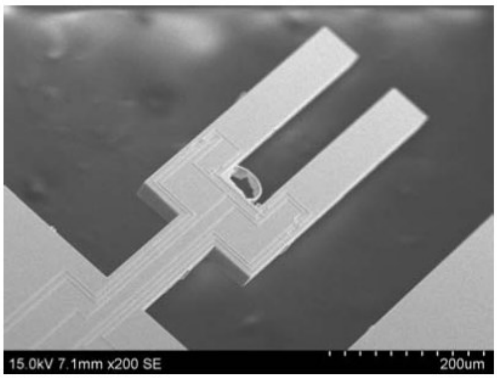

f) Si tuning fork for mass sensing
(2012, from [58]**)**

Figure 2.7: Summary of previously reported thermally actuated resonant devices with separate heating elements embedded in the structure. All of these devices incorporate a piezoresistive readout scheme utilizing implanted resistors.

Recently an alternative approach to thermal-piezoresistive resonant devices has been considered with the development of in-plane extensional mode resonators fabricated entirely by patterning a single layer of uniformly doped single-crystal silicon (SCS) [16], [22], [61]. This approach requires two-terminal (single-port) operation, where the piezoresisitive readout is integrated into the device structure[5]. Single port operation has the advantage of simplicity, since no additional readout resistors are required for operation, but is disadvantageous for signal feedthrough. The concept of operation is similar to the aforementioned devices except the localized regions in which the heating occurs are explicitly controlled through the geometry of the devices. These areas are referred to as actuator arms, since they are typically high aspect ratio, low cross-section areas of the design to maximize the joule heating and subsequent thermal expansion. During operation the modulation of thermal gradients of the actuator arms in turn causes stress fluctuations within them which causes proportional changes in electrical resistance through the piezoresistive effect. The measured AC component of this modulated output current of the device is termed the motional current [61].

[5] Hajjam reported a two-port variant of these devices through the use of embedded oxide beams in the structure in [122], but this geometry was not the subject of this work.

The merits to this approach are primarily two-fold: 1) The fabrication is simpler, as no additional patterning of resistors or doping is required, making aggressive size reduction possible and potential on-chip integration with electronics easier; and 2) if the piezoresitive coefficient of the material is negative and its small signal voltage to current gain, or motional conductance, is sufficiently high a phenomenon known as self-Q enhancement [62] can occur from internal positive feedback; This can allow device operation as a oscillator without the need for additional circuitry [63]. As mentioned, one disadvantage to this approach is that since the same physical and electrical portion of the resonator is used for both actuation and sensing, the feedthrough floor can be potentially higher than a thermally actuated device which has separate diffused resistors for actuation and sensing.

Figure 2.7 shows selected images of various geometries that have been pursued with this approach and their intended application. To date these devices have been demonstrated solely on silicon, which exhibits large piezoresistive coefficients when oriented in the appropriate lattice direction; but there is no reason for the principle not to work for other materials with similar properties as well. It is important to note that the challenge of frequency-temperature sensitivity has been addressed for such devices by phosphorus doping and adjustments of the bias current [64]. The demonstrated 100 ppb /K stability offers promise for both oscillator and sensing applications.

2.7.2. I-Shaped Device Geometry

The devices in this work are of the I-shaped or dogbone design similar to that shown in Figure 2.8d). This geometry utilizes the structures in-plane longitudinal (or extensional) mode for operation. It operates through the periodic thermal expansion of four actuator arms symmetric about its lateral axis which impose force on the adjacent proof masses. A graphical schematic of this geometry is shown in Figure 2.9.

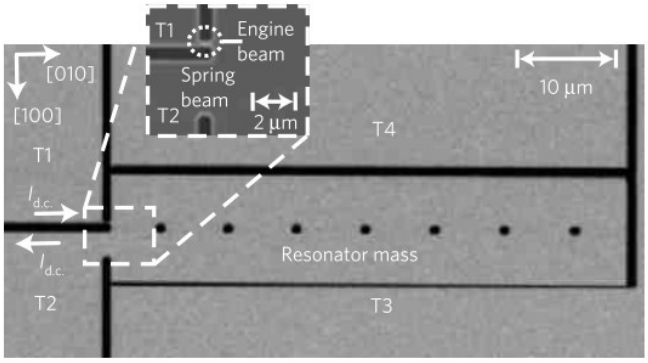

a) Single actuator torsional beam "heat engine" First demonstration of DC oscillation (2011, from [65] **)**

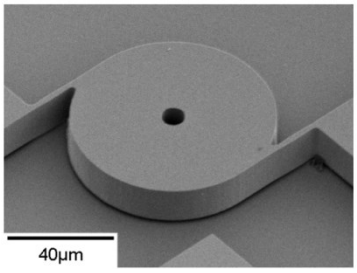

b) Rotational disk resonator
Liquid/chemical detection
(2010, from [66] **)**

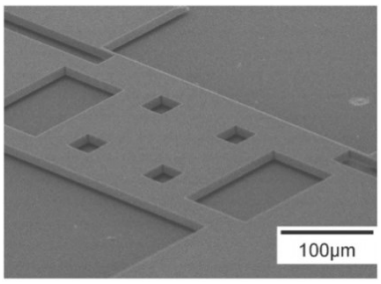

c) Lateral plate resonator
Airborne particle detection
(2010,from [16]**)**

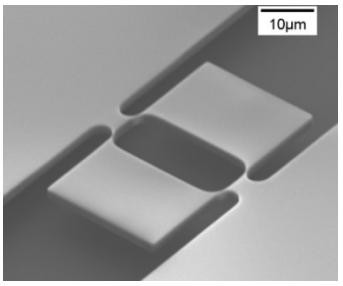

d) I-shaped resonator
18.1 Mhz DC oscillator
(2011, from [62]**)**

Figure 2.8: Summary of previously reported in-plane thermally actuated resonant device geometries that utilize inherent piezoresistance of n-type single-crystal silicon structure. The device geometry shown in d) is the focus of this work.

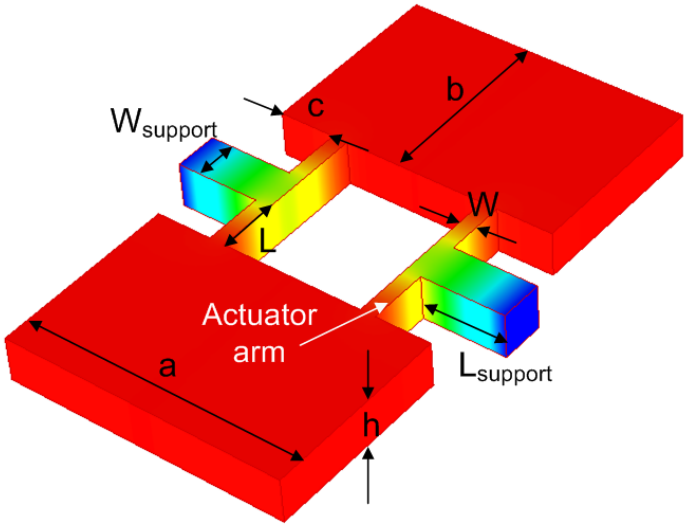

Figure 2.9: Graphical schematic of I-shaped or dogbone resonator geometry with dimensions. Colors are indicative of an arbitrary steady state temperature distribution for DC applied voltage with the support anchor ends acting as heat sinks at a fixed temperature. The temperature gradient evident in the actuator arms (width = W, length = L) is amplitude modulated by the addition of an AC drive voltage.

This geometry is acoustically advantageous since the longitudinal acoustic waves which propagate from these actuator arms are perpendicular to the support arm the amount of leakage through the support arms is reduced when compared to the device geometries shown in Figure 2.8a-c) where the actuator also acts as a structural support to the substrate.

2.7.3. Lumped Parameter System Model and Performance Scaling

The complete *frequency response* of these thermal-piezoresistive resonator devices in the *sinusoidal steady-state*[6] has been previously modeled by Rahafrooz and Pourkamali ([15], [61]), as a series of lumped parameter *linear time-invariant*[7] (LTI) subsystems. Each subsystem represents the individual frequency response (a.k.a. harmonic or Fourier response) in the thermal, mechanical, and electrical domains.[8] The resulting product of these subsystem transfer functions is the overall system transfer function which relates the input (applied) ac voltage, v_{ac}, to the ac (motional) current output, i_{ac}. These subsystems are depicted in the block diagram shown in Figure 2.10, where T_{ac} is the temperature fluctuation amplitude within the actuator beams, X_{th} is the elongation amplitude of the actuator beams, and $s = j\omega$. The block diagram is depicted in the sequence which matches the previously described concept of operation, although mathematically each of these subsystems is independent of the other.

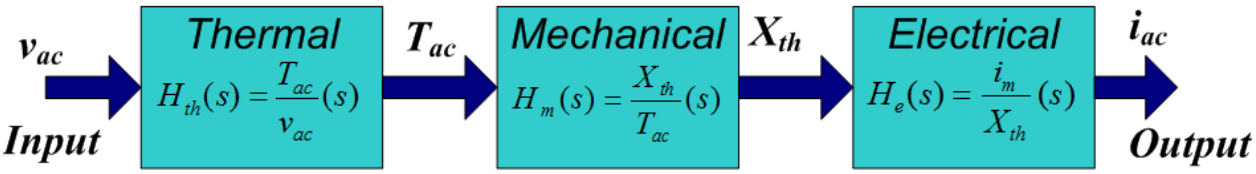

Figure 2.10: Block diagram of lumped parameter thermoelectromechanical model (adapted from [61] **)**

This modeling approach does not accommodate dynamic variations due to changes in material properties or geometry, but has been shown to provide an accurate estimate for the steady-state frequency response at the resonant frequency for devices previously reported in [61].

The lumped elements of each subsystem can be considered as equivalent circuit elements in their respective domains allowing similar representation to an electric circuit. Further detail on this topic is discussed by Senturia [1]. Figure 2.11 shows the equivalent electrical circuit for each subsystem noting the appropriate analogies to current and voltage for each domain.

The overall system transfer function for the device is the product of the three subsystem transfer functions,

---

[6] *Sinusoidal steady state* presumes that the system is in the zero-state upon initial sinusoidal signal application and that the system transients have died out [1].

[7] *Linearity* for a continuous time system implies that the *superposition* property holds (a combination of the *additivity* and *scaling* properties). Mathematically this means that for system inputs $x_1(t)$ and $x_2(t)$ and system response $y_1(t)$ and $y_2(t)$, the property $ax_1(t) + bx_2(t) \rightarrow ay_1(t) + by_2(t)$ holds true. *Time invariance* implies that the behavior and characteristics of the system are fixed over time. Specifically, a system with input $x(t)$ and response $y(t)$ is *time invariant* if the input $x(t - t_o)$ has the output $y(t - t_o)$. LTI systems, their properties, and representation in frequency space are all discussed in great detail by Oppenheim and Willsky [5].

[8] It is important to note that this formulation is only valid for *stable* LTI systems, where the impulse response $h(t)$ is absolutely integrable (i.e. the impulse response possesses a Fourier transform). Analysis for an unstable LTI system would require the use of the Laplace transform [5].

$$H_{Total}(s) = H_{th}H_{mech}H_{elec} = \frac{i_m}{V_{ac}} = \left(\frac{4\alpha E^2 A {I_{dc}}^2 \pi_l}{L_A(M(s)^2 + b(s) + k)}\right)\left(\frac{R_{th}}{1 + R_{th}C_{th}(s)}\right) \quad \{2\text{-}36\}$$

where $= j\omega$. This derivation for this relation, originally reported by Rahafrooz and Pourkamali in [61], is presented in Appendix 1 with additional details. Under the assumption that the mechanical resonant frequency is much larger than the thermal resonant frequency (i.e. $\omega_o \gg \tau_{th}^{-1} = (R_{th}C_{th})^{-1}$), the amplitude of this system transfer function at the resonant frequency, $\left|H_{T|s=j\omega_o}\right|$, which is equivalent to the peak motional conductance, g_m, can be shown to be

$$\left|H_{T|s=j\omega_o}\right| = g_m = \frac{i_m}{v_{ac}} = \frac{2\alpha E \pi_l Q I_{dc}^2}{C_{th}\omega_o} \quad \{2\text{-}37\}$$

where α, is the linear thermal coefficient of expansion, E, is Young's modulus, π_l, is the longitudinal piezoresistive coefficient, Q, is the quality factor, I_{dc}, is the DC current, C_{th}, is the thermal capacitance, and $\omega_o$is the resonant frequency.

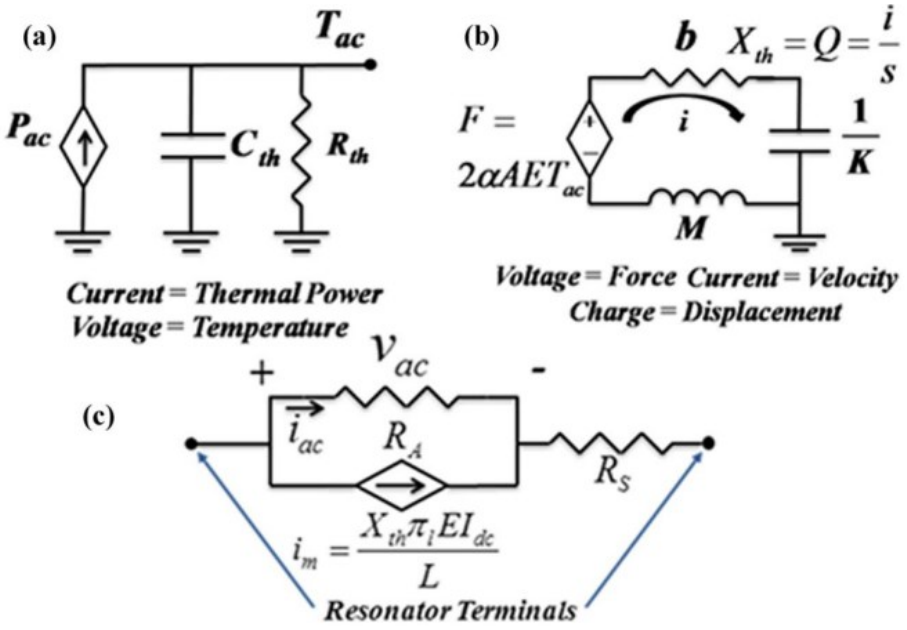

Figure 2.11: a) Equivalent circuit for thermal subsystem, b) Equivalent circuit for mechanical subsystem, and c) Equivalent circuit for electrical subsystem (from [61]**)**

The overall system representation of the resonators in this work is represented by Figure 2-11, where R_A is the resistance off the actuators and R_s is the additional series resistance, primarily due to the support arms.

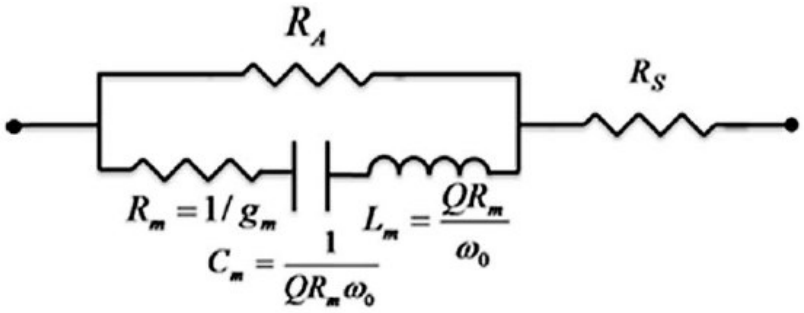

Figure 2.12: Equivalent circuit for thermal-piezoresistive resonators (from [61]**)**

The motional conductance, which is essentially the small signal gain of the measured output current to the input ac voltage, depends upon the DC current and hence the power to the device. Ideally, optimal performance seeks to maximize motional conductance while minimizing power consumption. The following ratio of the two has been used as a figure of merit for device comparison

$$FOM = \frac{g_m}{P_{dc}} = \frac{2\alpha E \pi_l Q}{C_{th}\omega_o(R_A + R_S)} \quad \{2\text{-}38\}$$

where R_A, is the resistance of an actuator arm. Normalizing this FOM with Q provides a means for comparing dissimilar devices.

The driving factor in the improvement with scaling lies with the thermal capacitance of the actuators arms, since they scale with volume of the actuator arm. From [15] a single pair of actuator arms can be considered to have an effective thermal capacitance, C_{th}, of

$$C_{th} = \beta C_{LE} = \beta 2\rho LWhC_H \quad \{2\text{-}39\}$$

where C_{LE} is the lumped-element thermal capacitance, β is a correction factor which has been established from finite-element analysis in [15] to be between 1.11 and 1.02, ρ is the density (2.33E-15 kg/μm^3 for silicon) , and C_H is the specific heat of silicon (700 J kg^{-1} K^{-1}). The additional factor of 2 is added because the capacitance is intended to represent a pair of individual actuators as defined in Figure 2.9.

For reference and comparison to the devices in this work, Table 2.4 shows a summary of the dimensions and performance of devices previously reported by Rahafrooz and Pourkamali [61].

2.7.4. Self-Q Enhancement and Self-Sustained Oscillation

As mentioned earlier, probably the most significant feature of these in-plane thermal-piezoresistive resonators is the potential for self-Q enhancement and DC powered oscillation. This was first reported for the heat engine shown in Figure 2.8 a) [65] and later demonstrated at higher frequencies for the I-shaped geometries shown in Figure 2.8 d) [62]. The ability to harness this phenomena can potentially allow higher Q values at higher frequencies then realizable with traditional capacitive and piezoelectric means.

As shown in by Rahafrooz and Pourkamali in [67], the expression for the *effective quality factor* during self-Q enhancement can be derived from the representative circuit diagram shown in Figure 2.12, minus the series resistance R_s, and using the same approach taken in Section 2.3 for the mechanical quality factor. The stored energy of the RLC circuit remains unchanged from Eq {2-31} with the actuator resistance, R_A, in parallel. The total dissipated energy however needs to be reconsidered to account for this additional element. A resonance the reactive components of the inductor and capacitor cancel leaving the two resistors, R_a and R_m in parallel. The current through each resistor is related as follows

$$I_A = I_{pk}\frac{R_m}{R_A} \qquad \{2\text{-}40\}$$

where I_A is the current through R_A and I_{pk} is current through R_m. The total energy dissipated is therefore

$$E_D = \langle P_D \rangle T = \left(\left(\frac{I_{pk}^{\,2}}{\sqrt{2}}\right)R_m + \left(\frac{I_A^{\,2}}{\sqrt{2}}\right)R_A\right)T \ . \qquad \{2\text{-}41\}$$

Table 2.4: Reported performance of previous MEMS scale device of this geometry (from Rahafrooz and Pourkamali [61]**)**

Scale Factor	Resonator Dimensions (μm)						Measured Parameters				Calculated Parameters					
	a	*b*	*c*	*L*	*W*	*H*(μm) *Resistivity (Ω.cm)*	Current (mA)	Q. Factor	Freq. (MHz)	g_m (mA/V)	Power (mW)	R_A (Ω)	C_{th} (nJ/°K)	g_m (mA/V)	F.M./Q. (10^{-6} V^{-2})	Power (mW) @ g_m=1 (mA/V)
1X	274	30	67	31	4	10	16.8	29000	7.94	2.53	6.00	5.81	2.02	2.93	16.8	2.05
							40.5	37000	7.75	27.0	34.9			23.3	18.1	1.49
0.7X	193	21	47	22	2.7		26	24000	10.87	10.2	16.3	6.11	0.968	9.12	23.2	1.79
						1.5×10^{-3}	30.5	16000	10.63	10.9	22.5			8.95	24.8	2.52
0.5X	144	16	35	16	2		21.3	12000	13.94	5.80	10.8	6.00	0.521	4.83	37.0	2.25
							30.2	7000	13.78	10.0	21.8			5.86	38.3	3.73
1X	80	53	16	64	17.4	10	55	28500	15.89	2.18	63.5	11.0	18.1	1.56	0.86	40.6
							80	29000	15.65	8.08	134			3.52	0.90	38.2
							50	10800	15.91	0.60	52.5			0.49	0.86	107
							90	10900	15.73	4.29	170			1.65	0.89	103
0.5X	39	25	8.5	32	8.5	6×10^{-3}	20	29000	31.18	0.319	9.09	11.3	4.43	0.48	1.82	18.9
							65	38500	30.72	11.3	96.0			7.04	1.90	13.6
							30	11000	31.17	0.271	20.4			0.41	1.82	49.8
							70	12000	30.9	2.88	111			2.50	1.87	44.5
NA	18.5	11.5	4.4	14.9	0.77	3	0.043	36000	30.52	2.07×10^{-4}	1.71×10^{-3}	645	5.61×10^{-2}	2.30×10^{-4}	3.73	7.44
							0.72	24400	30.52	4.36×10^{-2}	0.481			4.38×10^{-2}	3.73	10.9
							0.062	13250	30.52	1.42×10^{-4}	3.56×10^{-3}			1.76×10^{-4}	3.73	20.2
							2.69	9200	30.43	0.234	6.71			0.233	3.77	28.8
NA	18.5	12.3	4.4	12.9	1.03		0.544	3800	41.73	4.87×10^{-4}	0.220	417	6.50×10^{-2}	1.06×10^{-3}	1.26	208
							5.32	2600	40.60	1.98×10^{-2}	21.1			7.51×10^{-2}	1.37	280
						2×10^{-2}	0.363	2700	40.60	2.32×10^{-4}	0.098			3.63×10^{-4}	1.37	270
							5.21	2300	40.70	3.37×10^{-2}	20.3			6.34×10^{-2}	1.36	319
NA	12.9	9	3	8.67	0.43		0.441	1400	45.20	8.88×10^{-4}	0.182	672	1.82×10^{-2}	8.87×10^{-4}	3.49	204
							5.55	1700	43.78	5.28×10^{-2}	28.8			0.188	3.84	153
							0.266	1300	45.20	3.72×10^{-4}	0.066			3.00×10^{-4}	3.49	220
							5.47	1500	43.90	6.33×10^{-2}	28.0			0.160	3.81	175
NA	22	15	4.4	18	5	15	60	14000	61.64	5.73	32.3	4.20	2.20	5.4	11.8	6.01
							100	12000	60.85	21.5	89.8			15.7	14.5	5.73
						3.5×10^{-3}	60	7500	61.65	3.38	32.3			3.39	13.9	9.53
							100	7700	61.11	12.9	89.8			9.9	14.3	9.04
	= data obtained under atmospheric pressure															

Applying Eq {2-40}, Eq {2-41} simplifies to

$$E_D = \left(\frac{I_{pk}^{\ 2}}{\sqrt{2}}\right)\left(R_m + \frac{R_m^{\ 2}}{R_A}\right)\left(\frac{2\pi}{\omega_o}\right) = \frac{\pi}{\omega_o} R_m \left[1 + \frac{R_m}{R_A}\right] I_{pk}^{\ 2} \qquad \{2\text{-}42\}$$

The effective quality factor, Q_{eff} , can be solved for by substituting Eq {2-31}and Eq {2-42} into Eq{2-21}, yielding[9]

$$Q_{eff} = \frac{Q_m}{1 + R_A g_m}(R_A g_m) \qquad \{2\text{-}43\}$$

where Q_m is the mechanical quality factor defined by Eq {2-33}

Alternatively, Steeneken et al. [65] presents the derivation for effective quality factor with a more direct approach by examining the governing ODE for the system.

[9] The expression reported by Rahafrooz and Pourkamali [67] neglects the $R_a g_m$ term in the numerator. This may be because the term approaches -1 and is considered negligible.

$$X_{th}'' + \frac{\omega_o}{Q_m} X_{th}' + \omega_o{}^2 X_{th} = \frac{F_{te}}{M} = \omega_o{}^2 I_{DC}{}^2 \chi X_{th}$$
$$\chi = \frac{2\alpha E R_A \pi_l}{(\frac{1}{R_{th}} + j\omega C_{th})} \quad \{2\text{-}44\}$$

where X_{th} is the thermal deflection, F_{te} is thermoelastic force, and Q_m is the internal mechanical quality of the system (equivalent to the Q in Eq {2-37}). This approach is equivalent to the transfer function based derivation in Appendix 1 by treating the entire system as a forced MSD system with the thermal subsystem integrated into the forcing function. At resonance $\omega_o = \omega$ and Eq {2-44} reduces to

$$-\omega^2 + i\omega\omega_o \left(\frac{1}{Q_m} - I_{dc}{}^2 \,\mathrm{Im}(\chi) \right) + \omega_o{}^2 (1 - I_{dc}{}^2 \,\mathrm{Re}(\chi)) = 0$$
$$\frac{1}{Q_{eff}} = \left(\frac{1}{Q_m} - I_{dc}{}^2 \,\mathrm{Im}(\chi) \right) \quad \{2\text{-}45\}$$

As indicated, the central bracketed term in Eq {2-45} can be thought of as the inverse of the effective Q for the system. When the condition $\frac{1}{Q_m} = I_{DC}{}^2 \,\mathrm{Im}(\chi)$ is reached the effective quality factor approaches infinite. By assuming the mechanical resonant frequency is much larger than the thermal resonant frequency (i.e. $\omega_o \gg \tau_{th}^{-1} = (R_{th}C_{th})^{-1}$, which is the same assumption made in Appendix 1 for g_m) then the expression for Im(χ) simplifies to

$$\mathrm{Im}(\chi) = \frac{-R_A E \alpha \pi_l}{C_{th}\omega_o} \quad \{2\text{-}46\}$$

and Q_{eff} can be solved to be

$$Q_{eff} = \frac{Q_m}{1 + R_A g_m} \quad \{2\text{-}47\}$$

which is equivalent to {2-43} sans the extra term in the numerator.

Per [63], as evidenced by Eqs {2-43} and {2-47}, the opportunity for self-sustained oscillation and self-Q enhancement stems from the ability for these devices to have a negative motional conductance (or negative motional resistance). This will occur when the structural material has a sufficiently negative piezoresistive coefficient per {2-11} when the absolute value in the equation is removed. If the magnitude of the negative g_m is beyond the value of R_A^{-1} then, from [63], "instead of the resonator losing part of its energy in every cycle it gains energy in every cycle, which leads to instability of the system and self-sustained oscillation". The initial application of DC bias (unit step input) has enough frequency content to start the oscillations. The actuators heat up immediately upon application of the DC bias forcing the proof masses away from each other. From [63], "the inertia inherent to the proof masses causes them to

experience an over expansion and undergo a tensile stress." This tensile stress reduces the electrical resistance of the beams, and since the DC bias current is fixed the ohmic heating ($P = I^2R_A$) will reduce causing contraction. Once again due to the inertia inherent to the proof masses the actuators will undergo compressive stress increasing their electrical resistance. This in turn translates into thermal power (heating) resulting in an expansion. The amount of overcontraction and overexpansion occurring in each cycle can result in enough additional thermal energy being converted to mechanical such that the cycles are self sustaining. It's important to note that the 90° phase lag between the heating/cooling and the mechanical actuation facilitates the appropriate timing for this positive feedback. Figure 2.13 shows the process graphically.

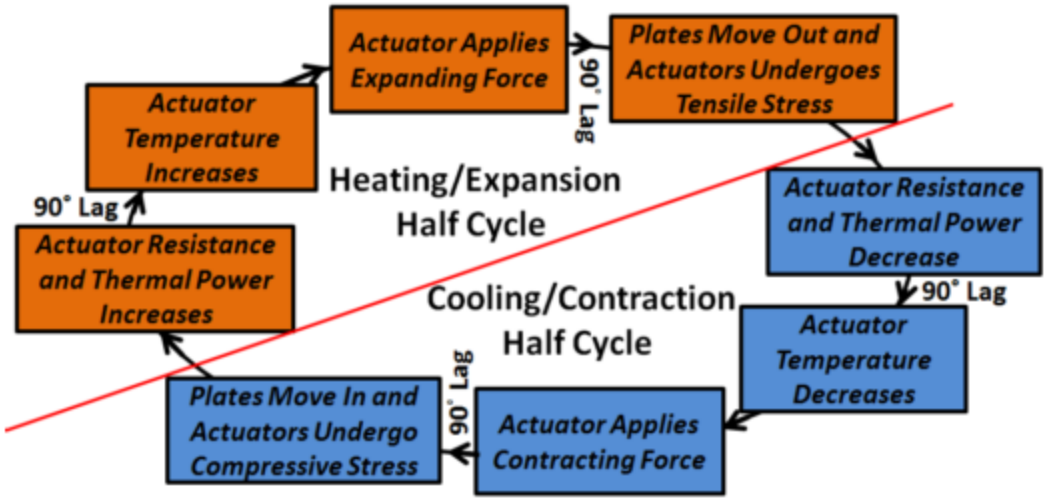

Figure 2.13: Sequence of phenomena causing an internal positive feedback loop in the thermal-piezoresistive resonators biased with a constant current that lead to self-sustained oscillation (from [63]**)**

It is interesting to note that if the effective quality factor is substituted back into the equation for g_m in place of Q the following expression for an effective g_m results

$$\left|H_{T|s=j\omega_o}\right|_{eff} = g_{m_{eff}} = \left(\frac{2\alpha E \pi_l I_{dc}^2}{C_{th}\omega_o}\right) Q_{eff} = \frac{\left(\frac{2\alpha E \pi_l I_{dc}^2}{C_{th}\omega_o}\right) Q_m}{1 + R_A\left(\frac{2\alpha E \pi_l I_{dc}^2}{C_{th}\omega_o}\right) Q_m} \qquad \{2\text{-}48\}$$

This expression is in the same form as that for the closed loop gain of a linear feedback system with negative feedback, shown graphically in Figure 2.14, which is

$$\frac{Y}{X} = \frac{A}{1 + AB} \qquad \{2\text{-}49\}$$

When the piezoresistive coefficient, π_l, is negative the denominator approaches zero as I_{DC} is increased and the overall effective g_m becomes strongly negative until the condition for oscillation is reached.

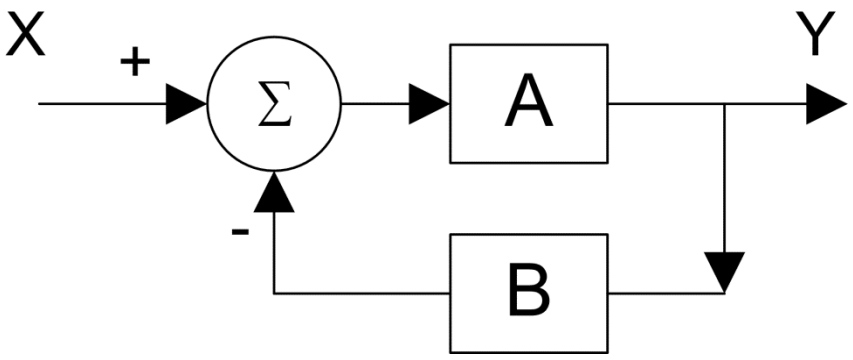

Figure 2.14: Closed Loop Feedback System

It is important to note that all oscillators (conventional and self-sustained) are inherently non-linear devices, where their steady-state operation can be described as a *limit cycle*. Complete modeling of this phenomena utilizes mathematical methods for non-linear dynamical systems, which is beyond the scope of this work (see text by Enns [68]). However, classical linear theory can provide a framework for modeling the conditions needed for "stable" operation as has already been demonstrated. The term stable is rather context dependent. Oscillators are essentially unstable systems (or marginally stable) with complex poles at the edge of the right side of the s-plane near the imaginary axis. So from a control system perspective they are very unstable. The term stable in the context of an oscillator is rather referring to the ability of the oscillator to generate a consistent waveform (typically sinusoidal) over time (i.e. the waveforms amplitude and frequency remain fixed over time). As already mentioned there are two criteria needed for initiating oscillation. The total phase shift should be 360° in the oscillator loop and the AB gain term should equal -1, which is met by the condition described by Eq {2-47}. In conventional oscillator theory these conditions are necessary for oscillation but not sufficient to sustain a stable oscillation. In addition, as explained by van Beek and Puers [12], conditions for phase stability and amplitude stability of the oscillator must be also be met. Developing these for the internal feedback system that is the subject of this work remains an open area for further investigation.

2.8. Effects on Single Crystal Silicon (SCS) Material Properties

The lumped parameter model described earlier does not account for variations of the material constants with respect to doping, temperature, crystal orientation, or geometric sizing. Consideration of these effects is critical for understanding the limitations of the design, modeling its operation and ultimately enhancing performance.

2.8.1. Young's Modulus

Silicon is an anisotropic material and its elasticity is more completely described by a high order tensor. By applying cubic crystal symmetry and equivalence of the shear conditions this tensor is reduced to a simplified 6x6 matrix of stiffness coefficients which can be used to calculate the

Young's modulus for any crystal orientation. Hopcroft et al. present a detailed review of this topic in [69], with the results for bulk silicon (100 plane) shown in Figure 2.15. This review paper further indicates that silicon that is heavily doped typically experiences no more than 1-3% deviation from these values.

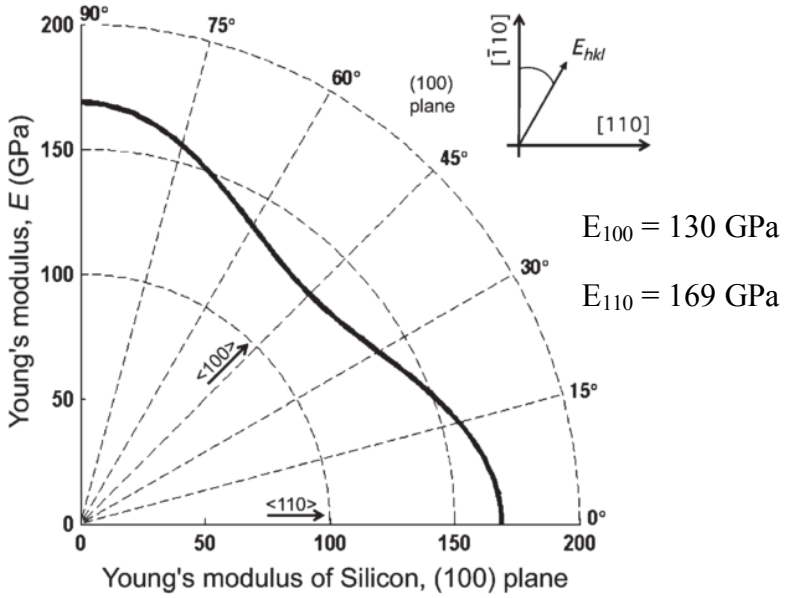

Figure 2.15: Young's modulus of Silicon, (100) plane (from [69] **)**

While the temperature behavior of elasticity is also most properly explained in the form of the temperature coefficients for each components of the elastic tensor, it is reported by [69] that the temperature coefficient of Young's modulus is largely invariant with respect to crystal orientation at nearly -60 ppm/°C at room temperature. Ono et al. reported in [70] the following fit relation for Young's modulus in the 100 plane for Boron concentration

$$E_{[100]} = (1.25 * 10^5 e^{\left(\frac{2.61x10^{-3}(eV)}{kT}\right)}) \text{ (MPa)} \qquad \{2\text{-}50\}$$

With regards to scaling, it has been reported that for <111> oriented Si nanowires between 100 nm and 600 nm the elastic constant remains invariant [71]. As the scale is decreased to less than 100 nm, it is expected that lattice defects and surface effects place a larger role as suggested most recently by [72] with <110> cantilevers.

2.8.2. Electrical Resistivity and Piezoresistive Effect

The electrical resistance of a prismatic structure (i.e. one with constant cross section) of a homogeneous material with a resistivity, ρ, is classically defined as

$$R_{electrical} = \rho \frac{l}{A} \qquad \{2\text{-}51\}$$

where l, is the length of the structure, and A is the cross section. Thus changes to resistivity and geometry cause changes in electrical resistance.

Electrical Resistivity

For a uniformly doped semiconductor the resistivity is defined as

$$\rho = \frac{1}{q(\mu_n n + \mu_p p)} \qquad \{2\text{-}52\}$$

where q, is the elementary charge, n and p, are the electron and hole densities respectfully, and μ_n and μ_p are their respective mobilities in the material. For semiconductors doped with a single species of donor or acceptor atoms, the majority carrier density can be assumed to be that of the doping and the minority carriers can be ignored. Carrier mobility is dependent upon the degree of impurity and lattice scattering within the material. The mobility is empirically defined by the following expression (from [73])

$$\mu = \mu_{min} + \frac{\mu_{max} - \mu_{min}}{1 + \left(\frac{N}{N_r}\right)^{\alpha}} \qquad \{2\text{-}53\}$$

where N is the doping density and μ_{max}, μ_{min}, N_r, and α are fit parameters. For phosphorus doping at room temperature $\mu_{max} = 68.5$ cm^2/(V·s), $\mu_{min} = 1414$ cm^2/(V·s), $N_r = 9.2 \times 10^{16}$cm^{-3} and $\alpha = 0.711$. Figure 2.16 shows the plot of resistivity vs doping concentration for both n-type (phosphorus) and p-type (boron) silicon using {2-52} and {2-53}.

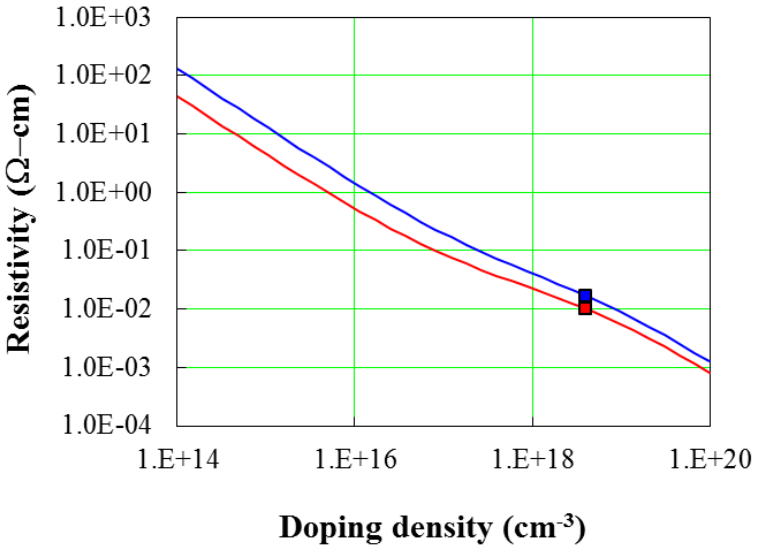

Figure 2.16: Plot of resistivity for n-type (red) and p-type (blue) uniformly doped silicon at room temperature. The markers show the resistivity for a doping level of 4E+18 cm^{-3} which is the approximate doping level for the devices in this work. (from van Zeghbroeck [73]**).**

Temperature dependence of an *intrinsic* (undoped) semiconductor generally decreases with increasing temperature from absolute zero as more electrons are thermally excited into the conduction band. The behavior of doped (*extrinsic*) semiconductors is substantially more complicated. Extrinsically doped semiconductors will initially decrease sharply in resistivity as temperature increases from absolute zero. This effect is due to the fact that thermal ionization of the dopants is exponential with temperature and the resulting increase in carrier concentration drives the resistivity.[10] However, once the majority of impurity atoms are thermally ionized, per {2-52} the trend is for the resistivity to increase due to the decreasing mobility from scattering mechanisms (lattice and impurity scattering). This temperature region is described as the *extrinsic T-region* or *saturated* region. This trend continues until the temperature reaches a point where the thermally generated intrinsic carrier concentration exceeds that of the extrinsic doping concentration (aka the *intrinsic T- region*). At this point the resistivity is dominated by the intrinsic carriers and resistivity decreases with increased temperature in the same fashion as the intrinsic semiconductor. Finally when the melting point of the semiconductor is reached it behaves as a metal as described further by Kim et al [74].

For this work, as with most semiconductor based electronic devices, the extrinsic T-region is most relevant. The following empirical equation from Arora et al. (1982) [75] expresses the electron mobility as a function of temperature and doping in this region by temperature scaling {2-53} appropriately to account for scattering

$$\mu_n(T,N) = 88\left(\frac{T}{300}\right)^{-0.57} + \frac{7.4\times10^{8}T^{-2.33}}{1+\left[\dfrac{N}{1.26\times10^{17}\left(\dfrac{T}{300}\right)^{2.4}}\right]0.88\left(\dfrac{T}{300}\right)-0.146} \qquad \{2\text{-}54\}$$

For n-type doping $\rho = \frac{1}{q\mu_n N_D}$ and the resistivity vs. temperature for different doping levels can be calculated.

While the mobility formulation is useful for precise estimation of resistivity it is less commonly utilized. In most practical application, the changes in resistance with temperature are often approximated to the first order by use of the following relation

$$R = R_o[1+\alpha_R(T_R - T_o)] \qquad \{2\text{-}55\}$$

[10] The analytical relation for intrinsic carrier concentration, n_i ,is $n_i = \sqrt{N_c N_v}e^{\frac{E_G}{k_B T}}$ where $N_{C,V}$ are the "effective" density of conduction band and valance states, E_G is the bandgap, k_B is Boltzman's constant, and T is the temperature. While $N_{C,V}$ also have a dependence upon temperature, the exponential term dominates. Further detail is provided by Pierret in [123].

where α_r, is the temperature coefficient of resistance (TCR) for the material. Extrinsically doped silicon in the saturation region thus has a *positive TCR*.

Piezoresistance

When a structure undergoes strain the resulting fractional change in resistance, $(\Delta R/R)$, is due to both the changes in the geometry $(1 + 2\nu)$ and fractional change in resistivity $(\frac{d\rho}{\rho})$ as described by

$$\frac{dR}{R} = (1 + 2\nu)\varepsilon + \frac{d\rho}{\rho} \qquad \{2\text{-}56\}$$

The derivation for this expression involves taking the total derivative of electrical resistance as defined by {2-51}and is presented by Beeby et al [76]. The geometric term is determined by Poisson's ratio which for silicon in the <100> direction is approximately 1.6. For silicon, the fractional change in resistivity however has been reported to be in the range of 50-100 times larger than the geometric term [77]. This change in resistivity with applied load is called *piezoresistance*. A recent (2009) review on the phenomena as applied to microsystems was performed by Barlian et al. [77]. Like other anisotropic material properties a complete description of piezoresistance requires a tensor formulation. However, for silicon this tensor can simplified to a 6x6 matrix, in similar fashion as the stiffness coefficients, to facilitate calculation of the longitudinal (parallel to current flow) and transverse (perpendicular to current flow) piezoresistive coefficients in any crystal direction[11]. The expression for the fractional change in resistivity is thus

$$\frac{d\rho}{\rho} = \pi_l\sigma_l + \pi_t\sigma_t \qquad \{2\text{-}57\}$$

where π_l and π_t are the longitudinal and transverse piezoresistive coefficients and σ_l and σ_t are the corresponding stresses [76].

The physical origins of the piezoresistive effect are attributed to changes in the mobility of the holes and electrons from the applied lattice strain altering the energy band structure of the material. Further detail on the modeling theories which describe this phenomena can be found in [77] and the numerous references it cites. As simply stated in [76], "With p-type materials, the mobility of holes decreases and so the resistivity increases. For n-type materials, the effective mobility of the electrons increases and hence the resistivity decreases with applied stress."

Polar plots of the longitudinal and transverse coefficients in the (100) plane for n-type silicon, originally portrayed by Kanda [78], are shown in Figure 2.17. While these charts are

[11] Sheer piezoresistivity also exists in silicon but is less commonly used in microsystems.

only strictly valid for low doping and room temperature conditions they portray an accurate representation of the tendencies of these coefficients. The devices in this work are fabricated from n-type silicon aligned in the <100> direction to take advantage of the large negative longitudinal piezoresistive coefficient.

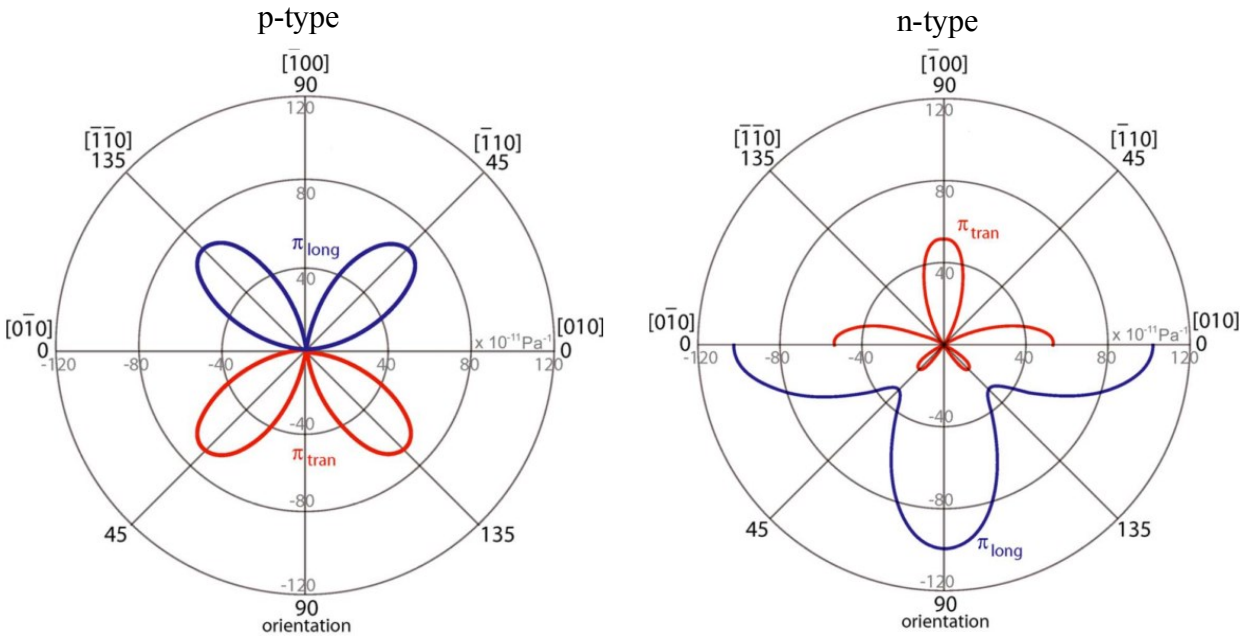

Figure 2.17: Room temperature piezoresistive coefficients in the (100) plane (from [77] **after Kanda** [78]**). These are considered accurate for low doping conditions.**

In 1956, Herring [79], developed the now conventional description for piezoresistance in the context of the "many-valleys" model of the band structure for a semiconductor.[12] As depicted in Figure 2.18, unstrained n-type silicon has six regions of lowest energy ("valleys") in momentum space (or k-space), symmetrically distant from the origin, aligned along the <100> principle directions. These regions are normally populated with electrons as they tend to occupy the lowest energy states first. Electron mobility in these regions is lowest in the directions perpendicular to the direction they are aligned upon (e.g. electrons in the regions along the x-direction have greatest mobility in y and z axes). In the case of n-type silicon when tension is applied along one of these principle directions the region shifts to higher energy. This causes the electrons to seek alternate lower energy states to occupy and so they populate the other two regions along the directions which are perpendicular. Since mobility in these regions is greater in the direction of the strain, the overall mobility, which is the average of carriers in all regions, goes up. Likewise the opposite is true for compression along this axis.

[12] This model can also be applied for formulations of carrier mobility and the role of scattering mechanisms. However empirical relations such as Eq {2-54} are more commonly used for practical usage.

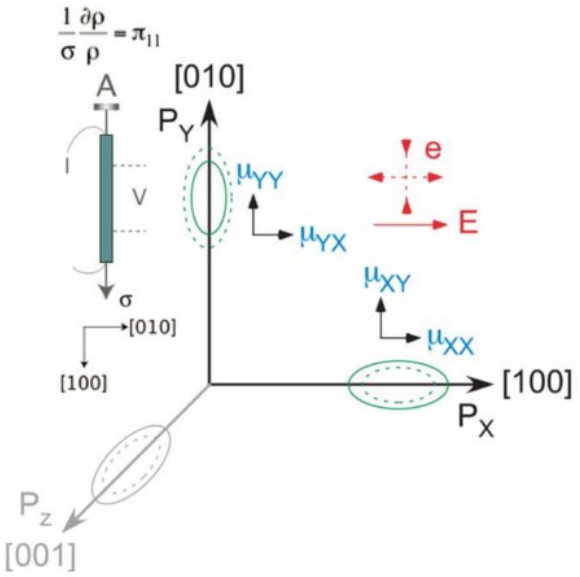

Figure 2.18: Probable constant energy surfaces in momentum space for a longitudinally strained sample of n-type Si in the test configuration shown. The applied potential, E, and applied strain, e, are depicted in for proper crystal orientation. The electrons are located in six energy valleys (each of the three shown is also mirrored in the negative axial direction) at the centers of the constant energy ellipses, which are shown greatly enlarged. The effect of longitudinal stress in the [100] direction on the two valley energies shown is indicated by the dotted ellipsoids. The mobilities of the several groups of charge carriers in various directions are roughly indicated by the arrows. Figure is from [77] **after Smith** [80] **who performed the first measurements of piezoresistance in silicon and germanium while at Bell Laboratories in 1954.**

Since piezoresistance, like electrical resisitivity, is an effect governed largely by electron mobility and the energy band structure it is unsurprising that the piezoresisitve coefficients also vary with doping and temperature. Figure 2.19 and Figure 2.20 summarize some of the more recent experimental observations for the longitudinal coefficient in n-type silicon [81], [82].

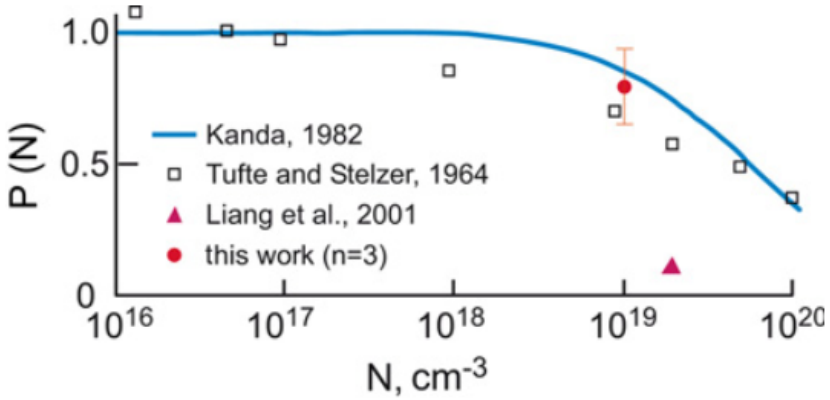

Figure 2.19: Experimental piezoresitive factor P(N) for the longitudinal piezoresistive coefficient in n-type silicon (from [81] **in 2009, the "this work" reference). To obtain the longitudinal piezoresistive coefficient for a specific doping, N, multiply the P(N) value by the room temperature piezoresistive coefficient (102×10^{-11} Pa^{-1} per Kanda** [78] **).**

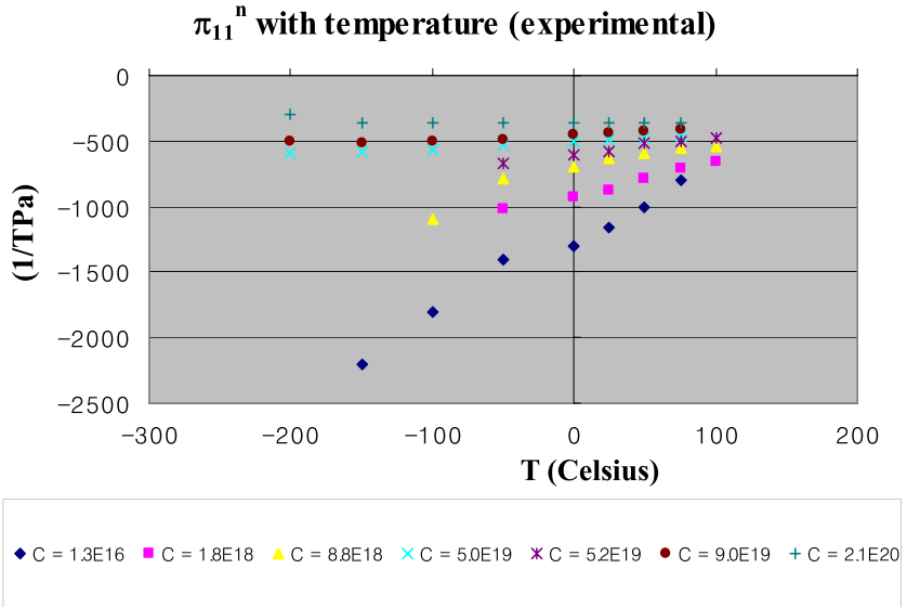

Figure 2.20: Summary of experimental measurements of the variation of piezoresistive coefficient for n-type silicon with temperature (from [82]**) For the <100> direction, π_{11} is equivalent to longitudinal piezoresistive coefficient.**

In 2006 He and Yang reported piezoresistance values for silicon nanowires several time greater than the bulk values [83]. This "giant" piezoresistance effect has garnered significant interest since and remains to be definitively explained. The effect has been attributed in part to electron trapping at the Si/SiO2 interface [84], [85] in addition to quantum confinement effects [86], [87]. Specific focus on top-down fabricated suspended nanowires from SOI wafers has been recently performed by Koumela et al [88] indicating piezoresistance values close to bulk. However they did report that the suspended nanowires had up to 100% higher gauge factor than unreleased nanowires and suspect that the surrounding SiO_2 affects the surface charge density of the nanowire. These studies all seem to have focused on p-type boron doped silicon nanowires with dimensions < 200 nm in both width and thickness.

2.8.3. Coefficient of Thermal Expansion

As explained by Senturia [1], thermal expansion is "the tendency for a free body to increase in size as it is heated". In cubic materials, such as silicon, this expansion is isotropic (i.e. the same in all three principle axis directions). From [1], the *linear thermal expansion coefficient* (or *linear coefficient of thermal expansion CTE*), α_T, is defined as the rate of change of uniaxial strain, ϵ_x , with temperature, T as shown below.

$$\alpha_T = \frac{d\epsilon_x}{dT} \qquad \{2\text{-}58\}$$

As strain is a unitless parameter, the units for α_T are K^{-1}. Typically, for most practical engineering purposes, α_T is approximated as being a material constant, invariant with temperature. Thus by approximating {2-58} with finite differences the change in uniaxial strain between temperature, T, and original temperature, T_o, is

$$\epsilon_x(T) - \epsilon_x(T_o) = \alpha_T \Delta T \qquad \{2\text{-}59\}$$

Since thermal expansion is a primary influence on thin film stress, the microelectronics industry has motivated numerous research efforts on measuring the CTE in silicon and how it changes with temperature. Arguably the most comprehensive work was that conducted by Okada and Tokumaru in 1984 [89], which summarized and expanded upon a multitude of previous findings to establish an empirical formula for CTE as a function of temperature between (120 K and 1500 K)

$$\sigma_T(T) = \left(3.725\left\{1 - e^{-(5.88\times10^{-3})(T-124)}\right\} + (5.548\times10^{-4})T\right)\times10^{-6} \ \ (K^{-1}) \qquad \{2\text{-}60\}$$

A plot of this relationship is shown in Figure 2.21.

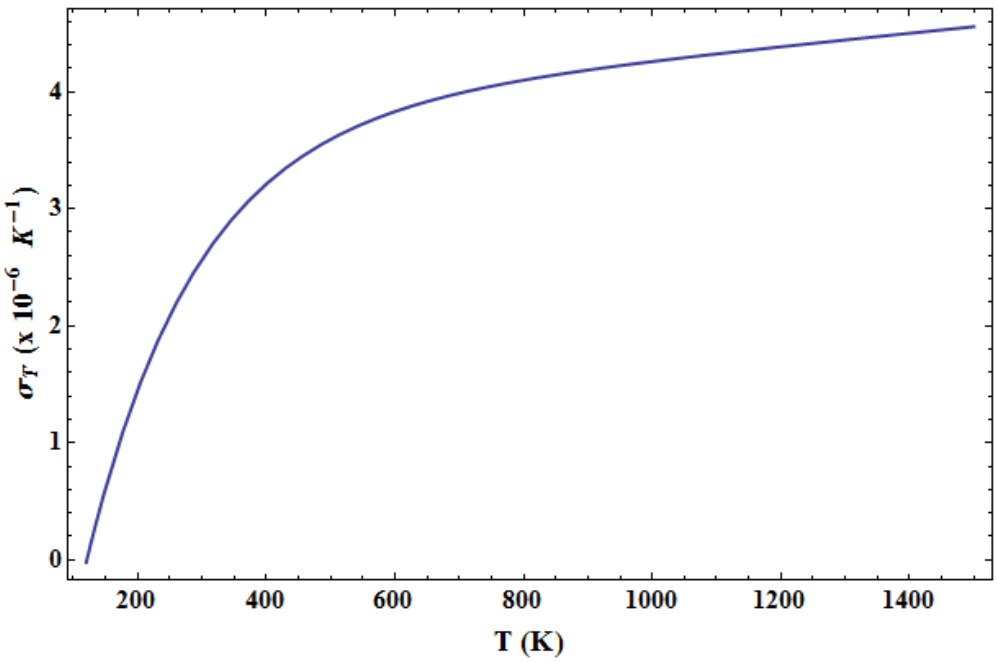

Figure 2.21: Temperature dependence of linear coefficient of thermal expansion of silicon based upon Okada and Tokumaru [89] **empirical formula {2-60}**

The relationship described by Eq {2-60} was derived for high purity silicon with the samples reported by Okada and Tokumaru having boron and phosphorus impurity concentrations less than 10^{14} cm^{-3}. At room temperature (298.2 K), they reported $\sigma_T = (2.59 \pm 0.05)\times10^{-6}$ /C°.

Fenchao et al. [90] later reported $\sigma_T = (2.45 \pm 0.05) \times 10^{-6}$ /C° at room temperature using a new technique stating "This value does not change for doped P-type and N-type silicon."

2.8.4. Specific Heat

The heat capacity of a solid volume of material is the amount of energy required to raise the solids temperature by one degree. The specific heat capacity is simply a mass normalized measure of heat capacity inherent to a material. The specific heat of silicon has been shown to vary with temperature, but is commonly cited as 700 J K^{-1} kg^{-1} at room temperature. Variation of specific heat in silicon has been characterized by multiple government standards offices and has recently been considered as a reference standard for measurement of this parameter [91]. Figure 2.22 shows recent (2011) experimental and reference data of specific heat capacity of undoped SCS between 0 - 400 K. A similar plot spanning up to 2000 K, cited as being from the 1975 Russian text book by Okhotin et al. is shown in Figure 2.23 for comparison. Variations of this property in SCS for different doping levels has not been reported.

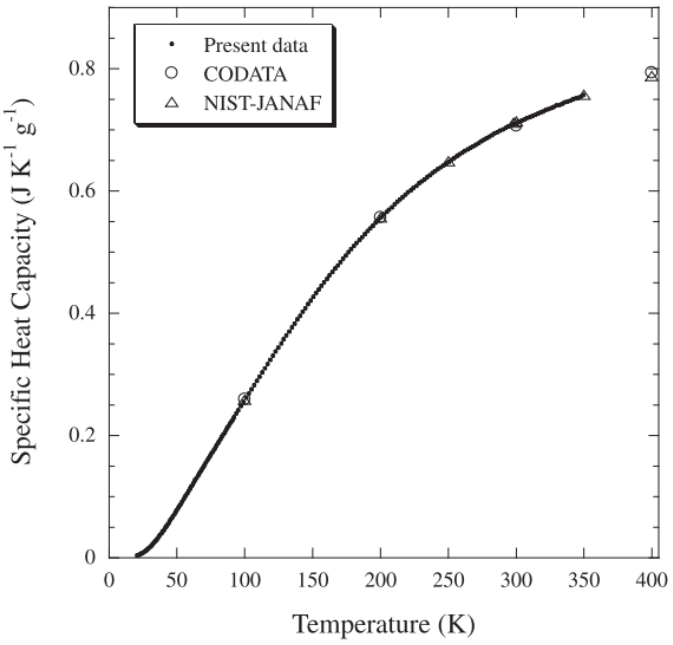

Figure 2.22: Specific heat capacity of single-crystal silicon as a function of temperature (from [91]**)**

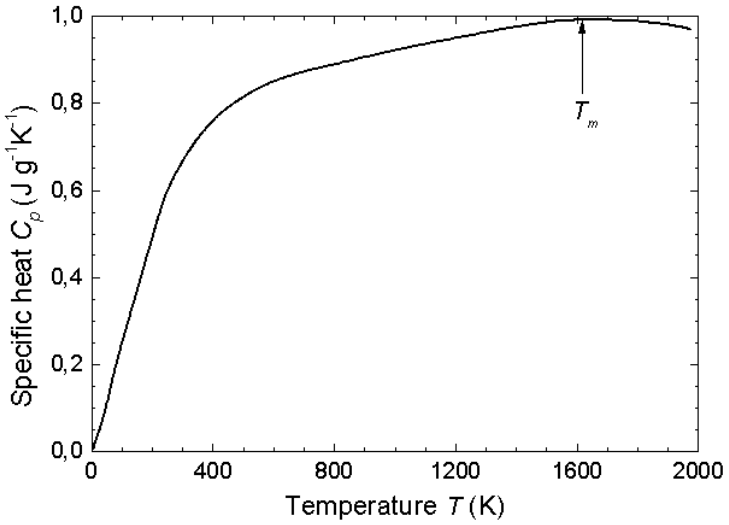

Figure 2.23: Specific heat capacity of single-crystal silicon for temperature (from [92]**).** T_m **is the melting point of silicon.**

2.8.5. Quality Factor Degradation Mechanisms

In practice there are several factors that can degrade the quality factor of a micromechanical resonator. The 2001 review paper by van Beek and Puers on MEMS oscillators provides an excellent summary of this area [12] and this section is largely derived from it. The classification of different loss mechanisms is shown by the block diagram in Figure 2.24. External loss mechanisms drive energy to leave the resonator and be dissipated outside of it. Internal loss mechanisms are those which occur within the structure of the resonator or at its surface. The individual Q loss mechanisms, Q_i, are related to the overall resonator Q through the following relation [12]:

$$\frac{1}{Q} = \sum_i \frac{1}{Q_i} \qquad \{2\text{-}61\}$$

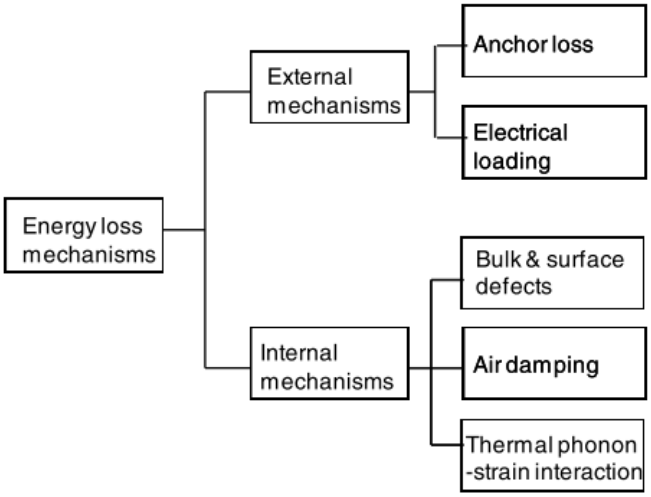

Figure 2.24: Classification of loss mechanisms for a mechanical resonator (from [12]**)**

The external Q loss mechanisms include anchor loss and electrical loading. Both of these can be significant for the devices presented in this work. The loss from electrical loading is simply the resistive power loss inherent in with any additional resistance in series with the resonator, R_{series}. *Anchor loss* refers to the acoustic energy reflected back into the substrate from imperfect reflection at the resonator boundaries. Typically, this is through the arms that support (or anchor) the suspended structure, which is the case for this work.

The internal Q loss mechanisms include viscous dampening from the medium operated in (typically air), thermal phonon strain interactions, and bulk and surface defects. As explained in [12], the effects of air dampening are greatest at **low frequencies and small scales.** This is shown by considering {1-6} and noting that Q is dependent upon both frequency and mass. If a dimensional scaling factor S,is considered, mass scales by S^3 while dampening will scale by S^2 since it is a function of the surface area of the device regardless of the type of dampening (i.e. squeeze film or sheer). Figure 2.25 shows a comparison of the Q dependence upon pressure for a 32 kHz and 55 MHz capacitive MEMS resonator. The higher frequency resonator can tolerate higher pressures before its Q degrades.

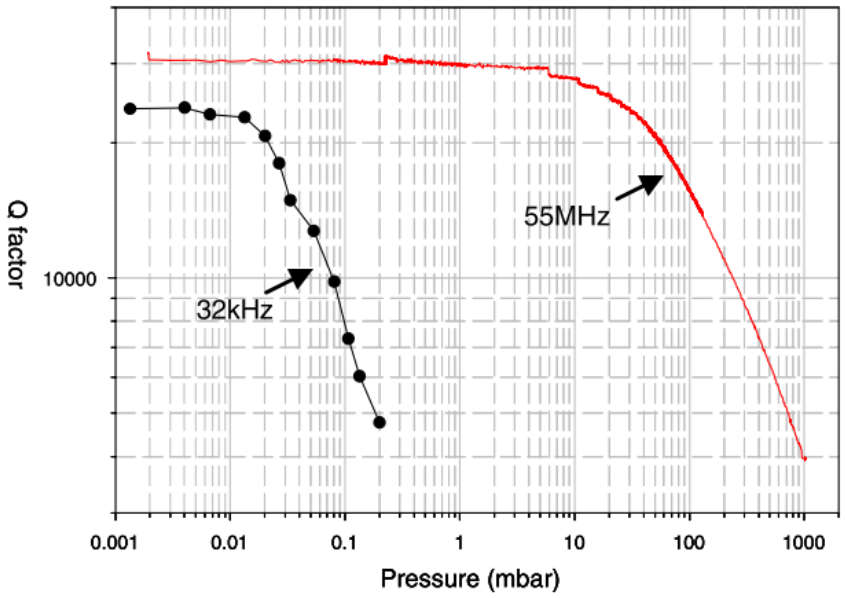

Figure 2.25: Pressure dependence of the unloaded (mechanical) Q-factor for 32 kHz and 55 MHz capacitive MEMS resonators. The 32 kHz capacitive MEMS resonator requires a cavity pressure below 0.01 mbar in order not to limit its Q-factor by air damping, while the capacitive 55 MHz MEMS resonator can tolerate up to 10 mbar before air damping starts to limit the Q-factor (from [12]**)**

The bulk and surface defects of the resonator are both considered to contribute to energy loss. Of the two surface effects are considered to dominate acoustic energy loss [12]. Thus coatings and particles on the surface of the resonator create an interface for this loss mechanism and thus reduce the Q. This is a drawback for traditional piezoelectric resonators which require patterning electrodes on the surface of the resonator. Trends have been reported, particularly for nanoscale resonant devices, regarding the R-Q product where R is the surface area to volume ratio [93]. These are suspected as being tied to surface loss effects in resonators

Thermal phonon-strain interactions (thermoelastic dissipation, phonon-phonon dissipation, and phonon-electron dissipation) are the mechanisms which set absolute Q limit for a given micromechanical resonator. These mechanisms are described by Tabrizian et al. in [94]. For devices < 1 GHz, the predicted maximum obtainable f-Q product for SCS silicon is predicted to be fixed and lie between 2.5×10^{13} and 3.9×10^{13} [12]. Numerous efforts have been made to achieve resonators that meet or exceed this limit in silicon, summaries of which can be found in [12], [35]. Figure 2.26 from summarizes reported values for several reported resonators.

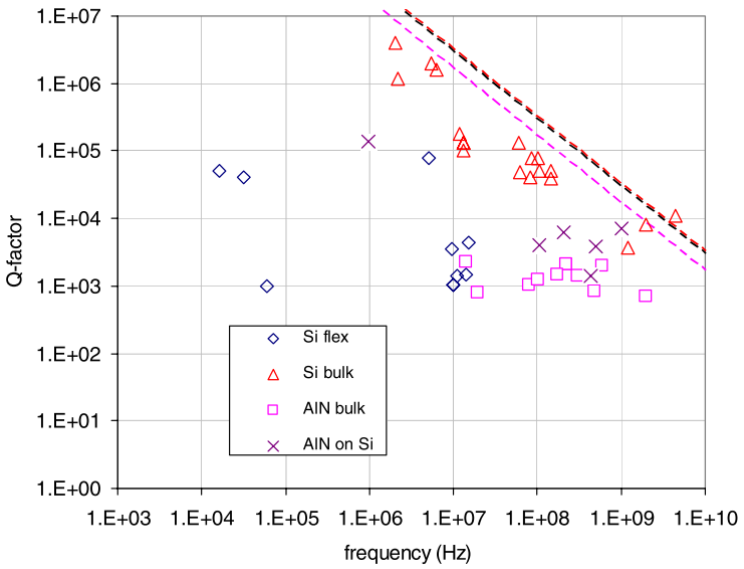

Figure 2.26: Overview of reported values of the mechanical Q-factor vs. frequency (from [12]**). The predicted *f-Q* limit lines for silicon (red), AlN (purple), and quartz (black) are shown.**

3. Device Modeling and Simulation

This work expands upon modeling and simulation efforts previously reported in several aspects through the use of the COMSOL multiphysics software package (v4.3a). The central motivation of this chapter is to demonstrate that a capable model has been implemented with this software to which experimental results can be used to potentially generate reasonable predictions suitable to aid future designs. Therefore, for simplicity, most of the results in this section are based upon a single representative device geometry (Device A3) and variations from it. The baseline parameters and settings (meshing settings, material parameters, environment assumptions, etc.) used for these simulations are discussed in Section 3.2. Section 3.2 examines the in-plane longitudinal structural mode that this device is intended to operate in in the absence of thermal stress and the effects of geometry changes on resonant frequency. Section 3.3 examines the steady-state response of the device in the presence of a DC current. The DC current establishes the baseline temperature and deformation conditions at which the device operates. Using these steady-state results and temperature dependent material parameters, modal analysis was reaccomplished with the model prestressed thermally. Section 3.4 presents these results which are useful for estimating the amount of frequency tuning that given geometry may offer. Section 3.5 presents time dependent DC analysis which establishes the time constant to reach steady-state, which in turn sets the upper limit on frequency with which these devices can be electrically turned on and off and be expected to operate repeatably. Section 3.6 presents the time-dependent results for both AC and DC excitation using the DC steady-state results as an initial condition. This is useful for estimating the magnitude in AC temperature fluctuations throughout the structure. While direct harmonic electrothermal excitation is not possible using COMSOL, without designing a custom module, the magnitude of the AC temperature fluctuations can be used to scale mechanically forced harmonic analysis, which is shown in Section 3.7. Finally, the individual subsystem and total system transfer functions for the device response are plotted and presented in Section 3.8 to further emphasize the phase relationship expected during operation of these devices.

3.1. Baseline Settings and Parameters

Using the COMSOL software package, the I-shape geometry was parameterized in a 2D layout, from which the silicon solid model is extruded. This chapter presents a series of simulation results for a single geometry, however dimensions can be easily changed to accommodate others. Table 3.1 summarizes the dimensions and material parameters used for the example presented in this chapter. The material parameters were chosen to reflect single-crystal silicon. For simplicity, a scalar Young's modulus was chosen to reflect the <100> orientation, although a full anisotropic formulation with temperature dependence is possible to implement.

Table 3.1: Summary of Example Device Dimensions (after Figure 2.9) and Material Parameters

Device Geometry (after Device A3)		**Material Parameters (of Si)**	
Dimension	**Value [μm]**	**Property**	**Value**
a	6.46	Density	2329 [kg/m^3]
b	4.17	Coefficient of Thermal Expansion (α_T)	2.6E-6 [1/K]
W	0.356	Heat Capacity (C_p)	700 [J/(kg*K)]
L	1.47	Young's modulus (*E*)	130E9 [Pa]
W_{sup}	1.54	Poisson's Ratio (*v)*	0.28
L_{sup}	2.56	Linearized Resistivity (per Eq {2-55})	
*ArmGap**	3	Reference Resistivity (ρ_o)	1E-3 (Ω-m)
h	1.6	Temperature Coefficient of Resistivity (α_R)	1.7E-3 (1/K)
W_{pad}	150	Reference Temperature (T_o)	318.25 (K)
		Internal Stress	0 MPa

*This was used instead of the c parameter, and is the internal spacing between actuator arms

With the exception of the unstressed modal analysis performed, which simply fixed the structure at the ends of the support arms, all the simulations used a solid model which incorporated mechanically fixed square pads. The outer ends of the pads acted as fixed temperature anchors (boundary conditions) as well as electrical boundaries for current or voltage. Convention cooling was incorporated when applicable with a heat transfer coefficient of 5 [W/m^2/K] which is a value often used to describe a typical laboratory environment. An adaptive tetragonal meshing was used with a maximum element size of 31.2 μm in the bulk of the structure and the pads, while a finer mesh with a maximum size of 0.1 μm was used exclusively in the actuator arms. Figure 3.1 shows a top view image of the example structure with the pads and an oblique magnified view of a device meshed as described.

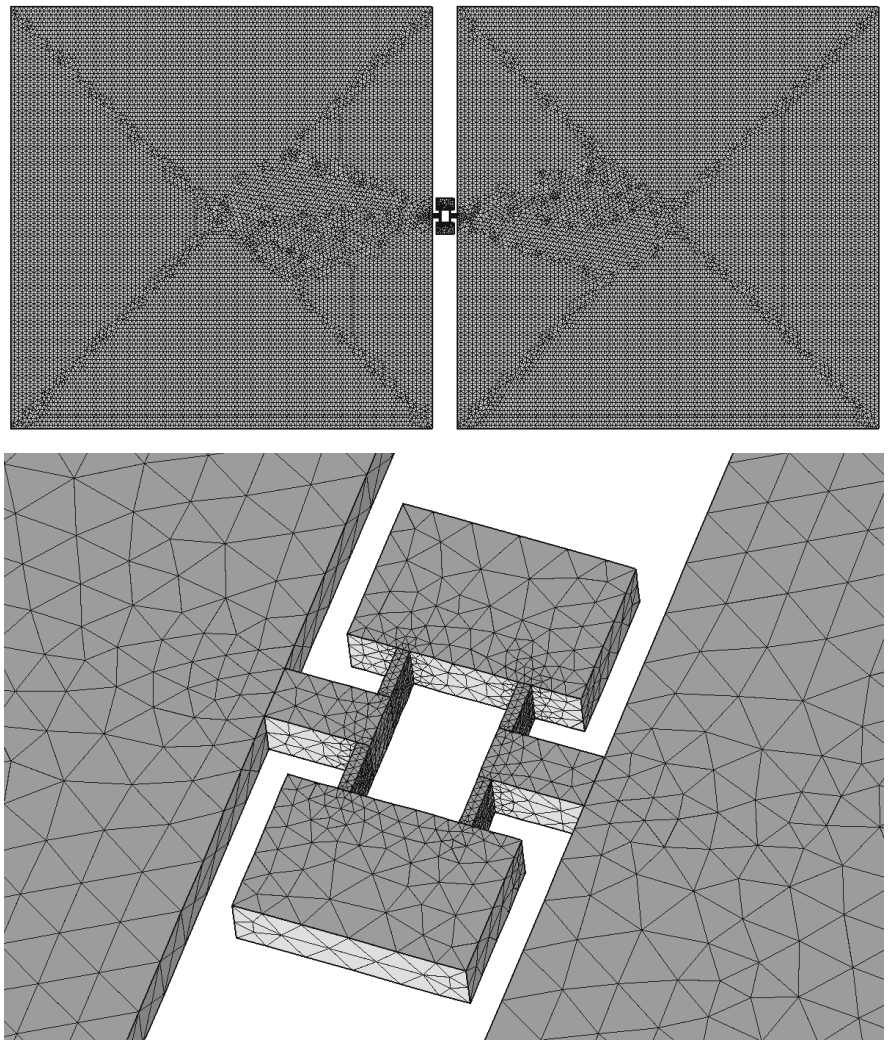

Figure 3.1: (top) Top view of meshed solid model of device with bonding pads (bottom) Oblique magnified view of the meshed device structure which served as the baseline model for this chapter.

3.2. Unstressed Modal Analysis

Modal analysis of the structure 3-dimensionally solves equations of motion for a series of time harmonic inputs. The result is a series of solutions which depict both the resonant frequency and mode shape for the structure. The boundary conditions applied simply included fixing the ends of the support beam of the structure. No additional constraints or stresses were applied to the structure. Figure 3.2 shows a summary of several different modes available and their frequency for the baseline geometry resulting from the analysis, including the in-plane longitudinal (extensional) mode at 119.8 MHz.

For a rough analytical comparison, the 1D forced MSD model presented in Section 2.2 can be used to estimate the frequency of the longitudinal mode. This can be accomplished by considering half of the structure (i.e. a single plate with two arms and half a support beam) to estimate effective quantities for the mass, M_{eff}, and spring constant, k_{eff}, as follows

$$k_{eff} = \frac{2WhE}{\left(L + \frac{W_{\text{support}}}{2}\right)} \quad \{3\text{-}1\}$$

$$M_{eff} = (a \cdot b \cdot h)\rho_{Si} + (W \cdot L \cdot h)\rho_{Si} \quad \{3\text{-}2\}$$

where E is the Young's modulus, ρ_{Si} is the density of silicon, and the remaining quantities are the device dimensions as shown in Figure 2.9. The effective spring constant approximates the actuator arms, and a portion of the support beam, as longitudinal beams. The effective mass essentially sums the mass of the plate and the mass of the actuator arm, with an additional ½ correction factor added to the later term to compensate for sinusoidal excitation. By substituting Eqs {3-1} and {3-2} into Eq {2-4} the estimate for resonant frequency, f_o, is found to be

$$f_o = \frac{1}{2\pi}\sqrt{\frac{2WE}{\left(L + \frac{W_{\text{support}}}{2}\right)\rho_{Si}(ab + WL)}} \quad \{3\text{-}3\}$$

Using Eq {3-3} and the dimensions listed in Table 3.1 yields f_o = 127.87 MHz which is < 7% difference from the unstressed modal analysis result of 119.8 MHz.

While the effect on the resonant frequency from varying each parameter can be gleaned from Eq {3-3}, it of particular interest to confirm these trends with modal analysis by sweeping the parameter of interest to different values. This was accomplished for the parameters, b, L, W, h, and $W_{support}$ for the in-plane longitudinal mode with the results depicted in Figure 3.3. As expected from Eq {3-3} , increasing b, L, and $W_{support}$ decreases the resonant frequency.[13] Likewise increasing W accomplishes the opposite. The effect of thickness was small with less than 2% variation in frequency over an order of magnitude increase in the thickness. As the frequency is expected to be thickness independent from Eq {3-3}, this result is logical. As shown in Figure 3.3, power and polynomial functions were fitted to the data for further comparison to Eq {3-3}. In addition, the derivatives of these curves with respect to frequency provide a measure of the sensitivity variations in each parameter on the frequency. As evident from these functions, designing and fabricating MEMS resonators to a precise frequency can be a significant challenge.

[13] While not shown it was also modeled that if the support beam width is large enough, and the plates are asymmetric in size, the resonant mode shapes for each plate will eventually split into separate modes. This was not a significant concern for this work however.

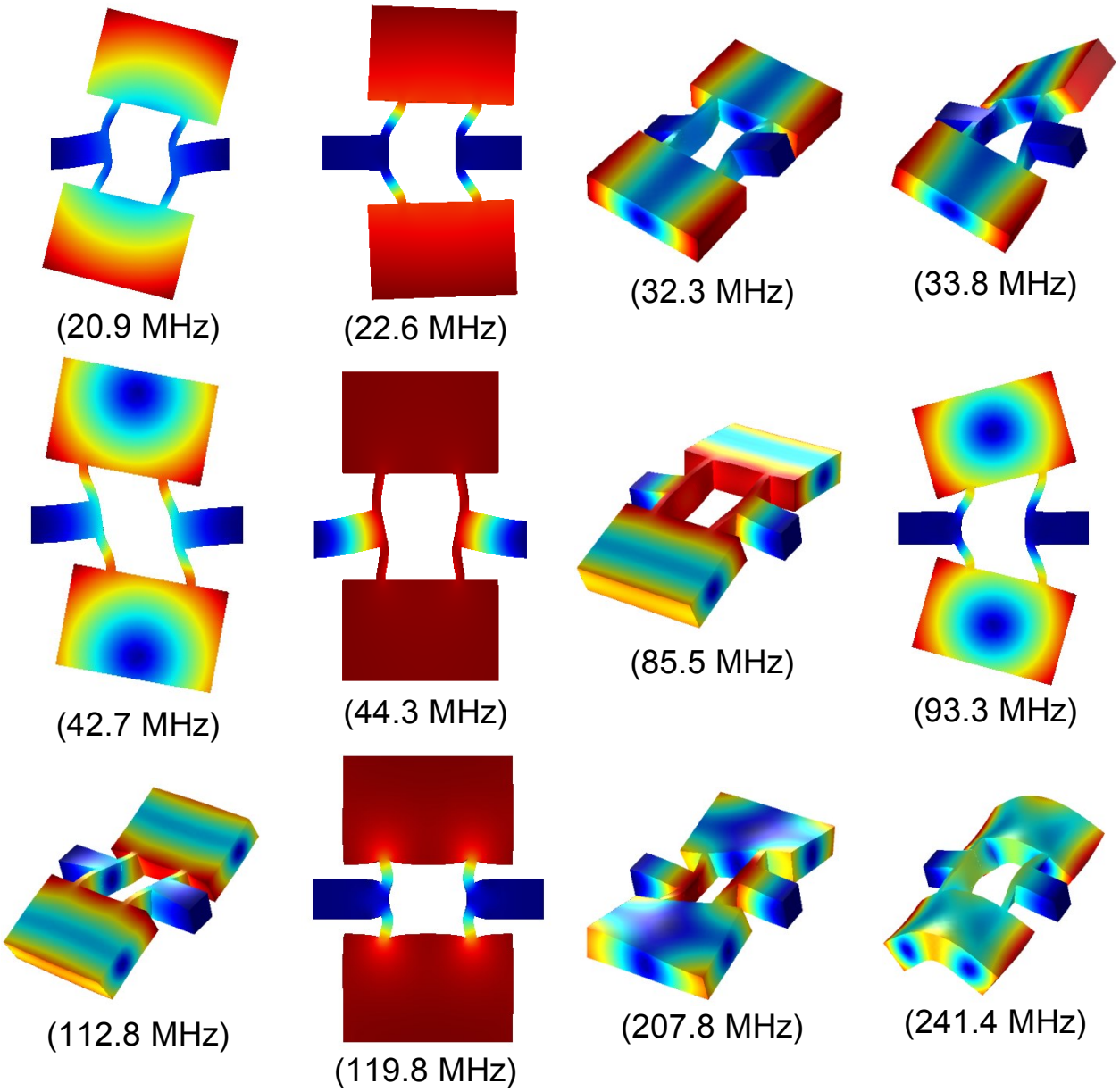

Figure 3.2: Different mode shapes generate using modal analysis for the I-shaped geometry subject of this work. The in-plane longitudinal mode which the devices in this work are intended to operate is at 119.8 MHz.

Since it is virtually impossible to fabricate structures with perfectly sharp corners, the effects of filleting of the inside corners was explored as well. As will be shown in Chapter 4, incorporating this effect reflects the realized geometries in this work closer. This effect was left out of the baseline model to simplify analysis, but was explored for the unstressed modal

analysis to examine its effect on frequency; the expectation being that the frequency would increase proportionally with the amount of material added by the fillet since the effect increases the effective width of the arms. Figure 3.4 shows the circular filleted model used with the corresponding results for a sweep of the fillet radius in Figure 3.5. Fillet material was incorporated into the layout by adding a square of width R_f to the inside corner and then subtracting a circle of the radius R_f (i.e. $R_f = 0$ is perfectly sharp corner). Thus larger R_f indicates more material is "filling" in the corner, which per Figure 3.5 increased the resonant frequency.

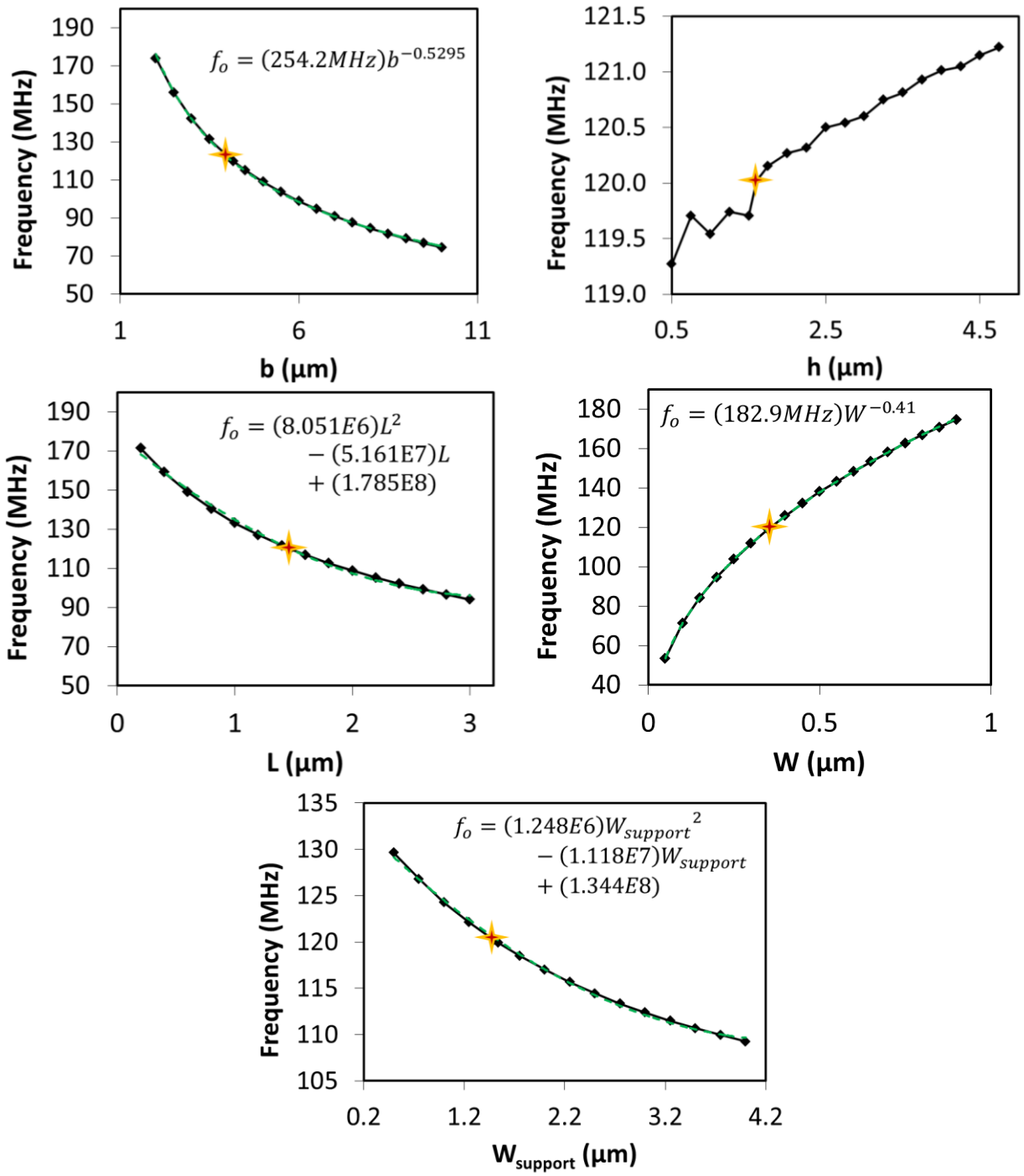

Figure 3.3: Results of unstressed modal analysis sweeps of the in-plane longitudinal mode for different aspects of device geometry. The trends displayed correspond to those expected from Eq {3-3}. The stars indicate the baseline geometry shown in Table 3.1. Fits to the results are displayed (dashed green line) when appropriate with units of frequency in Hz (unless noted otherwise) and the units of the dependent variable corresponding to that shown on the plot.

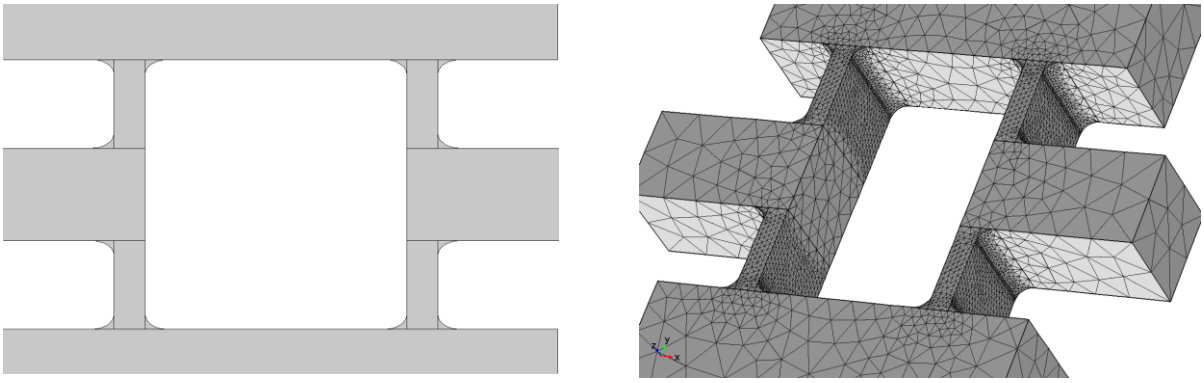

Figure 3.4: (left) Top view of filleted 2D layout, fillet radius = 25 nm (right) resulting meshed solid model

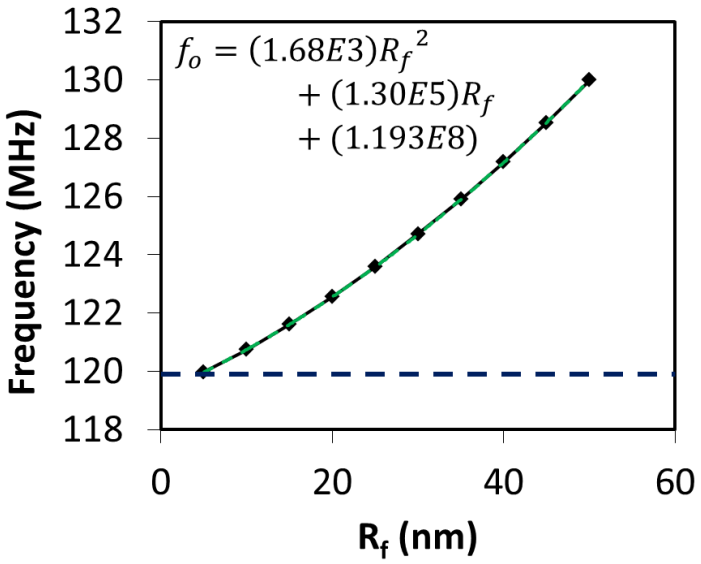

Figure 3.5: Effects of filleting as a function of fillet radius on frequency of the in-plane longitudinal mode. The dashed blue line shows the un-filleted baseline device frequency.

3.3. DC steady-state analysis

Applying a DC current to these devices is necessary for their intended operation as it allows a response to occur at the same frequency of excitation (see Chapter 5 and Eq {A1-1}). In addition, the DC current sets the thermal operating point of the device, which can change the devices operating frequency due to softening of the Young's modulus as discussed in Section 2.8.1. Thus steady-state heat analysis is useful for determining this setpoint for sophisticated analysis (such as the prestressed modal analysis presented in Section 3.4and the coupled electrothermomechanical AC and DC time-dependent analysis shown in Section 3.6). It is also useful for gauging the thermal operation limits. This analysis solves the steady-state heat

equation three-dimensionally for the case of internal (i.e. joule) heating and couples the solution to a solid mechanics solver which then incorporates thermal expansion of the material.

Figure 3.6 shows the results of a steady-state DC current sweep thermally and mechanically for the baseline device (see caption for locations) with the pad outer edges having a fixed temperature boundary condition of 293.15K. This analysis indicates that it is unlikely the device would survive much higher than I_{DC} = 2.4mA as the maximum temperature would begin approaching the melting point of silicon. The temperature distribution (K) and current density norm (A/m^2) for I_{DC}=2mA are shown in Figure 3.6

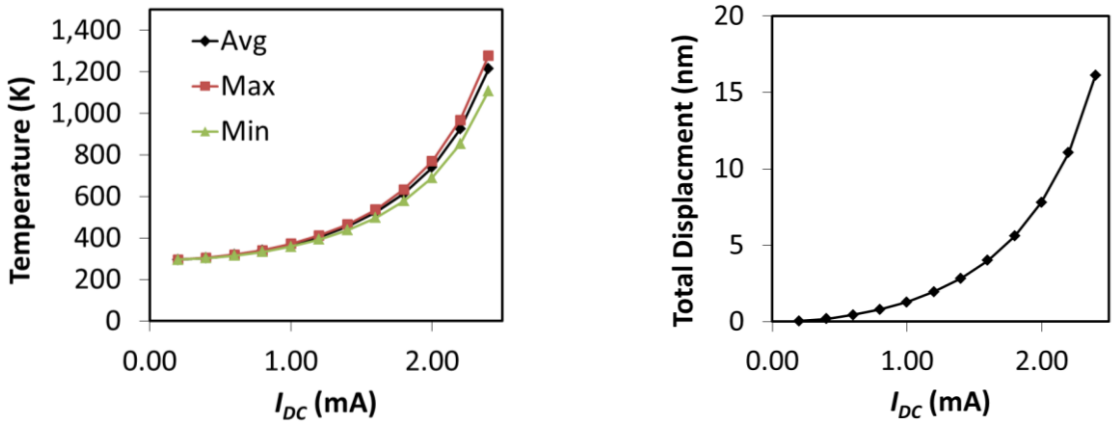

Figure 3.6: Steady-state DC response of baseline device (left) average. maximum, and minimum temperature in actuator arms for a DC current sweep (right) corresponding total displacement (in-plane) of the upper plate edge.

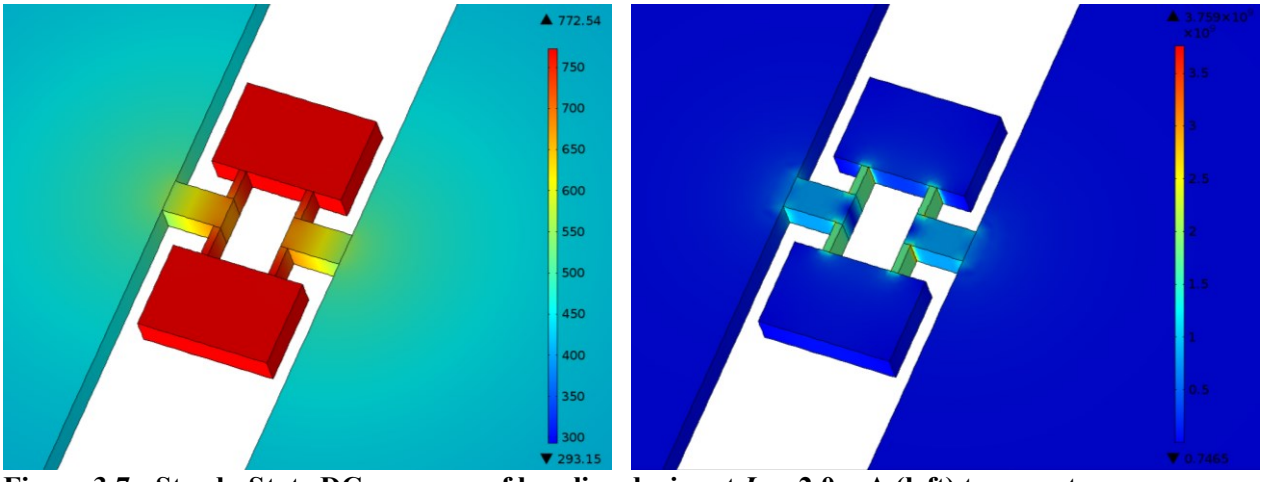

Figure 3.7: Steady-State DC response of baseline device at I_{DC}=2.0 mA (left) temperature distribution (right) current density norm

3.4. Prestressed Modal Analysis

One characteristic of the devices in this work is that the frequency of operation can be adjusted by varying the applied DC current. This characteristic is due to the elastic softening that occurs in the material at elevated temperatures, which lowers the effective spring constant of the structure. To reflect this softening a simple first order relation using the room temperature value of the temperature coefficient of Young's modulus (TCE), reported by Hopcroft [95], was applied to the parameter as follows

$$E_{[100]} = 130GPa + (-64\times10^{-6}/K)*(130GPa)*(T-293.15K) \qquad \{3\text{-}4\}$$

To accomplish the prestressed modal analysis a steady-stated DC analysis incorporating thermal expansion is first performed as described in the previous section. The resulting temperature and stress values are then used to establish an initial condition for the modal analysis. In the same fashion as the previous simulations, the I_{DC} parameter was swept across values to observe the change in frequency. Figure 3.8 depicts the results for both the prestressed modal analysis with fixed Young's modulus and the temperature dependent variant. In the fixed E case the frequency increases from the added structural stress imparted by thermal expansion of the structure with the support arms anchored. The temperature dependent case exhibits nearly 4 MHz of frequency shift (~3%) through the course of the sweep.

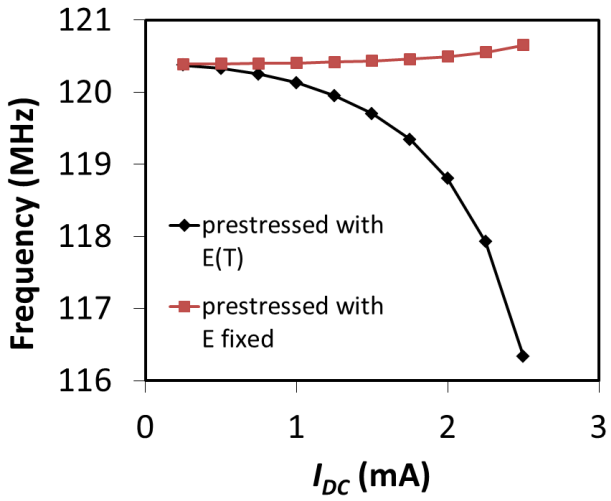

Figure 3.8: Variation of resonant frequency of the in-plane longitudinal mode by the incorporation of a prestressed condition prior to modal analysis established by performing a steady-state DC analysis with both joule heating and thermal expansion. The black curve (diamonds) utilizes the temperature dependent Young's modulus described by Eq {3-4}. The red curve (squares) utilizes a fixed Young's modulus and shows an increase in frequency from structural stress added from thermal expansion.

3.5. DC Temporal Analysis

The devices in this work are examined in their steady-state operation, however the transient analysis can be useful for future work aimed at estimating the temporal dynamics of the device response. Specifically, DC transient analysis can be used to ascertain the thermal time constant of the system, which mathematically is the time needed to reach 63% of the steady-state value. This analysis once again coupled the heat transfer and thermal expansion solvers to generate a solution. The results for the baseline device with an applied I_{DC} of 2 mA are shown in Figure 3.9. From the figure, the thermal time constant can be estimated to be ~2.5 µsec, which implies a thermal frequency response of ~500 kHz .

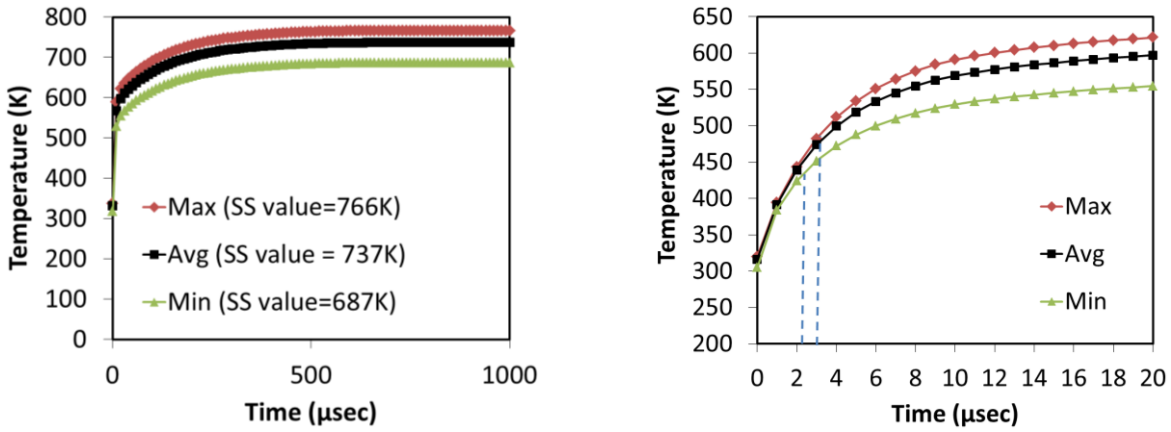

Figure 3.9: Time-dependent DC analysis of the baseline device for I_{DC} = 2 mA showing maximum, minimum, and average temperatures of an actuator arm. (left) 10 µsec stepped sweep used to determine the steady-state temperature (right) 1 µsec sweep used to determine the 63% rise time, the range of which is indicated by the dashed blue lines.

3.6. AC and DC Temporal Analysis

By applying a sinusoidally varying input current in addition to the DC current the time-dependent electrothermomechanical response of the device can be examined directly (using once again the coupled heat transfer and thermal expansion solvers). It is of particular interest to notice the deviation of the response from the DC steady-state values, as this mimics the conditions of steady-state device operation closest. Thus, steady-state DC analysis was performed first for this study as a means to establish the initial conditions for operation in the AC steady-state. The time dependent data then generated can have the DC components subtracted out to directly examine the AC responses (i.e. T_{ac} , X_{ac}, V_{ac}) throughout the structure.

This simulation was performed on the baseline device with a DC current of 2 mA and AC current of 50 µA amplitude at the structure's resonant frequency of 119.8 MHz. Plots of the temporal responses of the temperature of an actuator arm centerpoint compared to the displacement of the top plate edge and the voltage at the support arm are presented in Figure 3.10

and Figure 3.11 respectively. Note that these results do not incorporate any dampening, however simulations (not shown) with Rayleigh dampening incorporated for a quality factor of 2000, as will be described in Section 3.7, showed only minor variation in magnitude. Other than providing the magnitude of the AC values, the responses show relative phase shifts which correspond to the lumped element transfer functions of the thermal and mechanical subsystems (see Section 3.8). Figure 3.12 shows a top view image of the temperature deviation from steady-state at an AC temperature peak. The image shows that significant parasitic heating is occurring outside of the actuator arms, mostly in the support arms.

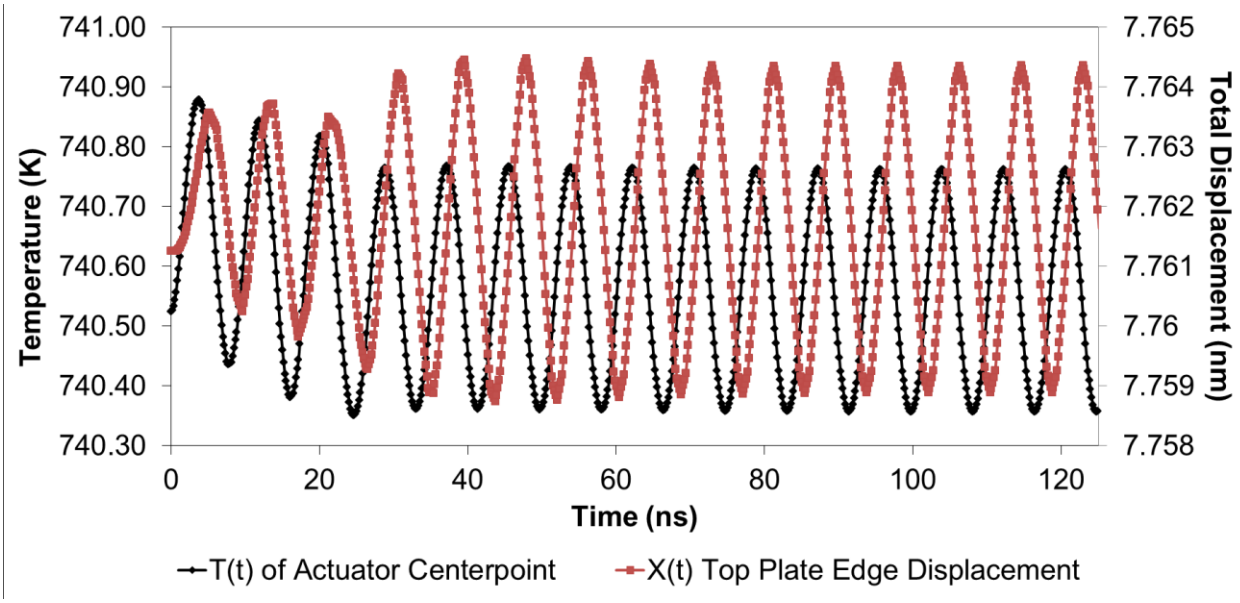

Figure 3.10: Temporal response of temperature at the actuator arm centerpoint and the top plate edge displacement. The responses indicate that the displacement lags the temperature by ~90° which corresponds to the lumped parameter transfer function for the mechanical subsystem.

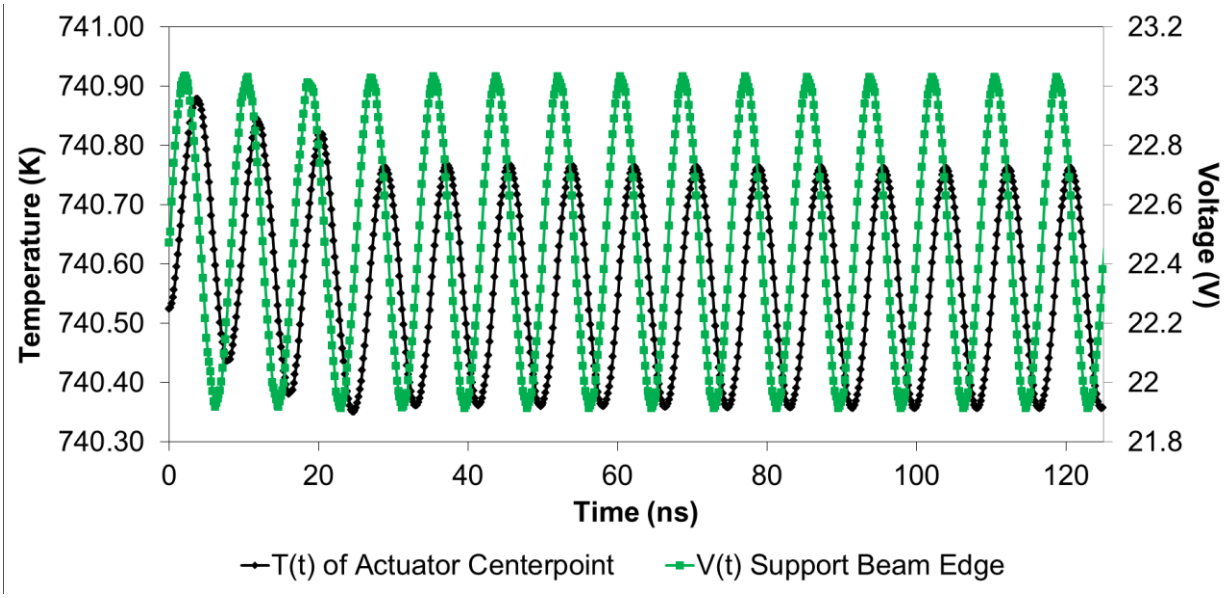

Figure 3.11: Temporal response of temperature at the actuator arm centerpoint and the voltage at the edge of the support beam. The responses indicates that the temperature lags the voltage by ~90° which corresponds to the lumped parameter transfer function for the thermal subsystem.

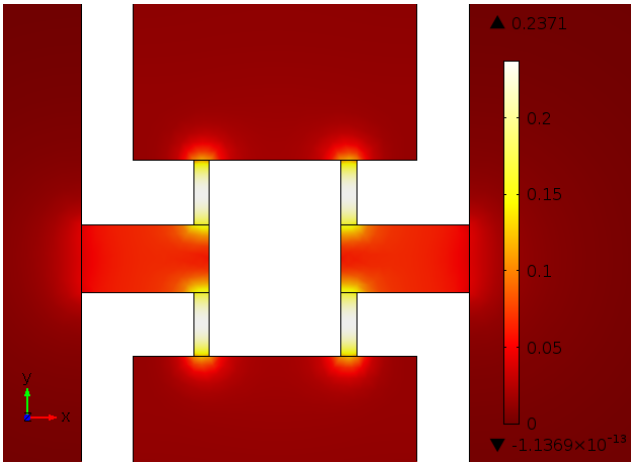

Figure 3.12: Top view of the temperature deviation from steady-state at t=1.2044E-7 sec, which is a time step corresponding to an AC temperature peak . The scale bar is in units of Kelvin. The majority of temperature fluctuation occurs in the actuator arms as desired, however significant fluctuation occurs in the support arms. The amount of temperature deviation outside of the actuator arms is an indicator of the degree of parasitic heating occurring in the structure.

3.7. Forced Harmonic Analysis

While direct harmonic thermal excitation of the structure is not possible in the software without designing a custom module, a forced harmonic analysis can be easily performed. By using the T_{ac} values determined in the AC and DC temporal analysis of the previous section, the forced

harmonic simulation can be setup and scaled to approximate the behavior of actuator arms being thermally excited. The first aspect to accomplishing this is to assign boundary loads appropriately to areas adjacent to each actuator arms to simulate the expansion. Figure 3.13 shows the direction and positioning of the necessary loads. The values of these loads (collectively for each direction) would then be

$$F_y = 4\alpha_T T_{ac} E \qquad \{3\text{-}5\}$$

This analysis was performed on the baseline device using a value of $T_{ac} = 0.15$ K with Rayleigh dampening incorporated into the structural model. Rayleigh dampening allows values for the dampening term, b, in Eq {2-1} to be set according to the following relation

$$b = \alpha_{dK} M + \beta_{dK} k \qquad \{3\text{-}6\}$$

where M and k are defined in Eq {2-1}. For this work $\alpha_{dK} = 0$ and the β_{dK} term is equivalent to

$$\beta_{dK} = \frac{b}{k} = \frac{\frac{b}{\sqrt{mk}}}{\sqrt{\frac{k}{m}}} = \frac{1}{4\pi Q f_o} \qquad \{3\text{-}7\}$$

Thus an experimental Q value can be fed accordingly to properly set this parameter. For the base line design the quality factor was set to 2000. The result which clearly depicts a sharp resonant response nearly coincident with the solution generated from the unstressed modal analysis is shown in Figure 3.14. The magnitude of deflection response is substantially larger than that shown in Figure 3.10 for the AC and DC time dependent study, suggesting that additional scaling of Eq {3-5} is required to portray the response more accurately.

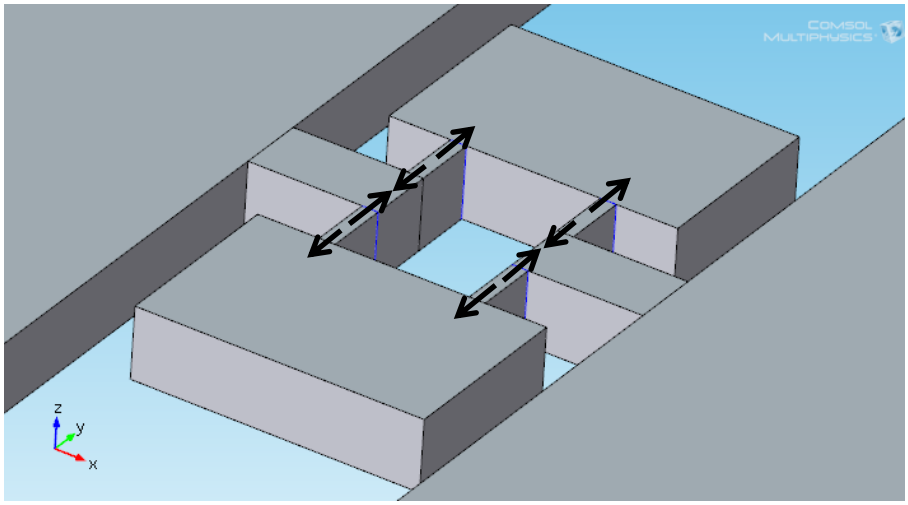

Figure 3.13: Direction and location of mechanical loads needed to simulate thermal expansion of the actuator arms.

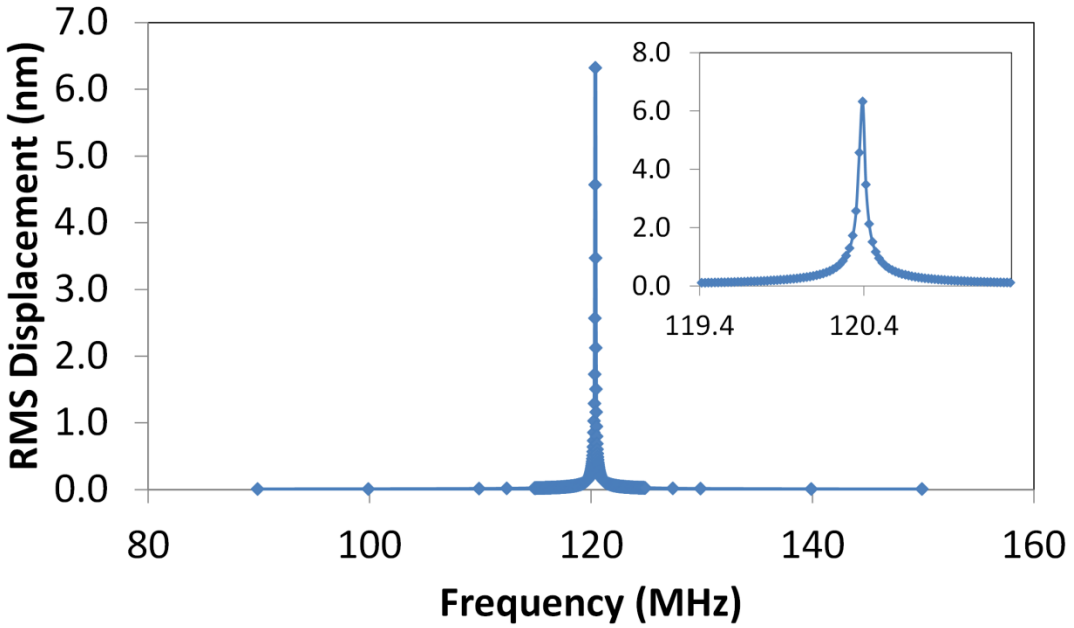

Figure 3.14: Forced Harmonic Response of the Baseline Device for T_{AC} = 0.15 K with Eq {3-5}.

3.8. Transfer Function Analysis

Before proceeding with discussing the fabrication and characterization portions of this work, it is important to appreciate the magnitude and phase response of the device and its subsystems as described by the 1D lumped element model detailed in Appendix 1. The thermal subsystem, assuming $\omega_o \gg \tau_{th}^{-1} = (R_{th}C_{th})^{-1}$, approximates to the following transfer function

$$H_{th}(j\omega) = \frac{T_{ac}}{V_{ac}} = \frac{2V_{dc}R_{th}}{R_A(1 + R_{th}\,C_{th}(j\omega))} \approx \frac{2I_{DC}}{C_{th}(j\omega)} \qquad \{3\text{-}8\}$$

The mechanical subsystem is

$$H_{mech}(j\omega) = \frac{X_{th}}{T_{ac}} = \frac{2\alpha_T EA}{(M(j\omega)^2 + b(j\omega) + k)} \qquad \{3\text{-}9\}$$

Figure 3.15 displays each of these transfer functions graphically in terms of magnitude and phase for the baseline device using the analytical approximations for M_{eff} and K_{eff} provided by Eq {3-1} and {3-2} with a quality factor of 2000. Of particular note, the phase is -90° across frequency for the thermal subsystem, which is apparent by the purely imaginary transfer function, and is -90° at mechanical resonance for the mechanical subsystem. This corresponds to AC and DC temporal analysis results shown in Figure 3.10 and Figure 3.11.

With a negative piezoresitive coefficient an additional -180° of phase shift is added to the system response resulting in 0° at resonance. This allows the self-sustained oscillation phenomena to occur. A positive piezoresisitve coefficient exhibit -180° at resonance which is a

condition supporting negative feedback to occur. The total system response function for each case is shown in Figure 3.16.

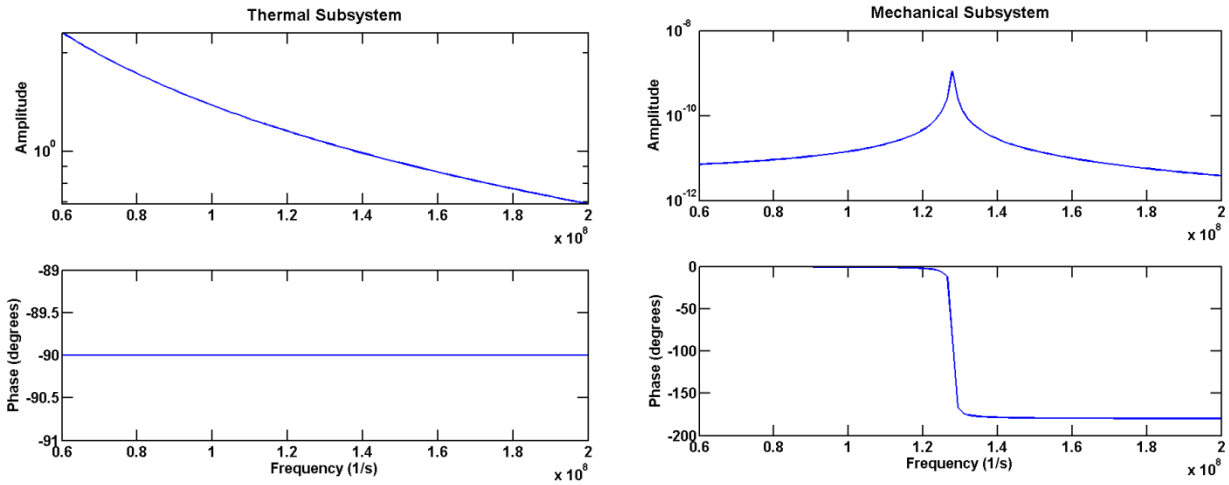

Figure 3.15: Device A3 transfer functions for the thermal (left) and mechanical (right) subsystems

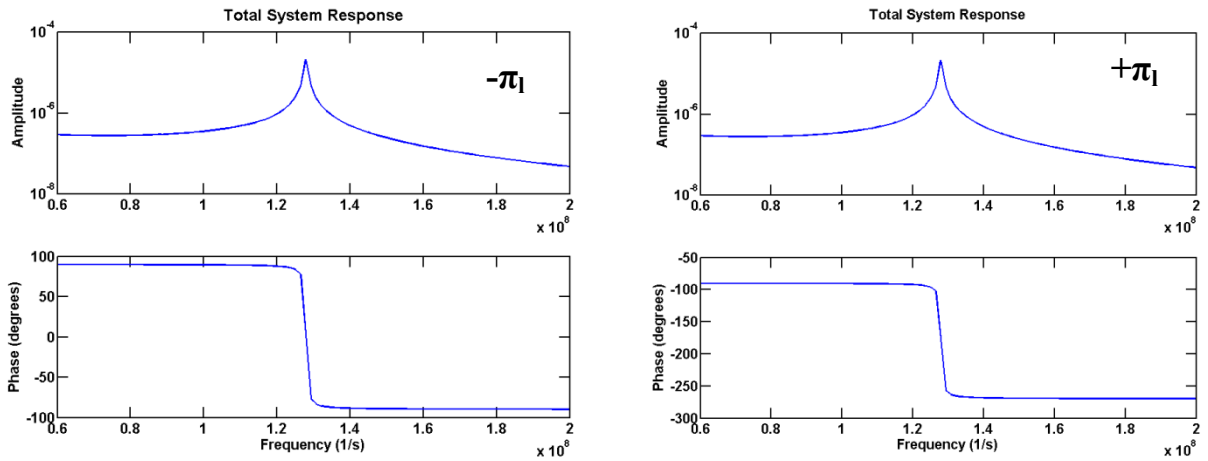

Figure 3.16: Device A3 total system transfer functions for a negative piezoresistive coefficient (left) and positive piezoresistive coeffient (right). At device resonance the negative piezoresistive coefficient offers 0° of phase shift, allowing self-sustained oscillation to be possible while the positive case has -180° phase shift which provides negative feedback.

4. Device Fabrication

As previously discussed, the devices which are the subject of this work were previously studied at larger scales. Section 4.1 begins by discussing the previous process was along with its advantages and disadvantages. MEMS fabrication, especially in a research environment is often a compromise between the design and the resources available to achieve it. Ideally, it is commonly desired to have a process that offers:

1. Simplicity - number of processing steps is minimal and physical resources are easy to obtain (conventional off the shelf)
2. Batch Processing – allows mass production at wafer scale
3. Compatibility with CMOS processing – utilizes techniques that minimize the potential to damage surrounding on-chip circuitry (i.e. low temperature, low risk of metal ion contamination, use standard thin film materials etc.).

The devices presented in this work were fabricated with submicron feature sizes from single crystal silicon of two different thicknesses. Section 4.2 describes the two different techniques used to fabricate devices with submicron thickness (h=340 nm). Section 4.3 describes the processing used for the thicker (h=1.6-1.9 μm) devices. The results of these fabrication efforts ar summarized in Section 4.4.

4.1. Previous micron scale device fabrication

Fabrication of larger micron-scale thermal-piezoresistive resonators in previous work [11], [55] ,[66],[67] which included I-shaped designs, was accomplished using an simple SOIMEMS process. Figure 4.1 show a cross-sectional overview of the process which begins by growing a ~200 nm layer of oxide on conventional silicon-on-insulator (SOI) wafers (3-20 μm thick device layer, 2-5 μm thick buried oxide layers). A layer of photoresist was then spun and patterned on the surface of the oxide using a conventional (2 μm resolution) optical lithography process. The pattern used incorporates both the device interconnect pads and the device geometry making it a single-mask process. Etching of the underlying surface oxide was not detailed, but it can be presumed that it was accomplished using a HF based wet etchant, such as buffered oxide etch. The pattern was then etched through the silicon device layer to the buried oxide using a deep reactive ion etcher (DRIE). The devices were then released using a standard HF wet release process, which effectively removed the underlying buried oxide layer and remaining surface oxide. Successive thermal oxidation and HF releasing, was then accomplished to thin out the actuator arms further to improve the device performance.

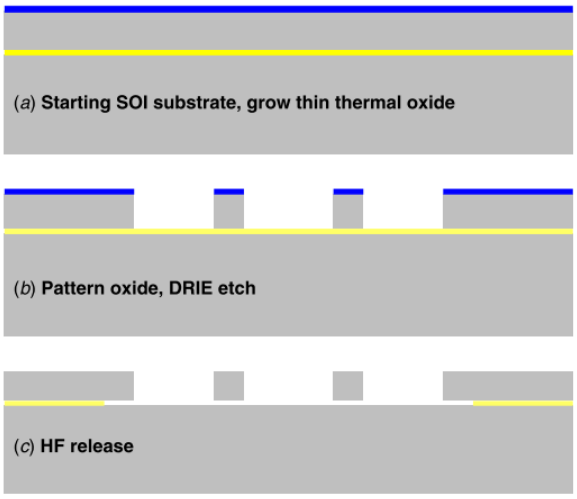

Figure 4.1: SOIMEMS process flow utilizing conventional lithography for micron scale devices (from [16] **)**

The benefits of this process lie in its simplicity and compatibility with conventional processing for large scale batch fabrication, largely due to the fact that the devices can utilize SCS as the structural medium without the need for any additional thin film materials. The fact it is a single mask process means that only a single alignment to the desired crystallographic orientation of the wafer is required. Further, the use of an oxide hard mask is compatible with most all DRIE systems and the thick device and BOX layers allow HF release without the need for critical point drying.

The motivation of this work was towards achieving high frequencies and performance by scaling down the device geometry. Specifically, per Eq {2-37}, the performance gains are realized by the reducing the size of the actuator arms and their effective thermal capacitance. While the successive oxidation discussed can thin the actuation arms (at the expensive of increasing their length), shorter actuator arms require improved resolution. The plate (or proof mass) size is the primary design factor for setting the operating frequency (structural resonance frequency) of the longitudinal mode to the desired value. As evidenced by Eq {2-34}, the smaller the plate size becomes the more sensitive the structural frequency is to mass differences resulting from process variations, such as edge sharpness and profile. Improved resolution of fabrication thus helps manage these variations for higher frequency devices. An obvious additional benefit of miniaturization is the reduction in area footprint required for these devices. For this work, utilizing the I-shaped geometry, the device area footprint (i.e. pad interconnects removed) can be estimated using the following formula

$$A_{device} = \left(2a + W_{\text{support}} + 2L\right)\left(2L_{\text{support}} + (b - 2c)\right) \qquad \{4\text{-}1\}$$

The feature resolution of the aforementioned process is limited by the quality of optical lithography resources available (mask maker, mask aligner, exposure lamp wavelength, etc.) and the etch method utilized to transfer the pattern from the photoresist into the oxide hard mask. At the Colorado Nanofabrication Lab, where fabrication was conducted for this work, 2 μm resolution is the best one can expect to obtain in a repeatable manner. This is a typical value for many academic institutions. Since submicron optical lithography was not readily available locally, to achieve the submicron geometries desired in this work, alternate approaches needed to be taken for fabrication.

4.2. Fabrication processing for submicron thick devices (h=340 nm)

Initial devices were fabricated from a silicon-on-insulator (SOI) 4" wafer with a 340 nm Si (100) device layer (DL) and 1 μm thick buried oxide (BOX) layer on a conductive silicon substrate (540 μm thick). Originally doped p-type with boron (14-22 Ω-cm per the manufacturer), the device layer was compensation doped to n-type with phosphorus. The compensation doping was not ideal, since its effect on the material parameters on silicon, particularly the piezoresistive coefficient, has not been experimentally confirmed. However, it was necessary as a custom n-type wafer of this thickness was cost prohibitive to the project. Resistivity of the device layer was measured by 4-point probe (KX model 3007) to be ~0.01 Ω-cm. Device patterning was performed along the <100> direction to maximize the negative amplitude of the longitudinal piezoresistive coefficient, $\pi_{L,}$ as shown in Figure 2.17.

Two different methods were applied towards these devices. The first utilized electron beam lithography (EBL) in conjunction with reactive ion etching (RIE) to pattern the DL. The second approach utilized a dual beam focused ion beam (FIB) scanning electron microscope (SEM) system to directly etch the device pattern into the DL. The logic towards pursuing thinner structures initially was two-fold 1) a deep anisotropic etch solution was not available locally, and 2) the immediate reduction in thermal capacitance of the actuator would be significant in comparison to previous work. Sections 4.2.1 and 4.2.2 describe each approach.

4.2.1. NPGS-based Electron Beam Lithography process

The primary method available for nanoscale fabrication at the Colorado Nanofabrication Lab is electron beam lithography implemented on a JEOL JSM-5910LV scanning electron microscope with Nanoscale Pattern Generation System software[14]. This is a system intended for prototyping and limited to patterning devices individually. The preceding process which utilized an oxide mask required modification to utilize this system since an oxide layer alone is not visible by the machine for pattern alignment - a limitation that is inherent to most all EBL systems which typically require a metal alignment marker pattern, preferably made of Au, for sufficient imaging contrast.

[14] For more details on this software refer to http://www.jcnabity.com/

The EBL based process developed is summarized graphically in Figure 4.1. It utilizes a combination of standard optical photolithography for the definition of large features (2 optical masks) and EBL (single write) for device features. The 2-terminal device interconnect pads (area ~145,000 μm^2 each) and alignment markers (optical and EBL) were initially patterned from a thermally evaporated 100 nm Cr / 25 nm Au metal stack using standard photolithography (~1.8um MICROPOSIT S1813 positive photoresist, MICROPOSIT MF-15 Developer) with the first optical mask and lift-off. The metal stack thickness was verified via profilometry (Dektak 3030) on select devices. The metal pads were interconnected by a 14 µm by 20 µm rectangular bridge from which the devices were patterned (see Figure 4.3) . Device alignment in the <100> direction was performed by aligning the mask to (110) primary flat and having the pad "bowtie" structure angled 45° relative to the mask edge.

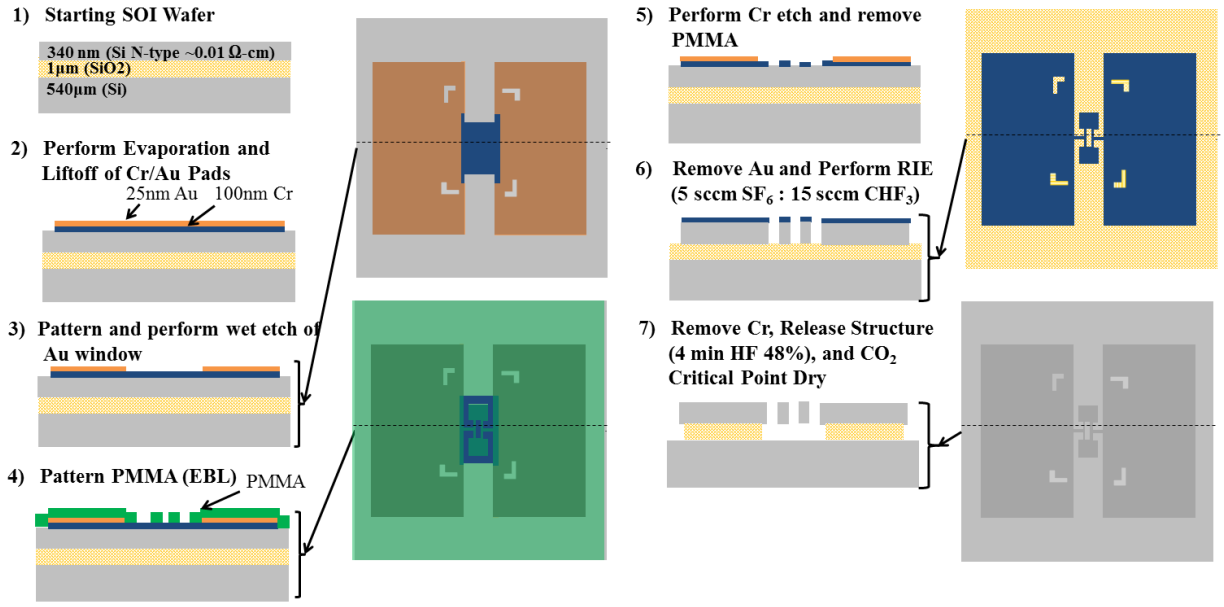

Figure 4.2: Electron Beam Lithography (EBL) Based Fabrication Process for h=340 nm thick devices.

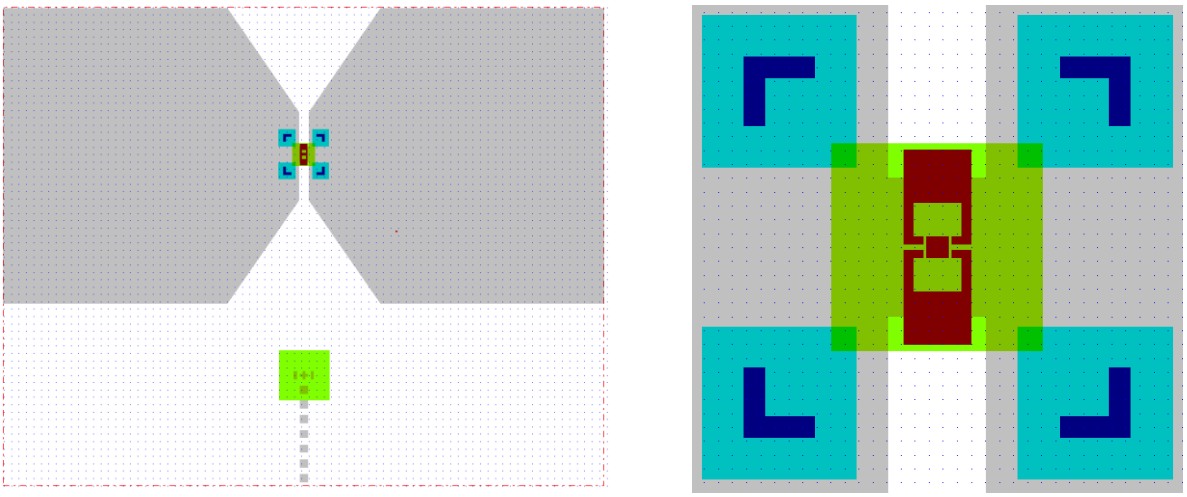

Figure 4.3: Images of optical masks and EBL write and alignment patterns for an individual device. (left) the overall bowtie shape of the Cr/Au metal stack is shown [in gray] with guide markers for manual positioning to the pre-write beam focus area [lower green square] (right) closeup view of the device area indicating a notional EBL write pattern [in red] over the connecting bridge [in gray], the Au optical mask [in green] which was equivalent to the available ebeam write area for the magnification setting used, the alignment markers [dark blue] in which metal is absent, and the alignment scan windows [in cyan].

The Au layer was needed only to provide necessary visibility of the EBL alignment markers as chromium alone was demonstrated to offer insufficient contrast during alignment for this particular EBL system. A second optical mask was used to pattern a 30 μm square area centered about the bridge using the same photolithography process previously discussed. The Au was removed from this area by a short immersion in an Au etch solution (Transene TFA Au Etchant, 10-15 sec). These optical lithography steps (Steps 1-3 in Figure 4.1) were performed across the entire wafer (4") which was then diced into 1 cm x 1 cm individual chips.

Patterning of the device geometry was then performed for each device individually using the NPGS EBL system to expose (Area Dose = 300 μC / cm^2) and develop (1:3 MIBK:IPA, ~90 sec) a conventional PMMA EBL resist (MicroChem 950K PMMA A5.5, ~500 nm). The pattern was transferred to the Cr using a timed wet etch (Cyantek CR-7S, ~30 sec). The PMMA was then removed (MicroChem Remover PG, 75°C), followed by the Au. Once rinsed and cleaned, Reactive Ion Etching (RIE) was performed (5 sccm SF_6: 15 sccm CHF_3, 150 W, 10 mtorr, 9 min) to etch the device pattern into the silicon device layer. Since the BOX acts as an etch stop for this RIE chemistry, profilometry scans (Dektak 3030) were performed on the pads to check the device layer thickness after metal stripping. Device layer thickness was confirmed to be 340 nm ± 10 nm. Two-point probe I-V measurements were also performed to confirm electrical isolation checks between devices and verify etch completion. Once etch completion was confirmed, the RIE polymer residue was removed by plasma ashing (50 sccm O_2, 1min, 100W) and the Cr mask was removed in wet etchant and rinsed in deionized water. To complete fabrication, the devices were released in 48% $HF_{(aq)}$ (4 minutes etch time) followed by CO_2 critical point drying. Imagery at different steps of fabrication for a representative device is presented in Figure 4.4.

This fabrication approach has several challenges associated with it, the most significant being that device patterning with the NPGS enabled SEM requires manual alignment and individual exposure by the SEM operator in a serial fashion. This makes processing very slow and costly for several devices. Furthermore, several iterations of EBL processing may be required to characterize the system for the proper dosage level, exposure time and alignment settings needed for a pattern on the specific substrate being used. Backscattering of electrons from the beam is an effect that limits resolution and is dependent upon the resist thickness and substrate being imaged [96]. However, a more significant issue observed with the NPGS enabled EBL system used, was slight movements in the beam position during pattern writes. This was attributed to environmental noise (mechanical and EMI) which can affect the smoothness of the patterned edges.

The second major limitation with the aforementioned fabrication process, is the use of the timed wet etch for the chromium mask, which like all isotropic wet etchants incurs pattern loss. Ideally a anisotropic plasma etch (RIE) recipe, such as the one presented in [97] which utilizes a Cl_2/O_2 chemistry, would be preferable. However, these resources were neither readily available nor cost effective to acquire for this project.

Despite these challenges there are simple improvements that could be pursued with this process. The EBL patterning can be potentially improved by utilizing a thinner PMMA layer as this would allow shorter lower dose exposures and would minimize resolution loss from backscattering. Similarly, utilizing a thinner chromium layer would reduce the pattern loss from isotropic etching. While these improvements were certainly possible, with additional characterization costs, processing of the 340 nm thick DL SOI chips was continued using the more direct method of FIB milling presented in the next section.

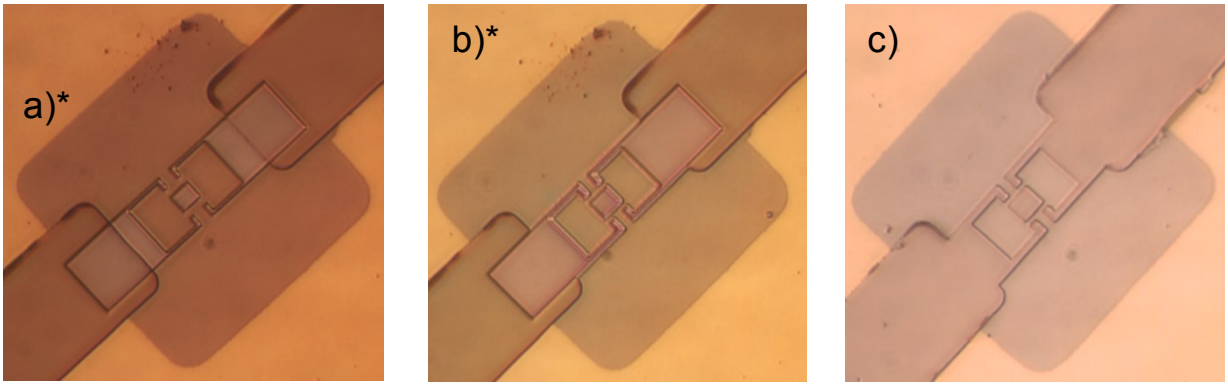

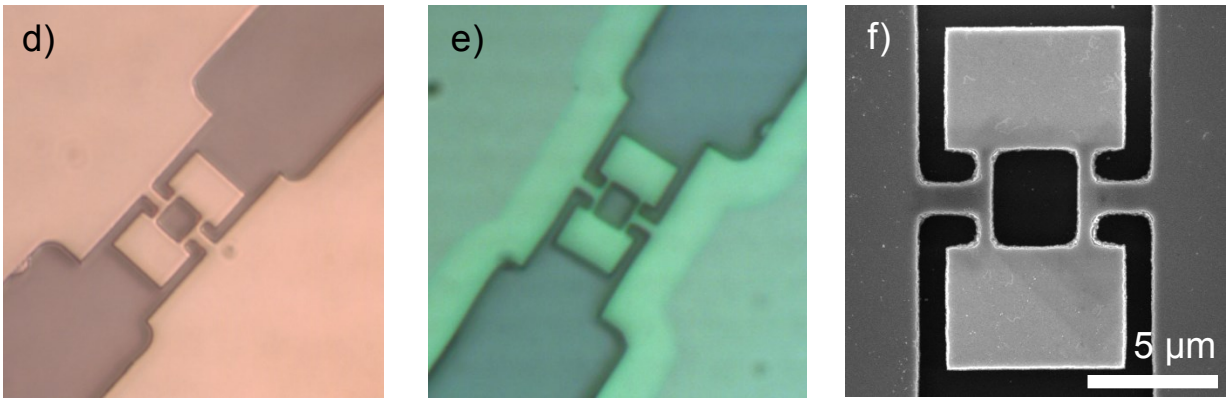

Figure 4.4: (a-e) Optical Imagery (x100, top view) of representative device at different stages of fabrication a) post-PMMA development (step 4), b) post Cr etch – metal bridge in exposed area has been removed, c) Post-PMMA stripping (step 5), d) Post-RIE and Cr removal, e) Post-Release (step 7), f) SEM image (top view) of fabricated device. (* steps a) and b) are actually from a different device with the same EBL write mask on a sister chip)

4.2.2. Focused Ion Beam Milling process

The focused ion beam (FIB) milling process, depicted in Figure 4.5, utilized the same chip samples prepared for the EBL process up to step 3) in Figure 4.2. For these devices bridge patterns of 7 µm by 7 µm on the chip were used in addition to the 14 µm by 20 µm. The FIB based process began with stripping the Au layer (Transcene TFA Au etchant 30 sec with agitation) as it wasn't needed for visibility in the FIB. A standard isotropic RIE (4 sccm O_2: 16 sccm CF_4, 150W, 8 minutes) was then performed to etch the pads and bridge interconnect into the silicon device layer.

FIB milling was then performed using the dual beam FEI Nova 600i FIB/SEM system through both the chromium and silicon layers and into a portion of the BOX layer for each device individually. The focused ion beam essentially bombards the surface with a beam of high energy gallium ions (Ga+) that impact the surface and sputter material away. This process can be viewed real time with a separate SEM column on the system.

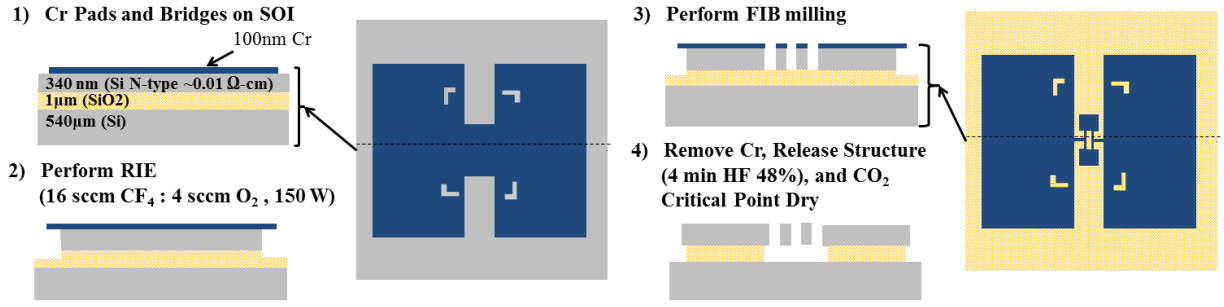

Figure 4.5: Focused Ion Beam (FIB) Milling based Fabrication Process.

FIB milling is a serial process that like the previous NPGS EBL system requires manual aligning to individual devices for the patterning to take place. However, it can afford exceptional resolution (100 nm or less) and offers an immediate result that can be viewed and imaged. There are some limitations to this approach. First, collateral Ga+ ion implantation damage can result in the area exposed to the Ga+ beam. The depth of this damage has been reported [98] to be up to 30 nm for a 30 kV ion beam, which was used in this work. A surface hard mask, like the Cr mask used in this work, can help protect the device surface from damage; however the sidewalls in the area being milled are unprotected, which can alter the material properties of the resulting structure. In the case of milling a narrow submicron or nanoscale structure, such as the actuator arms in these devices, this damage can occur from both sides of the structure while it is being etched. Second, the sputtered material being removed from the surface can be ejected onto the surface or sidewalls of the structure that is being milled. In the case of a resonating MEMS structure this can significantly affect the performance of the device. Third, the ion beam position will naturally drift over time, which can cause rounding of features. All of these effects are aggravated the deeper the milling is performed.

In general, to prevent rounding of features from beam drift, it is best to minimize the milling time. This is controlled primarily through the beam current and the size of the pattern used. However, it is also desirable to minimize the collateral Ga+ ion implantation damage from the beam to avoid altering the material properties. Since this ion damage is also a function of beam current, the optimal beam current and exposure time will depend on each specific pattern and the sample being etched. In this work, bitmap images (1350 x 1350 pixels) were used to describe the desired ion beam milling pattern. Devices E – I were patterned on the 20 μm wide bridges with an x and y size setting of 21.5 μm. Smaller higher frequency geometries (Devices J and K) were patterned on the 10 μm wide bridges with 11.2 μm and 12 .03 μm square patterns respectively. The beam current was fixed to 0.46 nA for all writes. Figure 4.6 shows SEM imagery an example device (Device J) immediately after the FIB milling process has been completed, along with the mask file used.

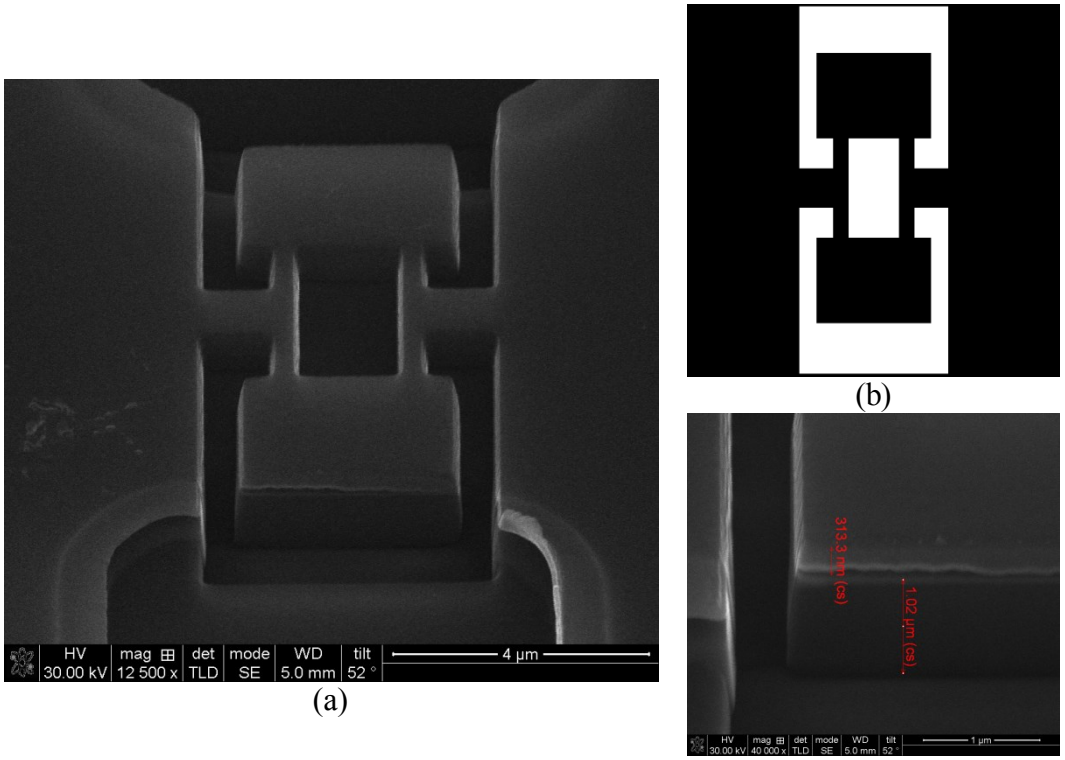

Figure 4.6: (a) SEM Image (x12500) of Device J immediately after FIB milling (step 3 in Figure Figure 4.5); (b) FIB bitmap image used; (c) Close up SEM Image (x40000) of corner of lower proof mass showing the layers of material. Device J was significantly over etched with minor detriment to the final result. In this instance some undercutting of the silicon device layer from the RIE reached the device patterning area causing some minor roughness at the corner.

As previously mentioned, ion damage, beam drift, redeposition of sputtered material become more of a challenge the deeper the milling is performed. Figure 4.7 shows the result of an attempted etch on a 2um thick SOI device illustrating these later two effects. The rounding of features and significant redeposition of material are clearly visible especially around the actuator arms which are critical to the device operation. Thus an alternate approach, discussed in the next section was required to achieve these thicker higher aspect ratio structures.

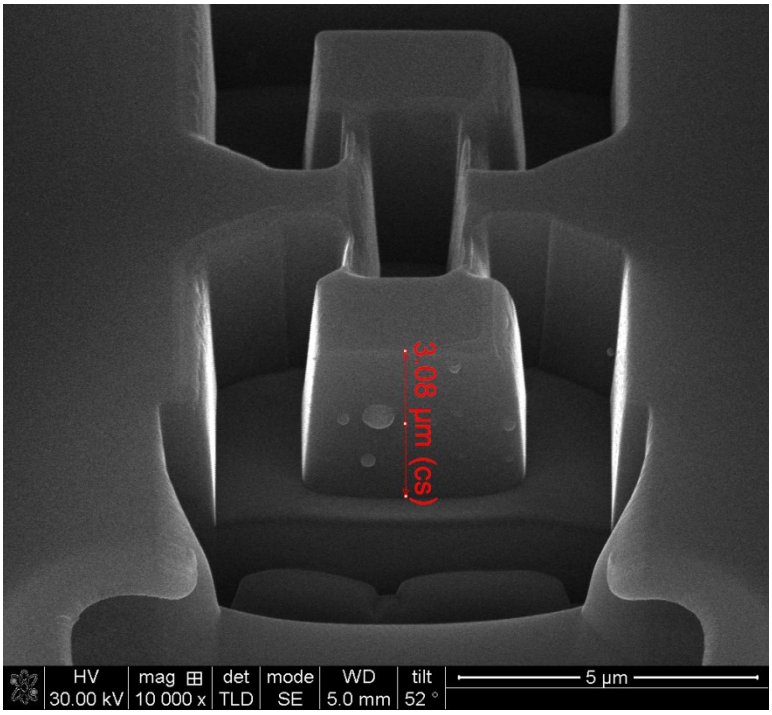

Figure 4.7: SEM Image x10000 of a 3µm deep device patterning attempt into a 2µm thick SOI DL.

4.3. Fabrication processing for high aspect ratio devices (h=1.5-2.0 µm)

To achieve, thicker structures the EBL process described in Section 4.2.1 was improved upon through leveraging fabrication resources at the Air Force Research Laboratory. Specifically, a commercial EBL system and time-multiplexed deep silicon etching (DSE) system were made available to this work. In an attempt to minimize unforeseen complexities in fabrication development, the decision was made to keep the chromium hard mask based subtractive pattern transfer approach discussed in 4.2.1 and simply utilize the DSE tool in-place of the conventional RIE etching. Section 4.3.1 provides a brief primer on time-multiplexed DSE, explains some of the challenges associated with it, including masking, and presents the recipe utilized in this work. Section 4.3.2 then presents the modified processing steps taken to fabricate these thicker devices and the successful use of chromium as a DSE mask for submicron features.

4.3.1. Deep Silicon Etching (DSE)

Micromachining silicon remains an active research area to this day [99–103]. The creation of thick structures is of obvious particular interest to the MEMS community, particularly resonators, as Q improves with size. Various descriptors have been used in literature to refer to deep silicon etching (DSE). These include high aspect ratio (HAR) silicon etch, deep trench silicon, silicon deep reactive ion etch (DRIE) and HAR trench silicon etch [99]. Aspect ratio in the context of DSE, is defined as the ratio of depth to width for a given feature. Alkaline-based wet chemical etch solutions, such as potassium hydroxide (KOH), ethylenediamine pyrocatechol

(EDP), and trimethyl ammonium hydroxide (TMAH), exploit the strong difference between the etch rates of <111> surfaces, which can etch up to 100x slower that the <100>, and <110> oriented surfaces [99], [104]. There are fundamental limitations in the sidewall profiles that can be achieved with this wet etching approach though and thus different plasma etching approaches have been devised.

Modern DSE systems are most commonly inductively coupled plasma reactive ion etch systems (ICP-RIE). Conventional RIE systems which rely solely upon capacitively coupled plasma (CCP) generation, require an increase in RF power in order to increase the plasma density, which in turn controls the rate of the chemical etching. However, this increase in RF powere also increases the self-biasing voltage on the cathode where the sample is positioned, which in turn increases the ion bombardment energy. Higher ion bombardment energy increases the mechanical milling of the mask being used and decreases the etch selectivity. For deep etching ideally high plasma density and low bombardment energy are desired to maximize both etch rate and etch selectivity. To achieve this ICP-RIE systems add an external induction coil which directs RF energy in the chamber and enhances plasma production, creating an inductively coupled plasma (ICP). As explained by Zheng [104], "the electromagnetic field generated by the inductive coupling coil can sustain electron cycling movement in plasma for a long time, which increases ionization probability while keeping the pressure low in the chamber". The CCP source remains to direct the ions in the plasma glow region toward the cathode, via self-bias, however the plasma density, primarily determined by the ICP, is now decoupled. A more detailed discussion on conventional and ICP-RIE systems can be found in Zheng [104].

Collectively, DSE plasma etch methods can be considered in two groups [99], [105] 1) Steady-state plasma etch processing (a.k.a. mixed mode) – where a specific blend of etch gas and inhibitor gas, typically SF_6 and O_2, is applied at the same time under a continuous set of conditions (temp, pressure, plasma density etc.) to form passivating sidewalls while etching 2) Time-multiplexed multistep processing (a.k.a. pulsed mode) – where the plasma conditions are pulsed in a specific step sequence that is repeated, to alternatively etch and deposit inhibitor on the sidewalls.[15]

The machine utilized for this work, the Plasma-Therm Versaline DSE (VL-8526), falls into this second category. The time-multiplexed approach to etching was initially patented by Robert Bosch GmbH as an two-step alternating process that switches process gases between a plasma etching chemistry (typically SF_6) and passivation chemistry, or polymerization (typically C_4F_8), in which the chemical reaction of the plasma with the silicon causes polymeric films to

[15] As explained by Jensen et al. [105], there are actually four different methods that can be used to created an inhibiting or passivating layer these " (i) inserting gases in the plasma which act as silicon oxidant forming non-volatile siliconoxy-halogens (ii) freezing the normally volatile reaction products at the structure's walls using, e.g., cryogenic wafer cooling, (iii) inserting gases which act as polymer precursor forming carbon–halogen layers, or (iv) eroding and redepositing mask material such as metal halogens or resist products". We focus on the third which is relevant for the DSE tool used in this work.

form on the silicon surface [99]. In the case of C_4F_8, long polymer chains of the fluorocarbon CF_2 are formed on the exposed silicon. These polymeric films impede lateral etching of the sidewalls and the kinetic bombardment of the plasma ions is relied upon to etch the bottom (horizontal) surface, exposing it to the subsequent etching step. The Versaline DSE tool improves upon this process by allowing any number of steps to be repeated in order to further tailor the etching and passivation. The primary advantage of this time-multiplexed multistep approach over continuous steady-state etching is that the control over the etch profile is considerably easier. In addition, many steady-state systems operate at cryogenic temperatures (<100 °C), which is not a requirement for time-multiplexed systems.[16] The primary disadvantage is that achieving smooth sidewalls can be rather challenging. Typically *scalloping* of the sidewalls occurs due to the cyclic etch processing. The formation of fluorocarbons is also a "dirtier" process making it less compatible with IC processing compared to cryogenic steady-state systems which leave no residue. In addition, the etch selectivity with respect to the mask is also often worse as higher energy bombardment is required to remove the horizontal surface film [105]. Lastly, the overall etch rate is usually slower than steady-state systems, due to the time required for pulsing.

The process utilized in this work is a three-step process, similar to that presented in [106], that adds a separate etching step for etching the polymer layer. This can result in improved anisotropy and etch control in comparison to the original "Bosch" process, since the plasma conditions can better facilitate removal of the surface polymer before the silicon etch is conducted. Figure 4.8 graphically illustrates each of these 3 steps in the process along with the previously mentioned scalloping effect.

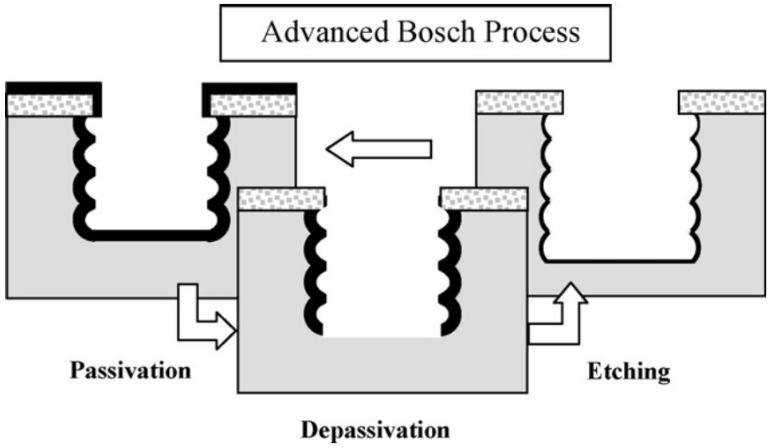

Figure 4.8: Schematic viewgraph of an advanced three-pulse Bosch process (from Abdolvand [106]**)**

[16] Cryogenic systems operate by inhibiting SF_4 removal, the compound that's formed when SF_6 reacts with silicon and normally flushed away. At cryogenic temperatures it can form a 10-20 nm layer over the silicon surface which can serve as a passivation layer[104]. Jensen et al. [105] does discuss the potential for cryogenic two step etching, however this approach is not widespread.

There are numerous challenges that can arise in developing a high-quality repeatable DSE recipe, many of which don't occur in low aspect ratio etching. Figure 4.9 from Rangelow [107] offers a good summary of these HAR effects, which overall become more challenging to manage as the desired aspect ratio and etch depth are increased, and the desired feature resolution is reduced. In addition to *sidewall roughness (scalloping)*, which has already been discussed, the two effects most relevant to this work are *loading effects* and *notching*.

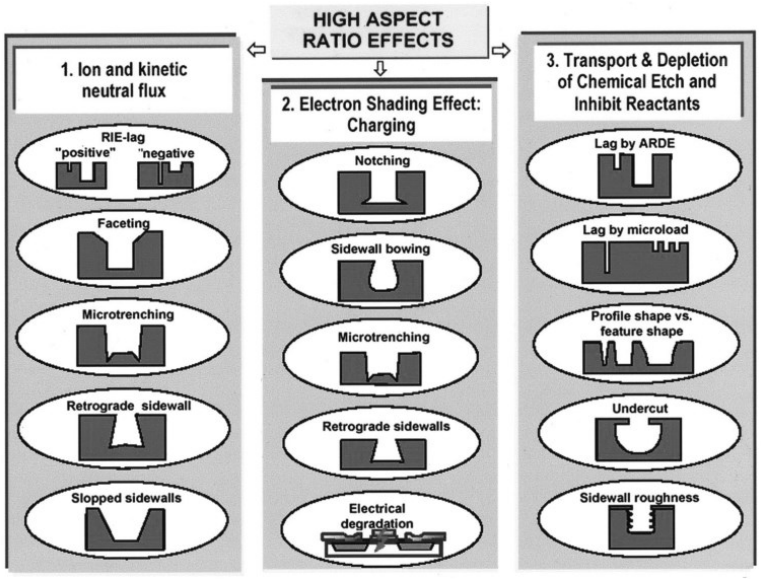

Figure 4.9: High aspect ratio dependent effects in high-density plasma etching of silicon (from Rangelow [107]**)**

Loading effects occur when the consumption of the chemically active species is greater than the supply granted by the fixed gas flow rate and corresponding etch conditions causing a decrease in etch rate. In a macro scale sense the overall etch rate of the wafer (or chip) is determined by the total area of material exposed to etching. Thus an etch rate reported for a given DSE recipe on one wafer mask pattern may yield significantly different etch rates than another if the etching areas are different. This change in overall etch rate is termed *macroloading*. Portions of a wafer that have a higher pattern densities can cause both the local depletion of reactive species and the local accumulation of etched compounds than adjacent low pattern density areas. This localized loading is termed *microloading* and can reduce the etch rate in the high pattern density areas. The most challenging loading effect to deal with however is termed *aspect ratio dependent etching (ARDE)*. This is the tendency for adjacent features of different dimensions to etch at different rates. The causes for this effect are complicated and beyond the discussion of this work, however it is important to acknowledge since most MEMS devices require patterns that have mixed resolution requirements. Thus ARDE can be limiting factor for the practical realization of desired designs. For detailed explanation refer to Henry [108] and Gottscho et al. [109].

Notching is a HAR effect commonly reported in SOI-MEMS DSE processing as it is caused by charging of a dielectric thin film underneath the silicon (the BOX in the case of SOI) during the end of an etch process (i.e. when the oxide is exposed). The charging of the oxide causes extra accumulation of reactive ions at the silicon/oxide interface and thus excessive etching. This effect and one example of its mitigation thru proprietary process control are described further in [110]. The effect is primarily relevant because most MEMS designs are prone to some ARDE. In a SOIMEMS process, since the BOX layer acts as an etch stop the simple solution is to overetch the pattern until all of features have finished etching. The notching effect however can potentially damage the resulting structure if an excessive amount of overetching is required.

Loading effects, notching, and the other HAR effects shown in Figure 4.9 only address the challenges associated with etching the substrate. Of equal importance are the challenges associated with the mask used for patterning with DSE. Expanding upon [108], the ideal mask meets the following requirements: 1) The mask can be easily patterned, using additive or subtractive methods, at the resolution and thickness required for the desired etch depth. As discussed for the Cr mask in Section 4.2.1, the thicker a mask is, the more challenging it becomes to maintain feature resolution. For nanoscale or submicron resolution patterning thin masks (<500 nm thick) are typically necessary. 2) The method used to remove the mask does not affect the substrate, as this may degrade the resolution of the structural pattern, 3) The mask is resilient to both the reactive chemical etching and the physical milling that occur in the ICP-RIE. The former is paramount as chemical etching of the mask will degrade both its thickness and the pattern resolution. The combination of both determine the mask selectivity, the ratio of the etch rate of the mask to the etch rate of the substrate, which limits the etch depth a given mask thickness can provide.

There is a fourth requirement often cited that the mask should be non-conductive to prevent detrimental electric field effects (image forces) between the plasma and the sample [111–113]. Specifically dramatic undercutting and notching effects have been cited with excellent examples presented by Henry [108] for Cr and Cu etch masks utilizing mixed-mode cryogenic etching. Jansen et al. [105] propose that the likely cause for these effects in these cases is the localized deactivation of oxygen radicals near the mask, which is not an issue with time-multiplexed etching. However, they do offer that a conductive mask causes more localized heating due to that fact that more thermal energy can be imparted to the sample from ion bombardment. In the case of SOIMEMS, transferring this additional heat away, even with a controlled temperature sample mount is a challenge as the BOX layer acts as a thermal insulator. Thermally non-conductive masks inhibit the amount of energy transferred to the substrate and should thus maintain a more constant temperature profile during DSE processing. Thus this fourth requirement may be better presented as a thermal requirement rather than an electrical one. Nevertheless the boundary conditions of the DC and AC electric field will change in the presence of a metal mask and these changes may be a factor.

Typically photoresist or oxide are used as masks in DSE processing for micron scale features as they can offer etch selectivity with respect to silicon as high as 100:1 and 200:1 respectively [104]. However, these conventional options are challenging for submicron patterning, which is typically accomplished using EBL as described in Section 4.2.1. The selectivity of PMMA, the conventional EBL resist, with respect to silicon is poor. Use of alternative EBL resists, such as ZEP or HSQ, offer a little improvement in selectivity, but still lack the resilience desired for deep etching. Pattern transfer from EBL resist to oxide would require an intermediary hard mask to address both the needed etch selectivity and visibility for EBL patterning. In addition an anisotropic etch method of the SiO_2 is needed to perform the transfer. Metal masks offer a robust thin film masking solution that is visible for EBL alignments, however as previously discussed can cause interference with the electric field and additional localized heating. In addition, redeposition of milled metal atoms can cause micromasking (black silicon) to occur [105]. The magnitude of these effects however has not been reported in the literature and the potential benefits associated with minimizing the complexity of fabrication were significant. Thus a time-multiplexed DSE recipe using a chromium mask was pursued. It is important to note though that the mask problem for DSE remains an active area of research as evidenced by recent work utilizing alumina masks (2009) [113], and silicon germanium masks [112].

Published work on the use of metal masks with time-multiplexed DSE at submicron resolutions is limited largely to aluminum [102], [114]. A DSE recipe for chromium is presented in [105] albeit for very large (50 μm wide) trenches. Abdolvand et al. [106] offer strong submicron DSE results, however these are for samples masked via the HARPS fabrication process In this work, the desired processing depth was 5 μm with structural aspect ratios up to 20:1 and feature resolutions as low as 250 nm. It is believed that this work is the first to report results using a 3-step time-multiplexed DSE recipe for submicron features with a chromium mask. After a characterization study was performed, the recipe used for the 1.5-2.0 μm thick devices presented in this work is shown in Table 4.1. As expected, this recipe was also demonstrated to be very effective for photoresist masks of micron resolution. The following section explains the remaining processing steps used for fabricating the thicker SOI devices and presents some DSE specific results.

Table 4.1: Time-multiplexed Deep Silicon Etch Recipe used with Cr hard mask

Step	Pressure (mTorr)	DC Bias (V)	Time (s)	Flows (sccm / species)
DEP	25	10	1	150 / C_4F_8
Etch A	20	650	1.2	125 / SF_6
Etch B	20	10	0.7	125 / SF_6
Additional Settings (Held Constant):	ICP Forward Power			1500 W
	Ar Flow Rate			30 sccm
	Temp. (°C)	Spool		175
		Lid		140
		Electrode		10

4.3.2. Wafer/Chip Scale EBL/DRIE processing

The thicker devices were fabricated using a process similar to that previously shown in Section 4.2.1 (see Figure 4.10), with the following differences. First, the starting SOI wafer had a ~1.5-2.0 μm thick device layer (n-type, ρ=0.04 Ω-cm), initially thinned by thermal oxidation (Tylan Oxidation Furnace, wet, 1150 °C, 3 hrs) and a ~3 μm thick buried oxide. Second, the submicron device patterning was performed using a direct write electron beam lithography (EBL) system across the entire chip on a standard PMMA resist (100 nm). Chromium (~145 nm thick, as measured using the Dektak 3030) alone was found to be sufficient for EBL pattern alignment (i.e. no Au layer was used) and served as the etch mask. Third, to accommodate the thicker Si device layer, the silicon etching was performed using the time multiplexed RIE system described in the previous section. The etch settings shown in Table 4.1 yielded a measured Si etch rate of ~2200 Å /cycle. The Cr mask did not appear to etch appreciably. Figure 4.11 shows an image of one device immediately after DSE was performed. The DSE scalloping effect is still visible as is some undercutting of the chromium layer, which was estimated to be ~200 nm +/-50 nm from the image. The device was clearly overetched as evidenced by counting the number of scallops and the visibility of a dark region of oxide beneath the device. However, notching at the DL/BOX interface was not visible nor was any other significant detrimental effect observed.

After DSE was performed the polymer film residue was removed by plasma ashing (50 sccm O_2, 1min, 100W) and the chromium mask was stripped (5min Transcene Chromium Cermet etchant TFE, 1 min DI water rinse, 10 min CR-7S, following by further rinsing in DI water, Acetone, and IPA). Additional cleaning steps were taken including additional O_2 ashing (~45 sec) and wet cleaning (1 min, Cyan-Tec Nano-Strip @ 80°C, 10 min DI water rinse) after mask removal. To reduce the scalloping from the DSE and thin the device dimensions further some additional dry oxidation was performed (Tylan Oxidation Furnace, dry, 1100°C, 50 min)

prior to release in HF and subsequent CO_2 critical point drying. The oxidation conditions were calculated to consume ~46 nm of silicon.

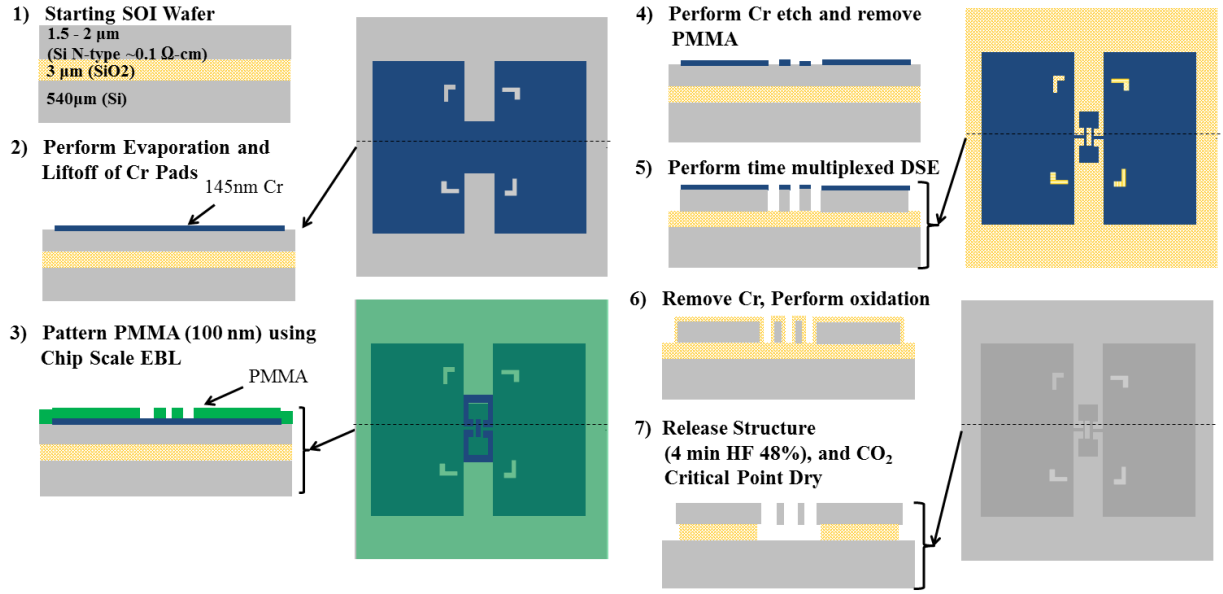

Figure 4.10: EBL and DSE Based Fabrication Process for h=1.5-2.0 µm thick devices

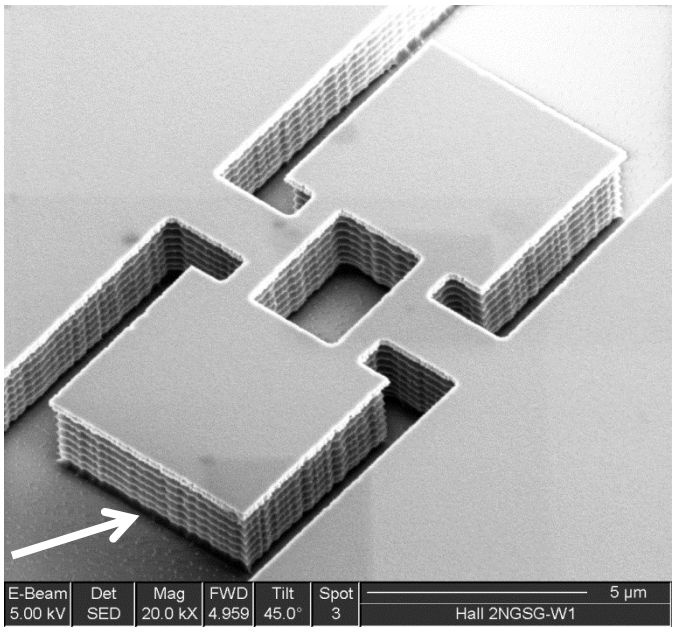

Figure 4.11: SEM Image (x20,000, 45° tilt) of a 2 µm thick device geometry immediately after 20 cycles (~1 min) DSE was performed using the settings in Table 4.1. The majority of etching is accomplished in the first 7-8 cycles as determined by counting the number of scallops on the sidewall. The white arrow points to the thin, comparatively darker, layer of oxide visible from overetching the underlying BOX layer (image courtesy of AFRL Sensors Directorate).

It is worth noting, that the DSE settings presented in Table 4.1 were also successfully applied to a 5 μm thick samples with little degradation in etch. One of the challenges to this fabrication process is that due to the ARDE DSE effect for HAR structures, detecting etch completion can be difficult. Careful inspection at high magnification with proper contrast adjustment is required during etch characterization to determine if the etch has been completed. Figure 4.12 shows images of two different 5 μm thick devices, one prior to release and one after release and subsequent oxidation, each of which was insufficiently etched. To further complicate matters, the SOI DL layers as delivered from the vendor are not uniform in thickness. This is evidenced by the devices presented in this work which were all resident on the same 1cm x 1cm silicon chip, but yet exhibited differences in thickness up to 500 nm, as will be shown in Section 4.4.2. Overetching is therefore desirable to ensure yields are significant.

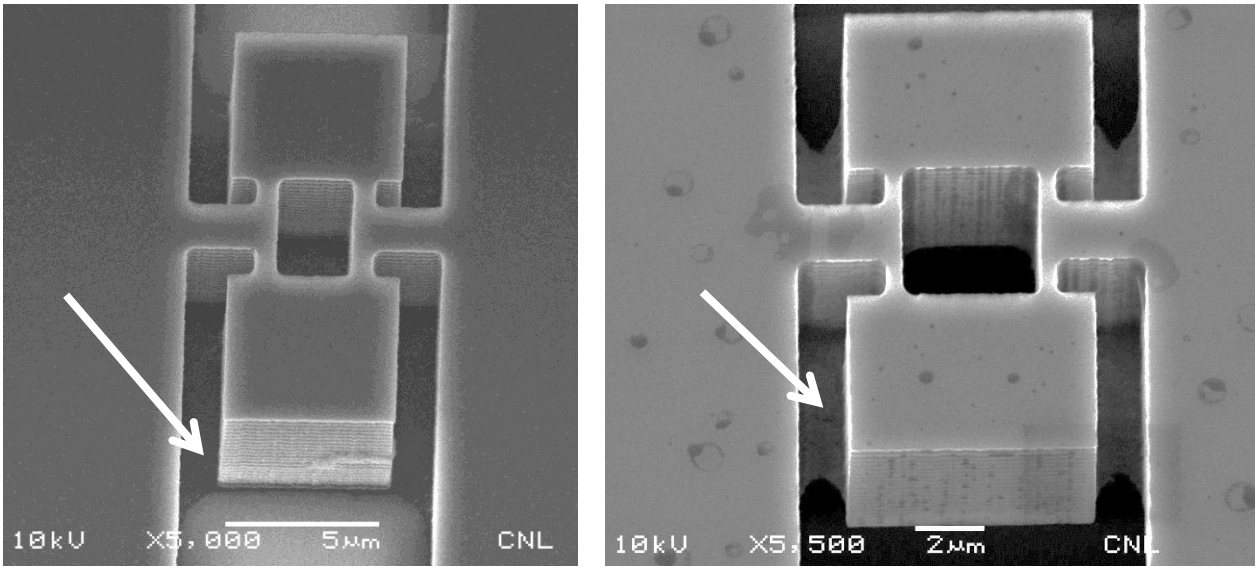

Figure 4.12: SEM Images of different 5 μm thick device geometries (left) (x5000, 30° tilt) prior to release (right) (x5500, 30° tilt) after release and subsequent oxidation. The images were contrast adjusted to show the lingering silicon (indicated by white arrows) in the narrower trench regions. It is also evident from the visible undercutting of the BOX that the larger gap regions adjacent above and below the devices etched faster. Both of these characteristics were a result of ARDE.

4.4. Fabrication Results

Device fabrication was successfully accomplished using each of the processes described in Section 4.3. This section presents the results and resulting dimensions of each of the devices examined in this work. The results are derived from three chips, one for each fabrication process, where each group of devices resided. The 340 nm devices are labeled A-K, while the 2.0 μm thick devices have a two digit designation of letter and number.

4.4.1. Submicron thickness (h=340 nm) devices

Close examination of the 340 nm thick EBL devices was accomplished using a scanning electron microscopy (SEM). Seven measurements were performed across the top surface for each

dimension of the four devices summarized in Table 4.2. Significant roughness along the edges and filleting of the corners was apparent. Actuator width measurements were made across each of the four arms individually and averaged for the indicated value. Imagery also clearly indicated that the etching was anisotropic with a positive tapered slope. Utilizing the average inner and outer width measurements of each arm, the slope was estimated using the following equation

$$\arctan\left(\frac{\frac{\overline{W_{outer}}-\overline{W_{inner}}}{2}}{h}\right) \qquad \{4\text{-}2\}$$

Per Eq. {4-2}, the slope was estimated to be ~15° for the devices overall. Based on these dimensions, and assuming a β=1.11, the thermal capacitance of the device actuators ranges is estimated to range from 5.3×10^{-13} J/K (for W=0.32 μm) to 9.8×10^{-13} J/K (for W=0.80 μm), per Eq. {2-39}. Figure 4.13 shows an image of released Device A.

As a measure of actuator edge roughness, the average standard deviation of the width measurements for all individual arms is shown in Table 4.2 in terms of percentage from the overall mean width. The standard deviation of the four individual arm width averages was also calculated, and is presented as a percentage from the overall mean arm width in order to quantify the degree of variation among the arms. Overall, Device B exhibited the best consistency of arm width and symmetry, while Device A was the worst. Figure 4.14 shows images of each for comparison. The overall device footprint is ~110 μm^2 excluding the bonding pads. The device active area is ~70 μm^2 [19].

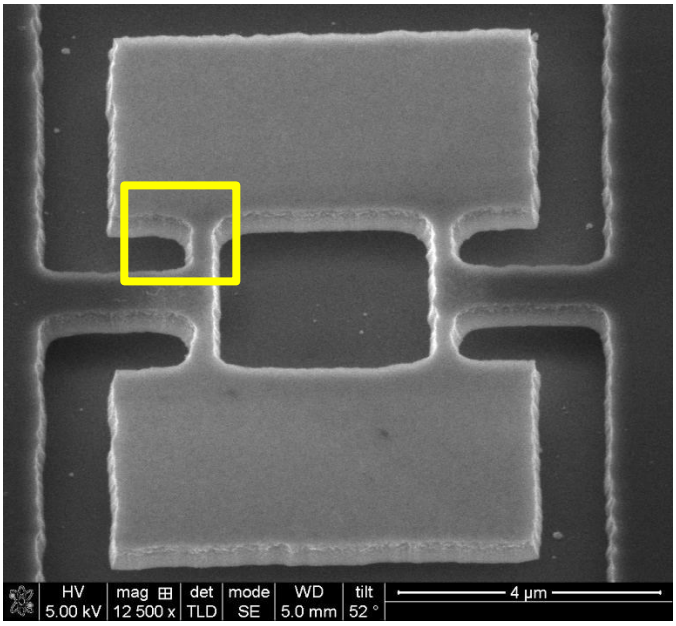

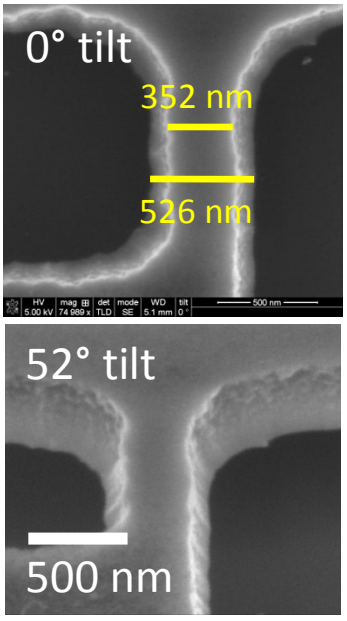

Figure 4.13: (left) SEM Image (x12,500, 52° tilt) of EBL based fabricated Device A after release (upper right) Example measurements used to measure the sidewall angle (~14.4° for this device) (lower right) closeup view of individual actuator arm region (highlighted by yellow square)

As previously discussed, the cause of the edge roughness and asymmetries in patterning is primarily attributed to the limitations of the EBL system used. A significant amount of noise was present in the environment where the EBL was conducted causing the write beam to jitter. In addition, the wet etch process of the Cr is isentropic and can add further rounding. Since the Cr was proven, as expected, to be very selective in the SF_6 base RIE etcher, a much thinner layer would likely suffice as a mask for future devices and would improve the wet etch pattern transfer.

Table 4.2: Average measured dimensions of EBL fabricated devices as defined in Figure 2.9 (thickness h = 340 nm). . Measurement statistics are listed for the actuator arms as indicators of roughness and asymmetry present.

Resonator Dimensions (µm)									
Device	***a*** (n=7)	***b*** (n=7)	***c*** (n=7)	***L*** (n=7)	***W*** (n=28)	$\%\sigma_{W\ single\ arms}$	$\%\sigma_{W\ between\ arms}$	$W_{support}$ (n=7)	$L_{support}$ (n=7)
A	6.47	4.40	1.24	1.35	0.32	5.24	9.06	1.03	2.37
B	6.49	4.45	1.24	1.41	0.35	4.05	2.44	1.00	2.42
C	6.51	4.43	1.14	1.27	0.44	3.93	8.46	1.13	2.18
D	6.70	4.72	1.13	1.00	0.80	4.76	6.81	1.38	1.88

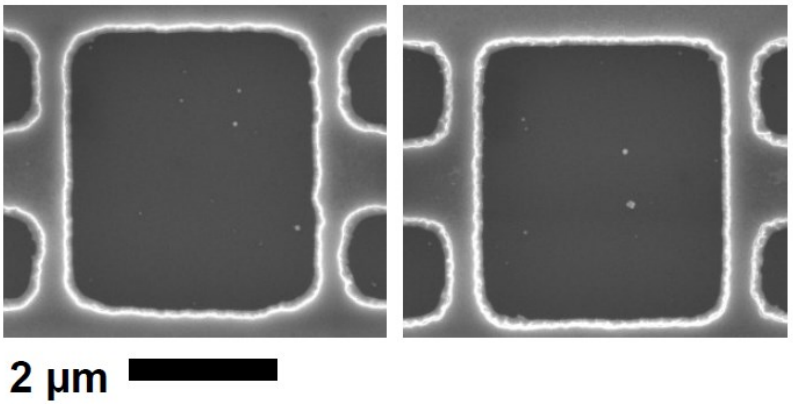

Figure 4.14: SEM images (x25,000, top view) of the actuator arms for Device A (left) and Device B (right).

Inspection of the FIB milled devices under SEM revealing much sharper patterning results (see Figure 4.15). Compared to Devices A-D, the edge roughness and any asymmetry between actuators was virtually eliminated and sidewalls appeared near 90°. Despite the Cr protection layer, some edge rounding and filleting did remain, however these effects are minimal and can be ignored. A summary of exact device dimension for the seven FIB milled device examined is provided in Table 4.3. Measurements of the SEM imagery indicated that the

variation in dimensions was minimal. Substantial measurement statistics were not performed as the variation of the device dimensions was nominal.

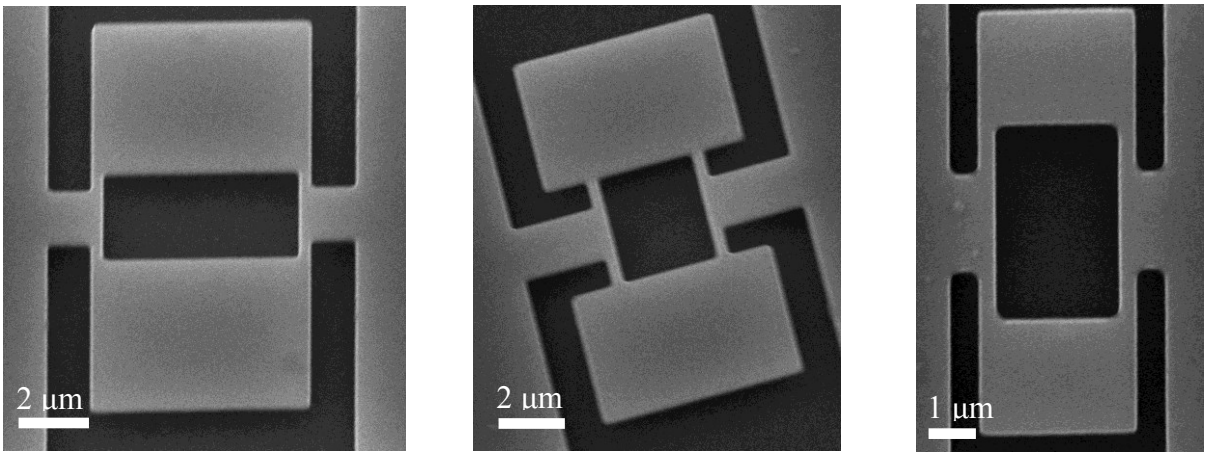

Figure 4.15: SEM Images of suspended FIB milled devices (a) Device I [x7,500, 30° tilt] , (b) Device F [x7000, 27° tilt], and (c) Device K [x10000, top view]

Table 4.3: Measured dimensions of FIB milled devices as defined in Figure 2.9 (thickness h = 340 nm).

	Resonator Dimensions (µm)							Derived	
Device	***a***	***b***	***c***	***L***	***W***	$W_{support}$	$L_{support}$	***L/W***	$\frac{R_A}{R_{support}}$
E	7.1	5.0	1.47	1.11	0.39	0.98	2.88	2.85	0.97
F	6.7	4.8	1.40	1.05	0.37	1.89	2.74	2.84	1.96
G	6.3	4.6	1.15	1.00	0.72	2.73	2.38	1.39	1.59
H	6.4	4.6	1.32	1.47	0.34	1.75	2.56	4.32	2.96
I	6.75	5.31	0.00	0.62	0.36	1.79	1.30	1.72	2.37
J	3.4	2.5	0.53	1.06	0.36	1.11	1.20	2.94	2.71
K	3.4	2.5	0.00	1.00	0.39	2.10	0.64	2.56	8.37

The dimensions shown in Table 4.3 were chosen to empirically gauge differences in performance. Device geometry E was considered the baseline geometry and was based on the intended mask layout used for the EBL process. The expectation is that wider support arms should lower their electrical resistance with the possibility of increasing their acoustic loss. This should decrease the overall DC power consumption needed to power the devices. Placement of the actuation beams was also considered with some designs having them inset closer to the proof mass center of mass, (Devices E-H and J) and others placing them near the edge of the structure (Devices I and K). The placement towards the edge should also be beneficial from a power consumption perspective, but may be detrimental towards efficiently exciting the longitudinal

model due to actuator offset from the center of mass . Device H was created with longer arms to verify the assertion that performance should decrease due to the additional thermal capacitance inherent to the actuator arms. It should be noted that Devices E-I were all originally intended to have the same proof mass size to isolate geometry changes to individual dimensions. However an error in sizing the bitmap, later caught for the higher frequency Devices J and K, resulted in the above.

4.4.2. High-aspect ratio (h=1.5-2.0 μm) devices

Similar examination of the ~2 μm thick EBL devices (chip 2W1) was also accomplished using a scanning electron microscopy (SEM). Post-release imagery, such as that shown for Device A3 in Figure 4.16, shows ~90° sidewalls with the time-multiplexed DSE scalloping clearly evident, although noticeably lessened by the thermal oxidation performed when compared to the post DSE image shown in Figure 4.11. Some non-uniformity of the edges was present and thus statistical measurements for each device dimension were made in the same fashion as in Section 4.4.1, the results of which are summarized in Table 4.4. The thickness of each device was also measured either directly using the dual beam FIB/SEM or by tilt correcting measurements from the 45° oblique view (h' as shown in Figure 4.16). In this later case the following trigonometric relation was used to correct the measurements

$$\cos\theta = \frac{h'}{h} \qquad \{4\text{-}3\}$$

where θ is the tilt relative to the vertical axis as depicted in Figure 4.17 (right). For θ=45° h is simply multiplied by a factor of $(2/\sqrt{2})$ to convert to h. This technique was validated with the direct measurements, shown in Figure 4.17 (left) to within 50 nm.

It is worth noting that the smallest devices fabricated for this work, Devices C4 and D4, had an area footprint, per Eq {4-1} of ~50 μm^2.

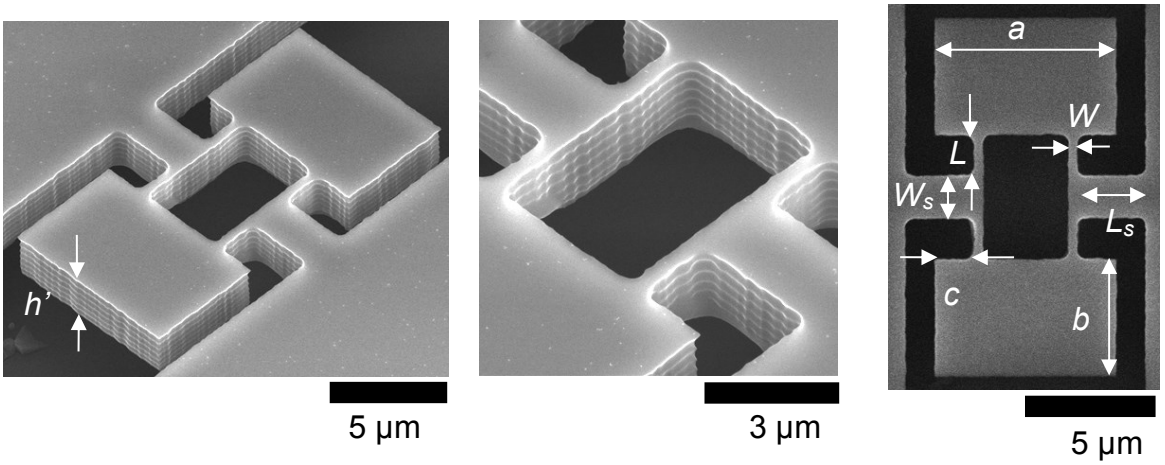

Figure 4.16: SEM images of Device A3 (left) (45° tilted, oblique) (middle) close up view of the actuator arms (right) top view with dimension labels added for reference

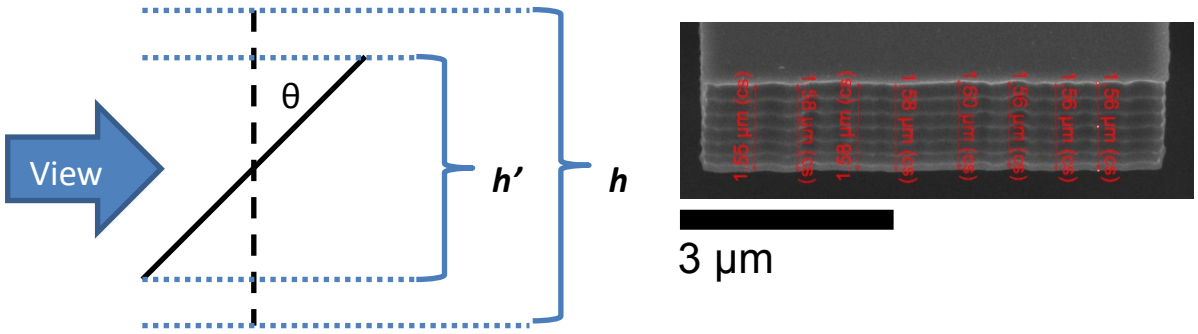

Figure 4.17: (left) Graphic depicting tilt correction for height using oblique view SEM images (right) SEM image showing direct measurements of device thickness at the plate edge of Device A3. Direct measurements yielded an average thickness of 1.57 µm, while the average corrected oblique measurement yielded 1.53 µm, verifying the technique to within 50 nm.

Table 4.4: Summary of Chip 2W1 Device Dimensions with average device dimensions [n=7] in µm. Device label with an asterisk (*) indicate that these devices operated as self-sustained oscillators in addition to resonators

	Resonator Dimensions (µm)									
Device	***h*** (n=7)	***a*** (n=7)	***b*** (n=7)	***c*** (n=7)	***L*** (n=7)	***W*** (n=28)	$\%\sigma_W$ *single arms*	$\%\sigma_W$ *between arms*	$W_{support}$ (n=7)	$L_{support}$ (n=7)
C4	1.70	3.53	2.45	0.676	1.545	0.338	8.64	2.56	1.595	1.80
D4	1.72	3.49	2.46	0.687	1.517	0.356	8.45	5.50	1.56	1.76
A3*	1.57	6.46	4.17	1.38	1.47	0.36	6.26	3.95	1.54	2.56
C6*	1.77	5.73	5.70	0.94	2.02	0.34	9.67	7.03	1.59	2.56
B8*	1.80	5.64	5.68	0.92	2.01	0.36	5.55	3.61	1.67	2.52
E6*	1.86	9.79	5.54	2.37	1.41	0.38	8.04	19.19	1.54	3.35
G8	1.91	7.72	5.58	1.36	1.46	0.44	13.71	18.65	2.05	2.83
E1	1.64	5.75	7.82	1.04	1.50	0.59	5.45	1.57	2.09	2.55
E7	1.88	9.81	5.58	2.38	1.21	0.42	9.14	12.65	2.06	3.34

5. Performance of VHF Thermal-Piezoresistive Resonators

The devices fabricated in the previous chapter were each characterized experimentally for linear operation as resonators. Section 5.1 discusses the experimental setup, including its advantages and limitations, and the method employed, including the de-embedding procedures to process the measured data. Section 5.2 presents the measured device resonator performance results and discussion. Section 5.3 concludes by presenting the compared values to those provided by the lumped parameter model in the form of Eq {2-37}.

5.1. Experimental Setup and Methods

Device performance as a linear resonator was examined electrically under both vacuum (~50-70 Torr) and ambient atmospheric conditions. This was accomplished by mounting the test chips to a printed test circuit board, shown in Figure 5.1, with carbon tape and individually wirebonding devices (Al wirebond) to signal feeds on the board. This board was then connected to electrical test equipment as depicted by the schematic in Figure 5.2. A network analyzer (Agilent Technologies E5061B) provided the input AC voltage and recorded the transmission behavior ($|S_{21}|$ parameter) of the signal through the circuit depicted. An additional DC voltage source (Agilent E3647A) was used to provide the necessary bias current to power the devices and ensure device response at the frequency of excitation. The DC current was measured using a digital multimeter (Agilent 34405A). The substrate was wirebonded to ground for the h=360 nm devices, but was this was later found to have no significant impact on the measurements and was not accomplished for the majority of h~2 μm testing. The additional resistive and capacitive components provided isolation of the sources as shown, acting as bias-T's. The low vacuum testing was accomplished by placing the test board inside a vacuum bell jar system with coaxial feedthroughs to provide electrical connection to the board.

Devices were generally examined by incrementally increasing the DC bias currents and performing network analyzer sweeps at each current**.** Sweeps were repeated multiple times at each condition before data was recorded to ensure a stable response. Initial acquisition of resonant peaks was typically accomplished from 10-250 MHz stepped across using a 5 MHz span (800 pt resolution setting). The power of the network analyzer was usually set to 10dBm, the maximum setting, for initial detection of modes and then decreased as the DC current was increased to avoid driving the devices in a non-linear fashion. It did become apparent however as device characterization progressed that some modes would be easier to acquire at a lower AC power setting, since their non-linear "saturated" response would be actually more difficult to discern. Testing would generally stop when the applied DC voltage needed to incrementally increase the current would increase disproportionately with previous test conditions, as this was considered a near "burn-out" condition.

5.1.1. Advantages and Limitations of Test Setup

The experimental setup described had several advantages. The first being that it was readily available through the University of Denver NEMS lab and the second being that the prior MEMS scale devices reported had been successfully characterized using this approach with the same equipment. Thus, it was an obvious low-cost low-risk approach to testing. Furthermore, the intent of this effort to explore higher frequency performance with these devices didn't necessarily demand higher precision measurement approaches.

It is important to note that there some inherent limitations to using this approach, the first being that it is limited in its ability to identify the contact impedance and resistivity of the device under test at the RF frequencies being considered. This challenge requires an appreciation for

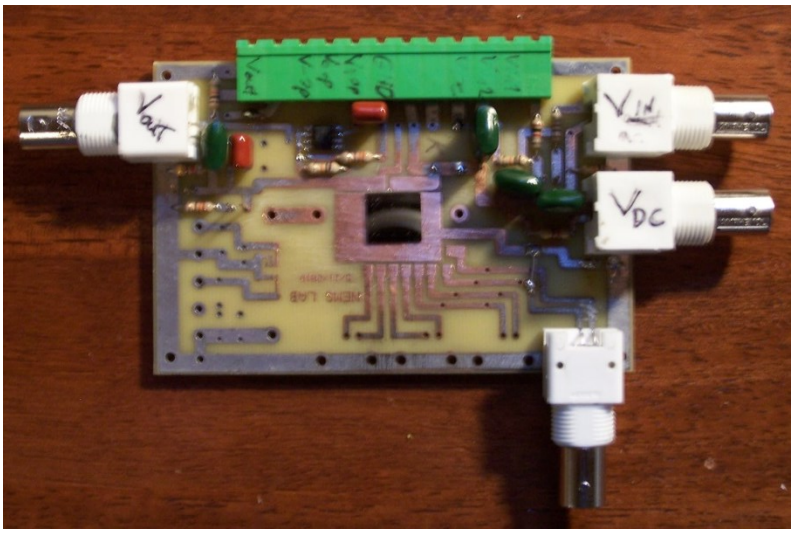

Figure 5.1: Image of printed circuit board (supplied by the DU NEMS group) used to implement the circuit shown in Figure 5.2 with test chip mounted. Please note, this board had additional components on it (not connected) to support other research efforts.

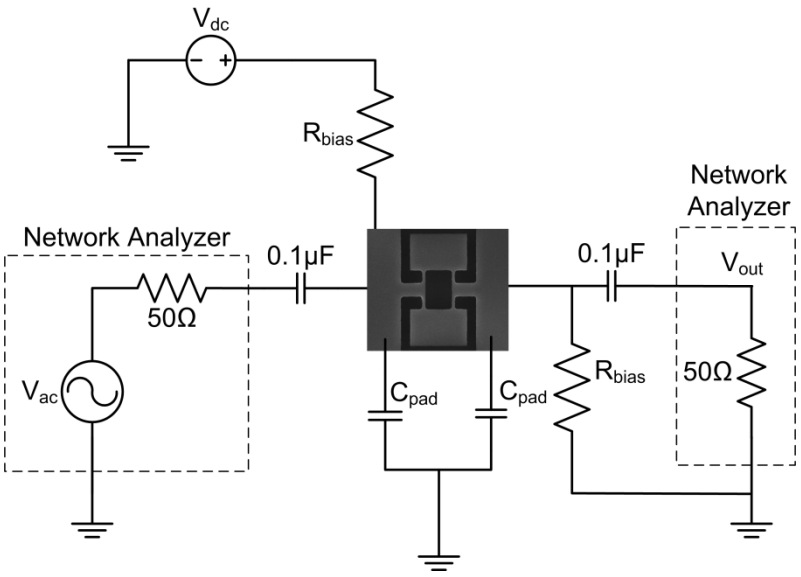

Figure 5.2: Electrical Test Circuit Schematic used for device testing as resonators. The bias resistors were 5.6 kΩ for the h=340 nm devices, and 5kΩ for the h ~ 2 μm thick devices.[17] Testing was accomplished with the substrate wirebonded to ground for the h=340 nm devices, which adds pad capacitance to the model as shown. The h~2 μm devices did not have the substrate wirebonded to ground for the majority of testing as no appreciable difference was detectable in device response.

the effects of device scaling on the propagation of RF signals. If the device dimensions are on the order of the RF wavelength they are operating at then the phase of voltage or current changes over the physical extent of the device. If the wavelength is large enough in comparison to the propagation distance through the device then the phase variation is insignificant and the lumped circuit element approximations of circuit theory are applicable. When the wavelength is much shorter than the dimensions of the component. Maxwell's equations can be simplified to the geometrical optics regime [10].

The devices in this work are on the scale of 5-10 μm in component length, which is much smaller than the wavelength of the signals which propagate through them. Thus, for *on-chip* signal propagation and processing, RF waveguides are largely unnecessary. However, when the connections required to test these devices on chip are considered the distances do become a concern. In particular, the length of the wire bond from a chip to a package and subsequent line distance from a package through a printed circuit board to an input or output node can become significant. In addition to line distance, the issue of signal power loss from mismatched impedance between your RF source and detector at the input and output nodes respectively arises. Thus many RF micro and nanoelectronic devices are tested using probes that have built-in waveguides which are then connected to properly impedance matched on-chip waveguides to maintain signal to and from the device (i.e. ground-signal-ground interconnects). Utilizing these probe waveguides with on-chip calibration structures can also allow for precise determination of

[17] The bias resistors used for the FIB milled devices (Devices E-K) were a 1 kΩ and a 5.1 kΩ parallel resistor pair (836 Ω).

parasitic and device impedances across the frequencies examined. In addition, this approach forgoes the need to wirebond devices, allowing much faster testing, including automated testing.

The devices in this work have a significant series resistance (on the order of several kΩ). Thus, a significant portion of the incident test signal is reflected back to the source and accepted as loss. This effect would occur regardless of the testing scheme used, since 50Ω impedance is standard throughout the RF industry. Impedance matching the devices to a 50Ω network analyzer is theoretically possible through the use of a matching network. However matching networks are only valid for a distinct narrow frequency range and for application to this work would require tuning to the frequencies of device operation. Their use may also introduce challenges in decoupling their effect from the data to ascertain the true response of the device under test, and it is often most prudent to simply accept the loss as was done in this work.

Another limitation with the approach describe is that it did not permit direct measurement of the applied DC device voltage during testing, which in turn can be used to observe and measure any dynamic changes that may occur in the DC device resistance. In lieu of this direct measurement, the series resistance of the resonator was determined before and after testing each device by measuring the voltage between pad contacts with a multimeter for a set DC bias current and applying Ohm's law. These DC device resistance measurements were in turn used to check the resistivity of the silicon as originally measured by 4-point probe on the source wafers prior to fabrication by considering the device resistance, $R_{device,}$ based upon the geometry,

$$\begin{aligned} R_{device} &= R_a + R_s \\ &= R_a + \left(2R_{\text{support}} + \frac{R_{plate}}{2} \right) \\ &= \left(\frac{L}{W} \right) \frac{\rho_{Si}}{h} + \left(2 \left(\frac{L_{\text{support}}}{W_{\text{support}}} \right) \frac{\rho_{Si}}{h} + \left(\frac{a-2c}{b} \right) \frac{\rho_{Si}}{2h} \right) \end{aligned} \qquad \{5\text{-}1\}$$

where the R_{plate} is the resistance of the plate or proof mass, often ignored for large scale devices, and the remaining parameters are defined in Figure 2.9.

5.1.2. The S_{21} Parameter and Data De-embedding

The network analyzer is designed to measure the *scattering parameters* , or *S-parameters* of the device under test (DUT) from the perspective of a two-port network. Ports are defined as a pair of terminals, and in this work the input/output ports are simply the combination of each respective terminal with ground. The S-parameters are complex values that effectively describe the ratios of power transmitted through one port into the other (S_{12} and S_{21}) and reflected back (or scattered) from the DUT to each port (S_{11} and S_{22}). It is critical to understand that the S-parameters are predicated upon the DUT being a linear system, meaning that the frequency of the system response is at the frequency of excitation. In fact, most network analyzers can only

measure system response in this fashion, with frequency sweeps being performed in a single direction. In order to measure non-linear behavior (such as hysteresis or spring softening) a non-linear network analyzer or a custom measurement setup would be required.

The S-parameter of interest for this work is the S_{21} parameter, which is effectively a measure of the forward gain (transmission to port 2 from port 1) through the device. This is expressed as a complex quantity below

$$S_{21} = 2\frac{V_o}{V_s}\sqrt{\frac{Z_{01}}{Z_{02}}}$$
$$|S_{21}|\angle\phi_{21} = 2\frac{|V_o|\angle\phi_o}{V_s} \text{ for } Z_{01} = Z_{02} = 50\Omega \qquad \{5\text{-}2\}$$

where Z_{01} and Z_{02} are the characteristic impedances of the transmission line to and from the 2-port network. An excellent source for the derivation of Eq {5-2} can be found in the textbook by Misra [115]. This relation allows the S_{21} parameter to be converted into voltages and ultimately admittance.

Electrically, it is most appropriate to consider the test circuit shown in Figure 5.2 as a combination of complex admittances (or impedances) represented as a two-port network. There are multiple ways to accomplish this, however for this work we can consider the Π network shown in Figure 5.3a) where Y_f is the complex actuator admittance, Y_p is additional parasitic admittance, and $Y_m = \frac{1}{Z_m}$ is the motional admittance describing the resonator. Recalling the RLC circuit analogue to the MSD system the total admittance can be mathematically described as

$$Y_t = Y_m + Y_f = \frac{1}{R_m + j\omega L_m + 1/(j\omega C_m)} + \left(\frac{1}{R_f} + j\omega C_f\right)$$
$$= \frac{j\omega A}{\omega_o^2 - \omega^2 + j\omega\omega_o/Q} + \left(\frac{1}{R_f} + j\omega C_f\right) \qquad \{5\text{-}3\}$$

, the amplitude of which is equivalent to

$$|Y_m| = \frac{A\omega}{\sqrt{(\omega_o^2 - \omega)^2 + \frac{\omega^2\omega_o^2}{Q^2}}} \qquad \{5\text{-}4\}$$

where $A = 1/L_m$. Eq {5-4} is the series RLC analogue to Eq {2-10} of the forced MSD system. The motional parameters and their relation to the constant A in Eq {5-4} are summarized below

$$R_m = \frac{1}{g_m} = \frac{\omega_o}{QA}$$
$$L_m = \frac{QR_m}{\omega_o} = \frac{1}{A} \qquad \{5\text{-}5\}$$
$$C_m = \frac{1}{QR_m\omega_o} = \frac{A}{\omega_o^2}$$

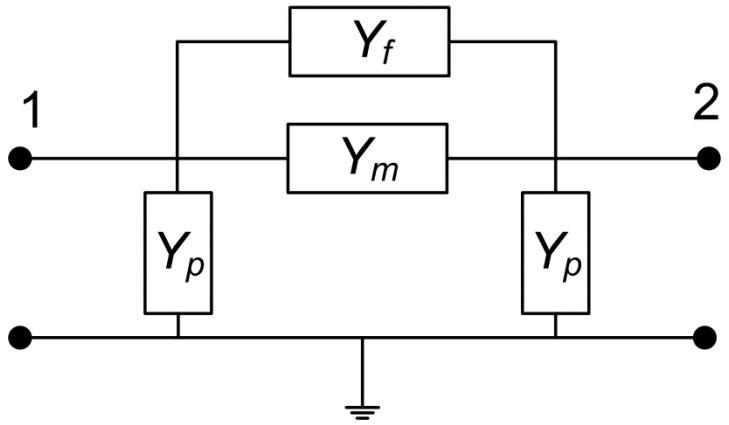

Figure 5.3: Representation of test circuit as two-port network of complex impedances

Thus the goal of device characterization becomes determining the quality factor, Q, resonant frequency, ω_o, and motional conductance g_m of the system, in order to describe it's response. This is most simply accomplished by recording both the magnitude and phase (or complex X and Y) data for the S_{21} parameter for all measurements. A feedthrough floor , the Y_f term in Eq {5-3}, can be fitted to both datasets using information outside the immediate bandwidth of the device response. This floor is then subtracted from each effectively isolating the motional admittance of the device. Figure 5.4 shows an example of this procedure with both the raw and floor removed data. The magnitude of the floor removed data corresponds to a 1D Lorentzian lineshape function, specifically the function shown in Eq {5-4} to which a least square fit can be performed to extract Q, ω_o, and g_m. [18]

[18] In this work, for situations where both magnitude and phase information were available, the fitting is actually performed to $\frac{|V_2|}{V_{s1}}$ as shown in Figure 5.4. This does not affect the Q and ω_o values, but requires further scaling the fitted A term to apply Eq {5-5} for motional conductance. Strictly speaking, a series admittance Y can be determined from the S_{21} parameter by applying the formula $Y = \frac{S_{21}}{2Z_o(S_{21}-1)}$ as described by Misra [115]. Dividing the fitted A value by the characteristic impedance (Z_o = 50 Ω) is a close approximation to this and was used for this work.

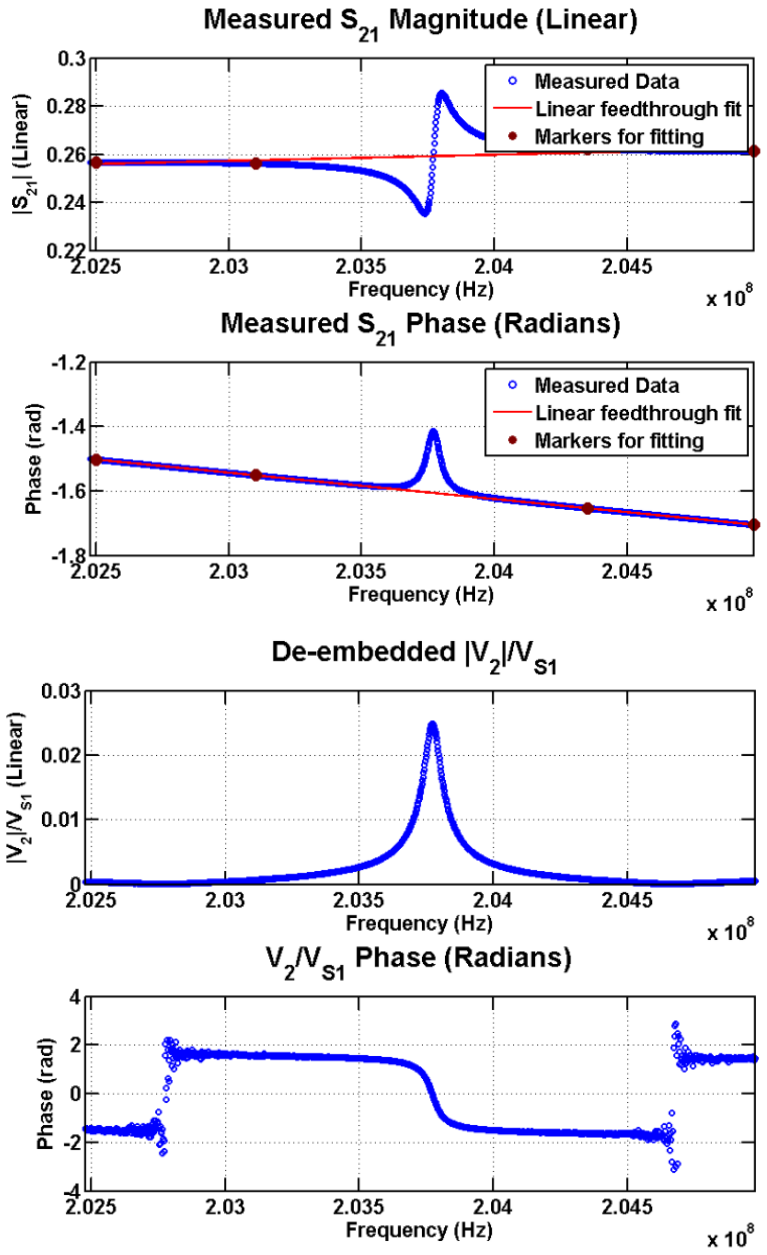

Figure 5.4: De-embedding of data using both magnitude and phase information. The example shown is for the high aspect ratio Device D4 at I_{DC}=3.5 mA at 50-70 Torr. The results of processing of this example using the alternate method are shown in Appendix 2, Figure A2.2 .

Unfortunately, the need to de-embed the data in this manner did not become apparent until after the majority of data was collected for this work and much of the phase collection of S_{21} was neglected. Instead an alternate method, presented in Appendix 2, which used a purely resistive interpretation of the system and solely the magnitude of S_{21} was employed. While this method introduces errors, potentially up to 20% for g_m , the values provided still offer a basis for comparing devices and examining trends in performance. Trends in quality factor need to be considered carefully however, since phase magnitude offset can artificially create sharper appearing peaks in magnitude when uncorrected. Furthermore it has been demonstrated that for

more accurate generation of these parameters, a least-squares fitting approach can be employed incorporating additional fitting offsets to effectively compensate for the phase information.

5.2. Measured Performance

The results of electrical device characterization as resonators using the setup and methods described in the previous section are presented here. Before presenting them it is first worth keeping in mind some of the theoretical expectations in performance between the submicron (h=340 nm) devices and the thicker HAR devices (h=1.6-1.9 μm).

For a given geometry, the figure of merit, *FOM*, as defined by Eq {2-38}, should remain unchanged as the thickness of the device is varied since changes in C_{th} , as specified by Eq {2-39} and the device electrical resistance R_{device}, as approximated by Eq {5-1} should cancel other and the resonant frequency ω_o, as approximated by Eq {3-3}, should remain largely unchanged. However, this theoretical expectation is predicated upon the remaining variables in Eq {2-38} remaining unchanged. While not easily quantifiable, the quality factor tends to decrease as the size of the resonator (surface area to volume ratio) decreases as mentioned in Section 2.8.5 so it is reasonable to expect that the FOM may be smaller for the thinner devices.

The DC power, P_{DC} and motional conductance g_m , can likewise be considered in similar fashion (with the same caveats) *for a given DC current value*. Based on Eq {2-37}, the thinner devices should yield higher g_m values for a given DC current as the C_{th} should be smaller. However, this gain in g_m comes at the expense of additional DC power required.

When considering the effect of thickness on the *maximum possible motional conductance* of the device, regardless of power, the thicker devices should be able to reach higher magnitudes of g_m due to the squared dependence on I_{DC} current which is in turn limited by the DC steady-steady device temperatures being below that of the failure point of the material. While the maximum I_{DC} values were not explicitly modeled it is reasonable to qualitatively presume that the since the overall device electrical and thermal resistance decreases for thicker devices, more current is required to reach the same level of maximum power delivered and the maximum steady-state temperature limit . The maximum possible motional conductance is of interest because it impacts the ability of a device to be able to reach the $g_m R_A$=-1 condition, described in Section 2.7.4, needed for self-sustained oscillation. This tendency, coupled with the likely higher quality factor, makes it more likely for the thicker devices to achieve self-sustained oscillation.

Regarding the expectation of signal shape from the network analyzer for all the devices in this work, the following explanation by Rahafrooz and Pourkamali in [67] holds valid, "…The measured resonance peaks are downward due to the negative piezoresistive coefficient of the structural material, resulting in a negative motional conductance. The negative motional conductance causes the motional current at resonance to be 180° out of phase with respect to the

input ac actuation signal. Therefore, at resonance, the overall current passing through the resonator decreases, showing up as a downward peak (reduced transmission or increased equivalent impedance) in the frequency response." However , as shown in Figure 5.4, the presence of feedthrough can alter the perceived response considerably.

5.2.1. Submicron thickness (h=340 nm) devices

The measured performance results for the EBL fabricated devices (Devices A-D) are shown in Table 5.1. Overall the frequency of operation increased with shorter and wider actuator arms ranging from 112 MHz to 176 MHz. This matches expectation as the spring constant can be estimated per Eq {3-1}. Overall device D showed the strongest performance in terms of Q, motional conductance, *FOM*, and *FOM* normalized by Q, while Device A exhibited the poorest. These results suggest that the quality of fabrication is influential.

While not realized at the time of collection, the shape of the peaks suggests that feedthrough is causing alteration in the magnitude of the peak response from the ideal 1D Lorentzian. However, additional aberrations were observed on some devices, as shown by the measured frequency response of Device B in Figure 5.5. This response clearly shows the presence of a spurious mode near the resonant peak, possibly due to device asymmetry. These aberrations are likely attributed to fabrication imperfections (filleting, edge roughness, and asymmetry).

Table 5.1: Measured EBL fabricated device performance. The data in bold corresponds to that depicted in Figure 5.5. Shaded cells correspond to data obtained during device operation in vacuum pressure (50-70 Torr)

	Measured Parameters				Calculated Parameters		
Device	**Current (mA)**	**Q Factor**	**Freq. (MHz)**	**$\|g_m\|$ (µA/V)**	**Power (mW)**	**FOM ($x10^{-3}$ V^{-2})**	**FOM / Q ($x10^{-6}$ V^{-2})**
A	0.703	2250	111.98	1.83	1.49	1.23	0.55
	1.303	2420	109.30	11.9	7.68	1.55	0.64
	1.103	1390	111.40	3.26	4.01	0.81	0.58
	1.411	1150	109.35	6.68	9.71	0.69	0.60
B	0.224	4240	135.87	1.84	0.110	16.72	3.95
	1.299	**5750**	**132.46**	**89.6**	**6.77**	**13.23**	**2.30**
	0.801	1350	135.63	19.9	1.45	13.72	10.17
	1.51	690	131.85	37.9	9.17	4.13	5.99
C	0.403	1730	156.02	2.32	0.316	7.34	4.24
	1.442	3440	154.95	41.9	4.67	8.97	2.61
	1.509	780	154.87	18.1	4.96	3.65	4.68
	1.604	570	154.48	13.6	6.29	2.16	3.79
D	0.699	2270	170.97	2.41	1.02	2.36	1.04
	1.7	2620	166.94	20.2	9.37	2.16	0.82
	1.713	870	169.40	10.3	7.20	1.43	1.64
	1.803	860	166.99	11.6	11.5	1.01	1.171
	= data obtained under vacuum pressure (50-70 Torr)						

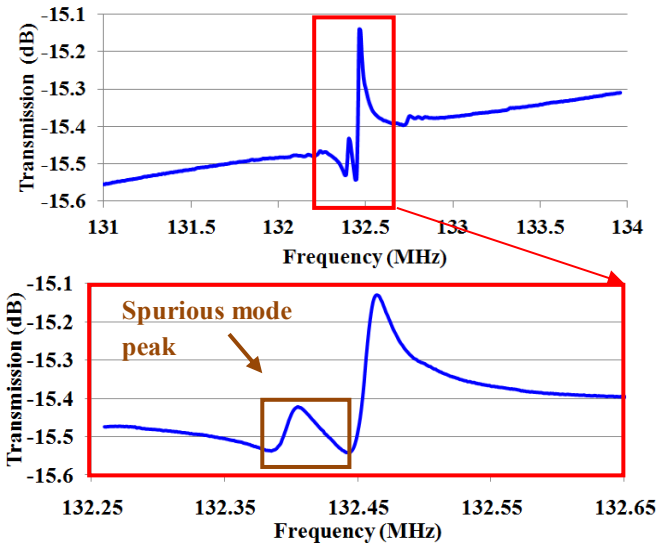

Figure 5.5: Measured frequency responses of Device B under DC bias current of 1.3 mA, directly taken from the network analyzer. (from [19])

The measured results for the FIB milled devices (Devices E-K) are shown in Table 5.2. It was considered, prior to the fabrication of the FIB milled devices that the symmetry of the arms and roughness may play a role. However based on the results from the FIB milled devices this does not appear to be a primary contributor. Surprisingly little overall improvement was seen for the devices, despite that fact that fabrication yielded high resolution patterning of the devices. Although, for these devices there was no indication of spurious modes in the measured signals, suggesting that these aberrations observed in the EBL devices were an artifact of an imperfect realized geometry.

Comparison of between Devices E and F suggests that the effect of a wider support was minimal. The close proximity of the resonant peaks of Devices E,F and I is expected since the actuator arm and proof mass dimensions are all similar. Interestingly Device H which had the largest L/W and longest actuator arms, was the top performer of the FIB milled devices. Devices J and K exhibited weak performance, but achieved the highest frequency of operation (~240 MHz) measured in this work, and presumably for all thermally actuated resonators reported. The measured signals of the lowest frequency FIB milled device (Device H) and the highest frequency device (Device J) are shown in Figure 5.6 for comparison.

Table 5.2: Measured Device Performance for devices fabricated with FIB milling. Shaded cells correspond to data obtained during device operation in vacuum pressure (50-70 Torr)

	Measured Parameters				Calculated Parameters		
Device	**Current (mA)**	***Q* Factor**	**Freq. (MHz)**	**$\|g_m\|$ (µA/V)**	**Power (mW)**	**FOM ($x10^{-3}$ V^{-2})**	**FOM / Q ($x10^{-6}$ V^{-2})**
E	0.655	1606	112.62	18.6	4.89	3.79	2.36
	0.697	1133	113.49	12.6	3.68	3.41	3.01
F	0.828	1374	110.11	32.0	6.71	4.77	3.47
	0.85	981	110.6	17.4	7.07	2.45	2.5
G	1.629	680	151.6	8.68	12.27	0.70	1.04
	1.484	618	153.4	6.69	8.7	0.77	1.24
H	0.616	1397	101.4	28.4	2.68	10.6	7.58
	0.74	987	101.35	29.3	3.48	8.42	8.53
I	1.01	1025	110.3	24.8	5.48	4.25	4.14
	1.25	830	110.12	31.1	7.16	4.34	5.23
J	1.112	473	240.63	2.29	8.33	0.27	0.58
	1.03	456	242.05	9.91	5.16	1.92	4.21
K	1.22	436	218.37	14.5	7.94	1.83	4.18
	1.18	402	218.82	11.4	7.38	1.54	3.84
	= data obtained under vacuum pressure (50-70 Torr)						

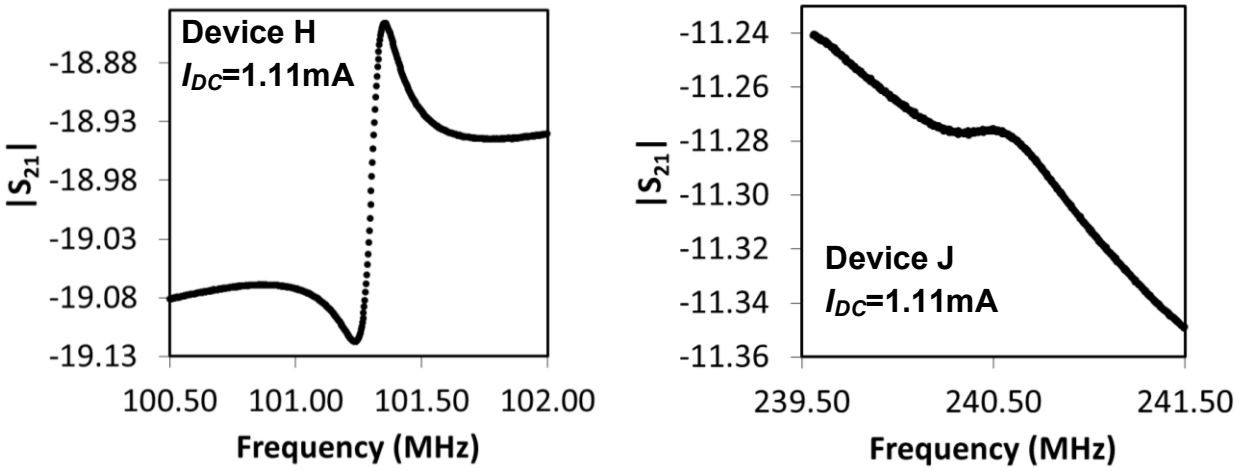

Figure 5.6: Measured $|S_{21}|$ data for Device H in Ambient Air (left) and Device J in Vacuum (50-70 Torr) (right)

One observation made was that the measured electrical resistance of the resonators was lower after testing then before testing (measurements were performed at similar current values). Table 5.3 lists the resistance values measured. The percent change observed was up to 33% lower. This is unlikely a simple reduction in the wire bond contacts during operation since the changes observed are up to several kΩ and causation likely lies with reduced device resistance after prolonged operation (possible annealing effect).

It is also apparent from the data that the device performance in air, while reduced, is not particularly dramatic, and at times near equivalent. This suggests that viscous dampening is not a limiting factor impairing performance.

Table 5.3: Measured device resistance values of FIB milled devices before and after testing

	R_{res} Before (Ω)	R_{res} After (Ω)	ΔR (Ω)	%Change
Device E	11402.60	7573.62	3828.98	-33.58%
Device F	9789.14	Not Measured	-	-
Device G	4627.20	3952.90	674.30	-14.57%
Device H	7078.49	6358.97	719.51	-10.16%
Device I	5726.94	4619.44	1107.50	-19.34%
Device J	6738.13	4869.18	1868.95	-27.74%
Device K	5317.24	4980.39	336.85	-6.34%

Similar to the previously reported larger scale devices [61], it was also observed that adjustment of the DC bias current allowed direct tuning of the operating frequency. The bias current was found to be inversely related to the operating frequency. The effect results from the temperature-dependent softening of the elastic modulus [116] as discussed in Section 3.4. Figure 5.7 shows the measured $|S_{21}|$ response for Device D at different DC bias currents, demonstrating frequency tuning capability of up to 2.1% in ambient and 3.66% in vacuum.

The performance of the devices was not entirely invariant throughout the tuning range of these devices. Figure 5.8 and Figure 5.9 show a scatter plots of the Q normalized with frequency (or $FWHM^{-1}$) vs. the ratio of DC power to total actuator volume, which serves as a gross measure of the power density within the actuators. This portrayal of performance allows easy comparison of devices with different operating frequencies and DC currents. Second-order polynomial fit lines for the EBL devices are shown to indicate that there tends to be an optimum operating condition for each device. The optimums for these devices fall in the range of 6-12 $mW/\mu m^3$. The initial increase in the $FWHM^{-1}$ with power density is likely an artifact of the signal rising above the feedthrough floor allowing better perceived Q. The drop in $FWHM^{-1}$ at higher power densities is likely due to the degradation in Q from the elevated temperature of the material. The FIB milled devices do not seem to have a clear optimum.

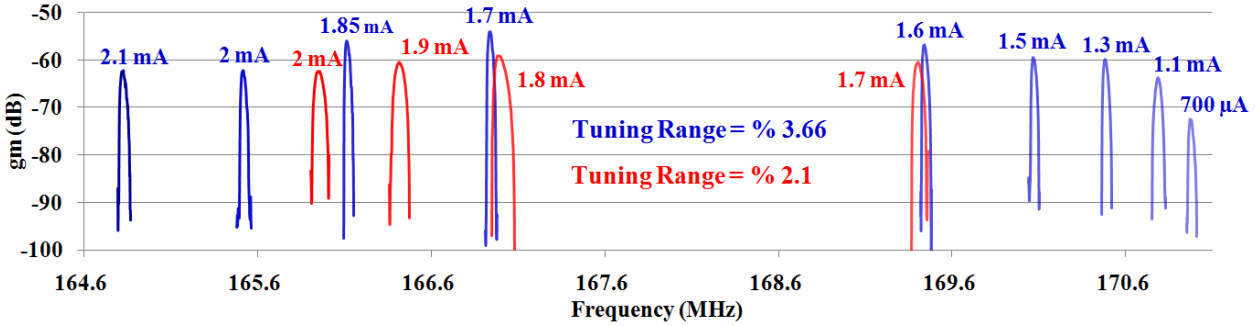

Figure 5.7: Measured frequency responses for device D with different bias currents. Red and blue plots refer to air and vacuum testing conditions respectively (from [19]**).**

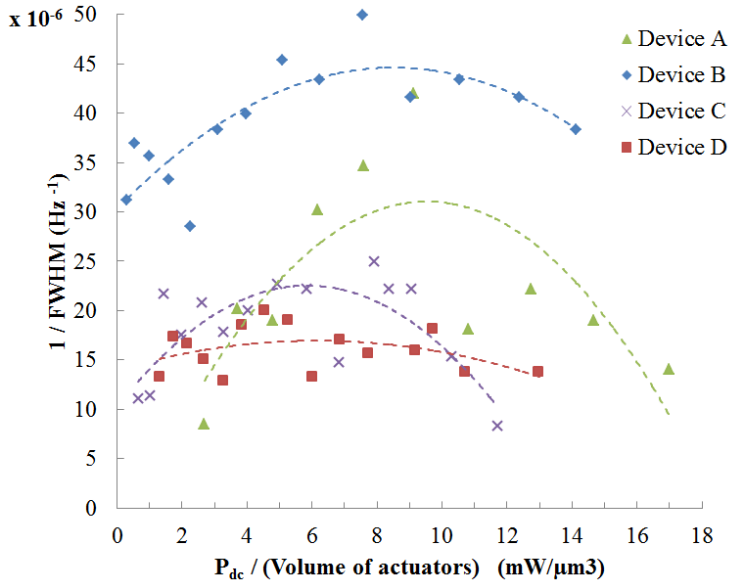

Figure 5.8: Plot of FWHM^{-1} vs. power density of actuators for each of the EBL devices under vacuum. Second order polynomial fit curves are presented for reference.

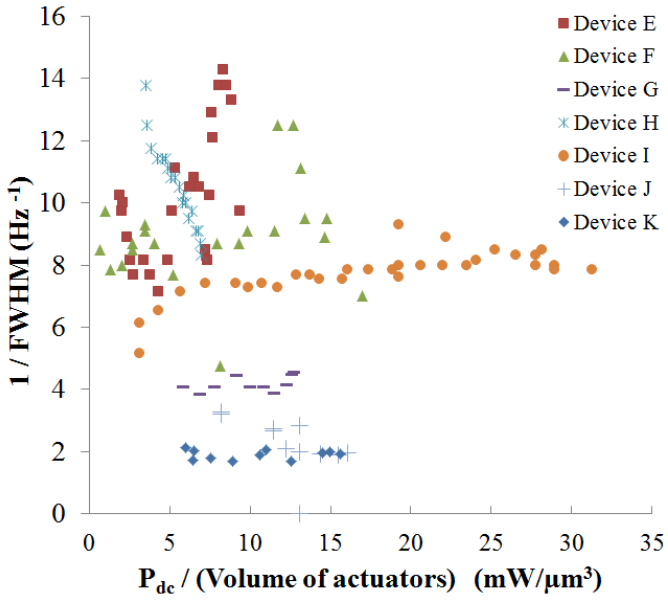

Figure 5.9: Plot of FWHM^{-1} vs. power density of actuators for each of the FIB cut devices under vacuum.

5.2.2. High-aspect ratio (h=1.5-2.0 µm) devices

The high aspect ratio devices exhibited markedly different results when compared to the submicron thickness devices. All the devices tested exhibited multiple resonant peaks in the frequency range examined (10-250 MHz). These additional peaks were most easily observed on the strongest performing devices, which similar to the submicron thickness devices discussed earlier, were the devices with smaller W (thinner actuator arms arms). An overview of the measured $|S_{21}|$ response for Device C6 is shown in Figure 5.10 as a representative example (see caption for the test conditions) showing four separate modes. These four peaks are the apparant result of driving the device electrically in two different structural resonant modes by different means. Examining the power applied to the lumped actuator resistance of the device, P_A, provides an explanation

$$P_A = \frac{V_A^2}{R_A} = \frac{(V_{ac}\sin\omega t + V_{dc})^2}{R_A} = \left[\frac{V_{ac}^2 + 2V_{dc}^2}{2R_A}\right] + \left[\frac{2V_{ac}V_{dc}\sin\omega t}{R_A}\right] - \left[\frac{V_{ac}^2\cos 2\omega t}{2R_A}\right] \quad \{5\text{-}6\}$$

where V_A is the voltage applied across the actuator arm and V_{ac} and V_{dc} are the respective magnitudes of the AC and DC components of that voltage.

The lower frequency peaks in Figure 5.10 are an artifact of excitation of the structural mode due only to the AC amplitude, a so called AC mode, which is described by the final term

of Eq {5-6}and previously reported in [117] as an alternate way to drive these devices without the need for a DC source. In this mode of operation, excitation of the resonators is occurring from the AC power at ½ the resonant frequency. The input power at this frequency is imparted to the resonator and thus creates a peak in transmission at that same frequencywhich can be recorded. The middle term of Eq {5-6} describes the conventional operation of the device which utilizes power from both the AC and DC sources (the AC+DC mode). The higher frequency peaks shown in Figure 5.10 are a result of this term and occur at the frequency of the structural mode. The initial term in {5-7} is DC power loss. The electrical resonant response of these devices was unexpected as previously reported work [61], [118] and the submicron device results in this work only indicated operation in what was presumed to be the higher frequency in-plane longitudinal mode.

Experimentally, the determination of a mode being AC only is found by first fixing the DC current and then increasing (or decreasing) the power of the network analyzer. Variation in the amplitude of the peak with respect to the input power is a non-linear response coinciding with AC amplitude excitation. Second, the response of the peak is examined in the same fashion as a conventional AC+DC peak, by fixing the power of the network analyzer and varying the applied DC current. While this may change the position of the feedthrough floor of the response, no variation is observed with regards to the amplitude. As an example, the measured AC mode excitation of Device D4 is shown in
Figure 5.11.

The network analyzer applies power to the device (measured in dBm) through the internal bias resistance of the terminals (50 Ω each). To convert into applied AC rms current values, as shown in
Figure 5.11, first the conversion from dBm to mW must be accomplished using the following formula

$$P_{mW} = 10^{\frac{P_{dBm}}{10}} \qquad \{5\text{-}8\}$$

where P_{dBm} is the AC power in units of dBm and P_{mW} is the AC power in units of mW. To translate the power applied into AC (RMS) current the following formula is applied

$$P = I_{rms}^2 (2R_{NA} + R_{dev}) \qquad \{5\text{-}9\}$$

where R_{NA} is the internal resistance of the network analyzer terminals and R_{dev} is the measured electrical resistance of the device. This formula assumes the test circuit is purely resistive and ignores any AC power dissipation through the bias resistors, since they are much larger than the resistance of the network analyzer.

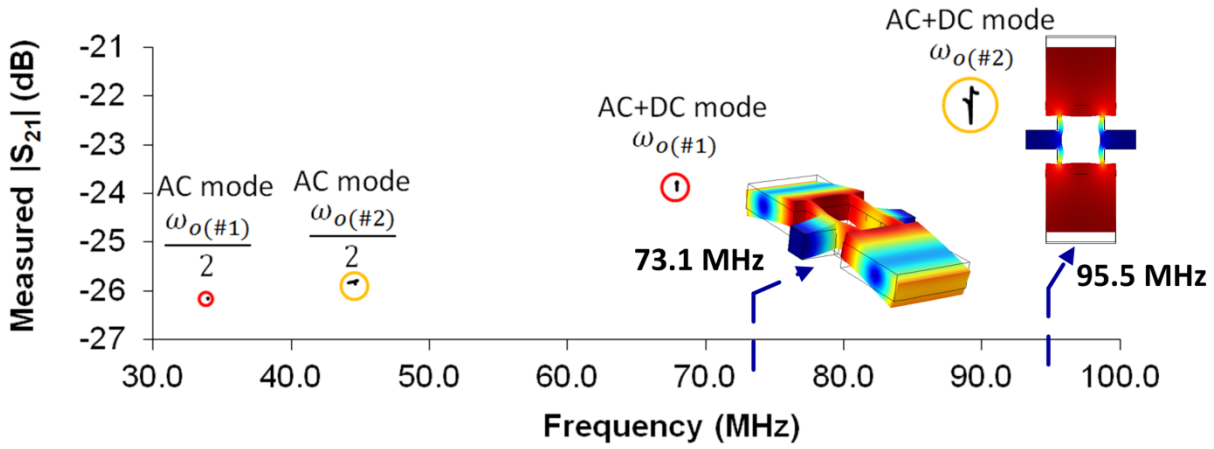

Figure 5.10: Measured $|S_{21}|$ data (vacuum) indicating position of resonant modes for Device C6. The AC mode data shown (~33.9 MHz and 44.7 MHz) was collected at +10 dBm input power with I_{DC} 1.45 mA and I_{DC} =0.747 mA respectively. The AC+DC (~67.8 MHz and ~88.9 MHz) were both collected at I_{DC} = 1.45 mA with -30 dBm input power. Inset are the two corresponding resonant structural mode shapes produced using COMSOL modal analysis (unstressed, Temp=285 K, E=130 GPa) and their resonant frequencies. The 73.1 MHz mode shown is a longitudinally symmetric flexural mode, while the 95.5MHz mode shown is the in-plane longitudinal mode. Device A3 (not shown) exhibited a similar response with $f_{o(\#1)}$=~81.6 MHz and $f_{o(\#2)}$=~105.6 MHz although the corresponding AC mode at $f_{o(\#1)}/2$ was below the noise floor.

Measured responses of each of the conventional AC+DC modes for Device C6 are shown in Figure 5.12. Using the alternate de-embedding procedure detailed in Appendix 2, the Q and g_m are listed for each. While this de-embedding method does not correct for background phase in the measurement, the data clearly indicates that self-Q enhancement, is occurring prior to self-sustained oscillation in the $\omega_{o(\#1)}$ mode. The amplitude of the $\omega_{o(\#2)}$ grows with I_{DC}, which is expected according to Eq {2-37}, however despite exhibiting stronger g_m values the self-Q enhancement effect does not occur.

Single mode operation in the in-plane longitudinal mode was based upon the presumption that this mode shape was the only one that offered the ability to both *actuate* the structural mode through AC thermal expansion of the actuator arms and *sense* the mode through the piezoresistive change occurring within them. Analysis of the structural modes using COMSOL (unstressed, room temp fixed Young's modulus), as shown in Section 3.2, suggests that the $\omega_{o(\#2)}$ mode is the in-plane longitudinal mode previously reported, and that the $\omega_{o(\#1)}$ is a longitudinally symmetric flexural mode (see inset images in Figure 5.10). One possible explanation for the actuation of the flexural mode could be attributed to slight non-uniformity of vertical profile in the actuator arms, creating a vertical AC temperature gradient.

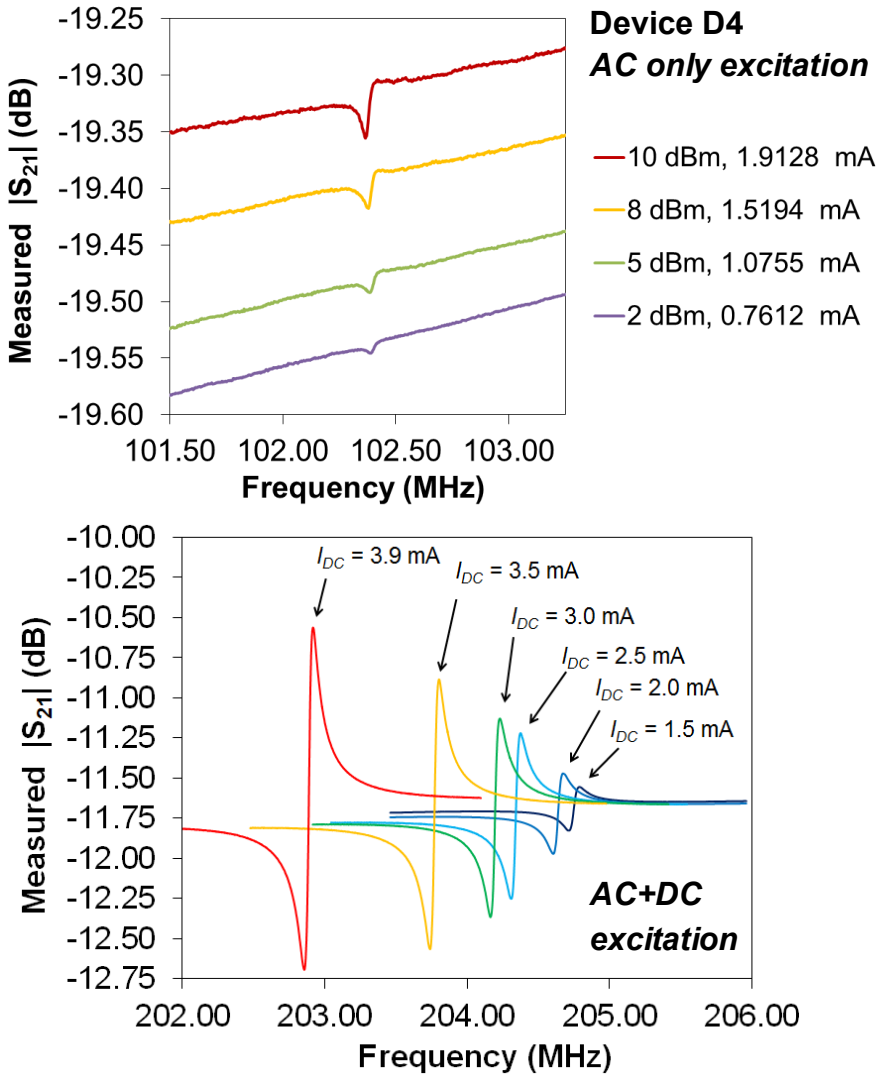

Figure 5.11: Measured responses of Device D4 (top) AC only excitation responses at I_{DC} = 1mA, 50-70 Torr (bottom) conventional AC+DC responses at DC currents listed.

As already stated, the response depicted for Device C6 in Figure 5.10 was representative of nearly all the devices tested, with only the highest frequency devices operating at> 200 MHz and a few poorer performing devices failing to display the lower $\omega_{o(\#1)}$ peak. All of the devices displayed a corresponding AC only peak for their $\omega_{o(\#2)}$ which is presumed to be the longitudinal mode. This additional peak became a useful predictive marker for detecting peaks during device testing and may have be observable for the submicron devices if it had been more actively searched for.

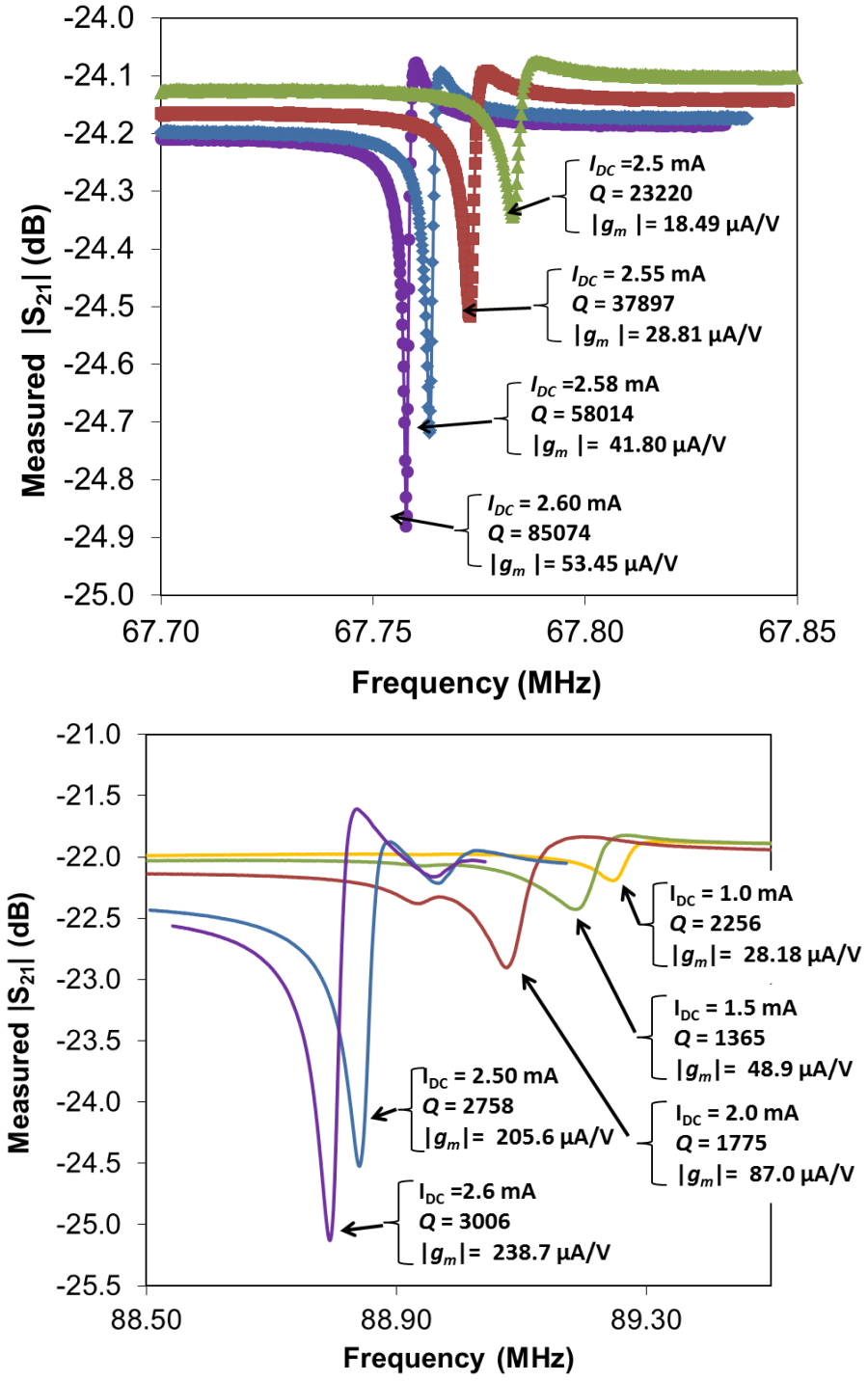

Figure 5.12: Measured $|S_{21}|$ data (ambient air) of Device C6 at $\omega_{o(\#1)}$ (Top) and $\omega_{o(\#2)}$ (Bottom) at different I_{DC} values with network analyzer power of -20 dBm.

A summary of the performance of the HAR devices at their $\omega_{o(\#2)}$ mode, presumable the longitudinal in-plane mode, is presented in Table 5.4. While less data was collected on the lower $\omega_{o(\#1)}$ mode, in part because it was so much weaker, a sampling of data for it across devices is

presented in Table 5.5. As will be discussed in the following chapter, several of the stronger performing devices exhibited self-Q enhancement and remarkably oscillation at the lower $\omega_{o(\#1)}$ mode. The strong performance of these devices under ambient conditions (see Device E6) is especially remarkable.

Table 5.4: Measured Device Performance of High-Aspect Ratio devices (h=1.5-2.0 µm) in the in-plane longitudinal mode. Shaded cells correspond to data obtained during device operation in vacuum pressure (50-70 Torr) Items in bold green were generated with both magnitude and phase information. The devices with a *operated as self-sustained oscillators .

	Measured Parameters				Calculated Parameters		
Device	**Current (mA)**	**Q Factor**	**Freq. (MHz)**	**$\|g_m\|$ (µA/V)**	**Power (mW)**	**FOM ($x10^{-3}$ V^{-2})**	**FOM / Q ($x10^{-6}$ V^{-2})**
C4	1.5	1809	206.68	39.31	6.04	6.505	3.596
	3.4	1922	205.91	203.30	31.04	6.540	3.403
	1	1554	206.73	12.98	2.69	4.832	3.110
	2.8	**1416**	**206.34**	**131.48**	**21.05**	**6.223**	**4.395**
	3.8	1489	205.09	220.04	38.77	5.674	3.818
D4	1	3557	204.7	36.7	2.63	13.938	3.919
	3.5	**3105**	**203.7**	**504**	**32.25**	**15.654**	**5.041**
	1	2318	204.85	24.4	2.63	9.267	3.998
	3.9	2556	203.1	368.75	40.05	9.206	3.602
A3*	1.0	5915	105.75	74.2	2.74	27.090	4.580
	2.1	6656	105.59	389.1	12.08	32.213	4.840
	1.2	2442	105.75	54.26	3.94	13.762	5.636
	2.4	3641	105.50	299.9	15.78	19.009	5.221
C6*	0.75	3402	89.23	24.8	1.93	12.828	3.771
	2.2	3949	88.76	154.6	16.64	9.294	2.353
	1.0	2256	89.24	28.2	3.44	82.048	36.369
	2.6	3006	88.79	238.8	23.23	10.278	3.419
B8*	0.5	12386	87.38	60.1	0.70	85.521	6.905
	1.0	19897	87.34	216.8	2.81	77.126	3.876
	1.3	12376	87.31	340.8	4.75	71.738	5.797
	1.25	5136	87.30	144.5	4.39	32.899	6.406
	1.90	5839	87.18	293.7	10.15	28.942	4.957
E6*	1.5	13980	83.32	206.8	7.19	28.767	2.058
	2.67	29253	83.10	836.9	22.78	36.743	1.256
	3.3	17652	82.81	665.94	34.79	19.140	1.084
	1.0	6116	83.37	36.7	3.20	11.487	1.878
	2.75	12916	83.14	350.7	24.16	14.514	1.124
	3.68	7358	82.47	585.9	43.27	13.541	1.840
G8	1.25	3410	92.08	45.2	4.37	10.333	3.030
	3.2	**4081**	**91.76**	**491.2**	**28.67**	**17.132**	**4.198**
	3.9	**4252**	**91.27**	**777.9**	**42.58**	**18.268**	**4.296**
	1	2869	92.12	21.3	2.80	7.619	2.656
	3.85	2194	91.49	243.8	41.50	5.876	2.678
E1	0.7	2639	105.37	4.1	1.26	3.248	1.231
	4.8	3432	105.20	248.5	59.24	4.195	1.222
	1	2583	105.43	7.7	2.57	3.002	1.162
	4.9	2742	104.38	216.7	61.78	3.508	1.279
E7	1.0	6011	87.38	-91.6	4.01	22.826	3.797
	4.0	8805	86.54	-746.3	64.21	11.623	1.320
	1.0	3815	87.44	-23.0	4.01	5.731	1.502
	4.0	**3319**	**86.88**	**-592.9**	**64.21**	**9.234**	**2.782**
	= data obtained under vacuum pressure (50-70 Torr)						

Table 5.5 : Measured Device Performance of High-Aspect Ratio devices (h=1.5-2.0 µm) at ω_o(#1) mode where self-sustained oscillation was experienced. Shaded cells correspond to data obtained during device operation in vacuum pressure (50-70 Torr). Items in bold green were generated with both magnitude and phase information. The devices with a *operated as self-sustained oscillators .

	Measured Parameters				Calculated Parameters		
Device	**Current (mA)**	***Q* Factor**	**Freq. (MHz)**	**$\|g_m\|$ (µA/V)**	**Power (mW)**	**FOM ($x10^{-3}$ V^{-2})**	**FOM / Q ($x10^{-6}$ V^{-2})**
A3*	2.1	273,000	81.5	2.75	12.08	0.228	0.00083
C6*	1.55	110,000	67.9	31.0	8.26	3.753	0.03396
	2.6	85,000	67.7	53.4	23.23	2.300	0.02704
B8*	1.0	45,600	66.3	8.54	2.81	3.038	0.06661
E6*	1.5	3665	60.7	21.6	7.19	3.0075	0.8204
E7	2.75	4527	64.57	71.6	30.35	2.3613	0.5215
	4.0	3837	64.44	134.7	64.21	2.0976	0.5466
G8	1.25	1078	76.60	8.4	4.37	1.929	1.789
	3.35	**1879**	**76.38**	**147.0**	**31.41**	**4.6804**	**2.4905**
	3.9	**5958**	**76.17**	**678.9**	**42.57**	**15.9477**	**2.675**
	3.928	**12690**	**76.12**	**1361**	**43.19**	**31.535**	**2.4848**
	1	1848	76.65	6.89	2.8	2.4644	1.3329
	4	6484	76.17	430	44.78	9.6095	1.4819
	= data obtained under vacuum pressure (50-70 Torr)						

In similar fashion as accomplished for the submicron thickness FIB cut devices, the electrical resistance of the resonators was measured by measuring the voltage across the device interconnects for an applied DC current (typically low current < 200 µA). Table 5.6 lists the resistance values measured for the HAR devices. Unlike the FIB cut devices, large positive changes in resistance were measured after sustained device operation , up to +100%, from the original value. This behavior can be of obvious detriment to device power consumption and the cause of it should be considered for further investigation.

Similar to the submicron thick devices, it is once again apparent from the data that the device performance in air, while reduced, is not particularly dramatic, and at times near equivalent to that of operation in vacuum. Again this suggests that viscous dampening is not a major limiting factor impairing performance.

The variation of device frequency with applied DC current was similar to previous devices. Figure 5.13 shows the frequency tuning of Device A3 in both Vacuum and Air. While the magnitude of the change is considerably less than that portrayed by the baseline example simulated in Section 3.4 with prestressed modal analysis, the trend shown is similar. As expected, the measured performance of the devices changed throughout the tuning range of these devices. Figure 5.13 and Figure 5.14 show the variation in the quality factor and the motional conductance for Devices A3 and E6. While the quality factor changes shown for E6

could (and likely are) artifacts of the de-embedding method used, the large trends shown are valid. While motional conductance did not appear to vary in a squared relationship to current, as Eq {2-37} suggests, it did increase strongly with current.

Table 5.6: Measured HAR device resistance values before and after testing (if applicable) (* indicates the device operated as a self-sustained oscillator)

Device	R_{res} Before (Ω)	R_{res} After (Ω)	ΔR (Ω)	% Change
A3*	2739	3718	979	+35.7%
B8*	2811	4102	1291	+45.9%
C4	2685	4208	1523	+56.7
E6*	3195	5306	2111	+66.0%
G6*	3461	6937	3476	+100.4%
G8	2799	Not measured	-	-
C6	3437	Not measured	-	-
E7	4013	Not measured	-	-
D4	2633	Not measured	-	-
E1	2570	Not measured	-	-

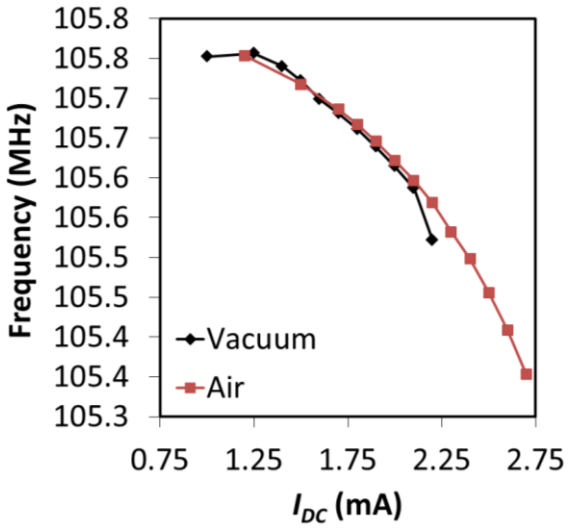

Figure 5.13: Measured Device A3 frequency tuning with DC current in vacuum and ambient air for the presumed in-plane longitudinal mode at $\omega_{o(\#2)}$ ~105 MHz

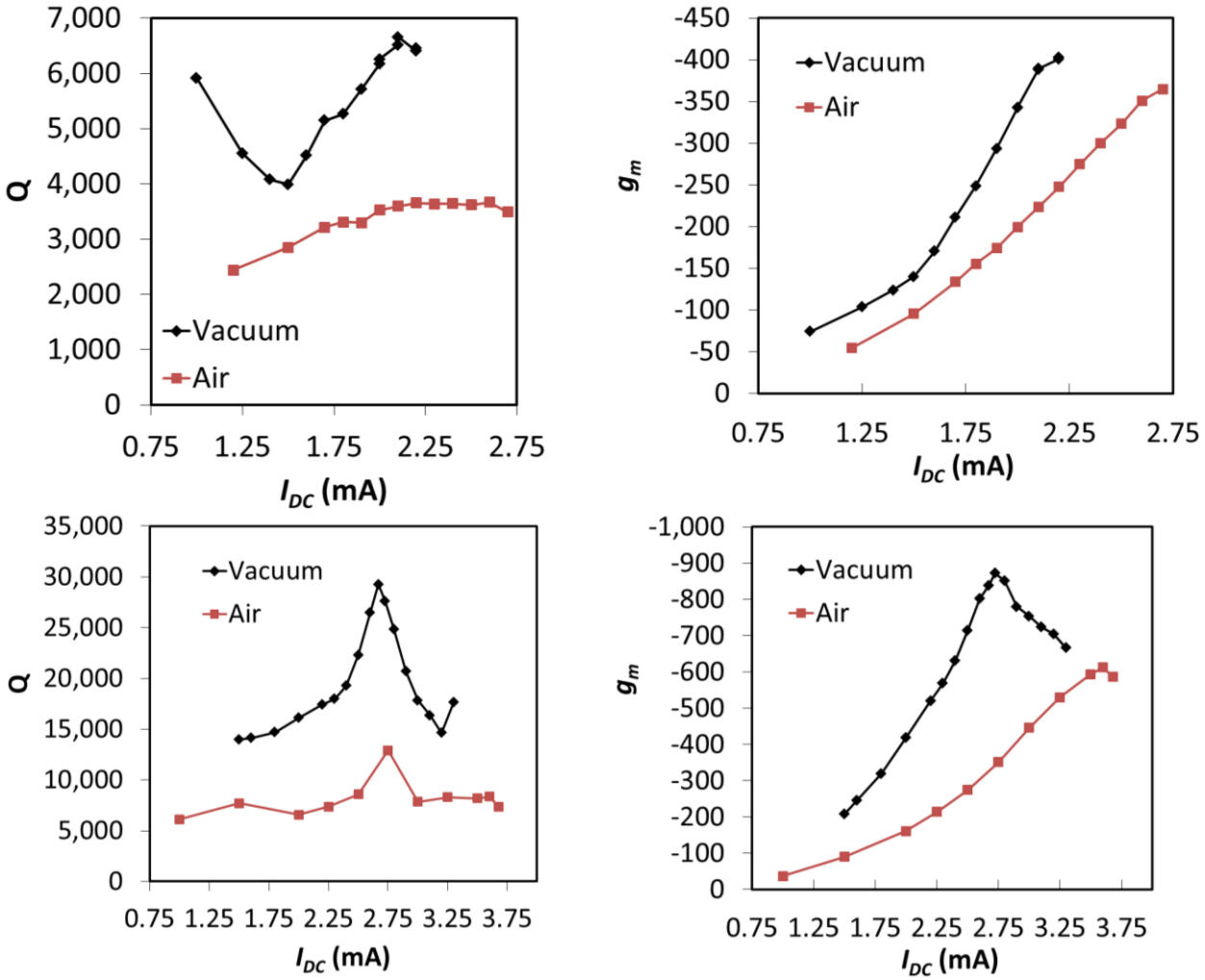

Figure 5.14: Measured quality factor and motional conductance values for Device A3 (top) and Device E6 (bottom) at their $\omega_{o(\#2)}$ frequencies, presumed to be the in-plane longitudinal mode. The gradual trends in quality factor, such as that shown in A3, should be considered with caution as they could be artificial from the alternate de-embedding method.

Before discussion turns towards the self-sustained oscillator performance, it is especially important to note that several of these devices continued to operate as resonators in the $\omega_{o(\#2)}$ mode while the device was in self-sustained oscillation in the $\omega_{o(\#1)}$ mode. This tendency made it initially difficult to tell when a device was in self-sustained oscillation during testing.

5.3. Performance Comparison to Lumped Parameter Model

Using the measured device geometry dimensions, quality factor, Q, and resonant frequency, f_o of each device in conjunction with the applied current and material parameters, estimates for the thermal capacitance C_{th} (using Eq {2-39} with a portion of the central support beam being included in the length) and motional conductance, g_m (using Eq {2-37}) can be generated. These are shown in Tables Table 5.7-Table 5.9. Simply stated, the data shows that the lumped parameter model appears to agree rather well (i.e. well within an order of magnitude) for the high

aspect ratio (h=1.6-1.9um) devices, with the exception of those data points where the *Q* is exceptionally high due to self–Q enhancement. The model fails to agree well for the submicron thick devices, being up to 2 orders of magnitude off in some cases. One source for error are the quality factor values fed into the model, which may be off significantly due the more approximate method used to measure them. However, this error source alone is not sufficient to attribute the difference between predicted and actual values of the submicron thick devices. One possibility that has been considered is that the effective thermal capacitance may be significantly higher for the thinner devices. This remains a subject for further investigation.

Table 5.7: Comparison of measured and predicted (*in italics*) motional conductance forthe submicron EBL devices

	Measured				Calculated	
Device	**Current (mA)**	***Q* Factor**	**Freq. (MHz)**	**$\|g_m\|$ (µA/V)**	**C_{th} (J/K)**	**g_m (µA/V)**
A	0.703	2250	111.98	1.83	*7.35E-13*	*139.20*
	1.303	2420	109.30	11.9		*526.96*
	1.103	1390	111.40	3.26		*212.80*
	1.411	1150	109.35	6.68		*293.51*
B	0.224	4240	135.87	1.84	*8.23E-13*	*19.60*
	1.299	5750	132.46	89.6		*916.81*
	0.801	1350	135.63	19.9		*79.93*
	1.51	690	131.85	37.9		*149.35*
C	0.403	1730	156.02	2.32	*9.94E-13*	*18.66*
	1.442	3440	154.95	41.9		*478.33*
	1.509	780	154.87	18.1		*118.83*
	1.604	570	154.48	13.6		*98.37*
D	0.699	2270	170.97	2.41	*1.67E-12*	*40.08*
	1.7	2620	166.94	20.2		*280.25*
	1.713	870	169.40	10.3		*93.12*
	1.803	860	166.99	11.6		*103.44*
	= data obtained under vacuum pressure (50-70 Torr)					

Table 5.8: Comparison of measured and predicted (*in italics*) motional conductance forthe submicron FIB cut devices

	Measured Parameters				Calculated	
Device	**Current (mA)**	***Q* Factor**	**Freq. (MHz)**	**$\|g_m\|$ (µA/V)**	**C_{th} (J/K)**	**g_m (µA/V)**
E	0.655	1606	112.62	18.6	*7.69E-13*	*82.02*
	0.697	1133	113.49	12.6		*65.02*
F	0.828	1374	110.11	32.0	*9.09E-13*	*97.01*
	0.85	981	110.6	17.4		*72.63*
G	1.629	680	151.6	8.68	*2.09E-12*	*58.48*
	1.484	618	153.4	6.69		*43.59*
H	0.616	1397	101.4	28.4	*9.81E-13*	*45.54*
	0.74	987	101.35	29.3		*54.85*
I	1.01	1025	110.3	24.8	*6.71E-13*	*145.41*
	1.25	830	110.12	31.1		*179.19*
J	1.112	473	240.63	2.29	*7.14E-13*	*35.02*
	1.03	456	242.05	9.91		*28.80*
K	1.22	436	218.37	14.5	*9.84E-13*	*31.09*
	1.18	402	218.82	11.4		*26.67*
	= data obtained under vacuum pressure (50-70 Torr)					

Table 5.9: Comparison of measured and predicted (*in italics*) motional conductance for the HAR devices

	Measured Parameters				Calculated	
Device	**Current (mA)**	***Q* Factor**	**Freq. (MHz)**	**$\|g_m\|$ (mA/V)**	**C_{th} (J/K)**	**g_m (mA/V)**
C4	1.5	1809	206.68	0.0393	*4.88E-12*	*0.0416*
	3.4	1922	205.91	0.2030		*0.2280*
	2.8	1416	206.34	0.1310		*0.1137*
	3.8	1486	205.09	0.2200		*0.2211*
D4	1	3557	204.71	0.0367	*5.16E-12*	*0.0347*
	3.5	3105	203.77	0.5049		*0.3730*
	1	2318	204.85	0.0244		*0.0226*
	3.9	2556	203.13	0.3687		*0.3824*
A3*	1.0	5915	105.75	0.0742	*4.62E-12*	*0.1247*
	2.1	6656	105.59	0.3891		*0.6197*
	1.2	2442	105.75	0.0543		*0.0741*
	2.4	3641	105.50	0.2999		*0.4432*
C6*	0.75	3402	89.23	0.0248	*6.14E-12*	*0.0360*
	2.2	3949	88.76	0.1546		*0.3616*
	1.0	2256	89.24	0.2820		*0.0424*
	2.6	3006	88.79	0.2388		*0.3843*
B8*	0.5	12386	87.38	0.0601	*6.68E-12*	*0.0547*
	1.0	19897	87.34	0.216.8		*0.3515*
	1.3	12376	87.31	0.3408		*0.3696*
	1.25	5136	87.30	0.1445		*0.1418*
	1.9	5839	87.18	0.2937		*0.3731*
E6*	1.5	13980	83.32	0.2068	*5.58E-12*	*0.6969*
	2.67	29253	83.10	0.8369		*4.6327*
	3.3	17652	82.81	0.6659		*4.2853*
	1.0	6116	83.37	0.0367		*0.1354*
	2.75	12916	83.14	0.3507		*2.1689*
	3.68	7358	82.47	0.5859		*2.2305*
E7	1.0	6011	87.38	0.0916	*6.41E-12*	*0.1106*
	4.0	8805	86.54	0.7463		*2.6180*
	1.0	3815	87.44	0.0230		*0.0702*
	4.0	3319	86.88	0.5929		*0.9830*
G8	1.25	3410	92.08	0.0452	*7.56E-12*	*0.0788*
	3.2	4081	91.76	0.4912		*0.6203*
	3.9	4252	91.27	0.7779		*0.9651*
	1	2869	92.12	0.0213		*0.0424*
	3.85	2194	91.49	0.2438		*0.4841*
E1	0.7	2639	105.37	0.0041	*8.92E-12*	*0.0142*
	4.8	3432	105.20	0.2485		*0.8682*
	1	2583	105.43	0.0077		*0.0283*
	4.9	2742	104.38	0.2167		*0.7285*
	= data obtained under vacuum pressure (50-70 Torr)					

6. Performance of Self-Sustained Thermal-Piezoresistive VHF Oscillators

As discussed in the previous chapter several of the ~2 μm thick devices exhibited strong performance thru self-Q enhancement as resonators, evidenced by the electronic transmission measurements performed. Upon further increase in the applied DC current the self-Q enhancement was sufficient to amplify the motional conductance beyond the necessary $R_A g_m = -1$ condition, described in Section 2.7.4, needed for oscillation. Section 6.1 describes the experimental setup and measurements taken to characterize the response of these devices electrically. As discussed in Chapter 5 the resonant peaks measured electrically were unlike those of devices previously reported. While electrical readout of resonant devices is generally preferred for the simplicity it offers – a necessary component for commercial viability, the possibility of unknown electrical mixing effects can complicate identification of the operating structural mode for device characterization. Section 6.2 describes the laser sensing setup used to verify the mechanical operating frequency of the structure and the results obtained for the three devices examined. During laser examination of the devices it became apparent that the laser power can affect the self-sustained electro-mechanical oscillation. Section 6.3 presents data collected on the frequency tuning and on/off control of devices using a laser explored on two devices.

6.1. Electrical Characterization

The device performance as self-sustained oscillators was initially examined electrically using the test configuration shown in Figure 6.1. This setup utilizes the same test board used for the resonator testing to which the chip is mounted and wirebonded to. The AC voltage output was recorded in the time-domain using a digital oscilloscope (Tektronix DPO 7254 or Agilent DSO7032A, DC coupled, 1MΩ input impedance). This testing was conducted in both vacuum (50-70 Torr) and ambient air conditions over an incremental range of I_{DC} values. Although not shown in Figure 6.1 a spectrum analyzer (HP8596A) was also employed periodically to verify the signal content, however capturing its response was limited to manual data collection of the amplitude and frequency. In addition, "hot swapping" the output of test board between the oscilloscope and the spectrum analyzer was not performed to prevent inadvertent damage to the measurement equipment. Thus, a concurrent measurement with both instruments was not possible.

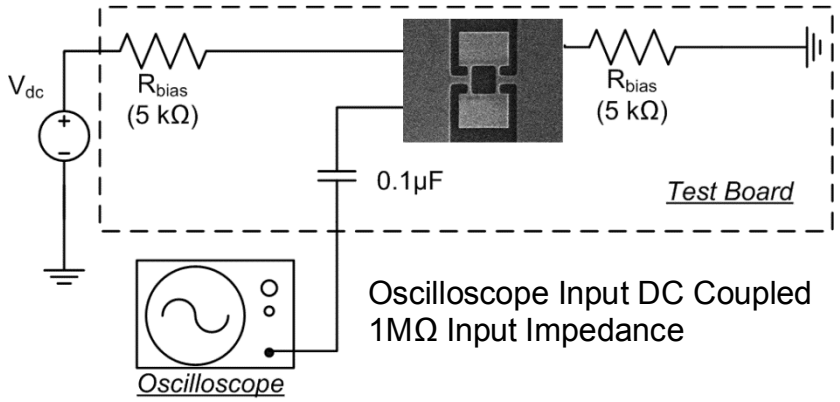

Figure 6.1: Electrical Test circuit for self-sustained oscillators

The immediate observation from the oscilloscope data, for most of the devices, was that the signal content was mixed in spectral content. The content was observed by the spectrum analyzer to be occurring at each device's lower frequency AC+DC mode (i.e. $\omega_{o(\#1)}$) observed during resonant testing in addition to its first harmonic. Thus the waveform output amplitude *Y(t)*, appeared to have the following form mathematically

$$Y(t) = y_o + a_1 \sin\left(2\pi f_o t + \phi_1\right) + a_1 \sin\left(4\pi f_o t + \phi_2\right) \qquad \{6\text{-}1\}$$

where y_o is an offset value, f_o is the primary resonant frequency, and $a_{1,2}$ and $\phi_{1,2}$ are the amplitude and phase of the primary and harmonic signals. A least-squares (LS) fit to Eq {6-1} was performed on the temporal data recorded, using the MATLAB scripts[19], at each I_{DC} value allowing for direct estimation of the percentage of signal content, by amplitude, at each frequency. Figure 6.2 shows sample traces with corresponding LS fits for different devices. The normalized sum of the squares of the residual (or the sum of square error, a.k.a SSE) metric was used as a rough metric to track the goodness of fit for each dataset. Most of the fits were well below an SSE value of 1 mV^2 with an average SSE ~0.4 mV^2, with the worst fit recorded at 1.6mV^2 . Figure 6.2c) shows a more challenging LS fit example with an SSE of 1.44mV^2. The raw peak to peak voltages were also measured for each dataset by simply measuring the difference between max and minimum signal values. The electrical performance of devices which operated as self-sustained oscillators is summarized in Table 6.1. It is important to note that the performance shown in Table 6.1 does not necessarily indicate performance at maximum possible I_{DC} as none of the devices were tested until a burnout condition was reached. This was done to ensure the possibility of further characterization using other methods.

The electrical mixing of the primary mode with its first harmonic corresponds with measurements reported by Rahafrooz and Pourkamali in [119] for similar lower frequency

[19] Specifically, the *fminsearch()* function was utilized to perform the fitting.

devices operating in their in-plane extensional mode[20]. The explanation provided for this behavior stems from the structural mode shape analysis showing the actuator arms have a combination of both flexural and extensional deformation. To quote the paper directly, "…as the resonator moves from its fully extended state to its fully compressed state in half of the resonance cycle, the narrow support beams go from a fully bent state to their normal straight shape and back into another bent state. Each time the beams flex there will be an increase in their length leading to a frequency component at twice the vibration frequency of the resonator. " [119]. They further reported that the harmonic content was dampened out as I_{DC} was increased. This observation was likely due to increased thermal expansion in the central beam reducing the available flexural deformation of the actuator arms.

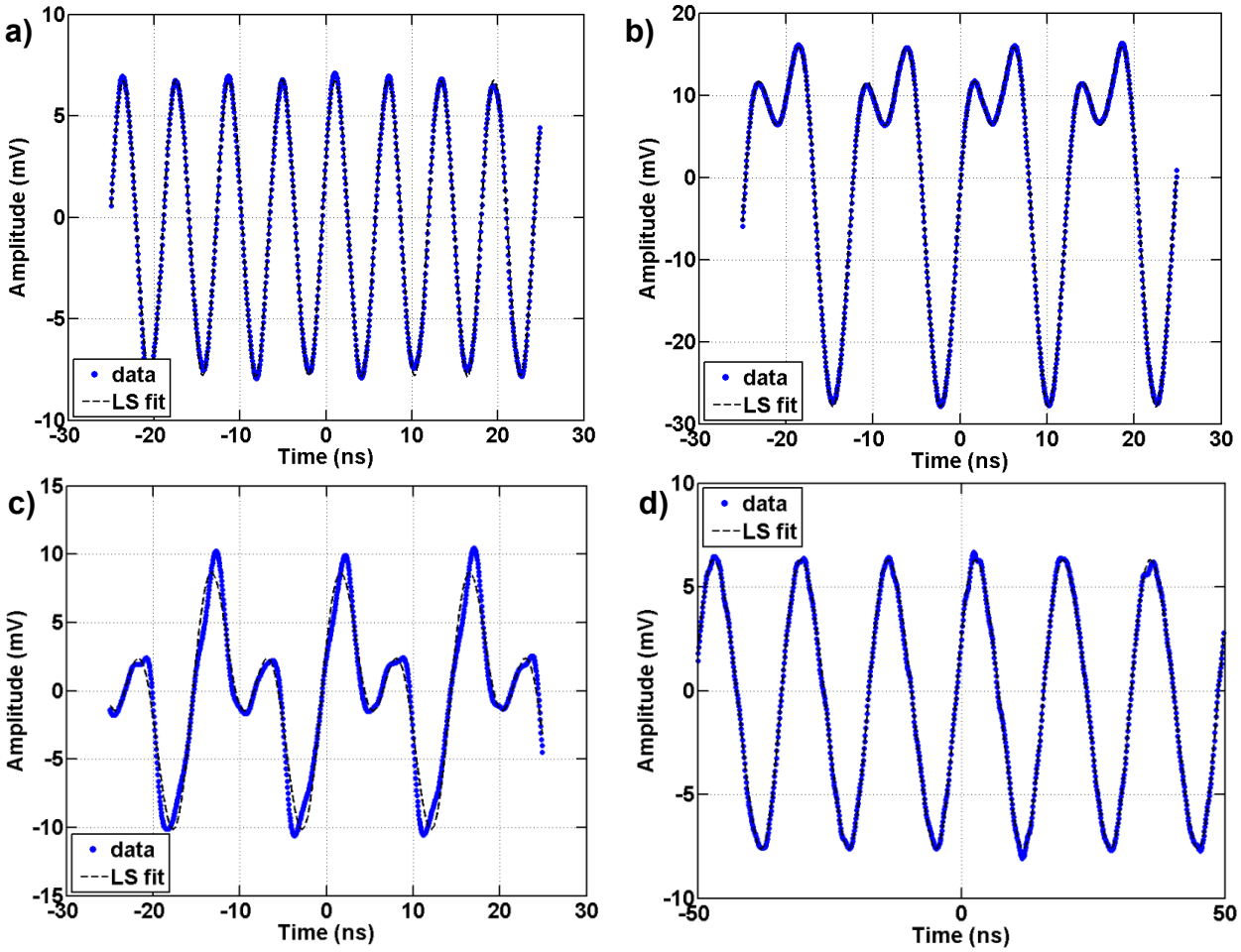

Figure 6.2: Measured oscilloscope data with least square fit (a) Device A3 in ambient air I_{DC}=3.075 mA with ~99.5% content at 162.2 MHz (b) Device A3 in ambient air I_{DC}=3.117 mA with 62.3% content at 80.83 MHz and 37.7% at 161.67 MHz (c) Device C6 I_{DC}=2.5 mA in vacuum with 50.7% at 67.19 MHz and 49.3% at 134.39 MHz (d) Device E6 I_{DC}=3.51mA in vacuum with 93.2% content at 60.35 MHz and 6.8% content at 120.71 MHz.

[20] The device geometry in this paper was called I^3-shaped because it had a third central beam in the middle to stiffen the device.

While the in-plane longitudinal mode in this work can clearly exhibit a similar non-linear flexural-extensional deformation of the actuator arms, a similar tendency is not readily apparent in the longitudinally symmetric flexural mode. This mode instead exhibits torsional deformation in the arms when actuated, as shown in Figure 6.3, which appears to be of the same frequency as that of the flexural motion. This brings into question the actual mode shape of operation. One possibility is that since the mode requires actuation from thermal expansion of the actuator arms, presumably in a longitudinal fashion, additional non-linearity is introduced into the deformation of the actuator arms. Another possibility, although less likely, is that the structure itself may have damage to the actuator arms not apparent with SEM imaging limited to top and oblique views (i.e. the bottom of the structure), which may be causing their deformation to be different than expected.

Table 6.1: Summary of Device Electrical Performance as Self-Sustained Oscillators

Device (R_{dev})	Oscillator Current (mA)	Power (mW)	Pressure*	$V_{p\text{-}pAC}$ (mV)	f_o (MHz)	$2f_o$ (MHz)	% f_o	% $2f_o$
A3☼ (2.74 kΩ)	2.45†	16.44	Vacuum	12.24	81.61	163.21	25.9	74.1
	2.6†	18.52	Vacuum	38.2	81.57	163.15	23.4	76.6
	3.075	25.89	Air	15.2	81.13	162.26	0.5	99.5
	3.117	26.61	Air	44.2	80.83	161.66	62.3	37.7
	2.5002	17.12	Vacuum	26.2	81.71	163.41	6.5	93.5
	2.7	19.96	Vacuum	36.4	81.57	163.14	8.1	91.9
C6☼ (3.44 kΩ)	1.685	9.76	Vacuum	6.5	67.86	135.73	52.7	47.3
	2.5	21.48	Vacuum	21.0	67.19	134.39	50.7	49.3
	2.7	25.06	Air	13.6	67.83	135.68	53.7	46.3
B8☼ (2.8 kΩ)	1.36	5.20	Vacuum	4.4	66.29	132.58	35.0	65.0
	2.1	12.40	Vacuum	15.2	66.11	132.23	33.0	67.0
	2.34	15.39	Air	3.4	65.98	131.96	50.0	50.0
	2.49	17.42	Air	11.3	66.08	132.17	35.0	65.0
E6 (5.3 kΩ)	3.505	65.18	Vacuum	12.0	60.33	120.66	93.42	6.5
	3.51	65.37	Vacuum	14.7	60.35	120.71	93.16	6.8
	3.52	65.86	Vacuum	5.6	60.34	120.68	97.35	2.6

* Vacuum = 50-70 Torr, Air = Ambient air conditions in lab
† This data point was part of a data series collected in vacuum prior to device testing in ambient air
☼ These devices were also examined using the optical setup described in Section 6.2

This work also differed from the previously reported dual mode oscillation [119] in that increasing I_{DC} did not select the lower mode for these devices. In fact significant variations in the device response were observed, including hysteresis in the onset and offset of self-oscillation, and changes in the frequency content during operation. While impractical to characterize for every device, these were experimentally captured more closely for Device A3. A series of experiments were conducted which sweeped the DC current applied to the device and measured it's response with the oscilloscope. It should be noted that these experiments were conducted after the device had already operated as a self-sustained oscillator in ambient air for over 2 hours just above the threshold needed for oscillation at I_{DC} = 3.08mA. In the first of these experiments

(Experiment #1) a bi-directional I_{DC} current sweep was performed first increasing and then decreasing the current. The results of this first experiment are shown in Figure 6.4. While not severe, the results indicate some non-linearity, including hysteresis, in the behavior of the signal amplitude and the LS fitted fundamental operating frequency of the device. Overall the fraction of signal content between f_o and $2f_o$ remains relatively fixed throughout the sweep with ~20% at f_o and ~80% at $2f_o$. Some of this behavior is likely due to the device resistance changing while the test is conducted, but it can also be presumed that the inherently non-linear operation of the device in a limit cycle is a significant causal factor. The overall decrease in f_o with increasing I_{DC} coincides with the resonator responses presented in Chapter 5 and is again attributed to the softening of the Young's modulus.

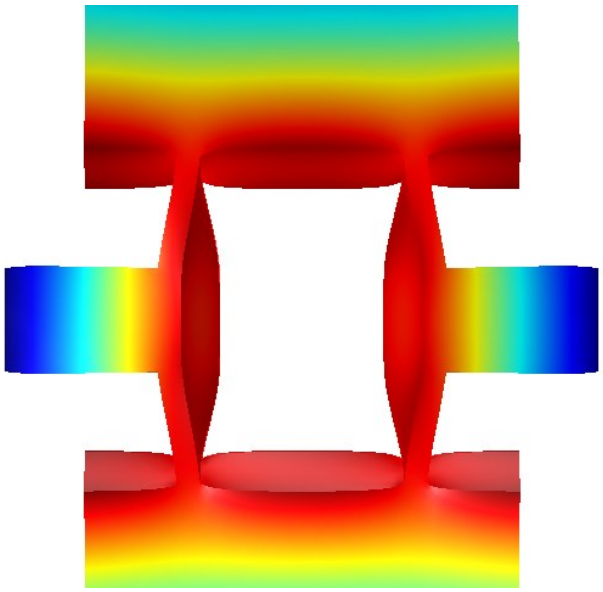

Figure 6.3: Top view of actuator arms torsional deformation in longitudinally symmetric flexural mode (deformation amplified for visualization).

After testing, the DC current was decreased to zero and the device was removed from vacuum for conduct of the second experiment. Experiment #2 consisted of simply increasing the current in ambient air conditions, with the results shown in Figure 6.5. When the applied DC voltage was increased to reach the initial DC current condition needed for self-sustained oscillation a drop in the DC current was observed at the start of oscillation (see Figure 6.5a). It was also apparent that the amplitude was significantly stronger at oscillation onset – near the V_{pp} value observed at the maximum I_{DC} tested under vacuum. As the DC current was varied there was significant change observed in the frequency content as shown in Figure 6.5c), with the content switching from $2f_o$ dominant to f_o dominant.

The current was decreased after the sweep was conducted and the test board was once again place under vacuum (50-70 Torr) for conduct of the third experiment. An increasing DC current sweep was performed once again under this condition to observe changes in response.

The results are shown in Figure 6.6 with the Experiment #1 results overlayed in gray. The amplitude and frequency varied in a similar fashion as Experiment #1 however the spectral content was significantly cleaner with the signal maintaining ~92% content at $2f_o$ throughout the sweep.

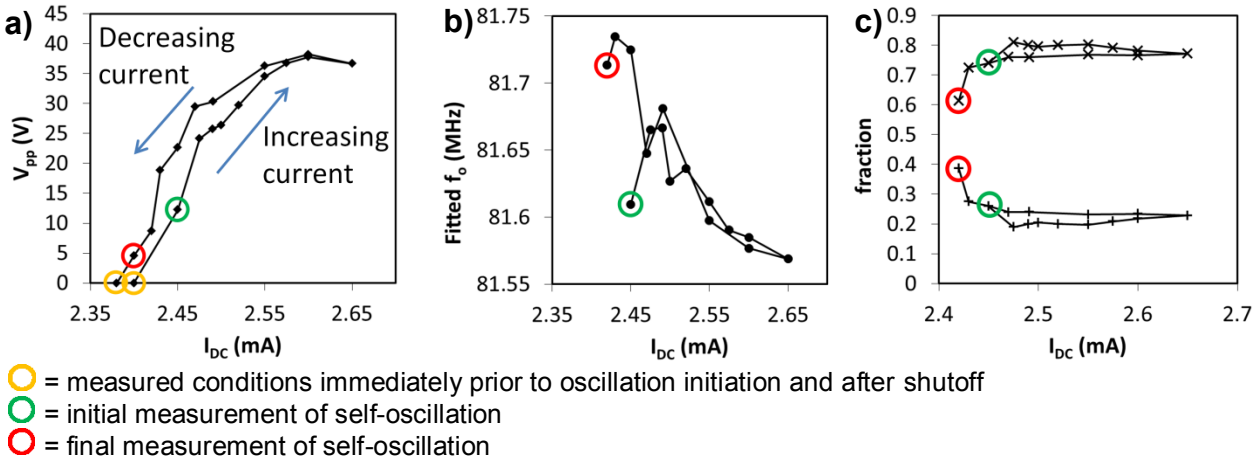

Figure 6.4: Device A3 self-sustained oscillation experiment #1 results- increasing and decreasing I_{DC} sweep conducted at 50-70 Torr. (a) AC output signal peak to peak voltage variation with I_{DC} (b) LS fitted fundamental oscillating frequency (f_o) variation with I_{DC} (c) fractional content by LS fitted amplitude at f_o ["+" ~81 MHz] and $2f_o$ ["x" ~162 MHz] variation with with I_{DC}. Device oscillated 65 min continuously during testing.

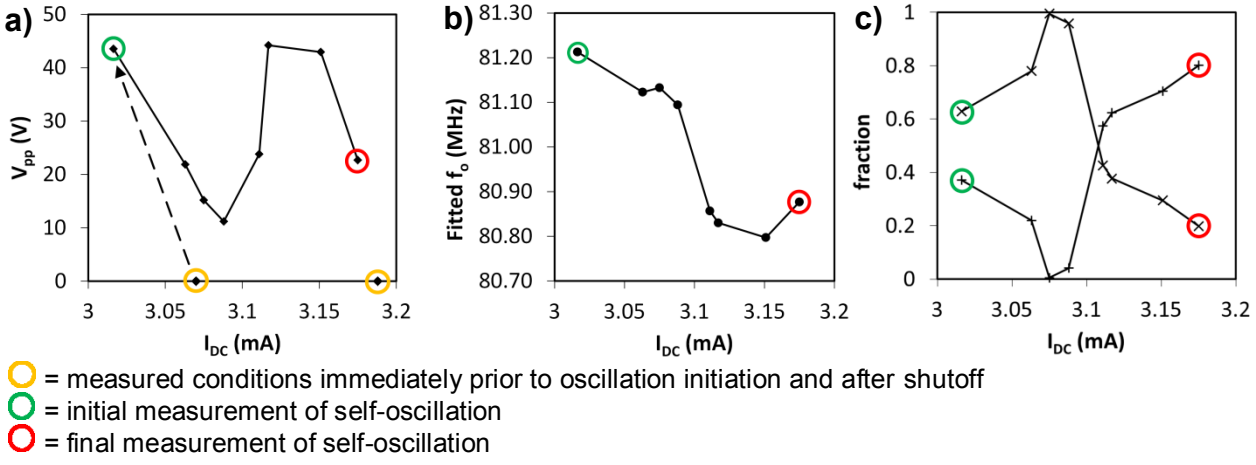

Figure 6.5: Device A3 self-sustained oscillation experiment #2 results - increasing I_{DC} sweep conducted at ambient air conditions. Oscillation shutoff occurred between I_{DC} = 3.175-3.18 mA. (a) AC output signal peak to peak voltage variation with I_{DC} (b) LS fitted fundamental oscillating frequency (f_o) variation with I_{DC} (c) fractional content by LS fitted amplitude at f_o ["+" ~81 MHz] and 2 f_o ["x" ~162 MHz] variation with with I_{DC}. Device oscillated 31 min continuously during testing.

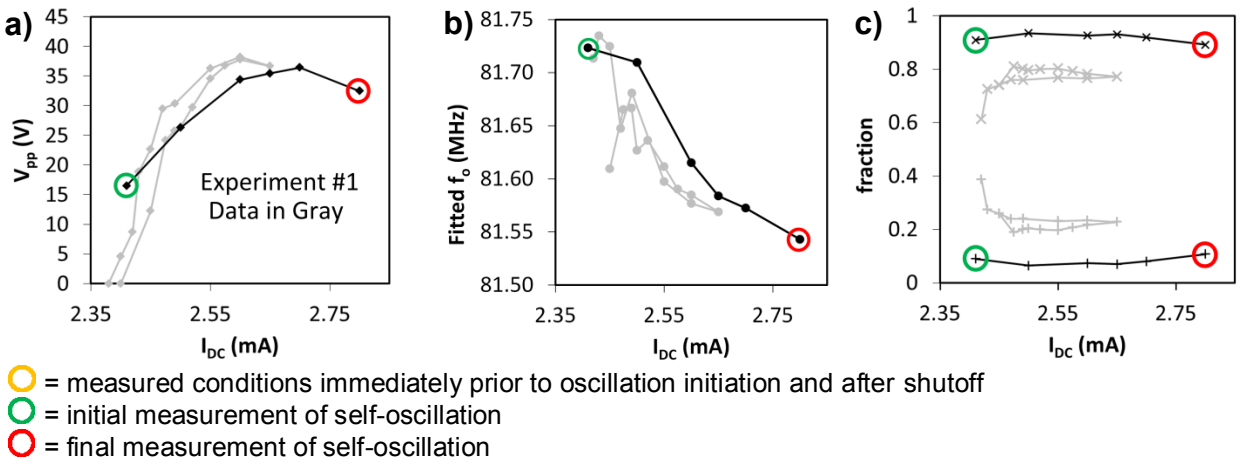

Figure 6.6: Device A3 self-sustained oscillation experiment #3 results - increasing I_{DC} sweep conducted at 50-70 Torr - with Experiment #1 results shown in gray (a) AC output signal peak to peak voltage variation with I_{DC} (b) LS fitted fundamental oscillating frequency (f_o) variation with I_{DC} (c) fractional content by LS fitted amplitude at f_o ["+" ~81 MHz] and 2 f_o ["x" ~162 MHz] variation with with I_{DC}. Device oscillated 15 min continuously during testing.

While the results for Device A3 are insufficient alone to conclude definitive behavioral variations of the devices collectively, this device clearly demonstrates that device operation can vary significantly over time and is dependent in part upon environmental conditions. The behavior of device A3 suggests that sustained operation under ambient conditions can alter the device response, in this case for the better, with a cleaner signal being produced after operation in ambient air at elevated I_{DC} values above oscillation threshold.

One final qualitative observation about these devices is that they display robustness in their ability to display self-Q enhancement and self-sustained oscillation despite significant physical degradation of the structure.
Figure 6.7 shows one example of performance under such degredation (Device A8) encountered during the device characterization efforts accomplished for this work. The actuator arms for this device were clearly damaged during the DRIE process. While the performance in the devices intended longitudinal mode was degraded, the device did exhibit self-Q enhancement and self-sustained oscillation (see
Figure 6.7 caption) albeit at a much lower frequency mode ~f_o =16 MHz. This result is significant because it further highlights that this phenomena is flexible to apply to different structural modes. Operation in alternate structural modes is potentially useful since it offers a designer a way to trade performance for device footprint (per unit cost), which may be useful for applications where the later is essential. Furthermore these devices also appear reasonably robust in their sustained ability to operate. While lifetime testing was not pursued in this work all these devices operated over the course of several hours without showing signs of failure. In the case of Device A3, the device operated during characterization efforts for over ~4.5hrs, the majority in ambient conditions, with improvement of spectral content rather than degradation.

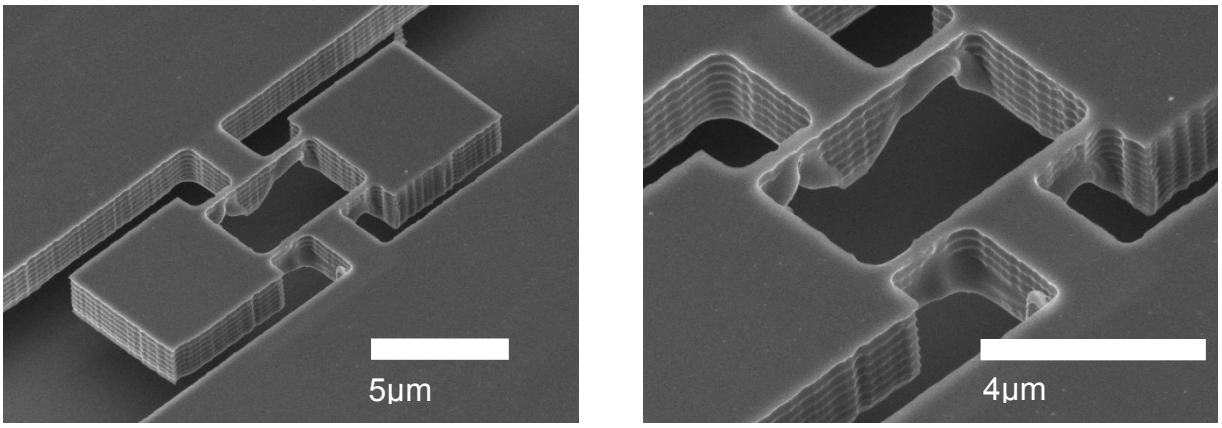

Figure 6.7: SEM Images (left – 6,000x, 45° tilt, right - 12,500x 45° tilt) of Device A8 which despite significant damage to the actuator arms during processing exhibited self-Q enhancement and operated as a self-sustained oscillator at a lower order structural mode (peak performance measured at *fo* = 16 MHz, Vp-p = 7.45 mV, I_{DC} = 2.075 mA, P_{DC} =16.1 mW)

As previously discussed, electrical testing alone is insufficient for definitively determining the mechanical vibration mode of the structure. The next section describes the active optical test setup and testing performed to address this challenge.

6.2. Optical Sensing of Electrically Driven Self-Sustained Oscillations

As explained in Chapter 5, the devices in this work operated as resonators at two different frequencies, with self-sustained oscillation being observed through one at higher I_{DC} values. While it is unlikely such sharp spectral response could be due to anything other than mechanical resonance, it is possible for mixing of electrical signals to confuse the interpretation of the electrical readout. To aid in this end a laser sensing testbed was employed while electrically operating the device in ambient air to identify the frequency of mechanical oscillation and, if possible, measure its Q as an oscillator. This testbed was developed by the Bunch Lab at CU Boulder for the excitation and sensing of graphene thin films (see [120]), however for this work only the sensing portion of the testbed was used[21].

Figure 6.8 graphically depicts this testbed which uses a HeNe laser, which is positioned manually, to illuminate the device under test (spot size ~1 μm). The incident laser light reflects off of the underlying Si substrate and the device itself and the return is captured with a photodiode. Mechanical motion of the device structure modulates the intensity of the laser return at the frequency of self-sustained oscillation. A quarter wave plate is used to ensure that the outgoing and return laser beams have orthogonal linear polarization. The relative orientation of the two beams allows the 2nd polarized beam splitter (i.e. the one that feeds the photodiode) to transmit the majority of the outgoing beam to the test sample and directs the majority of the return signal to the photodiode. The electrical output of the photodiode is then captured by a spectrum analyzer (Agilent 9320B) equipped with a custom LabVIEW data acquisition software interface which records the data. One benefit of utilizing only the sensing portion of this optical testbed was that enabled utilizing the highest resolution bandwidth setting, 10 Hz, available on the spectrum analyzer. The electrical output from the oscilloscope was simultaneously captured, but independently triggered, during testing to offer a comparison between readouts.

When used for the detection of vibrating suspended graphene membranes, the reflected laser interference between the vibrating membrane, which is highly transmissive , and the underlying substrate creates modulation of the return signal. The devices in this work are silicon which is less transmissive in the visible and over 1 μm thick. Thus interferometry in this fashion is thus less likely. There are two more probable ways mechanical motion would modulate the reflected laser light for these silicon structures. The first mechanism potentially applies to both in-plane and out of plane mode shapes, and that is that when the beam is positioned at an edge of the vibrating structure the light reflected off of the substrate around the structure can be subtly chopped by the motion of the plate. The second possible way, which only applies to a structure vibrating in an out-of-plane mode, is that the light reflected off of the structure can be steered away from the return path by its flexural motion. Since these mechanisms both seem possible

[21] Optical excitation of the devices in this work using additional separate modulated blue laser was also successfully demonstrated by illuminating individual actuator arms. However, this method only allows excitation of lower frequency asymmetric modes.

for these devices, determining the mode shape for a structure solely from the return amplitude is challenging. To further complicate matters the structural geometry surrounding the devices can potentially affect the return amplitude. For example, the gap spacing between the plates and the adjacent bonding pads is <1um and thus less light may be reflected off of the substrate in this area, reducing the potential signal of the first mechanism of modulation.

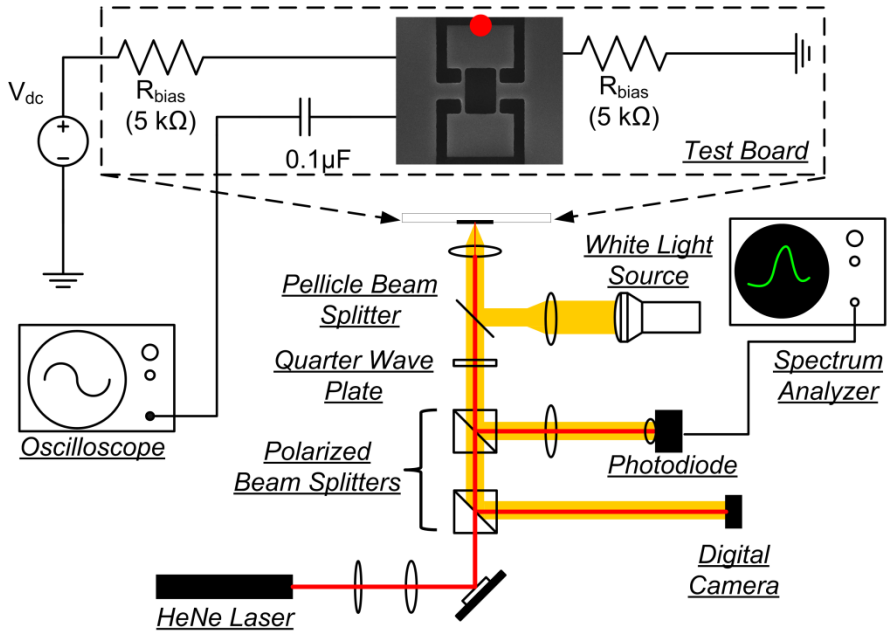

Figure 6.8: Sensing testbed (ambient air) used for sensing the spectral response of the structural mode while measuring electrical output of the device in self-sustained oscillation. Position of laser shown on inset SEM image.

Three devices, A3, C6, and B8 were each examined using this system at I_{DC} values just above the threshold needed for self-oscillation in ambient air conditions. The goal of this testing was to simply detect the mechanical vibration of each device while being electrically driven in self-sustained oscillation and identify the frequency of the vibration. Different laser positions on the devices were examined to verify symmetry of the mechanical vibratory response. These included top and bottom edges of the upper and lower plates respectively and additional side edge positions. Before data was recorded the noise peaks inherent to the system were first identified to ensure the device response and not a spurious peak was being recorded.

Since the photodiode measures optical power, its output (I or V) is proportional to the square of the amplitude of the oscillators' motion. Applying the 1D MSD model presented earlier, squaring Eq {2-10} yields

$$|x_o(\omega)|^2 = \frac{(F_o/M)^2}{({\omega_o}^2 - \omega^2)^2 + 4\omega^2\beta^2} \qquad \{6\text{-}2\}$$

which is equivalent to a Lorentzian lineshape. The output from the photodiode as measured by the spectrum analyzer can thus be fitted using a least squares approach to this function to extract

ω_o, β, and the peak amplitude. These parameters can in turn be used to calculate the loaded Q and FWHM of the oscillator.

The testing was successful in detecting vibrational modes of the devices, with results indicating that all three devices exhibited mechanical oscillation at their respective $\omega_{o(\#1)}$ resonant modes. Furthermore the frequency of oscillation corresponded well (<0.1 MHz difference) with the fitted f_o generated by LS fitting of the dual sine wave to the electrical signal. Strongest return signals were measured at the edges of the bottom and top plates with smaller amplitude signals detectable by positioning the laser at a side edge of a plate. Qualitatively speaking this suggests longitudinal symmetry of the vibrational mode, however as already discussed is not sufficient evidence to determine mode shape. A graphical summary of the results for each device is shown in Figure 6.9.

Using the fitted Lorentzian profiles in Figure 6.9, it is possible to generate estimates for the loaded quality factor of the devices. However the sampling of the peaks using the spectrum analyzer is not ideal with typically only 4-5 samples within the FWHM of the peak. In addition, the possibility for frequency drifting of the spectral response during a data collection sweep exists which can degrade the data recorded. Nevertheless, many of the spectral responses collected had 1D Lorentzian fits that appeared reasonable and ensemble statistics for each devices can be used as a rough estimate for reference in future device experimentation. These results are presented in Table 6.2.

It became apparent during testing that the laser power utilized had an effect on device operation. This was explored further as discussed in the following section.

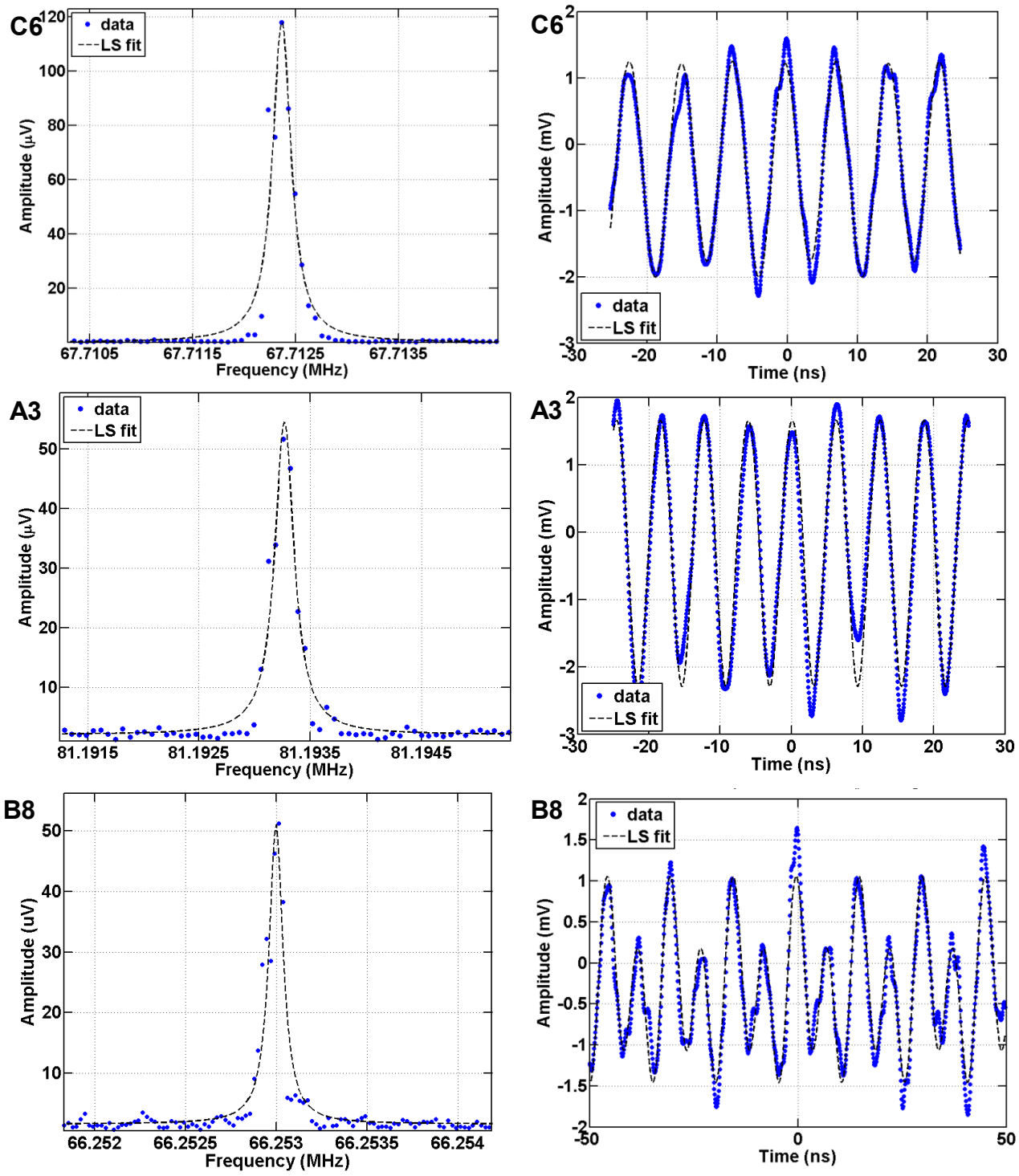

Figure 6.9: Measured photodiode output from spectrum analyzer with 1D Lorentzian fit and corresponding electrical output recorded by the oscilloscope (top) Device C6 at I_{DC} = 2.70 mA (w/ laser), 2.75 mA (w/o laser), P_{LASER}=1.21 mW, $V_{p\text{-}p}$=3.9 mV, f_o (7%)=67.8 MHz, $2f_o$(93%)=135.6 MHz (Middle) Device A3 at I_{DC} =3.13 mA (w/laser), 3.079 mA (w/o laser) , P_{LASER}=1.26 mW, $V_{p\text{-}p}$=4.75mV f_o (14%)=81.1 MHz, $2f_o$(86%)=162.2(Bottom) Device B8 at I_{DC} =2.36 mA (w/laser), 3.34 mA (w/o laser) , P_{LASER}=0.58 mW, $V_{p\text{-}p}$=3.49 mV, f_o (34%)=66. 2 MHz, $2f_o$(66%)=132.4 MHz. The HeNe laser was positioned at the edge of the top plate for each device.

Table 6.2: Averaged Loaded Quality Factor values (with standard deviation) of devices operating as self-sustained oscillators. Note: ***These values are presented to provide a general sense of the order of magnitude of the loaded Q.*** **The standard deviation in the measurement indicates they are not precise enough accurately portray individual device performance**

Device [n=# of samples]	I_{DC} (mA)*	P_{LASER} (mW) †	Average Loaded $\overline{Q}$	Std Deviation $\pm\sigma_Q$
A3☼ [n=10]	3.08	0.58 – 5.94	425,000	250,000
C6 [n=3]	2.70	1.21	260,000	52,300
B8 [n=5]	2.70	0.58	845,000	323,000

*DC device current listed is with laser off
†Additional room lighting illumination was present during measurement
☼ Data points are from laser powers spanning this range

6.3. Optical Tuning and Control of Electrically Driven Self-Sustained Oscillation

Effects of the HeNe laser power on the device response when operating as a self-sustained oscillator were examined experimentally on Devices A3 and B8 using the same setup described in Figure 6.8. The experiment conduct consisted of fixing the applied DC bias voltage to the devices above the threshold needed to initiate self-sustained oscillation. Once again the applied DC current was kept low for throughout these experiments to minimize risk of device burnout. The HeNe sensing laser was positioned at the center of either the top or bottom outer plate edge (edge with greater signal amplitude was chosen). The electrical and mechanical (optical) responses were then measured as the laser power was incrementally increased using a filter wheel. The applied laser power for each filter wheel setting was measured after the experiment using a calibrated photodetector.

The first two immediate observations made for both devices during experimentation was that as the laser power increased both the optically measured mechanical frequency of oscillation and the DC current increased. These results are shown graphically for both devices in Figure 6.10. Since the electrical signal was small (< 5 $V_{p\text{-}p}$) this trend in frequency was not immediately apparent from the oscilloscope. However, least squares fitting of the electrical data after testing suggests though that the electrical signal correspondingly increased as well. The third significant observation was that the both the electrical signal and the self-sustained mechanical oscillation shutoff after a certain threshold in laser power was reached. In Device A3 the electrical and mechanical shutoff of the oscillator were apparently simultaneous, while for Device B8 the electrical signal shutoff prior to the mechanical response. As shown in Figure 6.11 the signal

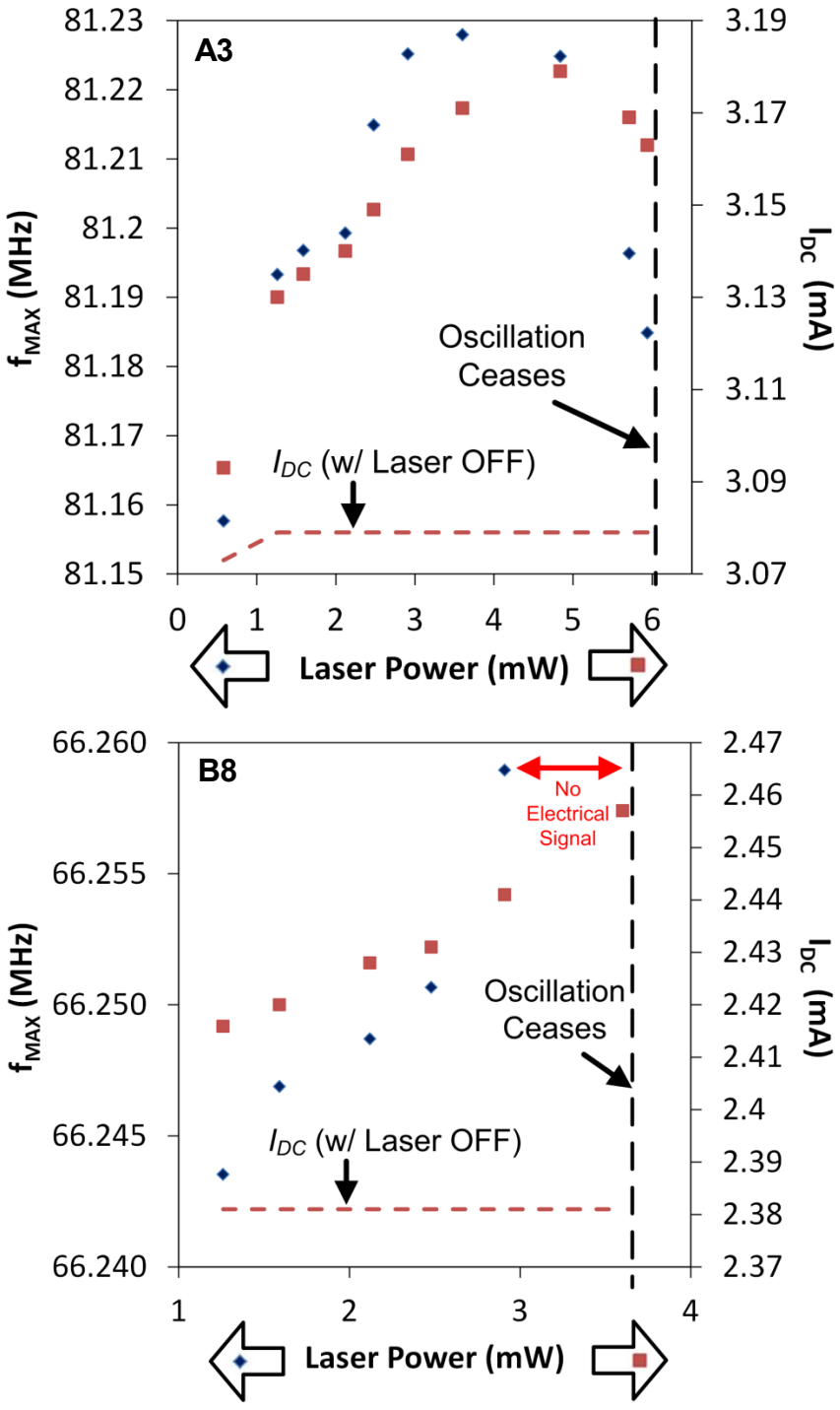

Figure 6.10: Effect of HeNe Laser Power on mechanical oscillation frequency and DC current (top) Device A3 – shutoff of mechanical oscillation coincided with electrical signal shutoff (bottom) Device B8 – electrical signal shutoff occurred prior to mechanical self-sustained oscillation shutoff. After shutoff, self-sustained oscillation was observed again upon lowering the laser power below the shutoff threshold.

strength (and quality) appeared to degrade in a linear fashion as the laser power was increased until the shutoff threshold.

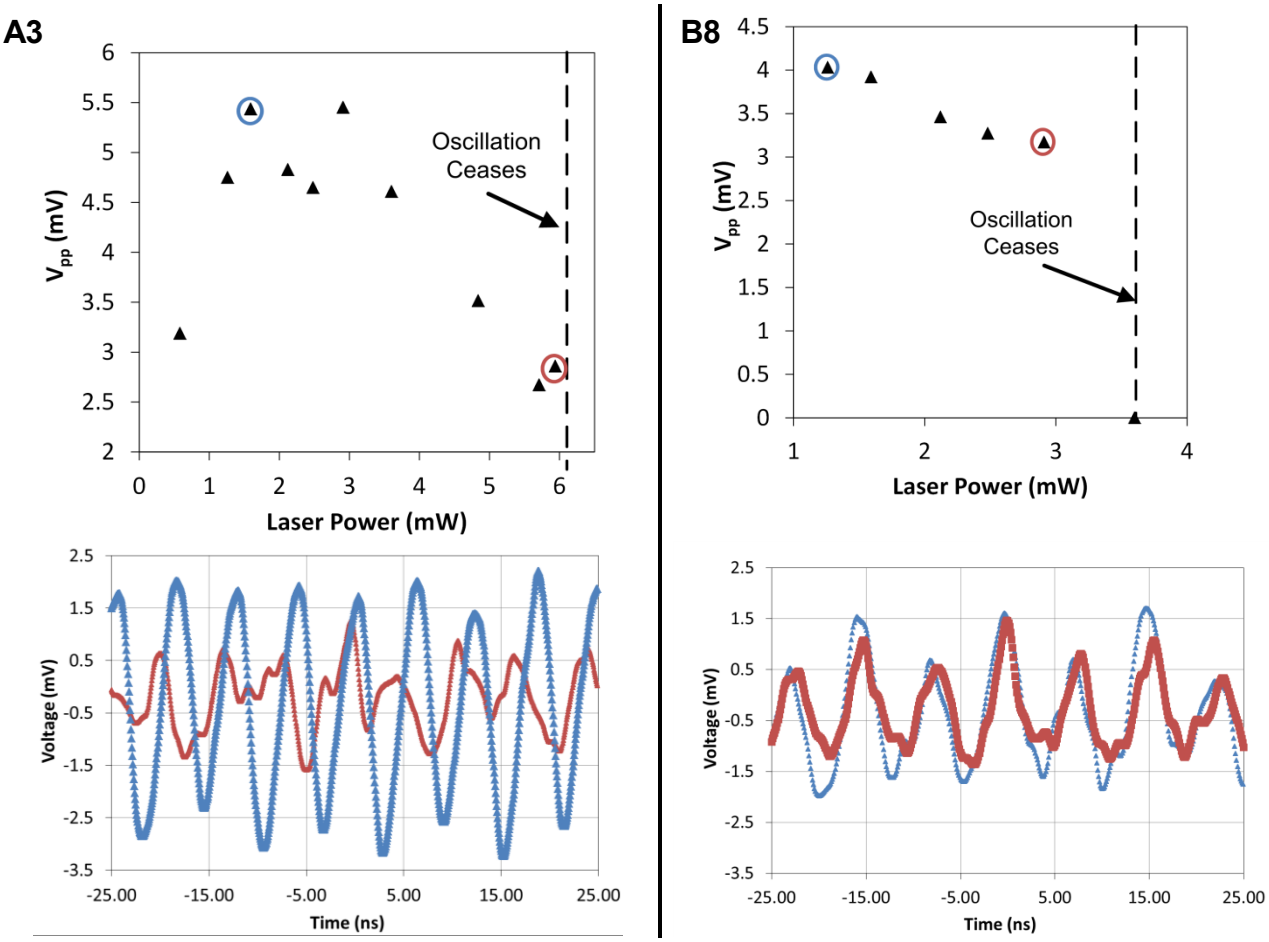

Figure 6.11: Variation in maximum $V_{p\text{-}p}$ with HeNe laser power as measured by oscilloscope for Devices A3 (left) and B8 (right). Corresponding measured signals are shown for high (red circle) and low (blue circle) laser powers.

One possible explanation for the device behavior observed and measured under increasing laser power can be found by considering the device as a self-oscillating photoresistor. Under this model, the laser light causes photoexcitation and or additional thermal excitation of electrons from the valence to the conduction band of the semiconductor. Regardless of which mechanism is occurring, the result is the same – the resistivity of the material in the area of illumination decreases. This causes an overall decrease of device resistance. The equivalent circuit for the device using this model is shown in Figure 6.12. Per Figure 6.12, equations can be derived for the DC current, I_{DC}, and the device power, P_{dev}, under un-illuminated conditions ("dark" for simplicity) as shown below

$$V_{dev(dark)} = \left(\frac{R_{dev(dark)}}{\left(2R_{bias} + R_{dev(dark)}\right)} \right) V_{DC} \quad \{6\text{-}3\}$$

$$I_{DC(dark)} = \frac{V_{DC}}{\left(2R_{bias} + R_{dev(dark)}\right)} \quad \{6\text{-}4\}$$

$$P_{dev(dark)} = I_{DC}{}^2 R_{dev(dark)} = \frac{V_{DC}{}^2 R_{dev(dark)}}{(2R_{bias} + R_{dev(dark)})^2} \quad \{6\text{-}5\}$$

Similarly for illuminated conditions (simply labeled "light") the following apply

$$V_{dev(light)} = \left(\frac{R_{dev(dark)} - \Delta R}{\left(2R_{bias} + (R_{dev(dark)} \text{-} \Delta R)\right)} \right) V_{DC} \quad \{6\text{-}6\}$$

$$I_{DC(light)} = \frac{V_{DC}}{\left(2R_{bias} + (R_{dev(dark)} \text{-} \Delta R)\right)} \quad \{6\text{-}7\}$$

$$P_{dev(light)} = I_{DC}{}^2 (R_{dev(dark)} - \Delta R) = \frac{V_{DC}{}^2 (R_{dev(dark)} - \Delta R)}{(2R_{bias} + (R_{dev(dark)} - \Delta R))^2} \quad \{6\text{-}8\}$$

where ΔR is the difference in device resistance between the two conditions.

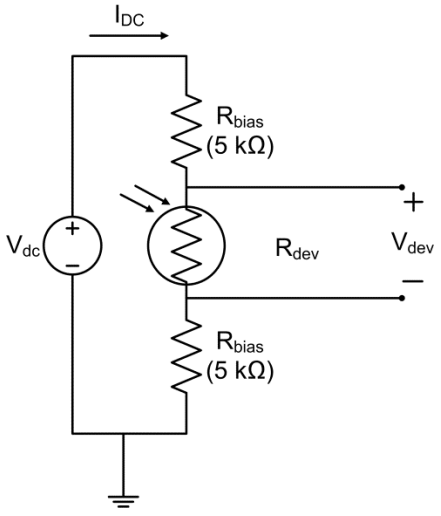

Figure 6.12: Equivalent circuit model for device operating as a self-oscillating photoresistor. The <u>un-illuminated</u> device resistance was ~2.7kΩ and 2.8 kΩ for Device A3 and B8 respectively.

Since under illumination $P_{dev(dark)} > P_{dev(light)}$ per Eqs {6-5} and {6-8}, the resistive power dissipated by the device decreases which subsequently leads to a decrease in device temperature.

The decrease in temperature stiffens the elastic modulus of the materials and the frequency of resonance increases. This process is outlined graphically in Figure 6.13. It is important to note that the area of illumination for this effect to occur can be anywhere on the device or on surrounding silicon that is connected in series to the devices. In the case of Devices A3 and B8, the laser was positioned on the edge of one of the proof masses of the resonant structure, so it is likely that both the series resistance, R_s, and actuator resistance, R_A, as indicated in Figure 2.12 are experiencing ΔR.

The reason for shutoff of the self-sustained oscillation at high laser power for these devices remains unclear, although there are two possible explanations. The first is that the increase in illumination is causing excitation of free carriers into the conduction band which in turn reduces the piezoresistive coefficient. This reduction of the piezoresistive coefficient degrades the motional conductance and the eventually disrupts the $R_A g_m = -1$ condition needed to sustain oscillation, as described in Section 2.7.4. Conceptually this seems plausible since the piezoresistive effect is dependent upon the change in electron distribution within the band structure of the material as described in Section 2.8.2. Large numbers of excited carriers throughout the material may limit the change in electron mobility when the material is under strain. Since the motional conductance should increase per Eq {2-37}as the DC current through the actuators increases with increased light illumination, assuming the material parameters remain unchanged, this change in piezoresistivity would need to be substantial. Unlike the photoresistivity theory proposed for the frequency tuning effect, under which illumination of any portion of the device would change the frequency, this possible change of piezoresistance would only be relevant in the actuator arm region where the stress is fluctuating during oscillation. Experimental observation showed that directing the laser closer to the actuator arms causes shutoff to occur at lower laser power levels, suggesting that the light interaction with the arms is causal adding some support to this theory. After shutoff, self-sustained oscillation was immediately recovered in all instances by simply lowering the laser power.

A second possibility is that the laser is that the laser may be establishing an undesireable change in the AC+DC electrothermomechanical response shown in Section 3.6, from additional heating from the laser. One possible contributing mechanism for this laser heating may be that the suspended device in combination with the substrate is acting as a resonant fabry-perot etalon. Self-oscillation of silicon structures (250 nm thick centrally anchored disks suspended 1 μm above the substrate) through parametric amplification using a He-Ne continuous wave (CW) laser was demonstrated by Zalalutdinov et al. in [49] with a laser threshold power of 250 μW. While the data does not suggest that any such behavior is occurring in the devices of this work, there may be potential for a structural-thermal interaction that dampens the electrically driven oscillation. This possibility seems less likely since raising the DC temperature setpoint, whether by joule heating or laser heating, shouldn't degrade the AC temperature fluctuations needed for actuation of the device unless it substantial enough to induce material failure (i.e. "burnout"), in which case oscillation would be unrecoverable. However, if this localized laser heating is

causing self-oscillatory structural deformation, similar to that shown in [49], that happens to be anti-resonant to the mechanical oscillation induced electrically, the two effects could conceivably cause dampening of the oscillation. Such an effect was not considered during the design of these devices and would be an unlikely coincidence, but remains a possibility as the analysis needed to rule it out remains a subject for future work.

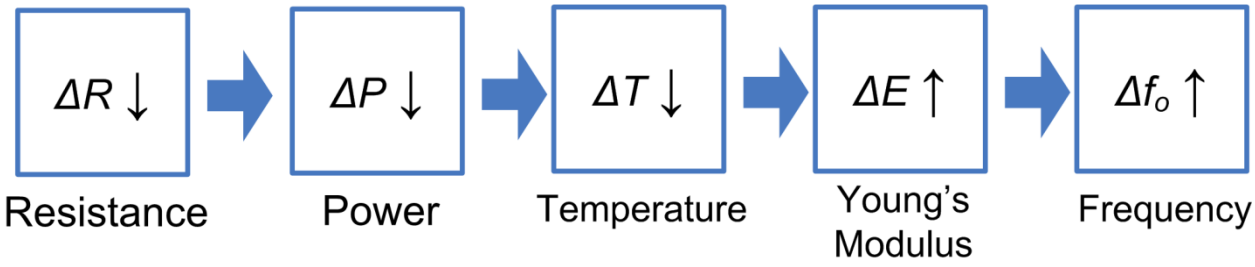

Figure 6.13: Flowchart depicting impact of decreased device resistance due to photoconductivity in thermal-piezoresistive self-sustained oscillators.

With the measured values of I_{DC} at different laser powers, the ΔR *and* $V_{dev(light)}$ values can be calculated for each data point collected using Eqs {6-6} and {6-7} and the un-illuminated device resistance, assuming $R_{bias} = 5\ k\Omega$. The ΔR values can in turn be translated into fractional changes of resistivity, $X\rho$, for the entire device at each illumination level. Utilizing the COMSOL prestressed modal analysis model presented in Section 3.4 with a resistivity that more closely represents Device A3 (ρ=0.05 Ω-cm) and a voltage boundary condition instead of a current condition, a sweep can be performed for the $V_{dev(light)}$ and X_ρ values to generate corresponding simulated frequencies at each point. Figure 6.14 shows a comparison of the frequency variation derived from the measured data (originally shown in Figure 6.10) and the frequency variation generated from the prestressed COMSOL modal analysis using the applied device voltages and fractional resistivity changes derived from the data using the circuit model shown in Figure 6.12. Significant differences exist between the effective device resistance of the COMSOL solid model and the ideal circuit model largely due to the pads and the pad edge voltage boundary condition used. Thus the $V_{dev(light)}$ values derived from the circuit model when applied to the COMSOL model do not generate the same magnitude of current resulting in the differences in magnitude variation of frequency between the two plots in Figure 6.14. However, the trends in frequency are consistent between the model and experiment.

While there may be some benefit in using these devices for the detection of light, there are numerous other technologies that have been developed for this purpose. However, the ability to tune the oscillator frequency and turn the oscillator on and off with laser illumination, without any additional components or circuitry, is an ability that is unique to most MEMS/NEMS resonant systems.

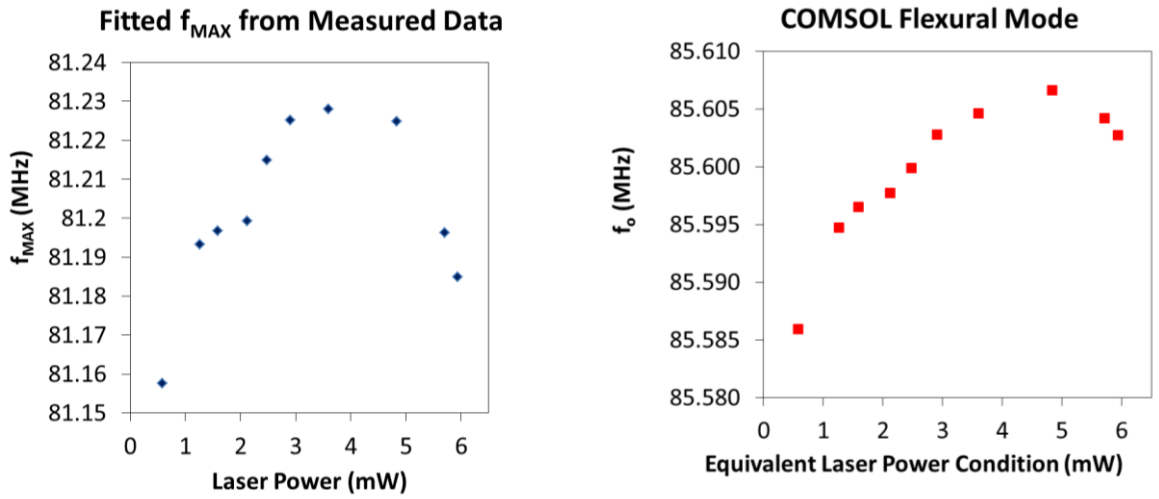

Figure 6.14: Comparison of the (left) LS fitted 1D Lorentzian peak frequencies generated from measured data at each laser power and the (right) COMSOL prestressed modal analysis frequencies for the relevant flexural mode utilizing the equivalent device voltage levels and overall fractional change in resistivity calculated from the measured data as simulation inputs.

7. Conclusions and Suggestions for Future Work

The work presented successfully demonstrated that the principle of thermal actuation for resonant devices can indeed extend into higher frequencies while maintaining useful performance. However, the assertion that reduced scaling improves performance remains to be proven. In fact in many regards this work raised more questions than it answered. The following paragraphs will attempt to summarize the conclusion from each chapter of this work and highlight the areas where further effort would be fruitful

The modeling and simulation work accomplish was the first to integrate thermal expansion to yield a coupled electrothermomechanical solution for these devices. While not presented, piezoresisitivity was incorporated into the steady-state simulations and shown to yield negligible difference in results. The time-dependent AC+DC simulation however, may benefit from incorporating this phenomena as the AC temperature fluctuations from steady-state are very small (~0.15K in amplitude). Development of a custom module to allow for direct harmonic excitation from joule heating, instead of the approximate forced harmonic method would also be desirable, particularly if it could be designed to incorporate prestressed conditions. Finally, developing nonlinear analytical modeling of the self-sustained oscillation phenomena for these devices operating as limit cycles would be a worthwhile pursuit.

The fabrication of these devices utilized standard processing and yielded acceptable results. The use of a Cr mask for submicron resolution DSE was an approach unique to most reported DSE work and further characterization and refinement of the etch recipe used may prove beneficial, particularly for very deep etches where conventional oxide masks tend to degrade. The current recipe successfully demonstrated to thicknesses of up to 5 μm, maintaining the same submicron areas layout making it already a useful recipe for submicron resolution silicon MEMS processing. Deeper etching however is not necessarily critical for these devices. Improvement of the patterning and limiting the undercutting observed would be a more worthwhile and may be causal for the second mode observed during device operation. One possible improved approach, would be to utilize a separate metal mask for EBL alignment and either an oxide mask for the device patterning area or an etch resistant EBL resist (such as ZEP). This approach would eliminate the undercutting experienced, would require adding additional lithography steps to the process, and in the case of the oxide mask would require an anisotropic oxide plasma etch to be developed.

Regarding device operation as resonators, when compared to the previously reported devices in Table 2.4, the power consumed and the FOM/Q values of the 1.6-1.9 μm thick devices are consistently similar. This distinguishes these as being nearly as capable as their predecessors, but at higher frequencies. In fact these devices likely represent the highest frequency demonstration of internally driven thermal actuation ever reported for any device. While the submicron thick devices did successfully operate, they offered no improvement in performance

in terms of power or motional conductance over their thicker counterparts. Their operation may be significant though for applications where performance doesn't need to be particularly strong and a thin silicon substrate is desired. The failure of the submicron thick devices to meet the expectations of the lumped element model raises questions on the extent of it's validity at small scales. In particular, the effective thermal capacitance of the material may also be changing with reduced scaling. Using modeling tools to capture these concepts for an analytical model would also be fruitful future work.

The changes in device resistance observed before and after resonator testing, suggest that the material is changing during this operation, further complicating matters. As this has a very significant impact on power consumption, pursuit of understanding this effect should be considered.

The demonstrated device operation in the VHF as self-sustained oscillators *under ambient air conditions* is significant as it potentially allows new levels of sensitivity for low cost sensing applications (as shown by Eq {2-34}) . They also invite stronger potential for use as on-chip oscillators in this frequency range, possibly as simpler lower cost alternatives to conventional MEMS oscillators with external feedback. However, a significant amount of further development would likely be required for any precision timing applications as significant phase noise, while not measured and quantified in this work was observed. Probably the most obvious question that remains is why the devices exhibited self-sustained oscillations at a different mechanical frequency. Capturing this effect through modeling seems unlikely judging from the analysis performed in this work. Experimentally ascertaining the mode shape would be useful in verifying the assumptions made by modal analysis. While the method by which the devices are doubling their electrical frequency output is likely a nonlinear stressing phenomena in the actuator arms, similar to that previously reported, it isn't clear from modal analysis how this is occurring since the flexural longitudinal mode doesn't appear to share this characteristic.

Lastly the frequency tuning and on/off control of the devices when operated as self-sustained oscillators introduces these devices for potential use with photonic devices. In particular the on/off control of the electrical and mechanical output with incident light energy seems unique to electrically driven MEMS and NEMS devices. While the tuning phenomena has been explained by considering the device as a self-oscillating photoconductor, the mechanism for on/off control remains to be fully understood.

Overall, thermal-piezoresistive high frequency actuation remains largely unexplored in comparison to capacitive and piezoelectric devices, but the benefits it offers, as detailed in Section 2.7 are significant There are many possible future experimental research directions to explore including alternate material implementations and different device geometries.

REFERENCES

[1] S. D. Senturia, *Microsystems Design*. New York: Springer, 2001.

[2] R. Fitzpatrick, "Oscillations and Waves Course Notes," 2010. [Online]. Available: http://farside.ph.utexas.edu/teaching/315/Waves/Waves.html.

[3] E. Kreyszig, *Advanced Engineering Mathematics*, 9th ed. John Wiley & Sons, Inc., 2006.

[4] M. D. Greenburg, *Advanced Engineering Mathematics*, 2nd ed. Upper Saddle River, New Jersey: Prentice Hall, 1998.

[5] A. V. Oppenheim, A. S. Willsky, and S. H. Nawab, *Signals and Systems*, 2nd ed. Upper Saddle River, New Jersey: Prentice Hall, 1997.

[6] A. B. Carlson, *Circuits: Engineering Concepts and Analysis of Linear Electric Circuits*, Prelim Ed. New York: John Wiley & Sons, Inc., 1996.

[7] E. L. Hixson, "Mechanical Impedance," in *Harris's Shock and Vibration Handbook*, 5th ed., vol. 1, A. G. Harris C.M.; Piersol, Ed. McGraw-Hill, 2002.

[8] E. Green, "The story of Q," *American Scientist*, vol. 43, no. October, pp. 584–594, 1955.

[9] M.J. Moloney, "Spring 2012 Course Notes PH314 Theoretical Mechanics." 2012.

[10] D. M. Pozar, *Microwave Engineering*, 2nd ed. New York: John Wiley and Sons, Inc., 1998.

[11] A. Grebennikov, *RF and Microwave Transistor Oscillator Design*. Chichester, UK: John Wiley & Sons, Ltd, 2007.

[12] J. T. M. van Beek and R. Puers, "A review of MEMS oscillators for frequency reference and timing applications," *Journal of Micromechanics and Microengineering*, vol. 22, no. 1, p. 013001, Jan. 2012.

[13] J. Lee and S. R. Manalis, "Second eigenmode operation of suspended microchannel resonators for high precision flow-through mass sensing," in *Solid-State Sensors, Actuators, and Microsystems Workshop*, 2010, vol. 1, no. 3, pp. 27–29.

[14] A. Hajjam, J. C. Wilson, and S. Pourkamali, "Individual Air-Borne Particle Mass Measurement Using High-Frequency Micromechanical Resonators," *IEEE Sensors Journal*, vol. 11, no. 11, pp. 2883–2890, 2011.

[15] A. Rahafrooz and S. Pourkamali, "Fabrication and characterization of thermally actuated micromechanical resonators for airborne particle mass sensing: I. Resonator design and modeling," *Journal of Micromechanics and Microengineering*, vol. 20, no. 12, p. 125018, Dec. 2010.

[16] A. Hajjam, J. C. Wilson, A. Rahafrooz, and S. Pourkamali, "Fabrication and characterization of thermally actuated micromechanical resonators for airborne particle mass sensing: II. Device fabrication and characterization," *Journal of Micromechanics and Microengineering*, vol. 20, no. 12, p. 125019, Dec. 2010.

[17] Y. Lu, S. Peng, D. Luo, and A. Lal, "Femtomolar Sensitivity DNA Photonic Crystal Nanowire Array Ultrasonic Mass Sensor," in *Proceedings of IEEE 25th International Conference on Micro Electro Mechanical Systems*, 2012, no. February, pp. 88–91.

[18] Y. T. Yang, C. Callegari, X. L. Feng, K. L. Ekinci, and M. L. Roukes, "Zeptogram-scale nanomechanical mass sensing.," *Nano letters*, vol. 6, no. 4, pp. 583–6, Apr. 2006.

[19] H. J. Hall, A. Rahafrooz, J. J. Brown, V. M. Bright, and S. Pourkamali, "Thermally Actuated I-Shaped Electormechanical VHF Resonators," in *IEEE 25th International Conference on Micro Electro Mechanical Systems*, 2012, no. February, pp. 737–740.

[20] Y. Hwang, F. Gao, and R. N. Candler, "Porous silicon resonators for sensitive vapor detection," in *Solid-State Sensors, Actuators, and Microsystems Workshop*, 2010, pp. 150–153.

[21] J. Lee, R. J. Houk, J. A. Greathouse, M. D. Allendorf, and P. J. Hesketh, "Microcantilever array sensors using nanoporous metal-organic frameworks for gas detection," in *Solid-State Sensors, Actuators, and Microsystems Workshop*, 2010, pp. 146–149.

[22] A. Rahafrooz and S. Pourkamali, "Characterization of rotational mode disk resonator quality factors in liquid," in *2011 Joint Conference of the IEEE International Frequency Control and the European Frequency and Time Forum (FCS) Proceedings*, 2011, pp. 1–5.

[23] L. Beardslee, K. Demirci, Y. Luzinova, J. Su, B. Mizaikoff, S. Heinrich, F. Josse, and O. Brand, "In-plane mode resonant cantilevers as liquid phase chemical sensors with ppb range limits of detection," in *Solid-State Sensors, Actuators, and Microsystems Workshop*, 2010, pp. 23–26.

[24] M. A. Hopcroft, B. Kim, S. Chandorkar, R. Melamud, M. Agarwal, C. M. Jha, G. Bahl, J. Salvia, H. Mehta, H. K. Lee, R. N. Candler, and T. W. Kenny, "Using the temperature dependence of resonator quality factor as a thermometer," *Applied Physics Letters*, vol. 91, no. 1, p. 013505, 2007.

[25] K. H. Kim and Y. H. Seo, "Self-Resonant Flow Sensor Using Resonance Frequency Shift by Flow-Induced Vibration," in *Micro Electro Mechanical Systems, 2009. 22nd IEEE International Conference on.(MEMS)*, 2009, pp. 511–514.

[26] W. B. Kuhn, S. Member, D. Nobbe, D. Kelly, and A. W. Orsborn, "Dynamic Range Performance of On-Chip RF Bandpass Filters," *October*, vol. 50, no. 10, pp. 685–694, 2003.

[27] J. Wang, L. Yang, and S. Pietrangelo, "RF MEMS resonators: getting the right frequency and Q," in *IEEE Compound Semiconductor Integrated Circuit Symposium, 2007. CSIC 2007.*, 2007, pp. 1–4.

[28] S. J. Orfanidis, *Electromagnetic Waves and Antennas*. Piscataway, N.J.: Rutgers University, 2010.

[29] "Vectron International Website." [Online]. Available: http://www.vectron.com/index.htm.

[30] A. Rahafrooz and S. Pourkamali, "Jitter characterization of fully-micromechanical thermal-piezoresistive oscillators," *2012 IEEE International Frequency Control Symposium Proceedings*, pp. 1–4, May 2012.

[31] M. Rinaldi, A. Tazzoli, J. Segovia-Fernandez, V. Felmetsger, and G. Piazza, "High power and low temperature coeffient of frequency oscillator based on a fully anchored and oxide compensated AlN contour-mode MEMS resonator," in *IEEE 25th International Conference on Micro Electro Mechanical Systems*, 2012, no. February, pp. 696–699.

[32] R. Tabrizian, G. Casinovi, and F. Ayazi, "Temperature stablee High Q AlN-on-silicon resontors with embedded array of oxide pillars," in *Solid-State Sensors, Actuators, and Microsystems Workshop*, 2010, pp. 100–101.

[33] T. Gryba, J. Carlier, S. Wang, X. Zhao, S. Guo, and J.-E. Lefebvre, "One port contour-mode ZnO piezoelectric MEMS resonator," *Microelectronic Engineering*, vol. 88, no. 9, pp. 3003–3010, Sep. 2011.

[34] M. Ziaei-moayyed and R. T. Howe, "Higher-order Dielectrically Transduced Bulk-mode Ring Resonator with Low Motional Resistance," *Electrical Engineering*, pp. 19–24, 2010.

[35] G. Wu, D. Xu, B. Xiong, and Y. Wang, "A high-performance bulk mode single crystal silicon microresonator based on a cavity-SOI wafer," *Journal of Micromechanics and Microengineering*, vol. 22, no. 2, p. 025020, Feb. 2012.

[36] J. E. Butler, D. S. Y. Hsu, and T.-C. Nguyen, "CVD polycrystalline diamond high-Q micromechanical resonators," *Technical Digest. MEMS 2002 IEEE International Conference. Fifteenth IEEE International Conference on Micro Electro Mechanical Systems (Cat. No.02CH37266)*, vol. 3, no. 2, pp. 657–660, 2002.

[37] M. Akgul, B. Kim, Z. Ren, and C. T. Nguyen, "Capacitively Transduced micromechanical resonators with simultaneous low motional resisitance and Q>70000," in *Solid-State Sensors, Actuators, and Microsystems Workshop*, 2010, pp. 467–470.

[38] L. Hung and C. T. Nguyen, "Capacitive-Piezo transducers for higher Q contour mode AlN resonators at 1.2 GHz," in *Solid-State Sensors, Actuators, and Microsystems Workshop*, 2010, pp. 463 – 466.

[39] D. Grogg, M. Mazza, D. Tsamados, and A. M. Ionescu, "Multi-Gate Vibrating-Body Field Effect Transistor (VB-FETs)," in *IEEE International Electronic Devices Meeting, IEDM*, 2008, pp. 1–4.

[40] J. T. M. Van Beek, G. J. A. Verheijden, G. E. J. Koops, K. L. Phan, C. van der Avoort, J. van Wingerden, D. Ernur Badaroglu, and J. J. M. Bontemps, "Scalable 1.1 GHz fundamental mode piezo-resistive silicon MEMS resonator," in *IEEE International Electronic Devices Meeting, IEDM*, 2007, pp. 411–414.

[41] C. Li, C. Chin, Y. Liu, and S. Li, "Capacitively-driven and piezoresistively-sensed CMOS-MEMS resonators," in *IEEE 25th International Conference on Micro Electro Mechanical Systems*, 2012, no. February, pp. 539–542.

[42] V. Russino, F. Pieri, and A. Nannini, "Mass Response of a CMOS-Compatible Magnetically Actuated MEMS Microbalance," in *Sensors and Microsystems*, vol. 109, A. D'Amico, C. Di Natale, L. Mosiello, and G. Zappa, Eds. Boston, MA: Springer US, 2011, pp. 205–209.

[43] E. Hwang and S. a. Bhave, "PN-diode transduced 3.7-GHZ silicon resonator," in *2010 IEEE 23rd International Conference on Micro Electro Mechanical Systems (MEMS)*, 2010, pp. 208–211.

[44] P. S. Waggoner, C. P. Tan, L. Bellan, and H. G. Craighead, "High-Q, in-plane modes of nanomechanical resonators operated in air," *Journal of Applied Physics*, vol. 105, no. 9, p. 094315, 2009.

[45] D. Weinstein and S. A. Bhave, "Internal Dielectric Transduction of a 4 . 5 GHz Silicon Bar Resonator," in *Int. Electron Devices Meeting (IEDM)*, 2007, no. 2, pp. 415–418.

[46] S. Venkatesh, "Optical microresonator sensor systems," *Journal of the Institution of Electronic and Radio Engineers*, vol. 58, no. 5 (Supplement), pp. S79–S88, 1988.

[47] E. Dieulesaint, D. Royer, and C. Bonnefoy, "Mechanical Excitation of a Membrane by an Optical Beam.," in *Ultrasonics Symposium*, 1981, pp. 802–805.

[48] K. Aubin, M. Zalalutdinov, T. Alan, R. B. Reichenbach, R. Rand, A. Zehnder, J. Parpia, and H. Craighead, "Limit Cycle Oscillations in CW Laser-Driven NEMS," vol. 13, no. 6, pp. 1018–1026, 2004.

[49] M. Zalalutdinov, a. Zehnder, a. Olkhovets, S. Turner, L. Sekaric, B. Ilic, D. Czaplewski, J. M. Parpia, and H. G. Craighead, "Autoparametric optical drive for micromechanical oscillators," *Applied Physics Letters*, vol. 79, no. 5, p. 695, 2001.

[50] N. V. Lavrik and P. G. Datskos, "Femtogram mass detection using photothermally actuated nanomechanical resonators," *Applied Physics Letters*, vol. 82, no. 16, p. 2697, 2003.

[51] A. M. Van Der Zande, R. a. Barton, J. S. Alden, C. S. Ruiz-Vargas, W. S. Whitney, P. H. Q. Pham, J. Park, J. M. Parpia, H. G. Craighead, and P. L. McEuen, "Large-Scale Arrays of Single-Layer Graphene Resonators," *Nano Letters*, p. 101116125413000, Nov. 2010.

[52] L. Hao, J. C. Gallop, and D. Cox, "Excitation, detection, and passive cooling of a micromechanical cantilever using near-field of a microwave resonator," *Applied Physics Letters*, vol. 95, no. 11, p. 113501, 2009.

[53] R. J. Wilfinger, P. H. Bardell, and D. S. Chhabra, "The Resonistor: A Frequency Selective Device Utilizing the Mechanical Resonance of a Silicon Substrate," *IBM Journal*, vol. 3, no. January, pp. 113–118, 1968.

[54] M. B. Othman and A. Brunnschweiller, "Electrothermally excited silicon beam mechanical resonators," *Electronics Letters*, vol. 23, no. 14, pp. 728–730, 1987.

[55] J. H. Seo and O. Brand, "High Q -Factor In-Plane-Mode Resonant Microsensor Platform for Gaseous / Liquid Environment," *Journal of Microelectromechanical Systems*, vol. 17, no. 2, pp. 483–493, 2008.

[56] I. Bargatin, I. Kozinsky, and M. L. Roukes, "Efficient electrothermal actuation of multiple modes of high-frequency nanoelectromechanical resonators," *Applied Physics Letters*, vol. 90, no. 9, p. 093116, 2007.

[57] R. B. Reichenbach, M. Zalalutdinov, J. M. Parpia, and H. G. Craighead, "RF MEMS Oscillator with Integrated Resistive Transduction," *October*, vol. 27, no. 10, pp. 805–807, 2006.

[58] L. A. Beardslee, J. Lehmann, C. Carron, J. Su, F. Josse, I. Dufour, O. Brand, and U. De Bordeaux, "Thermally actuated silicon tuning fork resonators for sensing applications in air," in *2012 IEEE 25th International Conference on Micro Electro Mechanical Systems (MEMS)*, 2012, no. February, pp. 607–610.

[59] H. Jianqiang, Z. Changchun, L. Junhua, and H. Yongning, "Dependence of the resonance frequency of thermally excited microcantilever resonators on temperature," *Sensors and Actuators A: Physical*, vol. 101, no. 1–2, pp. 37–41, Sep. 2002.

[60] G. S. Wood, I. Gual, P. Parmiter, and R. Cheung, "Temperature stability of electro-thermally and piezoelectrically actuated silicon carbide MEMS resonators," *Microelectronics Reliability*, vol. 50, no. 12, pp. 1977–1983, Dec. 2010.

[61] A. Rahafrooz and S. Pourkamali, "High-Frequency Thermally Actuated Electromechanical Resonators With Piezoresistive Readout," *IEEE Transactions on Electron Devices*, vol. 58, no. 4, pp. 1205–1214, 2011.

[62] A. Rahafrooz and S. Pourkamali, "Active self-Q-enhancement in high frequency thermally actuated M/NEMS resonators," in *2011 IEEE 24th International Conference on Micro Electro Mechanical Systems (MEMS)*, 2011, pp. 760–763.

[63] A. Rahafrooz and S. Pourkamali, "Fully Micromechanical Piezo-Thermal Oscillators," in *Int. Electron Devices Meeting (IEDM)*, 2010, pp. 158–161.

[64] A. Hajjam, A. Rahafrooz, and S. Pourkamali, "Sub-100ppb / ^{o}C Temperature Stability in Thermally Actuated High Frequency Silicon Resonators via Degenerate Phosphorous Doping and Bias Current Optimization," *IBAR*, no. 303, pp. 170–173, 2010.

[65] P. G. Steeneken, K. Le Phan, M. J. Goossens, G. E. J. Koops, G. J. A. M. Brom, C. van der Avoort, and J. T. M. van Beek, "Piezoresistive heat engine and refrigerator," *Nature Physics*, vol. 7, no. 4, pp. 354–359, Jan. 2011.

[66] A. Rahafrooz and S. Pourkamali, "Rotational Mode Disk Resonators for High-Q Operation in Liquid," *Quality*, pp. 1071–1074, 2010.

[67] A. Rahafrooz and S. Pourkamali, "Thermal-Piezoresistive Energy Pumps in Micromechanical Resonant Structures," *IEEE Transactions on Electron Devices*, vol. 59, no. 12, pp. 3587–3593, Dec. 2012.

[68] R. H. Enns, *It's a Nonlinear World*. New York, NY: Springer New York, 2011, pp. 29–69.

[69] M. A. Hopcroft, W. D. Nix, and T. W. Kenny, "What is the Young ' s Modulus of Silicon ?," vol. 19, no. 2, pp. 229–238, 2010.

[70] N. Ono, K. KItamura, K. Nakajima, and Y. Shimanuki, "Measurement of Young ' s Modulus of Silicon Single Crystal at High Temperature and Its Dependency on Boron Concentration Using the Flexural Vibration Method," *Japanese Journal of Applied Physics*, vol. 39, no. 2, pp. 368–371, 2000.

[71] Y.-S. Sohn, J. Park, G. Yoon, J. Song, S.-W. Jee, J.-H. Lee, S. Na, T. Kwon, and K. Eom, "Mechanical Properties of Silicon Nanowires.," *Nanoscale research letters*, vol. 5, no. 1, pp. 211–216, Jan. 2009.

[72] H. Sadeghian, C. K. Yang, J. F. L. Goosen, E. van der Drift, a. Bossche, P. J. French, and F. van Keulen, "Characterizing size-dependent effective elastic modulus of silicon nanocantilevers using electrostatic pull-in instability," *Applied Physics Letters*, vol. 94, no. 22, p. 221903, 2009.

[73] B. Van Zeghbroeck, "Semiconductor Fundamentals," *Principles of Semiconductor Devices*, 2011. [Online]. Available: http://ecee.colorado.edu/~bart/book/book/chapter2/ch2_7.htm. [Accessed: 22-Mar-2012].

[74] J. Kim, S. G. Kim, J. G. Koo, T. M. Roh, H. S. Park, and D. Y. Kim, "Characteristics of dynamic resistance in a heavily doped silicon semiconductor resistor," *International Journal of Electronics*, vol. 86, no. 3, pp. 269–279, 1999.

[75] I. Transactions and O. N. Electron, "Electron and Hole Mobilities in Silicon as a Function of Concentration and Temperature," *IEEE Transactions on Electron Devices*, vol. 29, no. 2, pp. 292–295, 1982.

[76] S. Beeby, G. Ensell, M. Kraft, and N. White, *MEMS Mechanical Sensors*. Boston: Artech House, Inc., 2004.

[77] A. A. Barlian, W.-T. Park, J. R. Mallon, A. J. Rastegar, and B. L. Pruitt, "Review: Semiconductor Piezoresistance for Microsystems.," *Proceedings of the IEEE. Institute of Electrical and Electronics Engineers*, vol. 97, no. 3, pp. 513–552, Jan. 2009.

[78] Y. Kanda, "A graphical representation of the piezoresistance coefficients in silicon," *IEEE Transactions on Electron Devices*, vol. 29, no. 1, pp. 64–70, Jan. 1982.

[79] C. Herring and E. Vogt, "Transport and deformation-potential theory for many-valley semiconductors with anisotropic scattering," *Physical Review*, vol. 101, no. 3, pp. 944–961, 1956.

[80] C. S. Smith, “Piezoresistance effect in germanium and silicon,” *Physical Review*, vol. 94, no. 1, pp. 42–49, 1954.

[81] A. A. Barlian and N. Harjee, “Sidewall epitaxial piezoresistor process and characterisation for in-plane force sensing applications,” *Micro & Nano Letters, IET*, vol. 4, no. 4, pp. 204–209, 2009.

[82] C.-H. Cho, R. C. Jaeger, and J. C. Suhling, “Characterization of the piezoresistive coefficients of (100) silicon from -150 to +125C,” in *Proceedings of IPACK2007 ASME InterPACK ’07*, 2007, no. 100, pp. 1–14.

[83] R. He and P. Yang, “Giant piezoresistance effect in silicon nanowires.,” *Nature nanotechnology*, vol. 1, no. 1, pp. 42–6, Oct. 2006.

[84] Y. Yang and X. Li, “Giant piezoresistance of p-type nano-thick silicon induced by interface electron trapping instead of 2D quantum confinement.,” *Nanotechnology*, vol. 22, no. 1, p. 015501, Jan. 2011.

[85] J. Milne, a. Rowe, S. Arscott, and C. Renner, “Giant Piezoresistance Effects in Silicon Nanowires and Microwires,” *Physical Review Letters*, vol. 105, no. 22, pp. 1–4, Nov. 2010.

[86] J. X. Cao, X. G. Gong, and R. Q. Wu, “Giant piezoresistance and its origin in Si(111) nanowires: First-principles calculations,” *Physical Review B*, vol. 75, no. 23, pp. 3–6, Jun. 2007.

[87] K. Nakamura, D. V. Dao, Y. Isono, T. Toriyama, and S. Sugiyama, “Electronic States and Piezoresistivity in Silicon Nanowires,” in *Nanowires*, vol. 1, no. March, P. Prete, Ed. 2010, pp. 297–313.

[88] A. Koumela, D. Mercier, C. Dupré, G. Jourdan, C. Marcoux, E. Ollier, S. T. Purcell, and L. Duraffourg, “Piezoresistance of top-down suspended Si nanowires.,” *Nanotechnology*, vol. 22, no. 39, p. 395701, Sep. 2011.

[89] Y. Okada and Y. Tokumaru, “Precise determination of lattice parameter and thermal expansion coefficient of silicon between 300 and 1500 K,” *Journal of Applied Physics*, vol. 314, 1984.

[90] L. Fengchao, “Confirmation of the new technique for measuring the linear thermal expansion of silicon,” *Powder Diffraction*, vol. 8, no. 1, p. 36, 1993.

[91] H. Abe, H. Kato, and T. Baba, “Specific Heat Capacity Measurement of Single-Crystalline Silicon as New Reference Material,” *Japanese Journal of Applied Physics*, vol. 50, no. 11, p. 11RG01, Nov. 2011.

[92] A. S. Okhotin, A. S. Pushkarskii, and V. V. Gorbachev, *Thermophysical Properties of Semiconductors (in Russian)*. Moscow, Russia: Atom Publishing House, 1975.

[93] R. A. Barton, J. Parpia, and H. G. Craighead, “Fabrication and performance of graphene nanoelectromechanical systems,” *Journal of Vacuum Science & Technology B: Microelectronics and Nanometer Structures*, vol. 29, no. 5, p. 050801, 2011.

[94] R. Tabrizian, M. Rais-Zadeh, and F. Ayazi, “Effect of phonon interactions on limiting the fQ product of micromechanical resonators,” in *Solid-State Sensors, Actuators and Microsystems Conference, 2009. TRANSDUCERS 2009. International*, 2009, vol. 1, no. 3, pp. 2131–2134.

[95] C.-H. Cho, “Characterization of Young’s modulus of silicon versus temperature using a ‘beam deflection’ method with a four-point bending fixture,” *Current Applied Physics*, vol. 9, no. 2, pp. 538–545, Mar. 2009.

[96] A. A. Tseng, C. D. Chen, and K. J. Ma, “Electron beam lithography in nanoscale fabrication: recent development,” *IEEE Transactions on Electronics Packaging Manufacturing*, vol. 26, no. 2, pp. 141–149, Apr. 2003.

[97] S.-Y. Kang, K.-H. Kwon, S.-I. Kim, S.-K. Lee, M.-Y. Jung, Y.-R. Cho, Y.-H. Song, J. H. Lee, and K.-I. Cho, “Etch Characteristics of Cr by Using Cl[sub 2]/O[sub 2] Gas Mixtures with Electron Cyclotron Resonance Plasma,” *Journal of The Electrochemical Society*, vol. 148, no. 5, p. G237, 2001.

[98] W. Y. Kwong and W. Y. Zhang, “Electron-beam assisted platinum deposition as a protective layer for FIB and TEM applications,” in *IEEE International Symposium on Semiconductor Manufacturing, 2005.*, 2005, pp. 469–471.

[99] B. Wu, A. Kumar, and S. Pamarthy, “High aspect ratio silicon etch: A review,” *Journal of Applied Physics*, vol. 108, no. 5, p. 051101, 2010.

[100] F. Laermer and A. Urban, “BOSCH-DRIE Shaping MEMS - History, Applications and Future Directions,” in *Solid-State Sensors, Actuators, and Microsystems Workshop*, 2010, pp. 1–6.

[101] K. J. Owen, B. Vanderelzen, R. L. Peterson, and K. Najafi, “High Aspect Ratio Deep Silicon Etching,” in *25th IEEE International Conference on Micro Electro Mechanical Systems (MEMS)*, 2012, no. February, pp. 251–254.

[102] F. Marty, L. Rousseau, B. Saadany, B. Mercier, O. Français, Y. Mita, and T. Bourouina, “Advanced etching of silicon based on deep reactive ion etching for silicon high aspect ratio microstructures and three-dimensional micro- and nanostructures,” *Microelectronics Journal*, vol. 36, no. 7, pp. 673–677, Jul. 2005.

[103] Y. Lee, Y. Jang, J. Kim, and Y. Kim, “Robust Silicon Deep EtchingWithout Thermal Isolation on Large Mass and Long Spring Structures,” in *25th IEEE International Conference on Micro Electro Mechanical Systems (MEMS)*, 2012, no. February, pp. 317–320.

[104] Z. Cui, *Nanofabrication*. Boston, MA: Springer US, 2008.

[105] H. V Jansen, M. J. de Boer, S. Unnikrishnan, M. C. Louwerse, and M. C. Elwenspoek, “Black silicon method: X. A review on high speed and selective plasma etching of silicon with profile control: an in-depth comparison between Bosch and cryostat DRIE processes as a roadmap to next generation equipment,” *Journal of Micromechanics and Microengineering*, vol. 19, no. 3, p. 033001, Mar. 2009.

[106] R. Abdolvand and F. Ayazi, “An advanced reactive ion etching process for very high aspect-ratio sub-micron wide trenches in silicon,” *Sensors and Actuators A: Physical*, vol. 144, no. 1, pp. 109–116, May 2008.

[107] I. W. Rangelow, “Critical tasks in high aspect ratio silicon dry etching for microelectromechanical systems,” *Journal of Vacuum Science & Technology A: Vacuum, Surfaces, and Films*, vol. 21, no. 4, p. 1550, 2003.

[108] M. D. Henry, “ICP Etching of Silicon for Micro and Nanosccale Devices,” California Institute of Technology, 2010.

[109] R. A. Gottscho, C. W. Jurgensen, and D. J. Vitkavage, “Microscopic uniformity in plasma etching,” *Journal of Vacuum Science & Technology B: Microelectronics and Nanometer Structures*, vol. 10, no. 5, p. 2133, Sep. 1992.

[110] S. Lai, S. Srinivasan, R. J. Westerman, D. Johnson, and J. J. Nolan, “Notch Reduction in Silicon on Insulator (SOI) Structures Using a Time Division Multiplex Etch Processes,” in *Micromachining and Microfabrication Process Technology X*, 2005, vol. 5715, pp. 33–38.

[111] M. Shearn, X. Sun, M. D. Henry, A. Yariv, and A. Scherer, “Advanced plasma processing: etching, deposition, and wafer bonding techniques for semiconductor applications,” in *Semiconductor …*, J. Grym, Ed. Rijeka, Croatia: InTech, 2010, pp. 79–105.

[112] M. Serry, M. Ibrahim, and S. Sedky, “Silicon Germanium as a novel mask for silicon deep reactive ion etching,” in *IEEE 25th International Conference on Micro Electro Mechanical Systems*, 2012, no. February, pp. 321–324.

[113] M. D. Henry, S. Walavalkar, a Homyk, and a Scherer, “Alumina etch masks for fabrication of high-aspect-ratio silicon micropillars and nanopillars.,” *Nanotechnology*, vol. 20, no. 25, p. 255305, Jun. 2009.

[114] B. A. Ganji and B. Y. Majlis, “Deep Trenches in Silicon Structure using DRIE Method with Aluminum as an Etching Mask,” in *2006 IEEE International Conference on Semiconductor Electronics*, 2006, pp. 41–47.

[115] D. K. Misra, *Radio-Frequency and Microwave Communication Circuits*. Hoboken, New Jersey: John Wiley & Sons, Inc., 2004, pp. 306–311.

[116] J. Jeong, S. Chung, S. H. Lee, and D. Kwon, “Evaluation of elastic properties and temperature effects in Si thin films using an electrostatic microresonator,” *Journal of Microelectromechanical Systems*, vol. 12, no. 4, pp. 524–530, 2003.

[117] A. Rahafrooz and S. Pourkamali, “Zero Bias Operation of Thermal-Piezoresistive Micromechanical Resonators via Internal Electromechanical Mixing,” in *Hilton Head 2012, solid-state sensor, actuator and Microsystems workshop*, 2012, pp. 375–378.

[118] H. J. Hall, A. Rahafrooz, J. J. Brown, V. M. Bright, and S. Pourkamali, “I-shaped thermally actuated VHF resonators with submicron components,” *Sensors and Actuators A: Physical*, pp. 6–12, Dec. 2012.

[119] A. Rahafrooz and S. Pourkamali, “High frequency dual-mode thermal-piezoresistive oscillators,” in *2011 Joint Conference of the IEEE International Frequency Control and the European Frequency and Time Forum (FCS) Proceedings*, 2011, pp. 1–4.

[120] L. Wang, J. J. Travis, A. S. Cavanagh, X. Liu, S. P. Koenig, P. Y. Huang, S. M. George, and J. S. Bunch, “Ultrathin oxide films by atomic layer deposition on graphene.,” *Nano letters*, vol. 12, no. 7, pp. 3706–10, Jul. 2012.

[121] R. V Dukkipati, *Engineering System Dynamics*. Harrow, Middlesex U.K.: Alpha Science International Ltd., 2005.

[122] A. Hajjam, A. Rahafrooz, and S. Pourkamali, “Input-output insulation in thermal-piezoresisitive resonant microsctructures using embedded oxide beams,” in *2012 IEEE International Frequency Control Symposium Proceedings*, 2012, pp. 1–4.

[123] R. F. Pierret, *Semiconductor Device Fundamentals*. New York: Addison-Wesley, 1996.

Appendix 1 – LUMPED PARAMETER RESONATOR MODEL DERIVATION

To derive the overall system transfer function for the device, derivations for each of the subsystem transfer functions shown in Figure 2.10 are presented beginning with the thermal domain. The resulting transfer functions shown here have all been previously presented by Rahafrooz and Pourkamali [15], [61]. The derivations shown here cover the additional details in arriving at them.

Thermal subsystem

The resistive heating in the actuator arms that initially drives the device operation is a function of the power dissipated. For an actuator arm with an ideal electrical resistance (constant current density throughout with zero reactance) of, R_A, the power dissipated for an applied voltage signal with both AC and DC components is

$$Power = \frac{V_{applied}^2}{R_A} = \frac{(V_{ac}\sin\omega t + V_{dc})^2}{R_A} = \frac{V_{ac}^2(\sin\omega t)^2 + 2V_{ac}V_{dc}\sin\omega t + V_{dc}^2}{R_A} \qquad \{A1\text{-}1\}$$

By applying the double angle formula, $(\sin\theta)^2 = \frac{1-\cos 2\theta}{2}$, this relation simplifies to

$$Power = \left[\frac{V_{ac}^2 + 2V_{dc}^2}{2R_A}\right] + \left[\frac{2V_{ac}V_{dc}\sin\omega t}{R_A}\right] - \left[\frac{V_{ac}^2\cos 2\omega t}{2R_A}\right] \qquad \{A1\text{-}2\}$$

The first term in Eq {A1-2} is the DC power bias applied to the resonator. In a sense this term sets the DC operating point of the device by adjusting the DC heating of the actuator arm from which oscillation occurs. The third term is the power dissipated at the 2nd order harmonic, which is the method by which AC only excitation can occur as described in Section 5.2.2. For this work this term is largely not being measured or utilized and it is not relevant to the derivation at hand. The second term is of primary interest as it represents the power dissipated at the input voltage frequency. The amplitude of the second term is designated P_{ac}.

To formulate the *generalized* thermal equivalent circuit (valid for power as an arbitrary function of time, $P_{in}(t)$), the input power term is equivalent to a thermal current source and creates the heat current within the device actuator. Temperature is the thermal equivalent of voltage in a thermal circuit. For these devices the reference temperature T_o is determined by the DC power bias component of {A1-2}. While the actuator arms are individual elements, their thermal capacitance and thermal resistance are considered separately in parallel (as the same Joule Heating is being applied to both simultaneously). Figure A1-1 shows the equivalent circuit for the thermal subsystem.

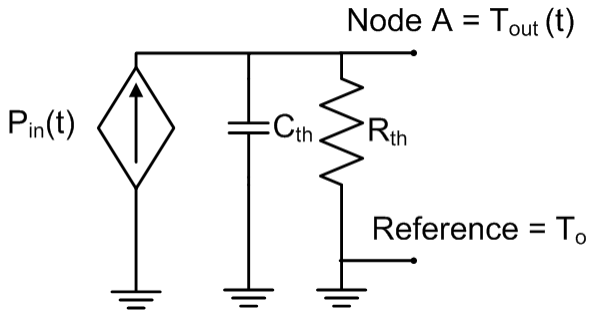

Figure A1.1: Generalized equivalent circuit for thermal subsystem

Applying the equivalent of Kirchoff's current law at node A shown in Figure A1-1 results in the following first order differential equation

$$P_{in}(t) = C_{th}\frac{dT_{out}(t)}{dt} + \frac{T_{out}(t)}{R_{th}} \quad \{A1\text{-}3\}$$

There are three closely related ways to determine the frequency response of an LTI system whose input, x(t), and output, y(t), can be described by linear constant-coefficient differential equations of the form

$$\sum_{k=0}^{N} a_k \frac{d^k y(t)}{dt^k} = \sum_{k=0}^{M} b_k \frac{d^k x(t)}{dt^k} \quad \{A1\text{-}4\}$$

The first method acknowledges the fact that complex exponentials are eigenfunctions of LTI systems, meaning that if the input function is $x(t) = e^{j\omega t}$ then the output function is $y(t) = H(j\omega)e^{j\omega t}$ [5]. Using this approach and by substituting $P_{in}(t) = P_{ac}e^{j\omega t}$ and $T_{out}(t) = T_{ac}e^{j\omega t}$equation {A1-3} becomes

$$P_{ac}e^{j\omega t} = \left(\frac{2V_{ac}V_{dc}}{R_A}\right)e^{j\omega t} = C_{th}(j\omega)T_{ac}e^{j\omega t} + \frac{T_{ac}e^{j\omega t}}{R_{th}} \quad \{A1\text{-}5\}$$

The complex exponential terms cancel in this equality allowing direct solution of the subsystem transfer function $H_{th}(j\omega)$

$$H_{th}(j\omega) = \frac{T_{ac}}{V_{ac}} = \frac{2V_{dc}R_{th}}{R_A(1 + R_{th}\,C_{th}(j\omega))} \quad \{A1\text{-}6\}$$

The second method to determine the frequency response considers the following Fourier transform property of {A1-4}

$$H(j\omega) = \frac{Y(j\omega)}{X(j\omega)} = \frac{\sum_{k=0}^{M} b_k(j\omega)^k}{\sum_{k=0}^{N} a_k(j\omega)^k} \quad \{A1\text{-}7\}$$

which allows determination of the transfer function by direct inspection. The derivation of this property involves applying the Fourier transform and some of its properties to equation {A1-4} and is presented in [5]. This method when applied to {A1-3} yields

$$\frac{T_{out}}{P_{in}} = \frac{T_{ac}}{P_{ac}} = \frac{R_{th}}{1 + R_{th}\,C_{th}(j\omega)} \qquad \{A1\text{-}9\}$$

To obtain the thermal subsystem transfer function multiplication by the ratio of input power to input voltage as shown below

$$H_{th}(j\omega) = \frac{P_{ac}}{V_{ac}} \times \frac{T_{ac}}{P_{ac}} = \left(\frac{2V_{dc}}{R_A}\right)\left(\frac{R_{th}}{1 + R_{th}\,C_{th}(j\omega)}\right) \qquad \{A1\text{-}10\}$$

which is equivalent to {A1-6}.

The third method directly considers the system from the perspective of AC circuit s-domain analysis in which the AC load impedances are consolidated into a single value, and the equivalent version Ohm's Law is applied to solve for the desired output. This output is then divided by the input to yield the subsystem transfer function. Following this approach the AC impedance of a capacitor with capacitance C_{th} is $\frac{1}{j\omega C_{th}}$ and the AC impedance of the resistor is simply R_{th}. The impedance of these two parallel elements is thus

$$Z_{th} = Z_1 || Z_2 = \frac{Z_1 Z_2}{Z_1 + Z_2} = \frac{\left(\frac{1}{j\omega C}\right)(R_{th})}{\left(\frac{1}{j\omega C}\right) + (R_{th})} = \frac{R_{th}}{1 + R_{th}\,C_{th}(j\omega)} \qquad \{A1\text{-}11\}$$

where Zth is the total thermal impedance of the circuit and Z1 and Z2 are the impedances of each element. Applying the equivalent of Ohm's Law yields

$$T_{ac} = P_{ac} Z_{th} = \left(\frac{2V_{dc}V_{ac}}{R_A}\right)\left(\frac{R_{th}}{1 + R_{th}\,C_{th}(j\omega)}\right) \qquad \{A1\text{-}12\}$$

Dividing by the AC input voltage, V_{ac}, yields the same transfer function shown previously in {A1-10} and {A1-6}.

Mechanical subsystem

The thermal expansion/contraction of the actuation arms is what drives the mechanical subsystem. From Hooke's Law, the change in stress within an actuator arm, $\Delta\sigma$, due to a change in temperature, T, from the reference temperature, T_o, is equivalent to

$$\Delta\sigma = \frac{\Delta F}{A} = \Delta\epsilon E = \alpha_T(T - T_o)E \qquad \{A1\text{-}13\}$$

where, ΔF, is the change in net force applied by the actuator arm, A, is the cross-sectional area of the actuator arm, $\Delta\varepsilon$, is the change in stress, α_T, is the coefficient of linear thermal expansion (K^{-1}),and E, is the Young's modulus of the material. For AC excitation the amplitude of sinusoidal temperature fluctuations is the effective temperature difference and the corresponding AC force amplitude is thus

$$F_{ac} = 2\alpha_T T_{ac} EA \qquad \{A1\text{-}14\}$$

where the additional "2" term is included to accommodate the additive effect of both actuator arms.

The mechanical subsystem represents the entire resonant structure as a 1D lumped element mass-spring-dampener system. This is graphically depicted in Figure A1-2 in both block diagram and equivalent circuit form where M, k, and b are the *effective* mass, spring constant, and dampening coefficient for the structure. The resulting displacement of the mass is represented by x. For the equivalent circuit the rate of change of displacement (velocity), $\dot{x}$, is the analog to current. This is the equivalent of the forced harmonic oscillator presented in Section 2.1.

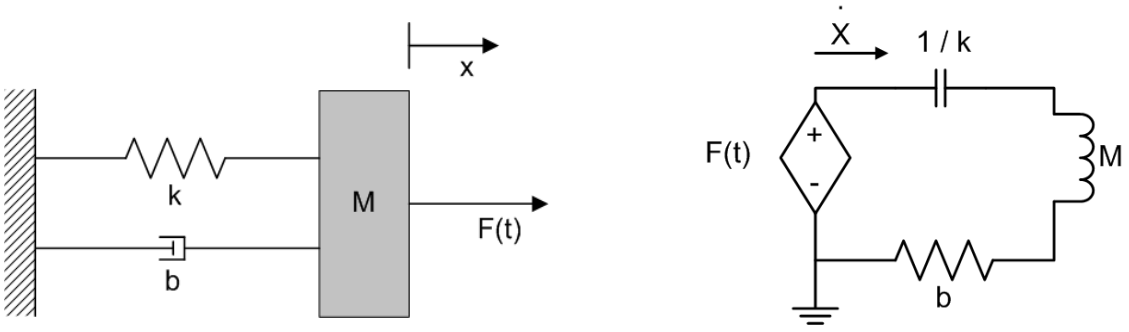

Figure A1.2: Mechanical subsystem: (left) mass-spring-damper block diagram (right) generalized equivalent circuit

By applying the principle of force conservation to the block diagram the governing 2nd order differential equation can be derived as below

$$F(t) = M\ddot{x} + b\dot{x} + kx \qquad \{A1\text{-}15\}$$

Recognizing that the applied force, $F(t)$, and the resulting displacement, X_{th}, are complex exponentials and substituting in {A1-14} for the force amplitude yields

$$2\alpha_T T_{ac} EAe^{j\omega t} = M(j\omega)^2 X_{th} e^{j\omega t} + b(j\omega)X_{th} e^{j\omega t} + kX_{th} e^{j\omega t} \qquad \{A1\text{-}16\}$$

From this expression the following transfer function for the subsystem can be derived

$$H_{mech}(j\omega) = \frac{X_{th}}{T_{ac}} = \frac{2\alpha_T EA}{(M(j\omega)^2 + b(j\omega) + k)} \quad \{A1\text{-}17\}$$

In a similar fashion as shown in the preceding thermal subsystem analysis this transfer function can derived directly by direct inspection using {A1-7} or by applying AC circuit analysis to the circuit shown in Fig A1-2 b).

Electrical Subsystem

The mechanical vibrations of the structure lead to fluctuations of stress within the actuator arms which in turn cause the electrical resistivity of the thermal actuators to change through the piezoresistive effect. From Equations {2-21} and {2-22} if the effect of geometry change is ignored (a valid assumptions since it is over an order of magnitude lower than the piezoresistive effect) then the fractional change in resistance from the longitudinal load is

$$\frac{\Delta R}{R} = \pi_l \sigma_l = \pi_l \frac{\Delta L}{L} E \quad \{A1\text{-}18\}$$

Considering the former expression in the context of the device actuator arms, with the amplitude of thermal expansion from the mechanical subsystem as the change in length yields

$$r_{ac} = R_A \pi_l \frac{X_{th}}{L_A} E \quad \{A1\text{-}19\}$$

where r_{ac} , is the amplitude of the sinusoidal change in resistance, E is Young's modulus, and π_l is the longitudinal piezoresistive coefficient. The resulting current output from the device is a combination of the DC current modulated with an AC current signal. This AC current is commonly called the *motional* current, i_m, since it originates from the mechanical motion of the resonator. Since the applied DC voltage is fixed the change in resistance is approximately proportional to the change in current which in conjunction with {A1-19} yields the following expression for motional current[22].

$$i_m = I_{dc} \frac{r_{ac}}{R_A} = I_{dc} \pi_l \frac{X_{th}}{L_A} E \quad \{A1\text{-}20\}$$

The transfer function for the electrical subsystem is thus

[22] If constant DC voltage is assumed then a positive change in current, Δi, and a corresponding negative change in resistance Δr yields the following relation $I_{dc}R_A = (I_{dc} + \Delta i)(R_A - \Delta r)$. This simplifies to $\Delta i R_A - \Delta r \Delta i - I_{dc}\Delta r = 0$. The $\Delta r \Delta i$ term is assumed insignificant yielding that shown in {A1-20}.

$$H_{electrical}(j\omega) = \frac{i_m}{X_{th}} = \frac{\pi_l E I_{dc}}{L_A} \qquad \{A1\text{-}21\}$$

As there are no energy storing elements in this subsystem, the transfer function is strictly a gain parameter.

The electrical subsystem circuit is shown in Figure A1-3. The amplification provided to the signal through the piezoresistive effect is represented as a controlled current source. This current source is in parallel to the actuator resistance, the current through which is the AC feedthrough current, i_{ac} , of the device from the applied AC voltage. If the resonator were fixed in position and acted simply as a resistive element then this would be the only AC current path and no amplification would take place, as is the case for a normal silicon resistor. An additional series resistance, R_s, is added to represent that additional resistance inherent in the support arms, pads, and contacts.

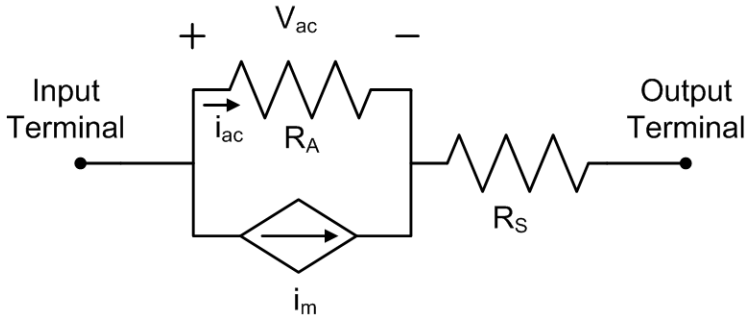

Figure A1.3: Electrical subsystem circuit diagram

The overall system transfer function for the device is the product of the three subsystem transfer functions,

$$H_{Total}(s) = H_{th}H_{mech}H_{elec} = \frac{i_m}{V_{ac}} = \left(\frac{4\alpha E^2 A {I_{dc}}^2 \pi_l}{L_A(M(s)^2 + b(s) + k)}\right)\left(\frac{R_{th}}{1 + R_{th}C_{th}(s)}\right) \qquad \{A1\text{-}22\}$$

where $= j\omega$. This is the expression shown in Eq {2-36}. Evaluating this transfer function at the resonant frequency of operation, and by applying equations {1-4} and {1-6} yields

$$H_{T,s=j\omega_o} = \left(\frac{4\alpha E^2 A {I_{dc}}^2 \pi_l Q}{jL_A k}\right)\left(\frac{R_{th}}{1 + R_{th}C_{th}(j\omega_o)}\right) \qquad \{A1\text{-}23\}$$

Further simplification can be accomplished by assuming the mechanical resonant frequency is much larger than the thermal resonant frequency (i.e. $\omega_o \gg \tau_{th}^{-1} = (R_{th}C_{th})^{-1}$). Effectively, this implies

$$\frac{R_{th}}{j(1+R_{th}C_{th}(j\omega_o))} \approx \frac{-1}{C_{th}\omega_o} \quad \{A1\text{-}24\}$$

since $R_{th}C_{th}\omega_o \gg 1$. In addition, the effective spring constant of the structure can be approximated using the analytical expression for a longitudinal beam

$$k = 2k_{eff} = \frac{2AE}{L_A} \quad \{A1\text{-}25\}$$

where the additional multiplier of 2 accounts for both actuation arms. The result is the expression for g_m shown in Eq {2-37}.

APPENDIX 2 – ALTERNATE DATA ANALYSIS METHODOLOGY

The data de-embedding procedure described in this appendix, is applicable under the assumption that the phase component of system offset being introduced into the measurement system is negligible. While it became evident through the course of this work, that it largely isn't, the following procedure was used regardless for the majority of the data recorded which consisted primarily of the $|S_{21}|$ parameter. The procedure shown, treats the system as a resistive network to remove the magnitude feedthrough floor in a similar fashion as described in Section 5.1.2 for the complex admittance, allowing the quality factor, Q, and motional conductance, g_m , and resonant frequency, ω_o, to be determined. While additional error is introduced into the values of determined parameters (up to 20% difference in g_m) with this method, the values provided still offer a solid basis for comparing devices and examining trends in performance.

To begin, following the discussion in Section 5.1.2, the S_{21} scattering parameter is effectively a measure of transmission through the device and is defined as

$$|S_{21}| = 2\frac{|V_o|}{V_s}$$
$$|S_{21}|\ (in\ dB) = 20\ log\left(2\frac{|V_o|}{V_s}\right) \qquad \{A2\text{-}1\}$$

where V_o is the voltage at the output terminal of the network analyzer and V_s is the voltage at the input (source) terminal. Each dataset collected during testing consisted of discrete S_{21} values across a span of discrete frequencies as defined by the settings of the network analyzer. To be clear regarding the nomenclature, the motional conductance can be extracted for each S_{21} value across all frequencies within the dataset and is referred to as G_m in this context. However, the motional conductance at the resonator's peak frequency, g_m ,is usually the only value reported (i.e. $G_m\ @\ peak = g_m$). For data analysis purposes the G_m values across the entire dataset are necessary for the determination of Q.

The electrical equivalent model shown in Figure A2-1 was used to extract the motional conductance values from the data collected. The bias resistors were neglected in this work as they were up to two orders of magnitude larger than the 50Ω impedance of the network analyzer. For testing in which the substrate was grounded, the pad capacitance was also determined to be negligible at the operating frequencies in this work. This model is limited in that the parasitic series resistance for the devices, which is likely significant based on the device geometry, is not accounted for, making the values extracted from the measurements somewhat conservative.

From this model, the ratio of the output voltage to the input voltage of the network analyzer at resonance for a specific frequency can be determined to be

$$\frac{V_o}{V_s} = \frac{50\Omega}{2(50\Omega) + \frac{1}{G_a + G_m}} \qquad \{A2\text{-}2\}$$

where G_a, is the conductance of the device actuator, and G_m is the measured motional conductance. At frequencies distant from the resonant peak G_m is zero. By interpolating between the distant transmission regions adjacent to the device's resonant response the transmission "floor", $T_{dBm\ floor}$, can be calculated. This value is effectively an estimate of the device's transmission with it's resonant capabilities removed allowing G_a to be solved per Eq. {A2-2}

$$G_a = \frac{-1}{\frac{-(50\Omega)}{10^{T_{dB\ floor}/20}} + 2(50\Omega)} \qquad \{A2\text{-}3\}$$

Likewise using {A2-2} the G_m is

$$G_m = \frac{-1}{\frac{-(50\ \Omega)}{10^{T_{dB}/20}} + 2(50\Omega)} - G_a \qquad \{A2\text{-}4\}$$

where T_{dB} is the measured signal level in dB from the network analyzer (i.e. measured S_{21}) at the resonant peak. Motional conductance was calculated for each device by applying the relations {A2-3} and {A2-4} at the device's resonant peak frequency (i.e. G_m @ $peak = g_m$). Examining the variation of G_M across the region of the resonant peak, after converting back to dB, allows for direct measurement of Q.

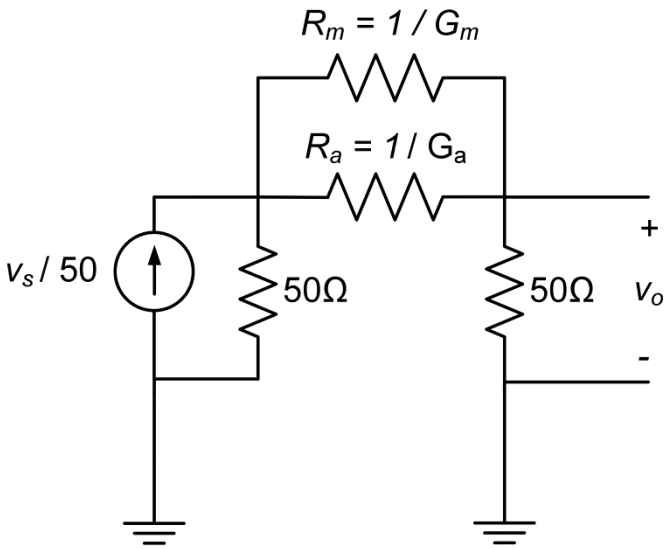

Figure A2.1: Electrical Equivalent Circuit for the measurement of G_m

In the case of devices which exhibit a positive resonant peak, Eq. {A2-3} can be further approximated under certain conditions. Specifically, if the actuator resistance is much greater

that the internal impedance of the network analyzer (i.e. $R_A \gg 50\Omega$) than for the out-of-band calculation of G_A the following approximation can be made

$$\frac{V_o}{V_s} = \frac{50\Omega}{2(50\Omega) + R_A} \sim \frac{50\Omega}{R_A} \qquad \{A2\text{-}4\}$$

Likewise, for the calculation of G_m, if the parallel combination of motional resistance and actuator resistance is much greater than the resistance of the network analyzer than the additional following approximation can be applied

$$\frac{V_o}{V_s} = \frac{50\Omega}{2(50\Omega) + \frac{1}{G_a + G_m}} \sim \frac{50\Omega}{\frac{1}{G_a + G_m}} \qquad \{A2\text{-}5\}$$

Considering {A2-4} and {A2-5}, Eq. {A2-3} would then approximate to

$$G_m = \frac{1}{2(50\Omega)}\left(10^{\frac{T_{dB}}{20}} - 10^{\frac{T_{dBfloor}}{20}}\right) \qquad \{A2\text{-}6\}$$

As an example, the data shown in Figure 5.4 is shown processed using this method in Figure A-1, which can be considered significantly suboptimal for this method.

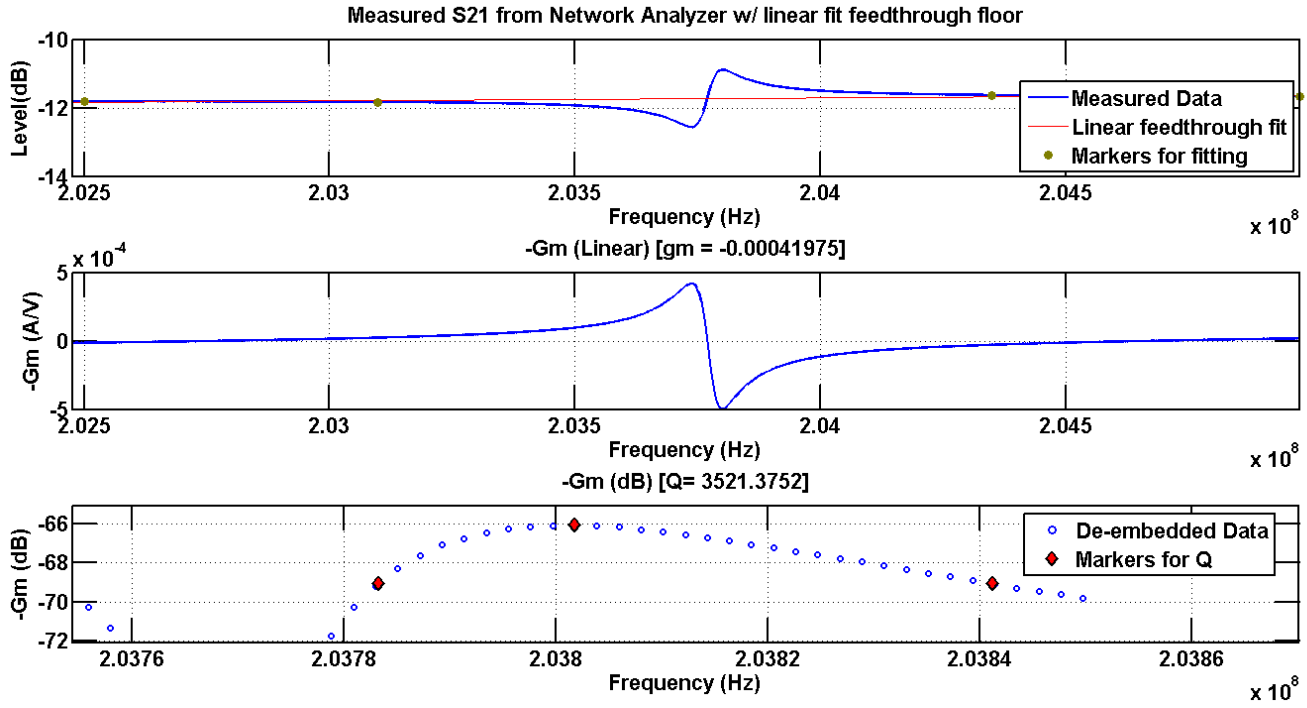

Figure A2.2: Example of alternate de-embedding method using a resistive model with magnitude only. The data shown is for Device D4 at I_{DC}= 3.5 mA , 50-70 Torr.